Dissertation zur Erlangung des Doktorgrades

der Fakultät für Chemie und Pharmazie

der Ludwig-Maximilians-Universität München

Controlling the Surface Growth of Metal-Organic Frameworks

Camilla Catharina Scherb

aus

München

2009

ERKLÄRUNG

Diese Dissertation wurde im Sinne von § 13 Abs. 3 der Promotionsordnung vom 29. Januar 1998 von Herrn Prof. Dr. Thomas Bein betreut.

EHRENWÖRTLICHE VERSICHERUNG

Diese Dissertation wurde selbstständig, ohne unerlaubte Hilfe erarbeitet.

München, den 23.07.2009 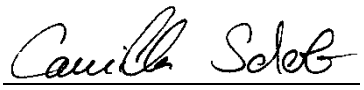

(Unterschrift des Autors)

Dissertation eingereicht am 29.05.2009

1. Gutachter: Prof. Dr. Thomas Bein

2. Gutachter: Prof. Dr. Peter Klüfers

Mündliche Prüfung am 21.07.2009

DANKSAGUNG

Meinem Doktorvater Professor Thomas Bein danke ich herzlich für die Aufnahme in seinen Arbeitskreis. Seine Unterstützung, die interessanten Diskussionen und ein sehr freundliches und freies Arbeitsklima haben es mir erst ermöglicht, diese Arbeit zu erstellen.

Ich möchte mich bei Dr. Maryiam Shöâée, Dr. Neena John, Prof. Martin Attfield und Prof. Michael Anderson für die erfolgreiche Zusammenarbeit in dem gemeinsamen *in situ* AFM Projekt und für die Gastfreundschaft bei meinem Aufenthalt in Manchester bedanken.

Dr. Enrica Biemmi danke ich für den perfekten Einstieg in das Thema dieser Doktorarbeit. Durch unsere Zusammenarbeit an ihrem letzten und meinem ersten Projekt konnte ich sehr viel von ihr und für meine weiteren Projekte lernen.

Dr. Jennifer Williams möchte ich für die gemeinsame Arbeit an meinem „letzten Kapitel“ danken. Ich habe mich sehr gefreut, dass sie sich während der letzten fünf Monate in unserem Arbeitskreis für das Thema begeistern konnte und mir mit viel Rat und Tat zur Seite stand.

Dr. Steffen Schmidt und Dr. Markus Döblinger möchte ich für die Geduld beim Aufnehmen zahlreicher SEM Bilder danken.

Für die große Hilfe beim Bau der neuen Röntgenzelle sowie für alle weiteren kleineren und größeren Spezialanfertigungen möchte ich mich bei Herrn Hiermaier und Herrn Straube von der Feinmechanik-Werkstatt bedanken. Herrn Bachmeier

danke ich sehr für seine Unterstützung beim Umbau der QCM und allen dabei auftretenden Schwierigkeiten.

Die Zeit im AK Bein war vor allem deshalb so einzigartig und lustig, weil ich viele besondere Menschen kennen gelernt habe, die zu sehr guten Freunden geworden sind. Hendrik und Enrica (und natürlich auch Ank und Sebastian) haben mich auf jede erdenkliche Weise unterstützt: Vielen Dank! Auch bei Monika möchte ich mich für die zahlreichen wissenschaftlichen Diskussionen und allen weiteren Erfahrungsaustausch, die vieles leichter gemacht haben, bedanken. Vielen Dank auch an Andreas, Johann, Johannes, Lea und Anderl die mich von Anfang an sehr herzlich im AK Bein aufgenommen haben und jederzeit bei Fragen und Problemen zur Stelle waren. Ich möchte auch Ralf für die große Unterstützung wären der ganzen Zeit meiner Promotion danken. U.a. für die vielen unterhaltsamen Kaffeepausen und das tolle Arbeitsklima im AK Bein bedanke ich mich bei Mirjam, Jörg, Axel, Huihong, Valentina, Dina, Karin, Johann, Benni, Doro, Hans und Florian, dem ich auch für die weitere Arbeit viel Glück und Erfolg wünschen möchte.

Ein großes Dankeschön geht an Regina, Dagmar und Tina, die durch ihre unermüdliche Arbeit für sehr gute Arbeitsbedingungen im AK Bein sorgen und deren Unterstützung in allen Belangen immer eine große Hilfe war.

Der größte Dank geht an meine Familie, meine Eltern, meine Schwester und natürlich an meinen Freund Alex. Für die Unterstützung in jeder Hinsicht, das Vertrauen in mich und meine Arbeit und die Ermutigung bin ich unendlich dankbar.

Abstract

This work is focused on the investigation of synthesis conditions for the direct growth of metal-organic frameworks (MOFs) on self-assembled monolayers (SAMs) used for surface functionalization. The characterization of the surface-grown crystals is a central part of this thesis, in order to learn more about the mechanism of MOF crystallization and the interesting properties of this class of materials leading to future applications.

The tuneable oriented growth of thin films of the porous MOF HKUST-1 ($Cu_3(C_9H_3O_6)_2(H_2O)_3 \cdot xH_2O$) on different functionalized SAMs is demonstrated. Films grown on carboxylate-terminated SAMs are highly oriented along the [100] direction, while alcohol-terminated surfaces induce a completely different orientation along the [111] direction. Homogeneous but less oriented thin films are also obtained on methyl-terminated SAMs. A combination of X-ray diffraction and scanning electron microscopy was used to study the film growth, including the morphological evolution of the crystals on the SAMs.

In situ atomic force microscopy was used to directly investigate the growth processes of the oriented MOF HKUST-1 grown on SAMs on gold substrates. This approach provides direct evidence for a layer-by-layer mechanism of the constituent 1.5 nm d_{111} crystal spacing step, its form during growth, and the influence of the step vertex on the rate of growth.

The orientation and structure of porous MOFs based on iron terephthalate can be controlled by heterogeneous nucleation on self-assembled monolayers of mercaptohexadecanoic acid (MHDA). The framework MIL-53 is the product of

homogeneous nucleation, whereas in the same crystallisation solution, oriented MIL-88B grows on the functionalized gold surface.

A new sample cell was developed to allow for the investigation of the structural changes of flexible, porous materials during adsorption and desorption of guest molecules. Crystals of the flexible MOF Fe-MIL-88B were investigated as bulk material as well as surface-grown, oriented crystals. We were able to follow the structural changes of the Fe-MIL-88B crystals upon ad- and desorption of water. Due to the orientation of the crystals on the gold substrates, structural changes in [001] direction could be observed. For the randomly oriented bulk crystals the structural changes in all crystallographic directions are observable and the changes of the lattice constants *a* and *c* and the cell volume could be determined quantitatively by indexing of the complete diffraction patterns. The sorption isotherms recorded with the help of the sorption@XRD method show two distinct steps of structural changes. During adsorption of water the lattice parameter *c* is slightly but still detectably decreased, whereas the lattice parameter a shows *a* prominent two step-increase resulting in an increase of the cell volume about 40 %. The conventional volumetric water sorption measurement also shows two distinct steps of the amount of adsorbed volume that can be correlated to the structural changes observed in X-ray diffraction.

We have demonstrated that advantages of functionalization can also be realized in oriented film synthesis of MOFs: We have shown for the first time that functionalized MOFs can be grown on self-assembled monolayers and that a preferred orientation of the crystals is achieved. This was demonstrated for NH_2-MIL-101 and to a lesser extent for NH-MIL-88B. Importantly for potential storage applications, it was also

shown that the adsorption capacity of NH_2-MIL-101 was not significantly reduced by the amino functionalization.

Table of Contents

Erklärung I

Ehrenwörtliche Versicherung I

Danksagung III

Abstract V

Table of Contents IX

1 INTRODUCTION 1

1.1 Metal-Organic Frameworks as a fast developing class of crystalline porous materials 1

Classical crystalline porous materials: Zeolites and zeotypes 1

Inorganic-organic hybrid materials 3

Prospects for applications of MOFs 8

Novel framework structures: covalent organic frameworks 11

1.2 Self Assembled Monolayers 13

1.3 Inorganic crystal growth on surfaces 16

Biomineralization 17

Crystal growth of inorganic materials on functionalized surfaces 17

1.4 Concept of direct growth of MOFs on functionalized surfaces. 20

1.5 Goals 26

2 CHARACTERIZATION 29

2.1 X-ray Diffraction 29

2.2 Electron microscopy 32

Scanning Electron Microscopy (SEM) 32

2.3 Atomic Force Microscopy (AFM) 35

Historical Background 35

Atomic Force Microscope working principle 37

MultiMode™ SPM 39

AFM in fluids 41

2.4 Vibrational Spectroscopy 42

2.5 Adsorption measurements 44

Characterization of porous solids 44

Quartz Crystal Microbalance (QCM) 49

2.6 Thermogravimetric analysis and Differential Scanning Calorimetry 51

3 ORIENTED GROWTH OF METAL-ORGANIC FRAMEWORK HKUST-1 TUNEABLE WITH FUNCTIONALIZED SELF-ASSEMBLED MONOLAYERS 53

3.1 Introduction 53

3.2 Experimental Section 56

Self-assembled monolayers on gold 56

HKUST-1 Synthesis Mixture 57

Thin-film growth 58

3.3 Characterization 58

3.4 Results and discussion 59

3.5 Conclusion 72

4 SINGLE LAYER GROWTH OF SUB-MICRON METAL-ORGANIC FRAMEWORK CRYSTALS OBSERVED BY *IN SITU* ATOMIC FORCE MICROSCOPY 73

4.1 INTRODUCTION 73

4.2 EXPERIMENTAL 76

Self-assembled monolayers on gold 76

HKUST-1 synthesis mixture and Preparation of HKUST-1 Thin Films 77

Preparation of the crystallisation solution for in situ AFM Measurements ... 77

In Situ AFM measurements 77

Quantitative Analyses of AFM Scans 78

4.3 RESULTS AND DISCUSSION 78

4.4 CONCLUSION 86

4.5 ADDITIONAL DETAILS 86

Dissolution in pure ethanol 87

Growth and dissolution in Cu(II)/BTC solutions 90

5 DIRECTING THE STRUCTURE OF METAL-ORGANIC FRAMEWORKS BY ORIENTED SURFACE GROWTH ON AN ORGANIC MONOLAYER. 95

5.1 INTRODUCTION 95

5.2 EXPERIMENTAL SECTION 101

Preparation of self-assembled monolayers on gold 101

Fe-MIL-53 synthesis mixture 101

Thin film growth 101

Fe-MIL-88B synthesis 102

5.3 CHARACTERIZATION 103

5.4 Results and Discussion 103

5.5 Conclusion 113

5.6 Additional Details 114

Optimization of the Synthesis pathway for MIL-88B films 114

Synthesis and Characterization of Fe-MIL-53 116

6 SORPTION PROPERTIES OF ORIENTED, THIN-FILM FE-MIL-88B CRYSTALS STUDIED BY X-RAY DIFFRACTION 121

6.1 Introduction 121

6.2 Methods 123

Experimental setup of the flow controlling system 123

Development of the new sample cell for sorption@XRD measurements 127

Synthesis and Sample Preparation 129

Further sample characterization 129

6.3 Results and Discussion 130

6.4 Conclusions 142

6.5 Additional Details 143

6.6 Documentation of the LabView control programmes 146

LabView control programme for automated Sorption@XRD measurements 146

Redesigned LabView control programme for automated QCM measurements 153

Excel sheet for the calculation of settings of digital MFCs during Sorption@XRD and QCM measurements 173

List of included SubVis in the programme QCM Main.vi 174

7 EXTENDING THE STRUCTURE-DIRECTING CONCEPT TO FUNCTIONALIZED METAL-ORGANIC FRAMEWORKS 177

7.1 Introduction 177

7.2 Experimental 179

Preparation of self-assembled monolayers on gold 179

Synthesis of bulk NH_2-MIL-101 179

Preparation of the crystallization solution for film growth of NH_2-MIL-101 180

Film Growth of NH_2-MIL-101 180

7.3 Characterization 180

7.4 Results and Discussion 181

7.5 Conclusion 187

7.6 Additional Details 188

Synthesis of NH_2-MIL-88B 190

Preparation of self-assembled monolayers on gold 191

Preparation of the crystallization solution for film growth of NH_2-MIL-88B on –COOH terminated SAMs 191

Film-Synthesis of NH_2-MIL-88B 191

8 GENERAL CONCLUSIONS 193

9 REFERENCES 197

10 APPENDIX: 217

10.1 List of abbreviations 217

10.2 Synthesis and Characterization of Fe-MIL-101 220

Synthesis of Fe-MIL-101 220

Characterization of Fe-MIL-101 220

11 CURRICULUM VITAE 225

12 PUBLICATIONS AND PRESENTATIONS 225

12.1 Publications 227

12.2 Oral Presentations 228

12.3 Poster Presentations 229

1 Introduction

1.1 Metal-Organic Frameworks as a fast developing class of crystalline porous materials

The classification of porous materials is usually given by the diameter of their pores. According to IUPAC, microporous (< 2 nm), mesoporous (2 – 50 nm) and macroporous (> 50 nm) materials are distinguished.[1]

The interest in porous materials results from their outstanding properties and their manifold applications. Zeolites being an important class of crystalline porous hosts are widely employed as catalysts[2] in the petrochemical industry, ion exchangers in detergents[3] and as molecular sieves in the separation technology,[4] to name some of the most important fields. During the last decades, several new classes of porous materials were discovered and much research work is focused on the exploration of new compounds and their properties. Within this chapter, a short introduction into classical crystalline porous materials will lead to the more detailed overview over metal-organic frameworks as interesting porous hybrid materials.

Classical crystalline porous materials: Zeolites and zeotypes

Zeolites were first discovered by the Swedish mineralogist Axel Fredrik Cronstedt in 1756.[5] The term “zeolite” was chosen based on the Greek words “zein” (“to boil”) and “lithos” (“stone”) as the crystals released evaporating water upon heating.

Zeolites are crystalline aluminosilicates built from $[SiO_4]$ and $[AlO_4]^-$ tetrahedra, that are connected in a way to form frameworks with channels and cavities in the range of 3 – 15 Å.[6-8] Negative charges resulting from replacement of silicon by aluminium ions are compensated by counter metal ions, typically alkali or alkaline earth cations inside the structure. Even before the structures of zeolitic frameworks could be revealed, several key properties were discovered by the investigation of natural zeolites, such as reversible dehydration[9] and ion exchange.[10] The first structure determinations of zeolite frameworks were achieved in 1930 by Taylor and Pauling.[11, 12] This led to the preparation of synthetic zeolite structures, starting with the pioneering work of Richard Barrer and Robert Milton.[13-16] In the following years important industrial applications were found for these new synthetic framework structures, such as the use of zeolite X as a cracking catalyst by Mobil Oil.[17] To date 48 natural zeolites and more than 150 synthetic framework structures are known.[17,18]

The partial or full substitution of silicon and aluminium by hetero-elements gives the so-called zeotypic compounds. One important representative class of these are (silico-)aluminophosphates (SAPO / $AlPO_n$), microporous crystalline molecular sieves, that were first described in 1982.[19, 20] Also metal phosphate open framework structures are known for many different metals, for example iron[21], copper[22] and titanium.[23]

In addition to the classical applications for zeolites and zeotypes mentioned above, in recent years, the fields of application shifted more and more to new areas such as gas storage,[24-26] sensor devices,[27, 28] solar cell technology,[29, 30] heat storage,[31, 32] biological carriers,[33, 34] medical technologies[35, 36] and many others.

The drawback for some applications of zeolites is the limitation of the pore size of these materials due to the construction of the framework structures from corner or edge sharing tetrahedra. This insight was fertile ground for the development of new porous compounds with tuneable and larger pore sizes. One class of materials that overcomes limits in pore dimensions are mesoporous materials, which are only crystalline in terms of pore structure, while the walls between the pores consist of amorphous silicon dioxide or other metal oxides.[37-39] A completely different approach led to the discovery of porous inorganic-organic hybrid materials with different tuneable pore sizes within the concept of reticular chemistry; this class of compounds shall be discussed in detail in the following section.

INORGANIC-ORGANIC HYBRID MATERIALS

Inorganic-organic hybrid materials can be crystalline or X-ray amorphous, the bonding between the inorganic and organic parts may be covalent, coordinative or based on van-der-Waals interactions. It is easy to imagine that this general definition comprises a large number of completely different chemical compounds. This work is focused on the subgroup of inorganic-organic hybrid material with coordinative bonding between the metal ions (inorganic parts) and the organic linkers: the so-called Metal-Organic-Frameworks (MOFs) or coordination polymers. The term “metal-organic framework” was defined by Omar Yaghi in 1995[40] and is nowadays widely used for all microporous materials emerging from the modular concept of combining metal centres and organic compounds for the formation of three-dimensional framework structures. However the first synthesis of MOFs - even though not named as such at the time - was reported by Tomic in 1965.[41] Currently many research groups are working on the synthesis and characterization of novel MOF structures

focussing on many different aspects of this interesting class of materials. Leading research groups in this field include the groups of Prof. Gérard Férey (France), Prof. Omar Yaghi (USA) and Prof. Susumu Kitagawa (Japan).[42]

Usually, MOFs are synthesized from solution under solvothermal conditions; typical solvents are water, ethanol, methanol, dimethylformamide (DMF) or acetonitrile, temperatures may vary from room temperature to 250 °C. As depicted schematically in Figure 1.1, MOFs form in a self-assembly process through coordination of organic ligands to metal centres.

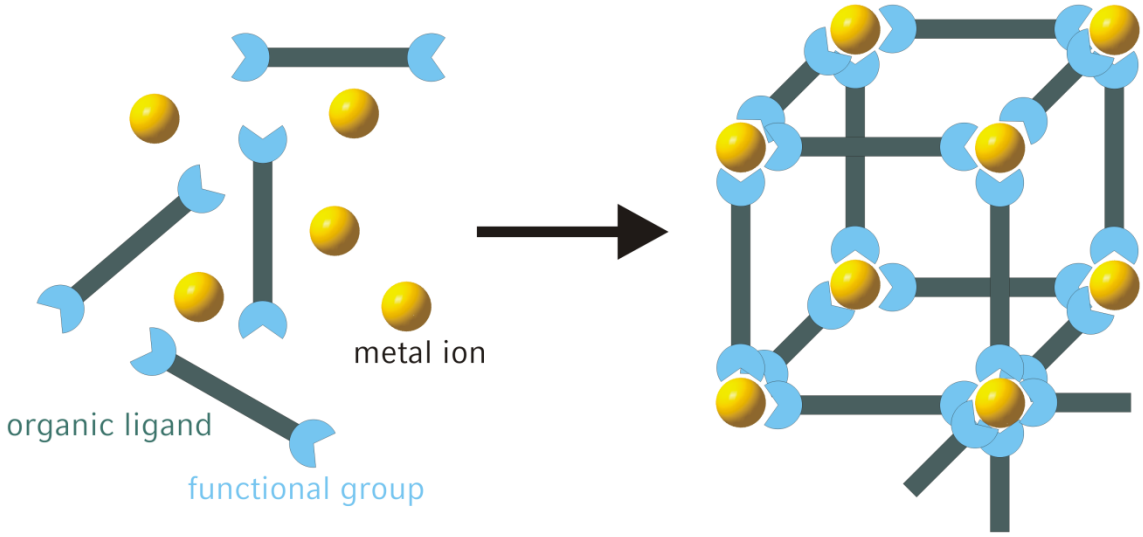

Figure 1.1: **General building scheme for MOFs: organic ligands with at least two functional groups coordinate to metal ions resulting in 3D framework structures.**

The functional groups appropriate for coordinative bonding to the metal ions are most commonly carboxylates, phosphonates, sulfonates and nitrogen derivatives such as pyridines and imidazoles. The organic linkers are often chosen to be rigid, so that

aromatic systems are preferred over alkyl chains for the carbon backbone. The coordination of the chelating ligands to the metal ions often leads to metal-ligand polyhedra, in most cases metal-oxygen polyhedra. These polyhedra may be linked to each other to form the so-called Secondary Building Units (SBUs).

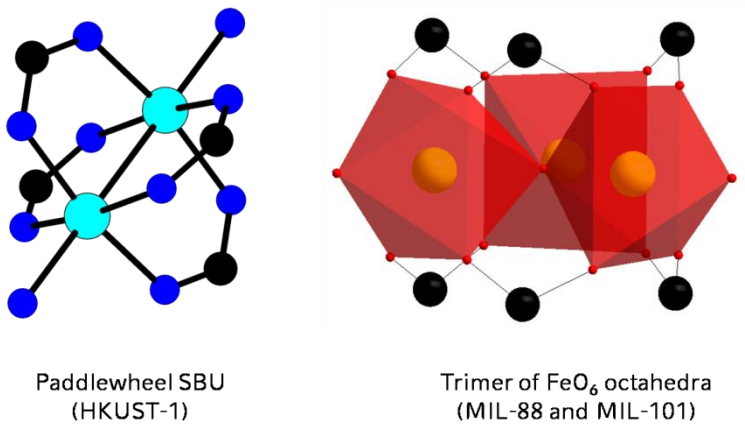

Figure 1.2: Secondary Building Units (SBUs) of HKUST-1 (left): paddlewheel unit consisting of two copper atoms coordinated by four carboxylate groups and two water molecules and of MIL-88 and MIL-101 (right): trimer of iron-oxygen octahedra linked by one μ3 oxide ion and six carboxylate groups.

Figure 1.2 represents the typical SBUs known from relevant MOF structures, namely of HKUST-1 (Hong-Kong University, structure 1, consisting of copper as the metal component and benzenetricarboxylic acid as the organic ligand) and MIL-88 (Matériaux de l'Institut Lavoisier, number 88) as well as MIL-101 (both consisting of trivalent metal ions like iron (III), chromium (III) or aluminium (III) and terephthalic acid) these are to be found in several additional MOF structures as well. There is evidence in the literature that some inorganic SBUs of the MOFs form prior to crystallisation of the inorganic-organic hybrid structure.[43]

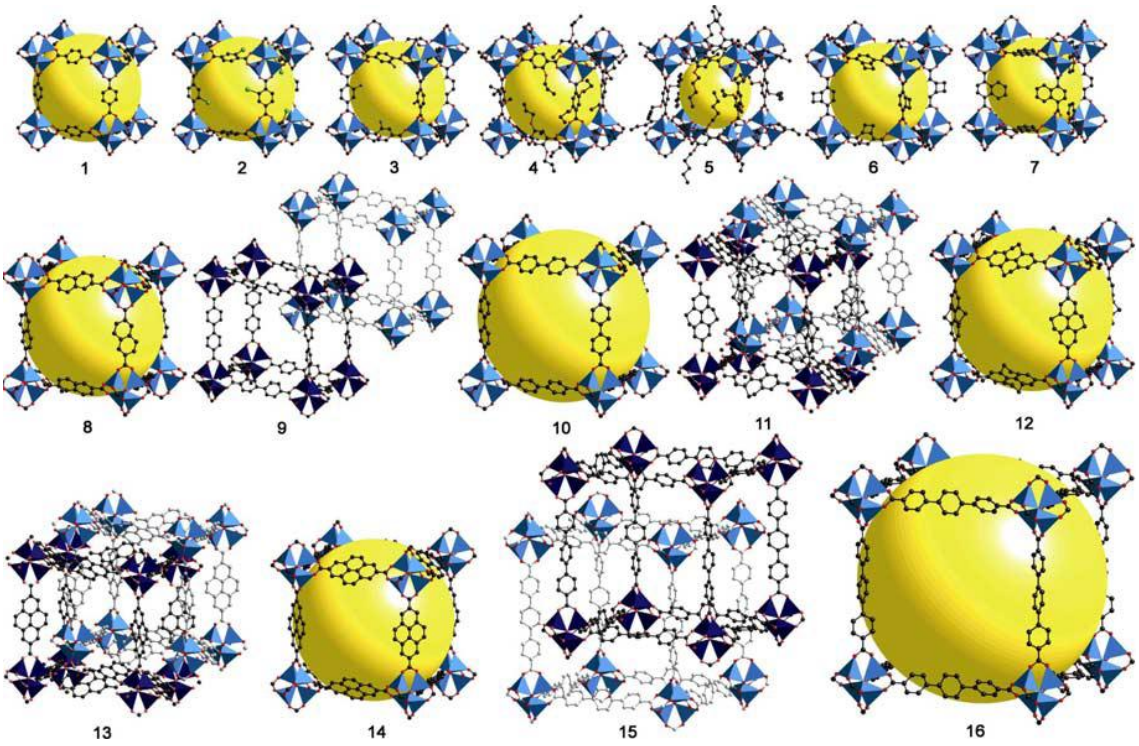

Figure 1.3: **Series of isoreticular MOF structures (IRMOFs) with the same cubic network topology, the particular linkers differ in functionality and length. While expansion of the linkers increases the internal void space (represented by yellow spheres), it also allows the formation of catenated phases.[44]**

The synthesis of MOFs gives rise to the concepts of network design and reticular chemistry.[45] The idea of tuning the properties, i.e. the pore size and functionality of a MOF structure with a certain network topology was first demonstrated by the group of O. Yaghi in 2002, where a series of isoreticular MOF-structures (IRMOFs), based on the network topology of MOF-5, a zinc-terephthalate with a cubic framework structure[46] was presented with 16 different molecules acting as organic linkers, with different length and functionality.[47] (Figure 1.3)

The concept of reticular chemistry is widely employed in the research in the field of MOFs to obtain porous crystalline compounds with engineered properties for different applications.[48-53] The use of longer ligands may lead to the formation of catenated (also called interpenetrating) phases with smaller specific surface area and smaller pore dimensions than the corresponding non-catenated structure (see also Figure 1.3).[54] The most impressive impact of catenation is a reduction of the free diameter of the pores, i.e., it represents a potential strategy for improving hydrogen uptake.[55]

Challenges associated with obtaining new structures with larger pores and consequently larger unit cells and different functionalities of the organic linkers, i.e., additional alkyl chains, amino, hydroxyl or carboxylic acid groups, may occur in the synthesis of the materials due to different solubilities of the larger compounds on the one hand, and in the solution of the crystal structures of compounds with such large unit cells on the other hand. One approach to overcome the difficulties with drastically different synthesis conditions is to investigate the parameters of the synthesis field systematically with the help of high-throughput methods.[56-59] The high-throughput method allows for the systematic investigation of synthesis parameters while using low amounts of chemicals, resulting in faster and less expensive access to the desired information over a broad range of parameters. To solve complex crystal structures with large unit cells, the group of Prof. Férey has developed the so-called AASBU (automated assembly of secondary building units) approach.[60] Here the inorganic and organic SBUs are assembled to give hypothetical crystal structures. The simulated X-ray diffraction patterns of these hypothetical structures are then compared to experimental patterns, obtained from the synthesis carried out with the

same compounds used for the simulation. If both patterns are in good agreement, the simulated structure obtained from the AASBU approach is used as the starting point for the refinement of the crystal structure.

The choice of organic linkers with certain functionalities is expected to lead to the design of MOF structures with particular properties (pore surface design). The group of S. Kitagawa has focused the research on this challenge by tuning the organic linkers in order to obtain the host-guest interactions desired for a particular application.[61] Another highly interesting approach is the use of chiral organic linkers to create specific asymmetric environments for guest molecules within the pores.[62-66]

The tuning of certain properties leads to the question of possible applications for this interesting class of materials, which will be the subject of the following section.

Prospects for applications of MOFs

Interesting features of MOFs such as high thermal stability and high metal content were already investigated in the aforementioned first publication reporting carboxylates of metals like zinc, nickel, iron and aluminium in 1965.[41] As described above, the reticular design of MOFs allows for the tuning of pore size and functionality, thus greatly influencing the properties of MOFs suitable for applications. The most promising application prospects shall be described within this section.

Catalysis

In comparison with zeolites, MOFs offer lower thermal stability and therefore are not expected to be a suitable substitution for the latter in high temperature processes such as catalytic cracking. First proof of the catalytic activity of MOFs was obtained in vinyl group esterification reactions on MOF-2 and MOF-5. It could be shown, that, compared to the zinc paddlewheel-containing MOF-2, MOF-5 with fully saturated zinc-coordination is quite poor in performing in the selective esterification, demonstrating the important role of accessible metal sites in MOF structures.[67] Successful catalysis on zinc-containing MOFs in the activation of alkoxides and carbon dioxide for the formation of polypropylene carbonate,[68, 69] and even entioselective conversions with an enantiomeric excess of 8 %[66, 70] have already been reported. Further catalytic reactions from different research groups were already reported, i.e. Ziegler–Natta-type polymerization, Diels–Alder-reaction, transesterification, cyanosilylation of aldehydes, hydrogenation and isomerisation reactions.[53] Future studies will have to prove the value of MOFs as catalysts in terms of efficiency, costs and stability and reveal the yet unknown mechanisms of catalytic activities of this class of materials.

Gas purification

The BASF AG was able to demonstrate that the volume specific uptake of tetrahydrotiophene was about ten times higher with the investigated MOF HKUST-1 (the structure of which is discussed in detail in chapter 3) than with conventional activated carbon materials. A dominant colour change of the HKUST-1 crystals for several enclosed molecules allows visible detection of breakthrough and contaminant

saturation. During removal of the contaminant by vacuum treatment or heating, the original colour reappears, indicating a possible regeneration of the adsorbent.[67]

Gas storage

The probably most striking property of many MOFs is the total lack of non-accessible bulk volume. Although high surface areas are already known from activated carbons and zeolites, it is the absence of any dead volume in MOFs which principally gives them the highest porosities and world record surface areas.[67] The highest surface areas of known MOFs are reported for MOF-177[71] and MIL-101[72] with 4500 m^2g^{-1} and 5900 m^2g^{-1}, respectively. This intriguing property of MOFs makes them interesting candidates for any application concerning gas storage, with special focus on hydrogen storage.[51, 55, 73-86] Safe and efficient gas storage is an important requirement for the employment of alternative energy resources in both mobile automotive as well as portable electronic device applications. Storage of a gas in MOF-filled canisters can be used to either enhance capacity in a given volume or transport an equivalent amount of gas at a far lower pressure. It was, for instance, possible to keep methane, propane and other hydrocarbons at a denser state by storing them in MOF-filled containers.[67, 69, 87] Especially promising materials are MOFs with light metal atoms such as Al-MIL-53, for which a hydrogen storage capacity of 3.8 wt.% when loaded at 77 K under 1.6 MPa could be shown.[88]

The temperature required for a possible application might direct the choice of particular structures: highly porous MOFs might be favourable for low temperatures, whereas rather small pore materials,[89, 90] or highly attractive and flexible ones,[88, 91] could be favourites for room temperature storage. Additional mechanisms including

chemisorption, as in hydrides, and physisorption, as in MOFs, might offer a solution to future challenges.[67]

Novel framework structures: covalent organic frameworks

A new class of porous hybrid materials was introduced by Yaghi *et al.* in 2005.[92, 93] Covalent organic frameworks (COFs) were either obtained by self-condensation of aromatic organoboronic acids or by condensation of organoboronic acids with aromatic alcohols. Both products present covalent bonding instead of the coordinative bond of metal-ligand interactions in MOFs. COFs consist exclusively of light elements, such as carbon, boron, hydrogen and oxygen, which is in contrast to MOFs containing heavier metal atoms. The employment of different rigid aromatic compounds leads to the formation of rings, tuneable in size, thus picking up the concept of reticular chemistry already established in MOF synthesis.[94] The size of the rings and therefore the size of the pores lie in the micro- to mesoporous range. The first described structures consist of porous 2D sheets, which can be arranged in the third dimension by π-stacking, such that the pores are aligned, resulting in 1D channels.[92, 95] The planarity of the 2D sheets directly results from the aromaticity of the condensating organic compound. The next step was to use triangular and tetrahedral nodes to construct 3D covalent structures. This approach led to the successful synthesis of COF-102, COF-105 and COF-108 (Figure 1.4).[96]

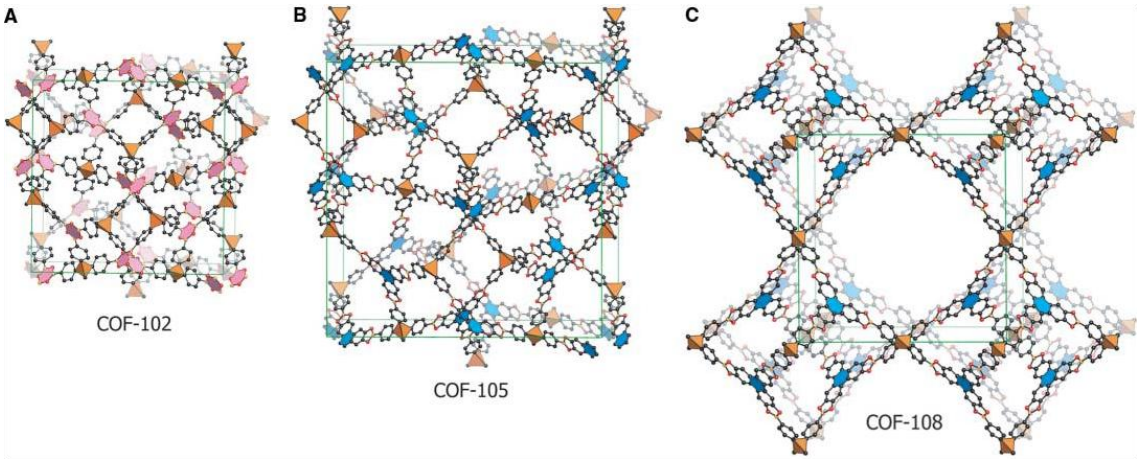

Figure 1.4: **Atomic connectivity and structure of COF-102 (A), COF-105 (B), and COF-108 (C), based on powder diffraction data and modelling. Carbon, boron, and oxygen atoms are represented as gray, orange, and red spheres, respectively.[96]**

Due to the construction of these materials from strong covalent bonds, the thermal stability of COFs is very high (400 – 500 °C) and they are also shown to have very high surface areas. These properties, in addition to their extremely low densities invoked research studies on the possible employment of COFs as hydrogen storage materials.[86, 97-100] As described for MOFs, it is possible to use substituted organic compounds as starting materials for the COF synthesis. This permits to tune the pore size of the materials through implementation of alkyl chains into a known COF structure.[101] Different substituents, such as functional groups, will lead to the formation of pores with tuneable functionalities, further increasing the design possibilities of this relatively new class of materials.

1.2 Self Assembled Monolayers

Self-assembled monolayers (SAMs) are organic assemblies formed by the adsorption of molecules from solution or the gas phase onto the surface of solids. The adsorbates organize spontaneously into crystalline or semi crystalline structures. The molecules assembling in SAMs feature a chemical functionality or "head group" with a specific affinity for a substrate, which is often so strong that the molecule displaces other adsorbed organic compounds from the surface. The most extensively studied class of SAMs consists of alkanethiols on gold and other noble and coinage metals;[102-112] a schematic representation of an ideal SAM of alkanethiolates on gold is depicted in Figure 1.5. The high affinity of thiols for noble metals offers the possibility to obtain well-defined organic surfaces with different chemical functionalities displayed at the exposed interface.[113] There are also different examples for organic monolayers on different substrates, for instance alkylsiloxane SAMs on oxidic materials like SiO_2. The discussion of SAMs within this section shall be limited to the alkanethiol / Au (111) system, as this is the only one employed for this work. Au(111) surfaces are the preferred substrates for the preparation of alkanethiolate SAMs due to the facile formation of the monolayers and due to the relatively low surface roughness of the (111) face of gold.[114] Au(111) surfaces can be obtained either form single crystals or by evaporation of thin gold films on planar supports, typically mica, glass or silicon wafers.[115-117]

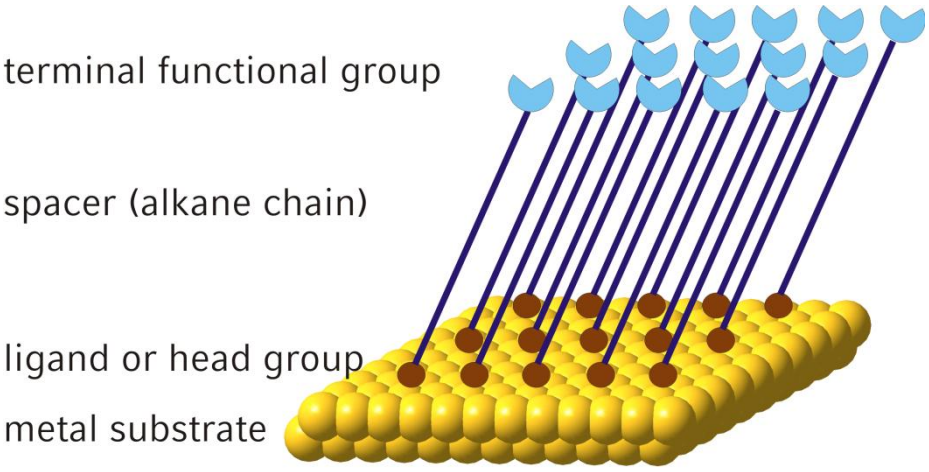

Figure 1.5: Schematic diagram of an ideal, single crystalline SAM of alkanethiolates supported on a gold surface with a (111) texture.

The important issues for the preparation of SAMs from solution are alkanethiol concentration of the solution, length of time for immersion, type of solvent and temperature.[118, 119] The commonly used preparation procedure to prepare thiol-based SAMs is the immersion of thoroughly cleaned gold substrates in a diluted ethanolic solution (1 – 10 mmol/l) of the desired thiol for 18 – 24 h at room temperature.[110] The mechanism of the SAM formation from solution is postulated to be analogous to the assembly of thiolates on gold from the gas phase.[120]

To investigate the structure of SAMs on planar substrates, a number of techniques for surface analysis have been applied, such as reflectance absorption infrared spectroscopy (RAIRS), optical ellipsometry, contact angle goniometry and electrochemistry, and scanning tunnelling microscopy (STM).[105, 118, 121-126]

The surface structure of thiolates on Au(111) is generally accepted to be based on a $(\sqrt{3}\times\sqrt{3})R30°$ overlayer.[103, 106] This structure most probably results from the sulphur

atoms being positioned in the 3-fold hollows of the gold lattice. There is agreement in the literature that the organization of the thiol molecules on the surface adopts a secondary ordering of the chains corresponding to a c(4 × 2) superlattice.[127, 128] This structure is shown schematically in Figure 1.6. The light gray circles with dashed lines indicate the approximate projected surface area occupied by the alkane chains. The red dashed lines in Figure 1.6 mark the formal c(4 × 2) unit cell, the blue dashed lines mark the $2\sqrt{3} \times 3$ unit cell. The alkane chains are tilted in the direction of their next-nearest neighbours; the dark wedges indicate the projection of the CCC plane of the alkane chain onto the surface. The distance between pinning sites in this geometry is 5.0 Å, resulting in an available area for each molecule of 21.4 $Å^2$. Since the van-der-Waals diameter of the alkane chain is too small (4.6 Å) for the chain to completely occupy that area, the chains will tilt, forming an angle of approximately 30 ° with the surface normal.[114]

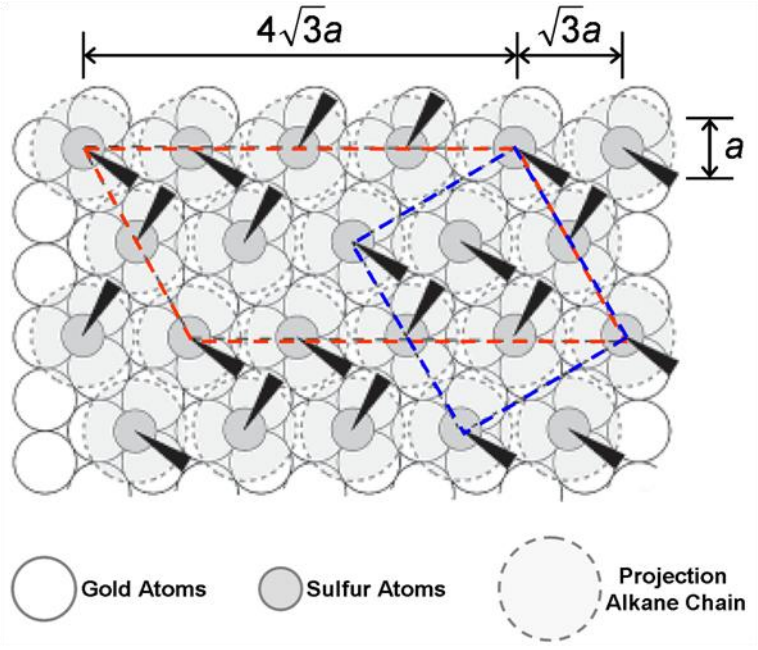

Figure 1.6: Structural model of the adlayer formed by thiols on the gold lattice.[103]

It has been shown that SAMs formed from thiols with an alkane chain length of twelve or more methylene units present well-ordered and dense monolayers. As the chain length decreases, the SAM becomes increasingly disordered with low packing density and coverage; this lack of order has been attributed to weak interchain interactions and to a greater concentration of gauche defects.[105]

The terminal functional group of the thiol determines the functionality of the SAM. The possibility to tune the organic functionality makes SAMs very interesting candidates for various purposes. The preparation procedure of SAMs from thiols with different functional terminal groups may depend on the nature of the functional group. For example, with carboxylated organothiols, which were also employed within this work, hydrogen bonds between the terminal carboxylic acid groups may occur. It was shown that the structural quality of the SAM strongly depends on the preparation conditions.[129]

In general, within the last decades SAMs have received considerable attention with respect to fundamental aspects[119] as well as in view of potential technical applications in fields such as molecular recognition,[130] corrosion protection,[131] organic-molecular electronics,[132-134] and, as employed within this work, as functionalized substrates for crystallization (see following sections).

1.3 Inorganic crystal growth on surfaces

„The systematic fabrication of advanced materials will require the construction of architectures over scales ranging from the molecular to the macroscopic. The basic constructional processes of biomineralization – supramolecular pre-organization,

interfacial molecular recognition (templating) and cellular processing – can provide useful archetypes for molecular-scale building or "molecular tectonics" in inorganic materials chemistry." (Stephen Mann, 1993)[135]

Biomineralization

The definition of biomineralization is the process by which living organisms produce minerals, often to harden or stiffen existing tissues. The concept of biomineralization refers to oriented nucleation, control over crystal morphology, formation of unique composites of proteins and single crystals, and the production of ordered multicrystal arrays.[136] It is an extremely widespread phenomenon; over 60 different minerals have been identified in organisms.[137]

The mechanisms involved in biomineralization, i.e. the processes that result in the construction of higher-order architectures, may serve as guide for materials scientists to develop new methods for the controlled synthesis of organized inorganic and composite materials.[138, 139] Interesting examples, where the concept of biomimetic materials was picked up, will be discussed in the following section.

Crystal growth of inorganic materials on functionalized surfaces

To mimic the influence of organic molecules on crystallisation observed in nature,[140] often SAMs are used to create organic functionalized surfaces.[141]

In 1994 Bunker *et al.* reported the formation of ceramic thin films on functionalized interfaces through biomimetic processing.[142] This approach covered the preparation of ceramic films on plastic and metal substrates leading to the formation of high-quality, dense polycrystalline films of oxides, hydroxides, and sulphides at

temperatures below 100 °C. For some ceramics preferred orientation of the crystallites was observed, therefore this process is considered a promising approach towards the production of inorganic-organic composites.

In 1999 oriented growth of calcite controlled by SAMs of functionalized alkane thiols on gold and silver substrates was studied by Aizenberg *et al.*[143] High level control over the crystal orientation could be achieved by employment of different terminal functional groups of the SAMs on the metal substrates; selective nucleation of calcite from six crystallographic planes could be obtained. The great influence of the geometry of the array of certain terminal functional groups is attributed to the highly ordered structure of the applied SAMs; patterned SAMs were applied and led to the formation of high-resolution patterns of differently oriented crystals.

Chemical deposition of lead sulphide from solution on carboxylic acid terminated SAMs was studied by Meldrum *et al.* in 1997.[144] The kinetics of crystal growth was followed with the help of surface plasmon spectroscopy. The results reveal that film growth proceeds by the formation of a thin layer over the substrate, followed by nucleation of crystals also demonstrated by transmission electron spectroscopy.

In order to show the possibility of using organic templates to direct the growth of technologically useful inorganic nanocrystals, organically functionalized silver surfaces were used to study the direct growth of ZnO nanorods.[145, 146] The authors suggest that the nucleation and growth morphology of ZnO on surfaces are governed by the surface free energy of the substrate, which can be altered by SAMs with different end groups. For SAMs with chemically active (carboxylic or thiol) end groups, the ZnO morphology is found to be three-dimensional nanorods on low-surface energy surfaces and two-dimensional thin films on high-energy surfaces.

Different functionalized glass substrates were used to investigate the surface-mediated growth of transparent, oriented, and well-defined nanocrystalline anatase titania films.[147] The surface mediated growth is explained with the help of the electrostatic attraction of ions, serving as nucleation sites, from solution to the charged surface groups under the given synthesis conditions.

The above examples of inorganic crystal growth on functionalized surfaces all focus on dense inorganic materials. The first studies presenting oriented, surface-controlled growth of molecular sieve crystals were presented by Sue Feng *et al.* in 1994.[148, 149] Zinco-phosphate and aluminium phosphate molecular sieve crystals were grown on gold substrates functionalized with metal-phosphonate multilayer films. The octahedral zinco-phosphate crystals were shown to grow in [111]-orientation while the hexagonal crystals of AlPO-5 were growing in [001]-orientation. The porosity of the surface-grown crystals could be shown with the help of quartz-crystal-microbalance measurements, thus demonstrating the accessibility of the pores and giving rise to interesting applications such as catalytic membranes or sensor materials. In a different study, oriented growth of TS-1 zeolite crystals was achieved on functionalized glass substrates.[150] The poly(ethylene oxide) SAMs are considered as 2D template leading to the formation of [010]-oriented zeolite thin films.

The studies described within this section on direct crystal growth on functionalized substrates build the basis for the investigations of direct growth of MOF crystals on SAMs. The existing work in this field of research shall be described in the following section.

1.4 Concept of direct growth of MOFs on functionalized surfaces

This work is focused on the investigation of the direct growth of MOFs on gold substrates functionalized with different self-assembled monolayers (SAMs, see section 1.2). Within this section, the concept of direct growth of MOFs on SAMs shall be explained and existing work on this subject will be introduced.

The mechanism of direct growth of MOFs on functionalized substrates is proposed to be analogous to the self-assembly process during the formation of MOF crystals discussed in chapter 1.1. The concept of direct growth of MOF crystals on organic monolayers is depicted in Figure 1.7. The central idea is to use or in fact mimic the particular functional groups of a certain MOF structure on the surface as functional terminal groups of the employed SAM. This enables coordination of the metal ions or SBUs from the solution to the surface. The attached metal centres or SBUs will subsequently be coordinated by the organic ligands present in the solution; this process further leads to the crystal growth of the desired MOF, with the crystals being directly attached to the surface.

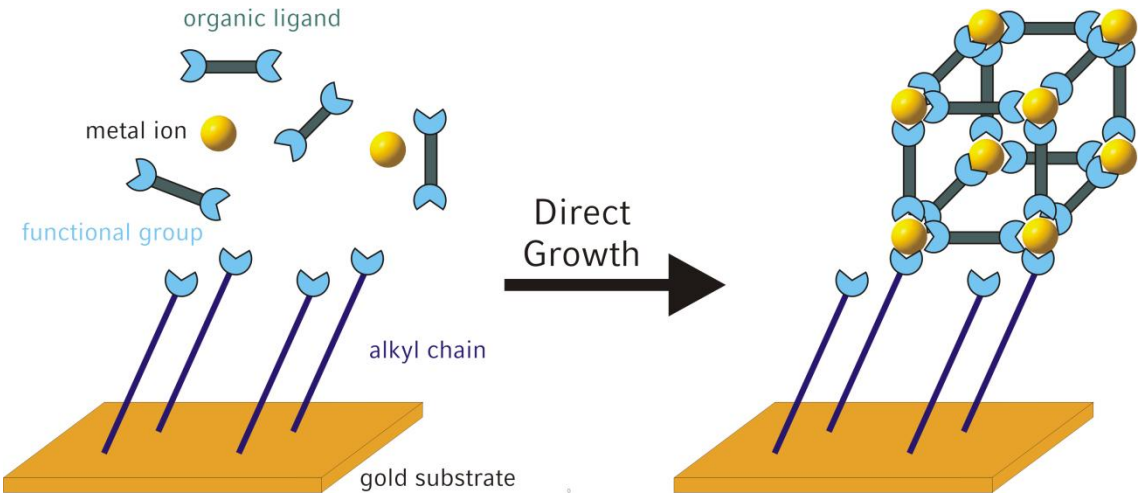

Figure 1.7: Concept of direct growth of MOFs on SAM-functionalized gold substrates.

The first study on nucleation and growth of a MOF structure on SAMs was published by Fischer *et al.* in 2005.[151] Here it could be shown for the first time that direct attachment of MOF-5 crystals on a functionalized gold substrate is possible. A patterned functionalization of 16-mercaptohexadecanoic acid and 1H,1H,2H,2H-perflourododecane thiol was used on the substrate, which was achieved with the help of Micro Contact Printing (μCP). The functionalized substrate was immersed into a pre-treated crystallization solution. Crystal growth could be observed on the carboxylic acid terminated SAM, whereas no crystallization occurred on the CF_3-groups (Figure 1.8).

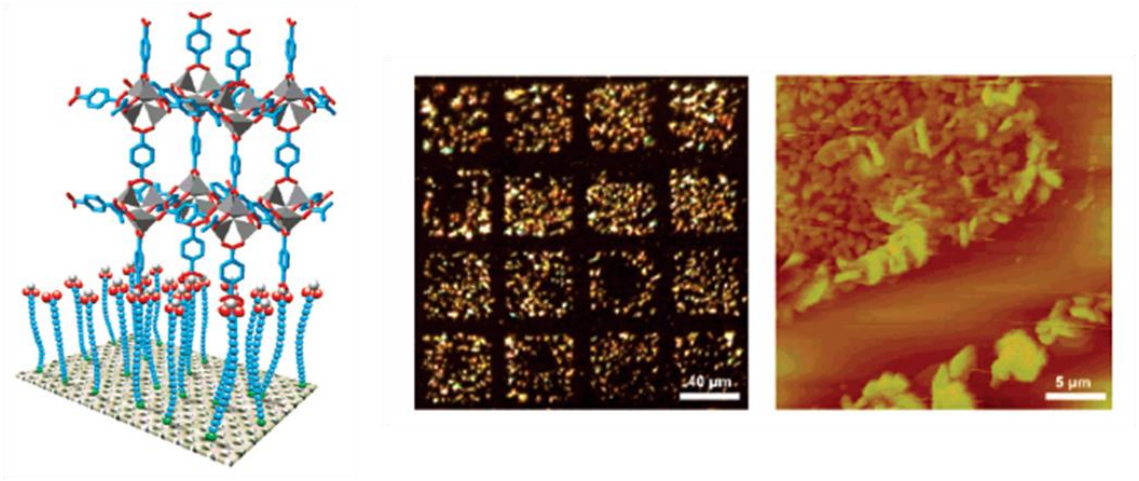

Figure 1.8: **The concept of anchoring a typical MOF-5 building unit to a carboxylic acid terminated SAM (left). Optical microscope (middle) and an AFM image (right) of a selectively grown film of MOF-5 on a patterned SAM.**[151]

The synthesis solution has to be pre-treated solvothermally to obtain crystal growth on the substrate; the authors attribute the necessity of this step to the formation of the typical SBUs of MOF-5 at higher temperatures. In order to grow the films, the crystallisation of the bulk material is then slowed down by reducing the temperature to room temperature. X-ray diffraction data of the synthesized MOF-5 films show all characteristic reflections of MOF-5, clearly proving the formation of the desired crystal structure, but also demonstrating that no preferred orientation of the crystals was observed. In a later publication, the same authors were able to show the growth of MOF-5 crystals on different substrates, such as carboxylic acid terminated SAMs on SiO_2 and ultrathin, amorphous Al_2O_3 adhesion layers (ALD), demonstrating the possibility to obtain thin MOF films on a great variety of substrates.[152]

As in the case of MOF-5, in many instances the functional group of the organic ligand in a MOF is a carboxylic acid group; consequently the carboxylic acid group is chosen

as the functional terminal group of the SAM. If there are different ligands coordinating at a metal centre in a MOF, as for example additional solvent molecules (water or alcohol molecules), different functional groups for the SAM may be chosen (e.g. alcohol group). If the coordination sites of the different ligands have distinct orientations in the crystal structure, different functionalities on a surface can lead to crystal growth in different preferred orientations. This could be demonstrated successfully for HKUST-1 crystals; the results of this study are discussed in detail in chapter 3.

In a similar study, Zacher *et al.* were able to show evidence of surface selective and oriented growth on functionalized alumina and silica surfaces under solvothermal conditions.[153] Direct growth of HKUST-1 could be observed with preferred [100]-orientation on plain sapphire substrates and in [111]-orientation on COOH-terminated Si/SiO_2 surfaces (see Figure 1.9), while on plain SiO_2 and on CF_3-terminated surfaces no crystal growth could be observed. The different results compared to our study discussed in chapter 3 can be assigned to the different substrates and reaction conditions. SAMs of silanes on silica do not present the same level of homogeneity as SAMs of alkanethiols on gold.[119] Furthermore, the experiments were carried out at different temperatures. HKUST-1 on silica substrates was deposited under solvothermal conditions at 120 °C, where the interchain forces that stabilize the self-assembled monolayer are weakened, while our experiments were carried out at room temperature.

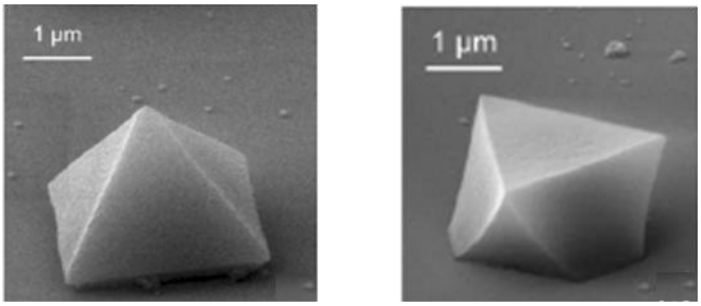

Figure 1.9: **left: Single HKUST-1 crystal in [100]-orientation grown on c-plane sapphire; right: [111]-oriented HKUST-1 crystal grown on COOH-terminated Si/SiO_2.**

The growth of a second investigated MOF ($Zn_2(bdc)_2(dabco)$) was observed to be not surface-selective at all; densely packed coatings were obtained on silica and alumina surfaces.

Continued research by the Bochum group led to the development of a step-by-step route for the synthesis of HKUST-1 on functionalized gold substrates, resulting in homogeneous and highly crystalline MOF films.[154] Instead of immersing the functionalized substrate into a pre-treated solution containing a mixture of the organic ligand and the metal salt, the substrate is exposed to the two building units in a sequential fashion (Figure 1.10). The step-by-step deposition of multilayers was characterized with the help of surface plasmon resonance and infrared spectroscopy. Whereas in a earlier study on the layer-by-layer growth of a different zinc-containing MOF no X-ray data for the identification of the desired crystal structure could be obtained,[155] the step-by-step route for the synthesis of [100]-oriented HKUST-1 on MHDA-SAMs could be proven by X-ray diffraction. The layer-by-layer approach is appealing due to the possibility to coat surfaces with MOF layers of defined thickness

and to potentially synthesize completely new types of MOFs with compositions not accessible by bulk synthesis routes.

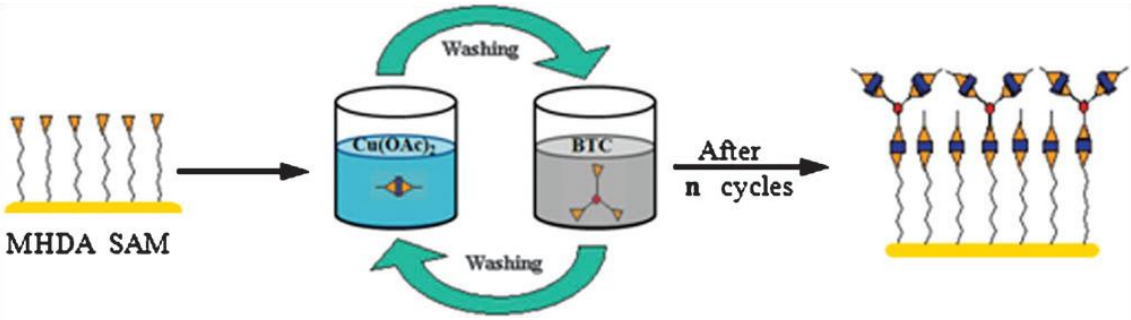

Figure 1.10: **Schematic diagram for the step-by-step route for the synthesis and growth of HKUST-1 on MHDA SAMs obtained by repeated immersion cycles in solutions of copper acetate and BTC.**[156]

The validity of the step-by-step preparation procedure could be verified with the help of a quantitative scanning force microscopy study.[156] The number of layers grown is observed to be proportional to the number of immersion cycles from 20 cycles on, indicating that after reaching a critical thickness a layer-by-layer formation during growth takes place.

Kubo *et al.* were able to demonstrate the preparation of oriented films of a different type of coordination polymer,[157] namely CPL-1, a coordination polymer with a pillared layer structure, first synthesized by the group of S. Kitagawa.[158] The reaction conditions for this film synthesis had to be tuned according to the relatively fast room temperature synthesis of bulk CPL-1: the supply of enough nutrients was achieved by replacement of the synthesis solution with a freshly prepared synthesis solution every two hours. This in-situ crystallization procedure was repeated for five cycles. The protocol for the oriented growth of CPL-1 is particularly interesting as it opens up the

way for the surface crystallisation of a completely different class of MOFs, the pore size of which is tuneable by employment of particular pillaring ligands. The pillared structure of this class of MOFs may help to synthesize crystals on surfaces consisting of alternating layers of different ligands.

The functionality of MOFs directly grown on functionalized substrates has been investigated by Allendorf *et al.*[159] HKUST-1 crystals were grown on functionalized, gold-coated microcantilevers and responses to different vapours of the hydrated and dehydrated form were investigated. It was found that HKUST-1 provides sensitivity to alcohols and CO_2 and insensitivity to N_2 and O_2. The authors indicate that the developed device is far from optimization and suggest that for MOFs exhibiting greater structural flexibility higher sensitivities can be expected.

1.5 Goals

The concept of direct growth of MOFs on SAM functionalized surfaces has been explained within the previous chapter and existing work in this area of research has been introduced. Although there are already a number of studies on direct growth of coordination polymers, many fundamental aspects of the growth mechanism during surface growth as well as during homogeneous nucleation of these materials are still not well understood. By focussing on the control of direct surface growth of MOFs on SAMs, the following work contributes towards the understanding of the growth mechanism of MOFs. Structural features of particular MOFs shall be correlated to the observations made during our studies, leading to explanations for the structure-directing properties of the functional groups of the SAMs. Furthermore, the ability to control the orientation of the crystals and thus the pore-system in such films will open

the way to more advanced applications such as selective gas-separation membranes or sensors.

In this context the oriented crystal growth of HKUST-1 will be investigated. The fact that there are two different coordination sites in the structure of HKUST-1 gives rise to the idea that different functional groups acting as termination of the SAM, such as carboxylic acid and hydroxyl groups, should have different effects on the crystal orientation with respect to the surface. In addition, to gain further insights into the formation of crystals on functionalized surfaces, the morphological evolution of the HKUST-1 crystals on different terminated SAMs is followed.

To further enhance the knowledge about the growth mechanism of MOFs, the unique platform of HKUST-1 crystals grown under ambient conditions in an oriented manner on gold substrates functionalized with SAMs is employed for *in situ* AFM studies. The oriented HKUST-1 crystals are appealing for in situ AFM due to their direct attachment to a gold-coated glass substrate that can be easily mounted in the *in situ* chamber of the AFM and, more importantly, the orientation of the crystals can be tuned by using different functional groups for surface functionalization, such that the growth of the (111) face can be monitored directly. In addition, the surface-grown crystals are essentially free from screw dislocations, and exhibit large micrometer sized terraces with a homogeneous (111) termination.[160] The possibility to use microscopic in situ techniques is very promising, as it allows for insights in processes otherwise not accessible for investigation.

HKUST-1 is a very popular MOF structure due to its straightforward synthesis and its interesting possible applications. Nevertheless, to verify the concept of direct growth of MOFs on functionalized surfaces, it will be necessary to enlarge the group of

surface-grown MOFs and to learn more about the level of control achievable in these systems. For example, in the system Fe(III)/terephthalic acid, several framework structures are known. It will be interesting to learn more about the structure-directing properties of functionalized surfaces in crystallization solutions containing competing MOF structures. Within such systems, it is easily accepted that the particular synthesis conditions have to play an important role in obtaining the desired structure.

A further part of this work aims at the detailed investigation of surface-grown crystals. The ability to control different aspects of direct crystal growth makes it possible to investigate the properties of these newly created systems with special attention to possible applications.

In summary, this thesis concentrates on the investigation of synthesis conditions for the direct growth of MOFs on SAMs and deals with the characterization of the surface-grown crystals, in order to learn more about the mechanism of MOF crystallization and the interesting properties of this class of materials leading to future applications.

2 Characterization

2.1 X-ray Diffraction

X-rays, electromagnetic radiation with a wavelength of around 10 to 0.01 nm, were discovered in 1895 by Wilhelm Roentgen. They are generated by hitting a cooled metal anode with a highly energetic, focused electron beam. As electrons collide with atoms in the target and slow down, a continuous spectrum of X-rays is emitted, which is termed Bremsstrahlung. Depending on the elemental composition of the target, there also exist characteristic narrow lines in the spectrum resulting from X-ray fluorescence. In this process the impact of primary electrons creates a hole in a lower shell of an atom. Electrons from upper shells can occupy this vacancy and the surplus energy directly related to the difference between the two energy states, is released as X-ray photons. By applying blocking filters, a single energy spike can be isolated resulting in fairly monochromatic X-ray radiation.

Interactions between X-rays and any kind of material are divided into absorption, reflection and scattering.

The idea that diffraction of X-rays should be possible by their passage through a crystal resulted from the insight that the wavelengths of X-ray photons lie in the Ångstrøm-sized range, which is in the same order of magnitude as the distances between atoms in solid matter.[161] The ordered lattice of a crystal allows one to gain structural information by observing the diffraction patterns caused by constructive and destructive interference of X-rays scattered by the lattice planes (Figure 2.1).

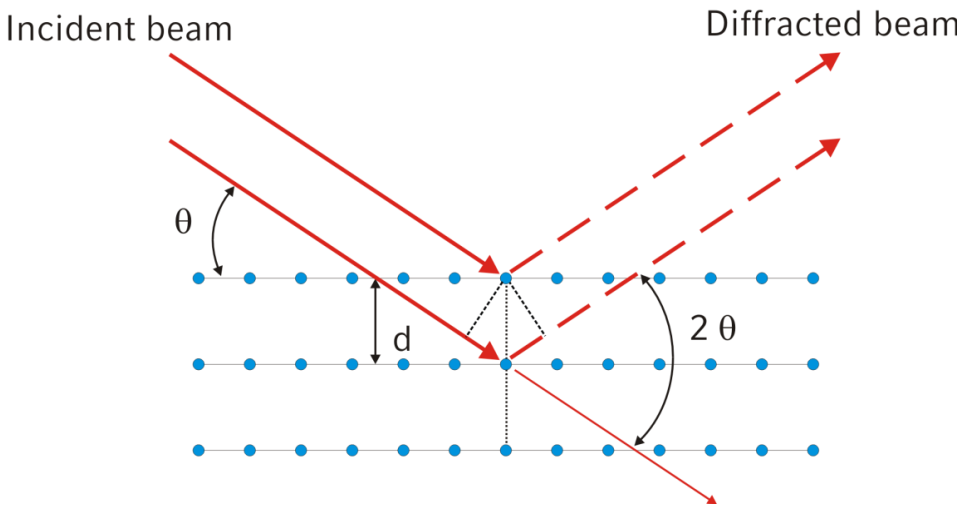

Figure 2.1 **Scheme illustrating the Bragg relation. Constructive interference is achieved when the path difference is a multiple integer of the X-ray wavelength.**

The path difference of two rays hitting a crystal surface is defined as:

$$\Delta S = 2d_{hkl} \sin\theta$$

where θ is known as Bragg angle and h, k, l are the Miller indices that are used to identify the lattice planes. Constructive interference of the scattered X-rays leads to the observation of diffraction peaks. According to Bragg's law, the diffracted beams show constructive interference if the path difference is a multiple integer of the applied wavelength:

$$n\lambda = 2d \sin\theta$$

n: order of interference

λ: X-ray wavelength

d: lattice plane distance

θ: angle of incidence

If θ is known, the distance d between the lattice planes can be easily deduced.

Monochromatic X-rays are employed for X-ray diffraction of single crystals. The single crystal rotates in the beam, such that the Bragg law is fulfilled for each lattice plane at least once.

For powder diffraction monochromatic X-rays are used, as well. As powder samples contain a large number of randomly oriented crystallites, the resulting diffraction patterns are formed by a set of cones from all planes that satisfy the Bragg condition. Powder diffraction patterns allow the identification of crystalline phases by comparison with data bases.

To obtain information about the domain size (D) of the crystals, the Debye-Scherrer equation can be applied:

$$D = \frac{K\,\lambda}{\beta \cos\theta}$$

D: crystalline domain size
K: Scherrer constant, in general set to 0.9
λ: wavelength
β: full width at half maximum in radians
θ: angle of incidence

For small crystalline domains, reflex broadening is caused by incomplete destructive interference of the out-of-phase X-rays. The mean size of the crystalline domains can be calculated using the given formula. As the results are volume-based, it should be noted that small amounts of larger particles will greatly influence the average size.

2.2 Electron microscopy

According to E. K. Abbe, in microscopy distances *d* are resolvable, if

$$d \geq \frac{\lambda}{n \sin \alpha}$$

where n sin α is defined as numerical aperture and α is half the angle of aperture of the objective. Increase of α leads to a maximum resolution of $d_{min} = \lambda/2$. The use of visible light in optical microscopy therefore limits the resolution to d_{min} = ca. 200 nm.

The decrease of λ leads to better resolutions. Electrons, for example, have a considerably smaller wavelength than visible light, the wavelength of electrons accelerated by 100 kV is 0.004 nm and therefore ~10^5 times smaller than that of visible light. We note, however, that certain aberrations and imaging artefacts prevent electron microscopy from achieving the extreme resolution predicted by Abbe's law. Two different microscopic techniques are commonly used, namely Scanning Electron Microscopy (SEM)[162] and Transmission Electron Microscopy (TEM)[163].

Scanning Electron Microscopy (SEM)

The first scanning electron microscopes were developed in the 1950s. Since this time they are used intensively for research in the fields of chemistry, biology, physics and medicine.

The working principle of a scanning electron microscope is given in Figure 2.2. The electrons are emitted by an electron gun (either a tungsten filament or a field emission gun) and accelerated through high voltage. Several condenser lenses focus the electrons to a thin, tight coherent beam with a diameter of about 2 – 10 nm when

hitting the specimen. Scanning of the specimen is provided by a set of electromagnetic coils that deflect the electron beam. The objective lenses focus the beam onto the desired part of the specimen.

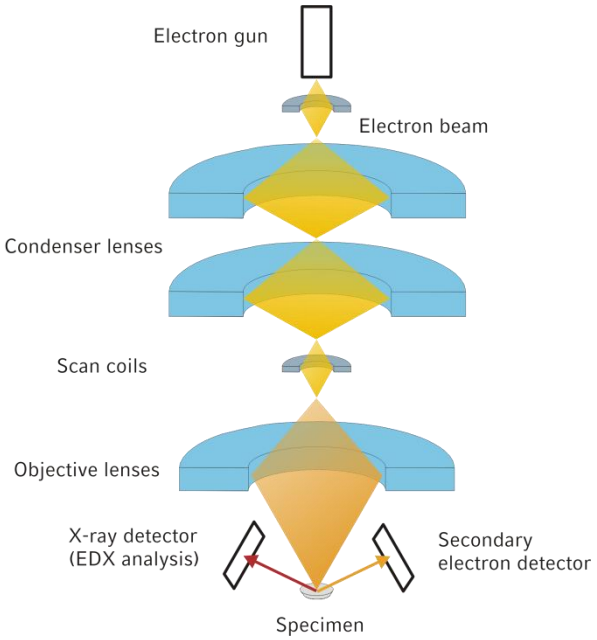

Figure 2.2 Electron pathway from electron generation to the surface of the specimen.[162]

There are several possible interactions between the electron beam and the sample. (Figure 2.3) The primary electrons dislodge so-called secondary electrons from the sample by transferring their energy to the sample by inelastic scattering. The signal generated by the detection of secondary electrons is amplified, and a pixel intensity proportional to the number of emitted electrons is obtained.

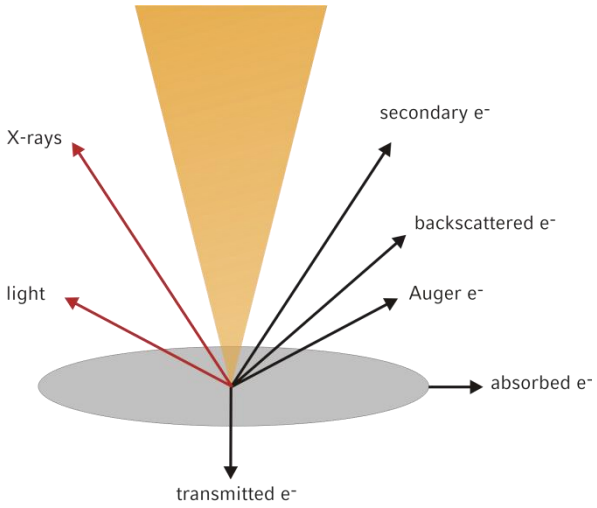

Figure 2.3 Possible interactions between electron beam and specimen.

Additionally, backscattered electrons, which result from elastic scattering with the atomic nucleus, can provide information about the composition of the scanned material. The amounts of secondary and backscattered electrons are dependent on the acceleration voltage of the primary electron beam and of course on the sample morphology.

Collisions of primary electrons with core electrons from atoms in the sample result in excited atomic states. The re-occupation of the vacancy by an outer shell electron leads to emission of X-ray photons with characteristic wavelength distributions for different elements. Therefore, with the help of SEM we can obtain information about the morphology and the elemental composition of the particular sample.

2.3 Atomic Force Microscopy (AFM)

Historical Background

The development of the first stylus profiler by Gustav Schmalz in 1929 marks the beginnings of scanning probe microscopy (SPM).[164] A sharp probe, mounted at the end of a cantilever, scanned the particular sample; the motion was monitored by means of an optical lever arm and recorded on photographic paper. This instrument was capable of reaching magnifications of about 1000, but the tip was prone to destruction due to collisions with the features on the surface. In 1972, Russell Young and co-workers published their work on the first non-contact type stylus profiler, the topographiner. This instrument scanned the surface of conductive materials in the *x* and *y* dimensions at a constant tip-sample distance, by keeping electron field emission current between a sharp tungsten probe and the sample surface constant. A piezoelectric ceramic, onto which the probe was mounted, was used to move the probe in the *z* direction. Thus, the topographiner was able to provide 3D images. It worked under a vacuum system of about 4×10^{-10} Torr.

In 1982 the first topographic images with atomic resolution, obtained on $CaIrSn_4$ and Au using a scanning tunnelling microscope (STM), were published.[165] The scanning tunnelling microscope has piezodrives that scan a metal tip over the surface in the *x* and *y* direction to maintain a constant tunnel current, with energies ranging from 1 meV to 4 eV. The voltages applied to the different piezos provide the information to image the topography of the surface. Owing to low energy tunnel currents - energy of the tunnel “beam” 1 meV up to 4 eV -, STM proved to be a non-destructive technique,

but as with the topographiner, in this first STM a vacuum system was required and only electrically conductive samples could be imaged.

The invention of atomic force microscopy (AFM) in 1986 by Binnig, Quate and Gerber, resulted from the combination of the fundamental principles of STM and the stylus profiler.[166] The first AFM consisted of a diamond tip attached to a cantilever which was positioned directly beneath an STM Au probe. The sample was positioned on a *xyz* piezoelectric and, as the diamond tip scanned the surface, the fluctuations in current between the STM probe and the contact tip were used as the feedback mechanism to maintain a small constant force between the diamond tip and the sample. Great progress was made by employing an optical system, consisting of a reflected laser beam and a photo detector, capable of detecting very small movements, for the feedback mechanism. In 1987 the first non-contact mode AFM was developed by Martin *et al.*,[167] who used an oscillating cantilever to scan the sample surface. As the tip approaches the sample surface, van der Waals attractive forces provoke changes in the amplitude of the cantilever, which are then used in the feedback mechanism to control the distance between the sample and the tip. Variations on the AFM technique, such as magnetic imaging and imaging under water with forces down to 10^{-9} N, are just some of the improvements made in the field. The first atomic force microscope was commercially available in 1989 and owing to its non-destructive nature, its capacity to image conductor and insulator materials with hard and soft surfaces and its ability to work in different environments such as air and liquids it has been widely used in many different scientific fields.

Atomic Force Microscope working principle

The probe used in an atomic force microscope consists of a very sharp tip, with a radius of curvature normally <10 nm that is attached to the underside of a thin, flexible cantilever. As the tip scans the surface of the sample, the cantilever deflects in response to interactions between the tip and sample. These interactions may be a combination of attractive and repulsive forces. The deflection of the cantilever is monitored by deflecting a laser off the back of the cantilever and then onto a four-quadrant photo detector. A feedback loop then enables the 3D piezoelectric scanner to maintain a constant force between the tip and the sample either by moving the sample or the cantilever, dependent on the design of the particular AFM. The scanner is designed to provide very precise movements in the *x*, *y* and *z* direction. A schematic representation of the mechanism is given in Figure 2.4.

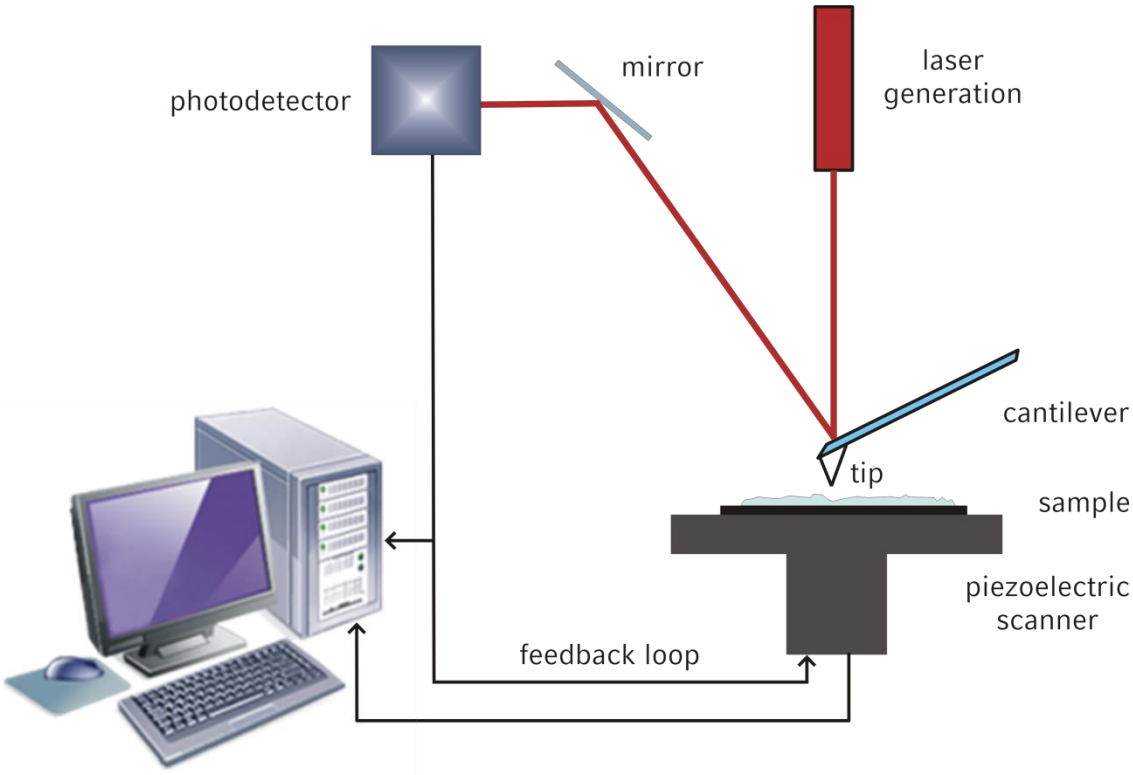

Figure 2.4 Functional schematic of an atomic force microscope.

In principle, different scanning probe microscopy modes are possible: For instance, non-contact mode where topography is measured by sensing van der Waals forces, contact mode which comprises scanning the sample at a constant force whilst the tip and the sample are always in contact, tapping mode where an oscillating cantilever is used in a way that the tip taps the sample softly with constant amplitude, magnetic force microscopy (MFM) which allows the measurement of magnetic force gradients above a sample surface and scanning tunnelling microscopy (STM) which measures topography and electronic properties by means of a tunnelling current. The information gathered to render the images depends upon the scanning mode used. The force applied to the sample when scanning in contact mode is relatively high and

in some cases this can lead to sample damage, thus it is important to consider the physical and chemical properties of the sample to select an adequate AFM mode.

The AFM specifications described in the following section refer to the Veeco MultiMode™ scanning probe microscope (SPM), with Nanoscope IIIa controller – the instrument used in this project.

MULTIMODE™ SPM

The MultiMode™ SPM works on the basis of keeping the probe motionless and scanning the sample beneath it. The sample is usually fixed to a metal stub that is magnetically attached to the top of the scanner tube. The MultiMode™ SPM is able to scan images from the atomic scale up to 175 µm in size by means of exchangeable scanners. Figure 2.5 shows the Veeco MultiMode™ scanning probe microscope comprising a scanning head, a scanner and the base.

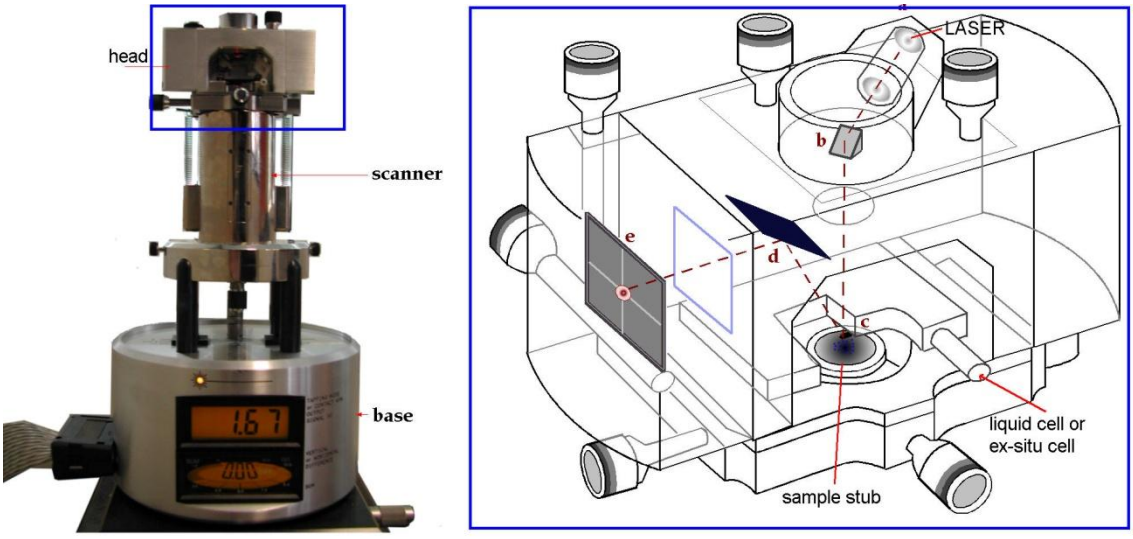

Figure 2.5 **left: Digital Instruments Nanoscope III Multimode™ scanning probe microscope; right: atomic force microscope scanning head mechanism.**

The scanning head, shown in Figure 2.5, comprises the essential optical AFM mechanism, where a laser beam is produced and directed towards the cantilever by a mirror. The laser beam reflects off the cantilever at different angles depending on interactions between sample features and the tip. Finally, the laser beam reaches the photo detector, which is a position-sensitive quadrangle detector that provides different information depending on the scanning mode used. The scanning head is attached to an *x*-*y* stage, connected to the scanner. The scanner limits the size and resolution of the image that can be obtained. The AC voltages applied to the conducting regions of the piezo tube cause piezo movement along the *x*, *y* and *z* axes. Movement in the *z* direction is determined by the feedback mechanism that applies a variable voltage to the piezo to maintain a constant force or amplitude between the tip and the sample. Piezo movement along the *x* and *y* directions are determined by parameters such as the scan size and scan rate. The smallest scan size achievable in a MultiMode^{TM} SPM is $0.4 \times 0.4\ \mu m^2$ with a vertical range of 0.4 µm using an "A" scanner, whilst the largest scan size is $200 \times 200\ \mu m^2$ with a vertical range of 8 µm using an "AS-200" scanner. When scanning at a scan angle of 0 ° the fast-scan is conducted along the *x* axis and the slow scan along the *y* axis.

The probes most commonly used in SPM consist of a tip attached to the underside or the end of a flexible cantilever extending from a rigid substrate. AFM tips are typically made of silicon or silicon nitride (Si_3N_4), and for most applications pyramidal silicon nitride tips are used. The resolution obtained from AFM scanning is greatly influenced by the shape of the tip, for instance the sharper the tip the better the resolution, and also by the topography of the sample.

AFM IN FLUIDS

One of the main advantages of imaging samples in fluid environments is that attractive forces due to surface tension are eliminated, while van der Waals forces are reduced; therefore the force between the tip and the sample is minimal. AFM real time in-situ observations in fluids may be conducted either using contact mode or TappingMode™. To conduct observation under liquids, a fluid cell is needed.

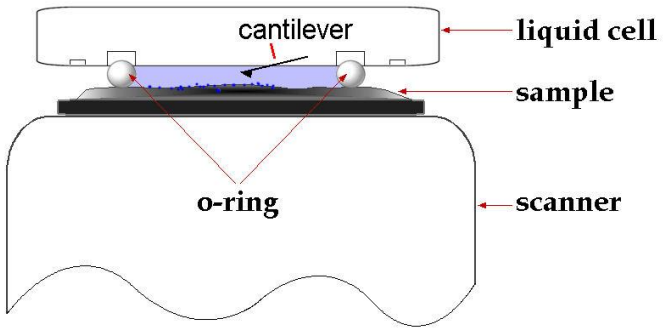

Figure 2.6 **Schematic of a typical fluid cell: Imaging a sample under liquids using an o-ring.**

In order to conduct AFM under liquids, the cell is inserted in the AFM scanning head as a normal tip holder and an o-ring is used to seal the gap between the sample and the fluid cell. Then the liquid chamber can be flooded using the inlet and the outlet. The laser is then carefully aligned on the cantilever to start scanning. Both the sample and the tip are submerged in the fluid as shown in Figure 2.6.

2.4 Vibrational Spectroscopy

FT-IR[168] and Raman[169] spectroscopy are applied to investigate the chemical bonding in materials by excitation of vibrational modes to higher energy levels by absorption of radiation of appropriate frequency.

For IR spectroscopy, radiation in a range of 200 – 4000 cm^{-1} (mid IR radiation) is employed. In MIR transitions between molecular energy levels are enabled, which delivers information about the chemical bonding of the investigated substance. Molecular vibrations are IR-active if the molecule has a permanent dipole moment or if the dipole moment of the molecule changes during the vibration.

Whereas FT-IR spectroscopy is typically employed to investigate powder samples, Reflection-Adsorption IR spectroscopy (RAIRS) utilizes an alternative geometry that allows examination of thin layers such as self-assembled monolayers on reflecting substrates (metals, polished metal oxides).[170] The set-up of the Reflection-Absorption FT-IR experiment is shown in Figure 2.7. IR radiation is directed onto the sample, the organic part of the sample, i.e. the investigated monolayer, interacts with the IR beam and the resulting beam is reflected by the underlying substrate. In addition to the described selection rules for IR spectroscopy, there is another selection rule for RAIRS.

If the reflection layer is a noble metal, only those vibrations whose transition dipole moments lie perpendicular to the reflection surface can be observed. This is because the incident and reflected p-polarised components of the radiation superimpose constructively (add together), enhancing the signal, whereas the s-polarised

components cancel each other out, (as they undergo a phase change on reflection from the reflection surface).

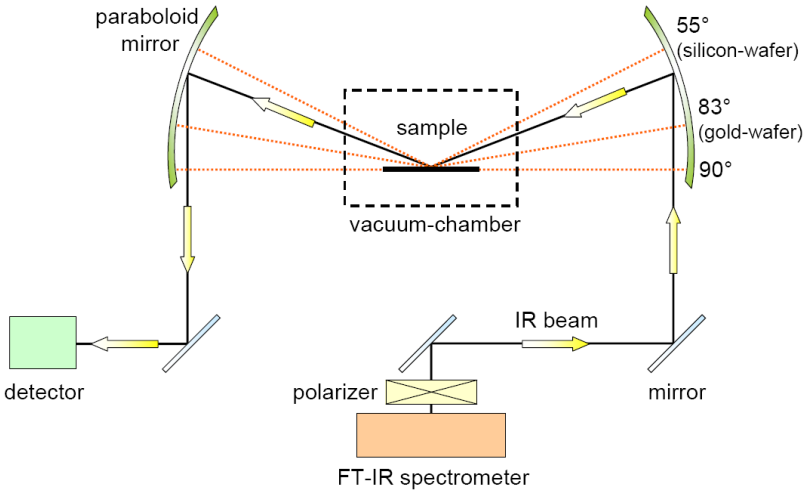

Figure 2.7 Schematic set-up of the reflection-absorption IR spectrometer.

In a Raman measurement, the sample is illuminated with monochromatic light, usually generated by a laser. The samples scatter the monochromatic light either elastically (Rayleigh scattering), or inelastically (Raman-scattering). Whereas IR absorption is the result of a change in the dipole moment, Raman absorption involves a change in the bond polarisability during the vibration. The latter is a two-photon process. Thus, the mechanism of Raman scattering is different from that of infrared absorption, and Raman and IR spectra provide complementary information. Vibrational spectra of solid samples present a large number of peaks, each corresponding to specific vibrational transitions. Thus, IR as well as Raman techniques are suitable for identification purposes of specific functional groups (e.g., in organic molecules), as well as the local structure of the solid material.

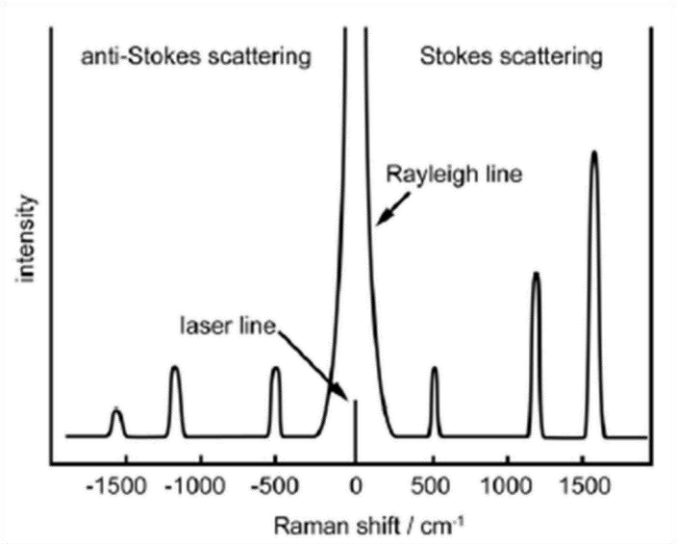

Figure 2.8 **Schematic Raman spectrum showing Rayleigh line, Stokes Raman scattering and anti-Stokes Raman scattering (after [169]).**

2.5 Adsorption measurements

CHARACTERIZATION OF POROUS SOLIDS

To characterize porous materials, adsorption is widely used, as it delivers information about properties like porosity, surface area or pore diameter.[171, 172] Adsorption is defined as the enrichment of one or more components in an interfacial layer and can occur when a solid material (adsorbent) is exposed to a gas (adsorptive). In general, two different types of adsorption, chemisorption and physisorption in dependence on the type of interaction between the adsorbent and the adsorptive, can be distinguished. Chemisorption involves the formation of chemical bonds between the gas molecule and the pore surface, whereas physisorption is mediated by van der Waals forces such as dipole-dipole, London forces or hydrogen bonding. Therefore, in contrast to chemisorptions, physisorption is a completely reversible process, where

the adsorptive is in equilibrium with the adsorbed gas molecules (adsorbate) in dependence of the relative pressure p/p_0. Equilibrium isotherms are obtained by plotting the adsorbed volume as a function of p/p_0. Adsorption isotherms can be classified as one of six types according to the IUPAC[1] (Figure 2.9), each type being characteristic for certain material types (see Table 2.1).

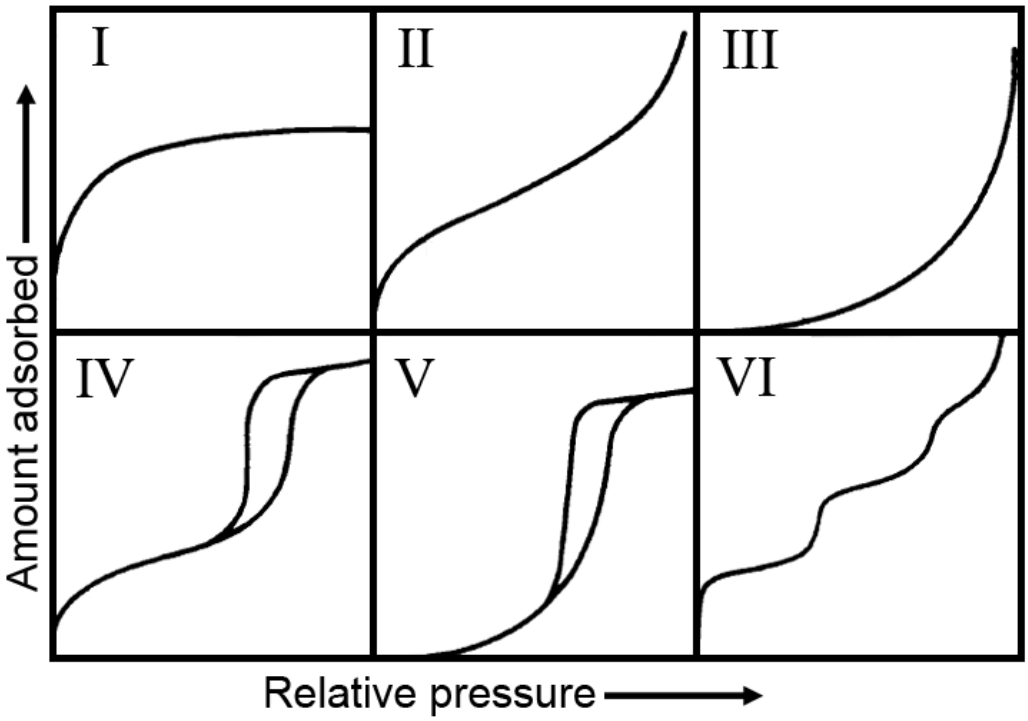

Figure 2.9 IUPAC classification of sorption isotherms: Type I to Type VI isotherms.[1]

Table 2.1 Classification of adsorption isotherms.

Type	Interpretation
I	Chemisorption isotherms or physisorption in microporous materials, where a plateau is reached after filling of the micropores
II	Nonporous and macroporous materials with high energies of adsorption
III	Nonporous and macroporous materials with low energies of adsorption
IV	Mesoporous materials with high energies of adsorption, often contain hysteresis loops attributed to mesoporosity
V	Mesoporous materials with low energies of adsorption, often contain hysteresis loops attributed to mesoporosity
VI	Several possibilities, including multiple pores sizes and multiple distinct energies of adsorption

Classical microporous materials commonly show isotherms of type I. They are characterized by a steep increase of adsorbed volume at very low relative pressures, typically below 0.1. This step corresponds to the formation of an adsorbate monolayer within the micropores of the material. As the dimensions of the pores are in the range of the adsorbate, the monolayer formation is equivalent to a complete filling of the pores, and no further increase of adsorbed volume is observed until a high pressure close to $p/p_0 = 1$ is reached. If the adsorbent particles have nano-scale dimensions, the interparticle voids may fall into the mesoporous range, leading to textural porosity. Hence, a steady increase in adsorbed volume is observed after micropore filling.

For evaluation of the adsorption isotherms several different models exist. The Brunauer-Emmett-Teller (BET) theory is widely used for porous materials and is based on a number of simplifying assumptions in order to extend the Langmuir model[1] to multilayer adsorption. For low partial pressures ($p/p_0 < 0.3$) the BET equation can be expressed in a linear form:

$$\frac{p/p_0}{n(p_0 - p)} = \frac{1}{n_m C} + \frac{C - 1}{n_m C} \frac{p}{p_0}$$

p/p_0 : relative pressure; p_0 is the saturation pressure of the adsorptive

n: amount of adsorbate

n_m: monolayer capacity

C : BET constant.

From the obtained experimental data the monolayer capacity n_m can be deduced and the surface area A_S can be calculated according to

$$A_S\ (BET) = n_m N_A a_m$$

N_A: Avogadro constant

a_m: cross-sectional area of the probe molecule.

In a strict sense, the BET method is not applicable for microporous solids, because the diameter of the micropores is too small to allow multilayer formation.[173] However, the BET theory is sometimes used for microporous materials to deliver comparative values.

Most Metal-Organic Frameworks are microporous and possess surfaces that are far from flat. Many of these materials have been shown to exhibit very large BET surface areas. It is suggested that adsorption occurs through a pore filling mechanism rather than by layer formation,[51] thus it is unclear whether the reported BET surface area numbers are really meaningful.[174] By comparison of the geometrical surface area calculated from the particular crystals structures with the simulated adsorption isotherms, deduced from grand canonical Monte Carlo simulations, Walton et al. could demonstrate that the BET theory is applicable for the evaluation of sorption data of MOFs.[174]

Nowadays, in addition to the macroscopic theories for describing adsorption, there are several microscopic models including molecular simulations (Monte Carlo simulations), molecular dynamics, statistical mechanics techniques, and density functional theory (DFT), which yield more realistic results. The validity of the DFT method has already been shown, using various reference materials. However, specific knowledge about the structure and surface atoms of the investigated materials is required in order to correctly calculate the forces and input parameters of these models. Therefore, such approaches cannot be applied to unknown surfaces, and the macroscopic theories are still frequently employed.

The two principal experimental methods for the collection of adsorption isotherms are volumetric and gravimetric techniques. In both cases, the adsorbent is held at a constant temperature, which is usually at or near the boiling point of the adsorptive, i.e., by cooling with liquid nitrogen in the case of nitrogen sorption. By step-wise increase of the adsorptive pressure followed by equilibration of the system, the increase in the amount of adsorbed molecules can be measured. Volumetric

measurements are carried out by dosing a certain gas volume into the sample chamber, and by measuring the pressure decrease due to adsorption in the pores. In contrast, in gravimetric systems the mass gain of the sample is recorded after each addition step of the adsorptive.

QUARTZ CRYSTAL MICROBALANCE (QCM)

The Quartz Crystal Microbalance (QCM) is one of the gravimetric techniques for recording adsorption isotherms. The central element of the QCM is a so-called QCM chip, a small disc AT-cut of a quartz crystal with key-hole gold electrodes patterned on both sides (Figure 2.10).

Figure 2.10 **Quartz crystal microbalance chip (XA 1600, KVG Quartz Crystal Technology) next to a 1 Euro coin.**

The working principle of the QCM chip is the piezoelectric effect, which was first described in 1880 by Chaques and Pierre Curie. Piezoelectric materials are charging if a force such as traction, torsion or pressure is applied on them. The inverse piezoelectric effect is defined as the mechanical deformation of these materials upon application of an electric field. For quartz crystals, i.e. the QCM chips, application of an electric field leads to an oscillation of the chip, in the present work with a basic

frequency of $f_0 \sim 10$ MHz. The change of this fundamental frequency upon mass changes on the QCM chip was demonstrated in 1959 by G. Sauerbrey.[175] The relation between mass change and frequency change is given in the so called Sauerbrey equation:

$$\Delta f = -\frac{2 f_0^2 \Delta m}{A\sqrt{\rho_q \mu_q}}$$

Δf: frequency change

Δm: mass change

f_0: resonant frequency of the basic mode of the crystal

A: piezo-active area of the electrode

ρ: density of quartz

μ: shear modulus of quartz

This gives a frequency change of 1 Hz corresponding to a mass loading of $4.42 \cdot 10^{-9}$ g onto a surface area of 1 cm^2 on a quartz disc. This very high gravimetric sensitivity can be employed to record the adsorbed amount of an adsorptive by a small amount of porous material. The porous material is usually prepared as a thin film onto the QCM chip. The adsorptive can be any gas or liquid. The experimental setup given in Figure 2.11 refers to using a liquid sorptive; the usual applied temperature is 25 °C. The control of the partial pressure of the adsorptive in the sample chamber is done by diluting the evaporated compound with a carrier gas, for example nitrogen, using digital mass-flow controllers and a calibrated gas-flow system.

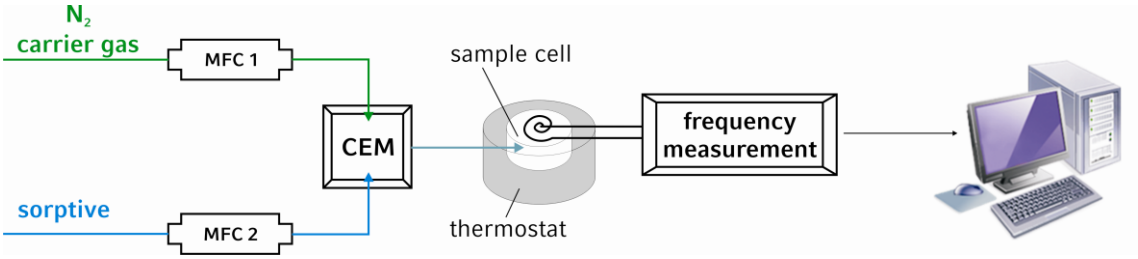

Figure 2.11 **Experimental set-up for the collection of sorption data with the help of a QCM device: the carrier gas (N_2) and the sorptive are dosed with the help of two digital mass flow controllers (MFC 1 and 2) and are mixed in the controlled evaporation mixer (CEM) to be transported into the sample chamber, the temperature of which is controlled by the thermostat. The data collected during the frequency scans are transferred to a computer.**

2.6 Thermogravimetric analysis and Differential Scanning Calorimetry

With the help of Thermogravimetric analysis (TGA) it is possible to detect mass changes of a sample as a function of temperature or time. The sample is heated at constant or variable rates and the evolving weight changes are determined with the help of a thermobalance and recorded. The mass changes are typically evoked by evaporation or decomposition of volatile components or by oxidation or reduction of the investigated material. For porous materials, TGA is of great interest because it enables the quantification of water or template molecules inside the pores and gives information about the particular temperature which leads to removal of the guest molecules. In addition it is possible to determine thermal framework stabilities.

A complementary method is Differential Scanning Calorimetry (DSC). Here the heat flux from or to a sample as a function of the sample temperature is measured. The

detected signal is direct proportional to the exchanged heat. Therefore, DSC is a method to determine quantitatively exothermic and endothermic processes in the sample during heating, i.e., combustion steps, phase transitions and evaporation of absorbed molecules.

3 Oriented Growth of Metal-Organic Framework HKUST-1 tuneable with functionalized self-assembled monolayers

This chapter is based on a publication in the "Journal of the American Chemical Society".[176] The project was a joint project in collaboration with Dr. Enrica Biemmi.

3.1 Introduction

The chemistry of metal organic frameworks (MOFs) has been intensively studied, with particular attention to porous compounds due to their many potential applications such as gas sorption, molecular separation, storage, and catalysis.[50, 53, 72, 79] To date, the research efforts have been mainly focused on bulk materials; the preparation of thin films of those compounds is an important challenge. The successful oriented growth of inorganic compounds, such as calcium carbonate,[143] lead sulfide,[144] anatase,[147] zinc and iron oxide,[142, 146] and zeolites,[148, 177] on functionalized surfaces has inspired us to explore the effect of self-assembled monolayers (SAMs)[114] with different functionalities on the growth of the metal-organic framework HKUST-1.[178] The growth of one other MOF structure, such as MOF-5, has been reported on a SAM of COOH-terminated alkanethiols; however, this film did not show preferred crystal orientation.[151] The ability to control the orientation of the crystals and thus the pore system in such films will open the way to more advanced applications such as selective gas separation membranes or chemical sensors.

The structural features and stability of HKUST-1 as well as its intriguing sorption and catalytic properties [76, 179, 180] make this material an interesting candidate for the growth of thin films.

The metal-organic framework compound HKUST-1 with the chemical composition $Cu_3(BTC)_2(H_2O)_3 \cdot xH2O$ has a cubic framework structure with an open 3D pore system. Two Copper (II) ions are linked to dimers, also referred to as paddlewheel units, by four 1,3,5-benzenetricarboxylic acid (BTC) molecules. (Figure 3.1) Such bimetallic units are common features and often highly stable arrangements found for many other transition metal carboxylates.

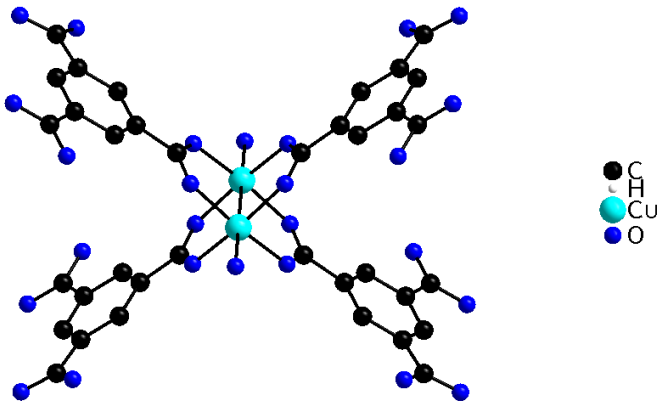

Figure 3.1 **Building block of the HKUST-1 framework (paddle-wheel unit): Cu_2 dimers are coordinated by four carboxylate groups arranged in a square.**

The primary building blocks, i.e. the paddlewheel units are arranged in the open framework structure (Figure 3.2) to give a porous network consisting of main channels of a square cross-section of about 0.9 nm diameter and tetrahedral side pockets of ca. 0.6 nm, connected to the main channels by triangular windows of ca.

0.35 nm. The pore volume has been determined by N_2 as well as H_2 sorption; depending on the sample preparation it varies between 0.33 and 0.62 $cm^3\ g^{-1}$.[76, 181]

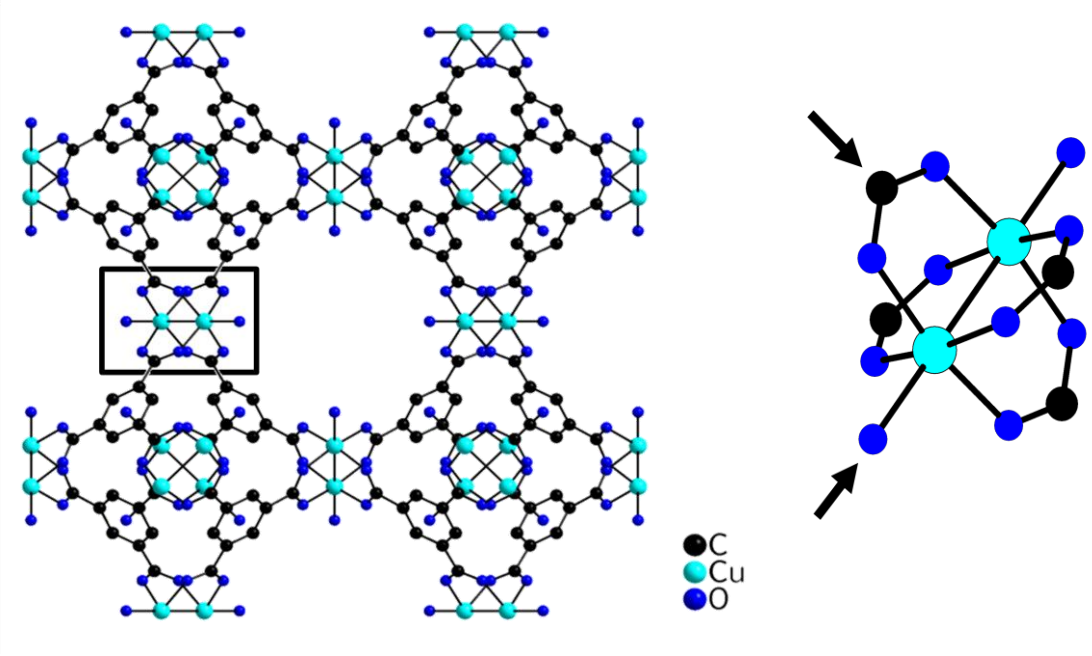

Figure 3.2 **left: View into the pore of the 3D framework structure of HKUST-1 right: two different types of oxygen atoms coordinating the copper ions.**

In Figure 3.2 (right) the two different types of oxygen atoms coordinating the copper atoms are marked with black arrows. There are oxygen atoms from the carboxylate groups and oxygen atoms from weakly bound water molecules occupying the axial coordination sites. This building characteristic is fundamental for many of the interesting properties of the HKUST-1 framework structure. The weakly bound water molecules point towards the centre of the main pores. Thus, a hydrophilic interior characterizes the main cavity. On the other hand, the smaller pores surrounded by the planar BTC-units present a more hydrophobic character.[182] Furthermore, the local structure of the framework has been characterized in detail.[183] This has been

motivation for several studies concerning the catalytic properties of HKUST-1. After removal of the coordinated water molecules in vacuum, Lewis acidic Cu (II) sites are created and accessible for catalytic transformations.[179] Gas purification and separation[184], as well as hydrogen adsorption and storage,[55, 76, 78] have been studied in relation to the intriguing sorption properties and the high structural stability of HKUST-1. Employing HKUST-1, the removal of sulphur odorant components from natural gas as well as amines and ammonia, water traces, alcohols and oxygenates have been demonstrated.[67] Interestingly, in all cases a dominant colour change (from deep blue to turquoise in the case of water) allows visible detection of breakthrough and contaminant saturation on the MOF. During removal of the contaminant by vacuum treatment or heating, the original colour reappears, indicating the regeneration of the adsorbent.

In addition to all these interesting results from literature, the fact that there are two different coordination sites in the structure of HKUST-1, gave us the idea that different functional groups as termination of the SAM, like carboxylic acid and hydroxyl groups, should have different effects on the crystals orientation in respect to the surface.

3.2 Experimental Section

SELF-ASSEMBLED MONOLAYERS ON GOLD

The gold-coated slides (glass slides (76 × 26 mm^2) coated with 10 nm Ti and 100 nm Au by electron-beam evaporation, Advalytix AG) were cut in smaller pieces (10 × 13 mm^2), cleaned in a piranha solution (H_2SO_4 (95 – 98 %) : H_2O_2 (30 %) = 3:1),

and treated in an 12 mbar oxygen plasma for 20 min. The cleaned gold slides were immersed in a 1 mM ethanolic solution (6 pieces in 30 mL) of the desired thiol, and left at RT for 48 h. The SAM-functionalized gold slides were repeatedly washed with ethanol, and stored in absolute ethanol until needed. The following alkanethiols employed in this work were 11-Mercapto-1-undecanol (97 %, Aldrich), 11-Mercaptoundecanoic acid (95 %, Aldrich) and 1-Mercaptoundecan (98 %, Aldrich).

HKUST-1 Synthesis Mixture

A solution of 0.837 g (3.6 mmol) $Cu(NO_3)_2 \cdot 2.5\ H_2O$ (98 %, Aldrich) in 12 mL double distilled water was added to a solution of 0.42 g (2.0 mmol) of 1,3,5-benzentricarboxylic acid (98 %, Fluka) in 12 mL absolute ethanol in a sealed-glass reactor and left in a preheated oven at 75 °C for 8 days.

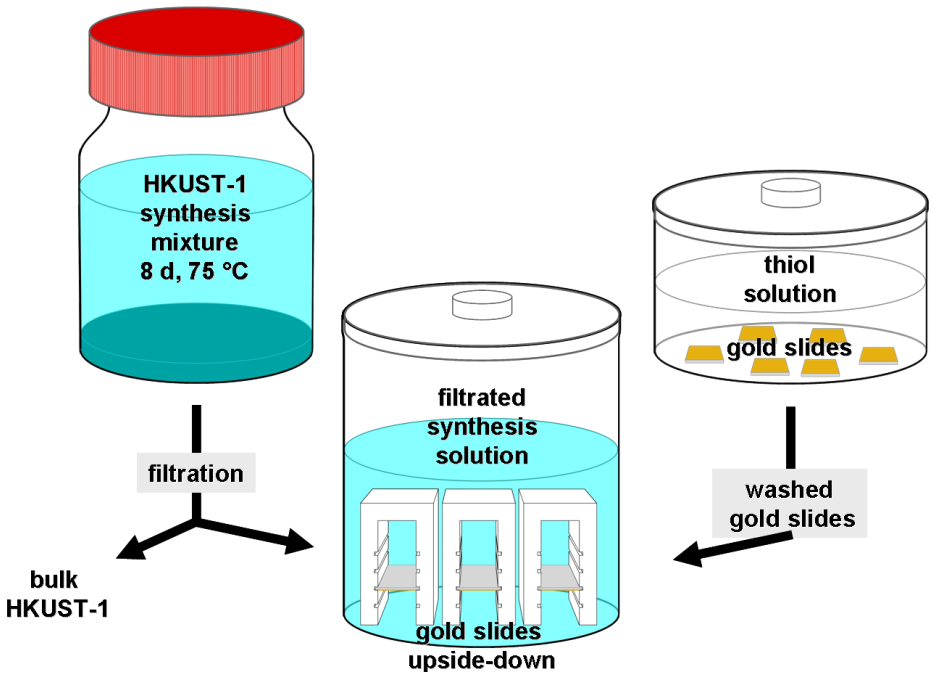

Figure 3.3 **Schematic illustration of the preparation procedure of HKUST-1 thin films on SAM-functionalized gold slides.**

THIN-FILM GROWTH

After cooling the HKUST-1 synthesis mixture in a water/ice bath, the crystalline product was filtrated and stored for further characterization. The filtrated solution was used as crystallization sol for film growth. The SAM-functionalized gold-slides (3 pieces) were placed upside-down on Teflon®-supports in 20 mL of the clear HKUST-1 crystallization solution (Figure 3.3). The growth step took place at room temperature in a sealed glass vessel. For the kinetic investigations the slides were removed after various immersion times (8-210 h).

3.3 Characterization

X-ray diffraction (XRD) measurements of powders were performed on a STOE powder diffractometer in transmission geometry (Cu-$K_{\alpha 1}$, $\lambda = 1.5406$ Å) and of films using a Scintag Inc. XDS 2000 in theta-theta geometry (Cu-$K_{\alpha 1}$, $\lambda = 1.5406$ Å; Cu-$K_{\alpha 2}$, $\lambda = 1.5444$ Å). Characterization of the self-assembled monolayers was performed by RAIR spectroscopy, using a Bruker IFS 66v FTIR spectrometer. The sample chamber mounting a high performance variable angle reflection accessory (A-513) is maintained at 2 mbar during the entire measurement by means of an Edwards rotary-pump. In a typical measurement for gold surfaces, an incidence angle of 83 ° to the surface normal was used. Furthermore, a cleaned gold slide was measured as background prior to the measurements. The morphological evolution of the crystals during thin film growth was followed with the help of a JEOL JSM-6500F scanning electron microscope.

3.4 Results and discussion

For the growth of the HKUST-1 crystals, gold substrates were modified with monolayers of $HS(CH_2)_{10}X$ (with X = -COOH, $-CH_2OH$, $-CH_3$) following known procedures[119, 185] (see section 3.2). As described above, the carboxylic acid functionality imitates the organic linker (1,3,5-benzenetricarboxylate (BTC)) in the open framework structure, the alcohol group mimics the coordinating water, while the methyl group presents an inert reference surface. The formation of the self assembled monolayers has been proven by RAIR, as shown in Figure 3.4. The characteristic absorption bands indicating the -OH, -COOH, and -CH3 functionalized surfaces are marked in red in the graphs. Common to all alkanethiol SAMs are the methylene groups of the aliphatic chains, which present high-frequency modes at 2920 and 2850 cm^{-1} associated with the asymmetric and symmetric stretching vibrations, respectively; as well as the band at 721 cm^{-1} assigned to the stretching vibration of the S-C bond. For the 11-mercaptoundecanol SAM band at 1060 cm^{-1}, the characteristic C-O stretching vibration absorption band is proof of a successful synthesis. For the -COOH functionalization the presence of the 11-mercaptoundecanoic acid-SAM is verified by the typical -C=O stretch absorption band at 1714 cm^{-1}. The -CH3 groups can be identified by the asymmetric and symmetric stretching vibrations at 2954 and 2875 cm^{-1}, respectively. The stability of the -OH and -COOH SAMs was studied, via RAIR, after immersion of the gold slides in a Cu^{2+}/H_2O/EtOH solution for the longest immersion time of 112 h. No indications of damage to the SAM were found. Interestingly, in the case of the -COOH-terminated SAM it is possible to observe a shift of the -C=O band, from 1714 cm^{-1} in the as synthesized SAM typical of a -COOH group, to lower wavenumbers (1554 and 1454 cm^{-1}) typical of the asymmetric and

symmetric stretching of the carboxylate units,[183] which indicates the binding of copper ions to the SAM (but no damage to the SAM).

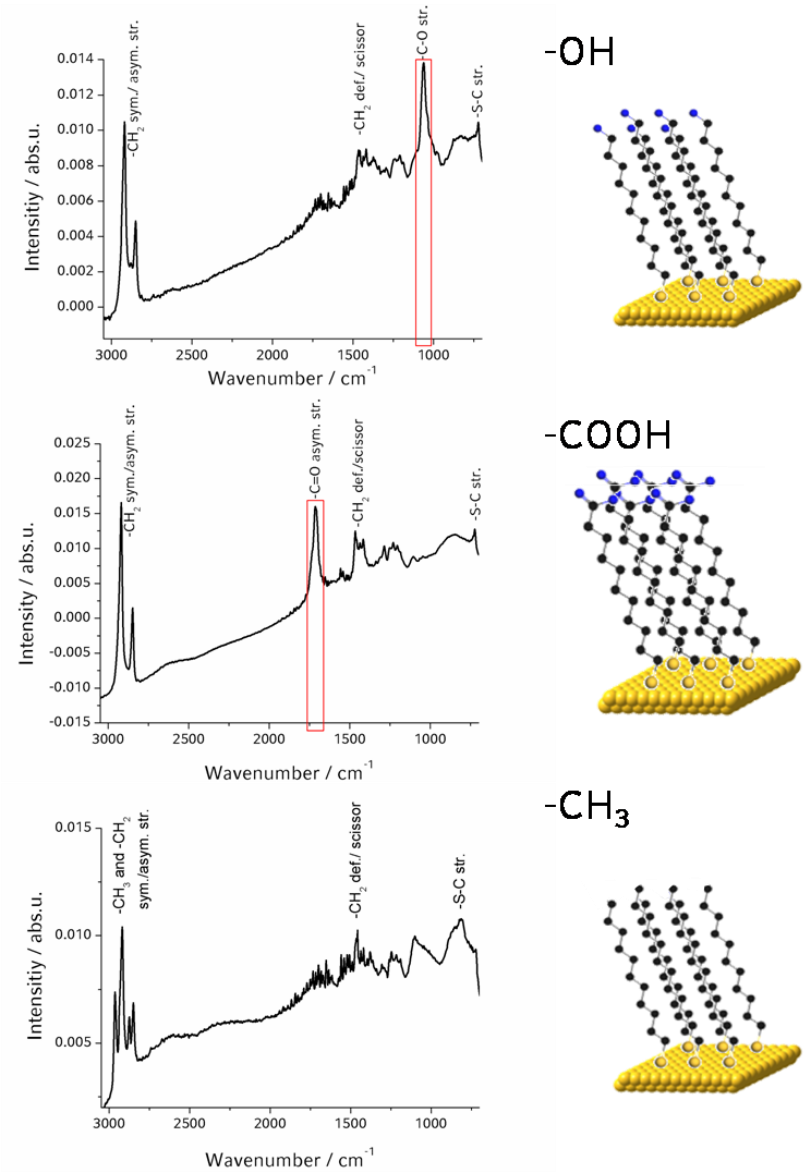

Figure 3.4 **RAIR-spectra of alkanethiol self-assembled monolayers on gold substrates: -OH: 11-Mercapto-1-undecanol-SAM, -COOH: 11-Mercaptoundecanoic acid-SAM, and –CH3: 1-Mercaptoundecan-SAM. (The alkanethiol self-assembled monolayers are represented with a tilt of about 30 ° from surface normal as reported in the literature.)[114]**

The synthesis of HKUST-1 thin films as described in chapter 3.2 (Figure 3.3) is carried out within two steps. In the first solvothermal step bulk HKUST-1 crystals are obtained, which can be seen easily from the powder pattern of the bulk product compared to the simulated pattern of HKUST-1 (Figure 3.5). The solution, after filtration of bulk HKUST-1, is directly used for thin film growth by immersing the functionalized gold slides upside down for various reaction times. Thin films of HKUST-1 crystals were obtained on each modified gold surface. No crystallization takes place on bare gold slides.

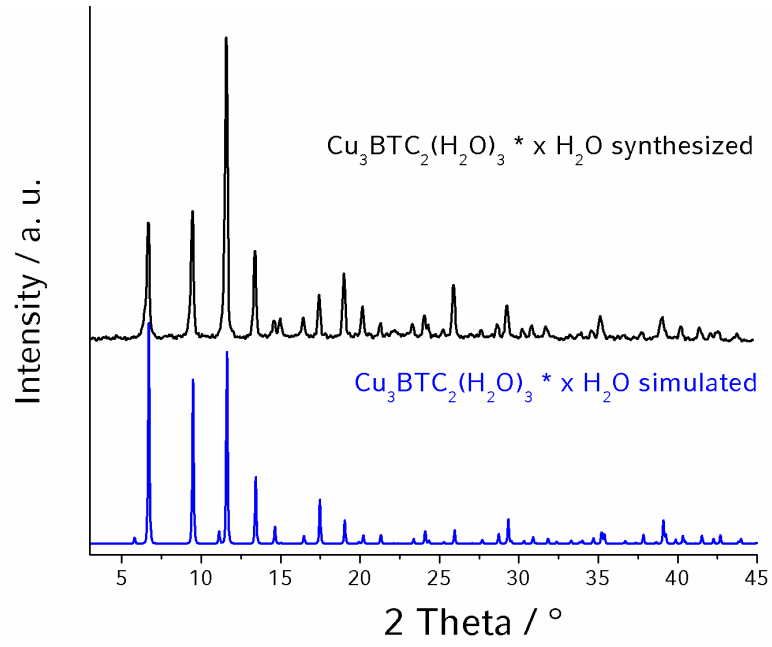

Figure 3.5: **X-ray diffraction data of bulk HKUST-1, synthesized in the solvothermal step during thin film synthesis, compared to the simulated powder pattern of HKUST-1.**

Highly ordered thin films of HKUST-1 were formed on the SAMs as demonstrated by the diffraction patterns shown in Figure 3.6. The film grown on the -COOH self-

assembled monolayer is highly oriented along the [100] direction, while the OH-modified surface induces a completely different orientation along the [111] direction. Homogeneous thin films but with no preferential orientation are obtained on the methyl SAM. Figure 3.7 shows a schematic illustration of the surface-induced oriented growth of HKUST-1 crystals.

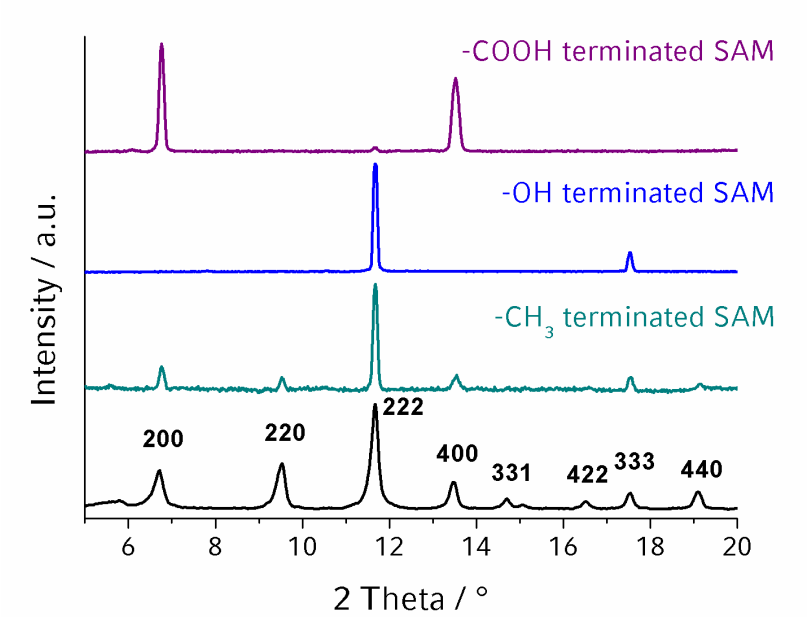

Figure 3.6 **X-ray diffraction patterns (background corrected) of thin films of HKUST-1 on functionalized gold surfaces, compared to powder diffraction data of bulk HKUST-1.**

The strong effect of control over the orientation of the crystals can be explained by the different coordination sites of the paddlewheel units in the structure. The two different termini of the SAMs (-COOH and -OH) force the oriented attachment of appropriate growth species at the molecular interface, followed by oriented crystal growth on the molecular layer on the substrate.

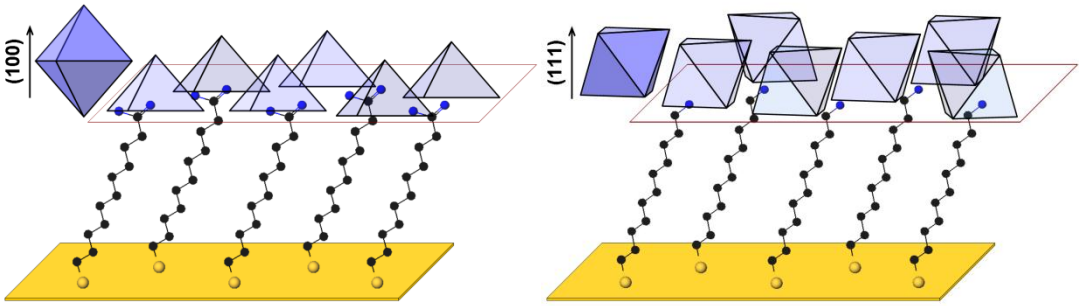

Figure 3.7 **Schematic illustration of oriented growth of HKUST-1 nano-crystals left on an 11-mercaptoundecanoic acid SAM, and right on 11-mercaptoundecanol-modified gold surfaces.**

For –OH terminated SAMs we observe crystal growth in [111] orientation. Following our hypothesis, the hydroxyl could mimic the axially coordinating water molecules, and therefore a close-to-upright orientation of the paddle-wheel unit with respect to the self-assembled monolayer interface would be expected. Both the [100] and the [111] crystal orientations present planes with tilted Cu_2-units. In [111]-orientation the Cu_2-units are tilted about 35 ° with respect to the vertical, in contrast to the 45 ° tilt in the [100] case. (Figure 3.8) Taking into account steric factors (crowding by the BTC ligands), in our view, this difference could be the deciding factor in favouring the [111]-orientation for the OH-functionalized gold surfaces.

For optimal coordination of the carboxylate groups of the SAM at the copper dimers, the dimers should be oriented with their axis parallel to the surface. In [100] orientation of the crystal the copper dimers are aligned in a way, that enables coordination of two carboxylate units per bimetallic cluster rather than one accessible

coordination site in the case of [111] orientation. Statistically the first option should be preferred on a SAM presenting a rather dense population of –COOH groups.

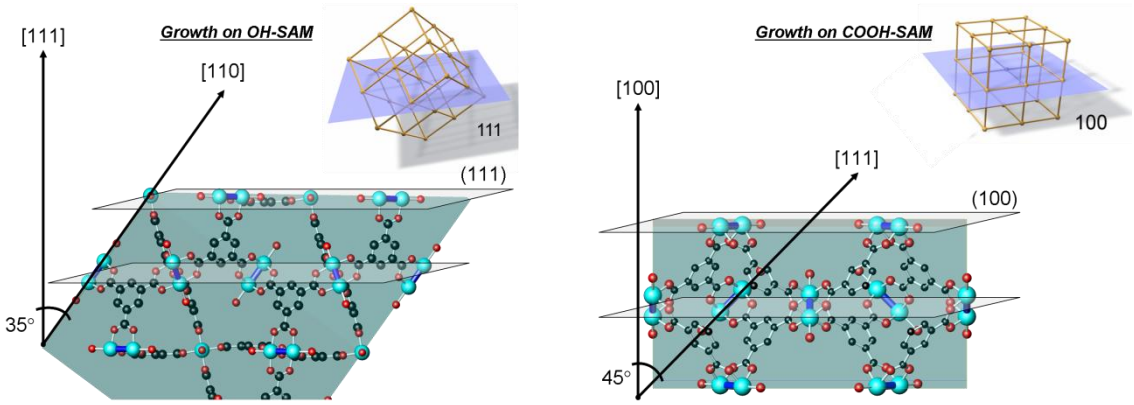

Figure 3.8 **Schematic illustrations of the respective lattice planes of HKUST-1 in (111) and (100) direction.**

After long immersion times (> 100 h), about 600 nm thin films composed of a monolayer of close-packed intergrown crystals are found on all functionalized gold substrates. (Figure 3.9) Therefore, after this stage, it is not possible to investigate the crystals orientation with the help of electron microscopy. In order to learn more about the mechanism of formation of the thin films on each modified surface (-OH, -COOH, and -CH_3) the temporal evolution of the growth process was followed. The samples were removed from the crystallization solution after different immersion times, dried at room temperature, and characterized. The growth process could be followed employing X-ray diffraction (in reflection geometry) and scanning electron microscopy could confirm the preferential crystal orientation on the different functionalized gold surfaces. The compared samples where all obtained from the same batch, and different batches are comparable: the difference in the amount of HKUST-1 obtained in different batches is always consistent with variations smaller

than 1 %. The original solutions were all prepared in the same way with particular attention to composition, aging time and temperature.

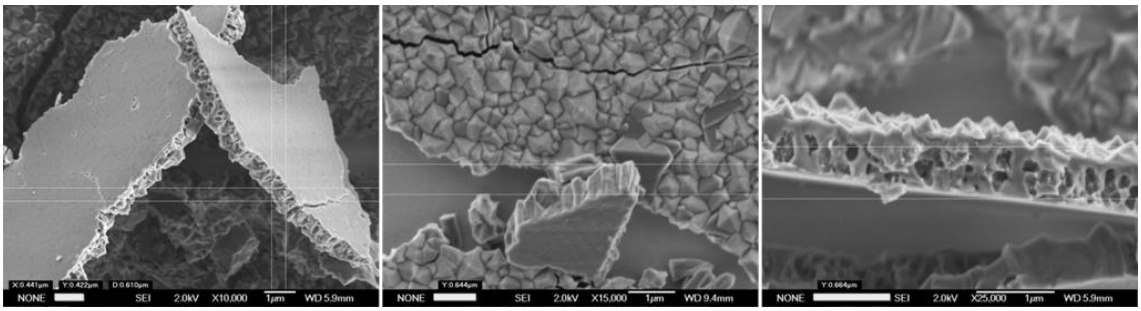

Figure 3.9 **SEM-pictures of HKUST-1 thin films after an immersion time of 112 h on an 11-mercapto-1-undecanol-SAM (left), 11-Mercaptoundecanoic acid-SAM (middle), and a 1-Mercaptoundecan-SAM (right). The thickness is similar for all three samples (ca. 600 nm).**

For –OH terminated SAMs, the diffraction patterns of [111]-oriented HKUST-1 crystals, collected after immersion times between 16 and 210 h, are displayed in Figure 3.10. The intensity of the reflections increases with the reaction time because both the number and the size of the crystals on the surface increase. The scanning electron micrographs presented in Figure 3.11 show, in detail, the morphological development of the crystals from “rounded” octahedra of 150 – 200 nm in diameter at the first stages (after 16 h) up to 1 µm well-shaped crystals after 45 h .

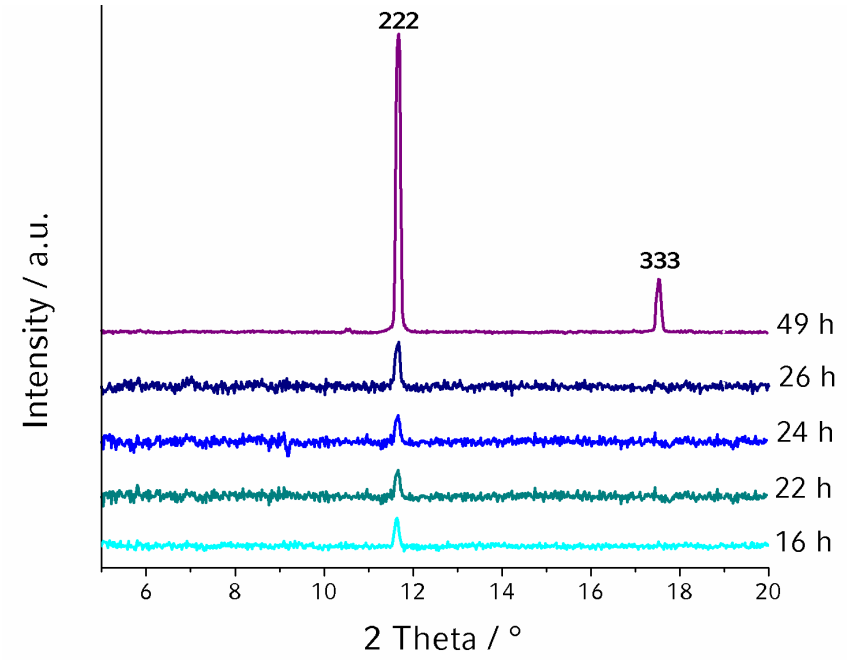

Figure 3.10 **Diffraction patterns of [111]-oriented HKUST-1 crystals on -OH SAMs collected after immersion times between 16 and 210 h.**

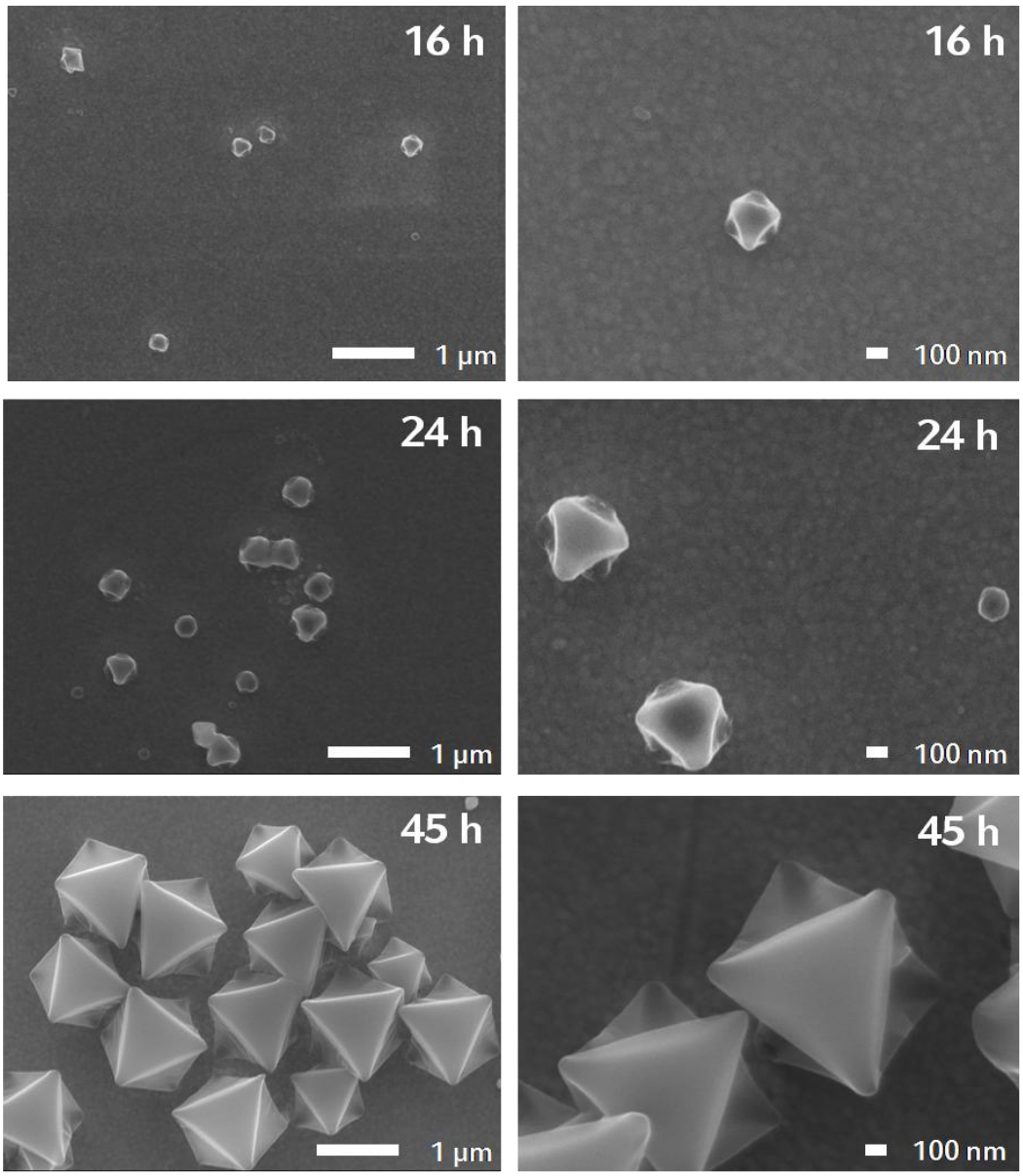

Figure 3.11 **Scanning electron micrographs of [111]-oriented HKUST-1 crystals grown on -OH functionalized gold-slides after immersion in the crystallization solution for 16, 24, and 45 h.**

An analogous investigation was performed on the -COOH and -CH_3 functionalized samples. Figure 3.12 shows the diffraction patterns of the gold slides modified with the carboxylic acid SAM. After about 62 h, the (200) and (400) reflections of the

HKUST-1 crystals appear, followed by further growth until the end of the experiment (112 h). With the exception of a minute (222) peak, the (200) and (400) reflections completely dominate the pattern, thus demonstrating the growth of a highly oriented crystalline film of HKUST-1.

A close look at the morphology of the film after 32 h (Figure 3.13) reveals that already after 32 h in solution many small [100] oriented crystals can be detected "growing out" of the SAM gold substrate, in addition to a few [111]-oriented crystals which cause the minute additional (222) reflection.

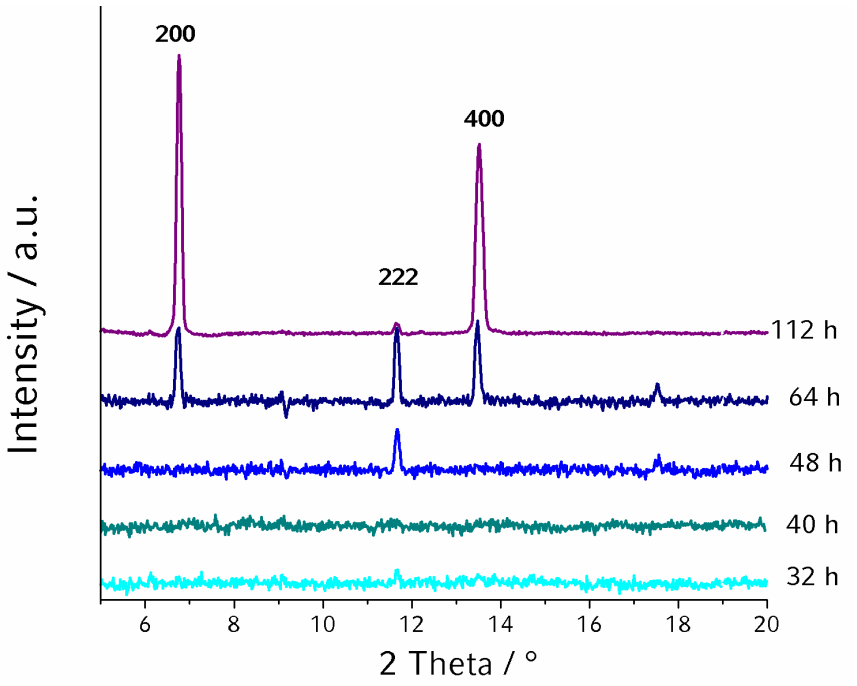

Figure 3.12 **X-Ray diffraction patterns of [100]-oriented HKUST-1-crystals on -COOH terminated SAMs collected after immersion times between 16 and 210 h.**

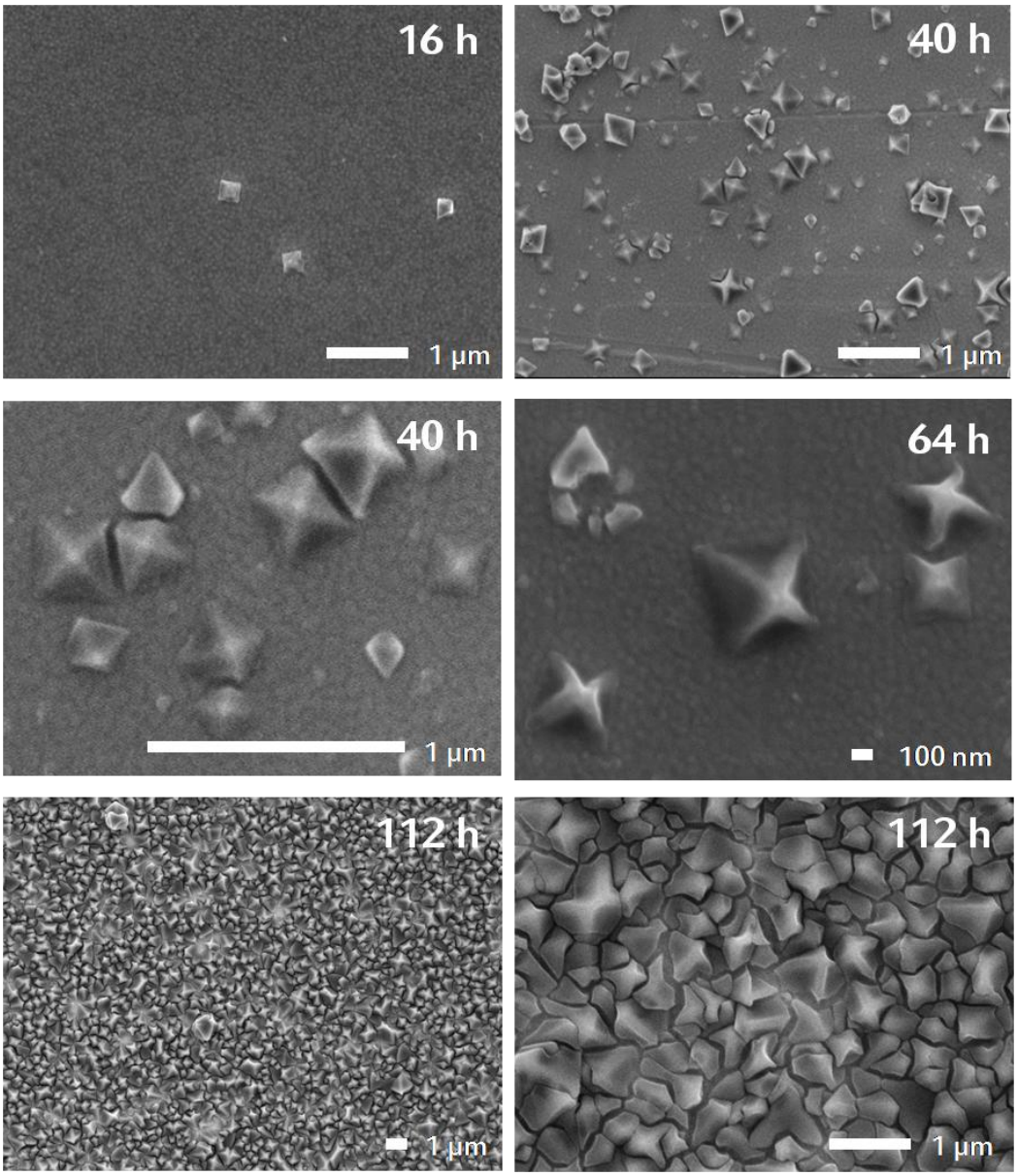

Figure 3.13: **Scanning electron micrographs of [100]-oriented HKUST-1 crystals grown on -COOH functionalized gold-slides. The measurements were performed on different samples after immersion times of 32 h, 40 h and 112 h.**

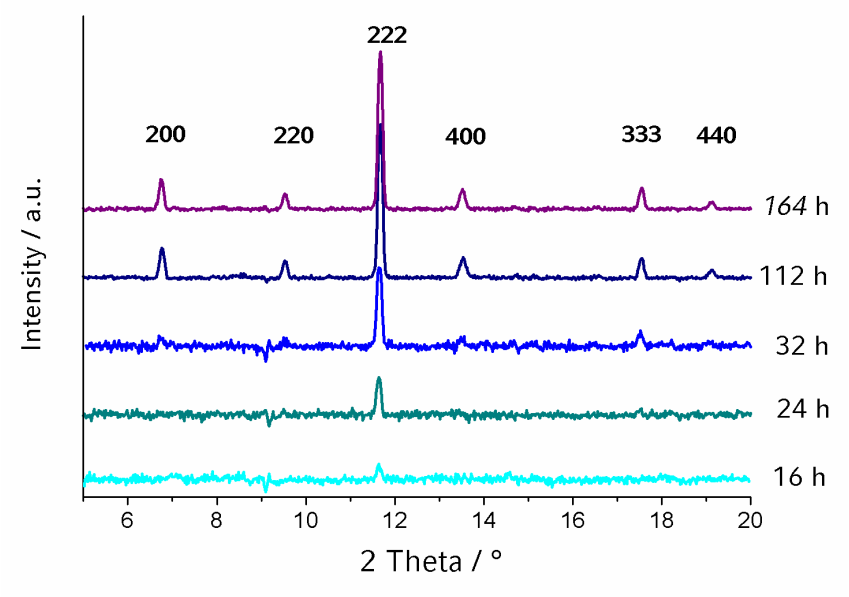

Figure 3.14: **X-Ray diffraction patterns of thin films grown on methyl-functionalized gold surfaces after immersion times between 16 and 164 h.**

The HKUST-1 crystal layer on the methyl-terminated SAM shows a faster growth process than on the other two polar layers, with no unique orientation (as shown in the SEM pictures presented in Figure 3.15). The X-ray diffraction patterns present all typical reflections of HKUST-1, while the (222) reflection is predominant (Figure 3.12). Thus the [111] direction appears to be favoured for less selective crystal growth; we propose that, in this case, the growth species have already assumed an octahedral shape with (111) faces that can attach to the surface. This should constitute a favourable attachment mechanism if dispersive forces between the organically terminated crystal faces and the alkyl-terminated SAM are dominant.

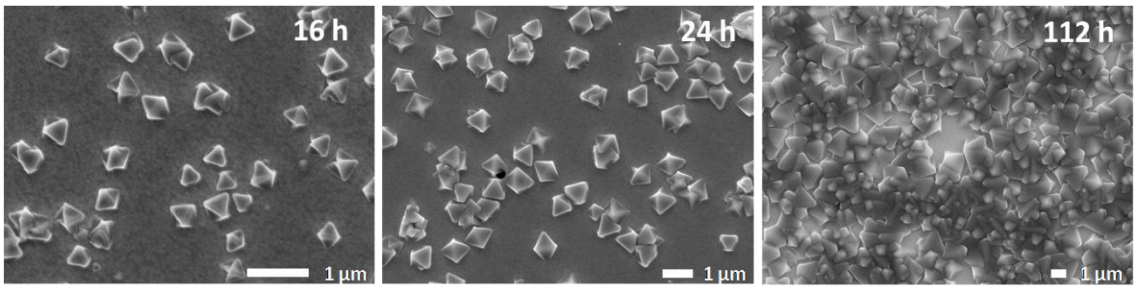

Figure 3.15: **Scanning electron micrographs of HKUST-1 crystals grown on $-CH_3$ functionalized gold-slides. The measurements were performed on different samples after immersion times of 16 h, 24 h, and 112 h. No unique orientation can be observed.**

Noteworthy, the deposition of microcrystalline HKUST-1 under solvothermal conditions on silica surfaces modified with -COOH self assembled silane monolayers has been reported (as discussed in section 1.4).[153] As described above, we observed [111]-oriented growth of HKUST-1 on 11-mercaptoundecanoic acid-SAMs. In contrast, the crystals on silica surfaces modified with -COOH self assembled silane monolayers are oriented in [111]-direction. However, these results are difficult to compare, as drastically different reaction conditions were employed. SAMs of silanes on silica do not present the same grade of homogeneity as SAMs of alkanethiol on gold.[119] Furthermore, the experiments were carried out at different temperatures. HKUST-1 on silica substrates was deposited under solvothermal conditions at 120 °C, where the interchain forces that stabilize the self-assembled monolayer are weakened, while our experiments were carried out at room temperature. Conclusively, the -COOH silane functionalized surface does not present the same features as the thiol-SAM. Thus, the influence on crystals orientation is not comparable.

3.5 Conclusion

The above results clearly demonstrate that different molecular functionalities of the self-assembled monolayers induce different, well-defined orientations of the HKUST-1 crystals grown on gold. Although the mechanism of this remarkable effect is still unknown, a reasonable model could invoke selective interactions of crystal building blocks in solution with the functionalized surfaces. The thermal pre-treatment of the synthesis solution (8 days at 75 °C) induces the crystallization process; after filtration of the solid product, we anticipate the existence of colloidal or molecular building blocks of $Cu_3(BTC)_2$ in the solution. Taking into account the paddle-wheel motif in the open framework structure, different coordination modes of the carboxylic or the alcoholic groups might control the selective nucleation on the substrate, thus mimicking either axial (as with water) coordination with the alcohol terminus or chelating coordination (as with BTC) with the -COOH terminus of the SAM, respectively.

The results, described in this chapter, represent the "proof of concept" that by mimicking characteristic structural features of metal-organic frameworks in the terminal group of the self-assembled monolayers, it is possible to control the orientation of crystals during direct growth on gold. In the following chapters of this thesis, this proof of concept shall be further verified and extended. After employing the control over MOFs grown on gold substrates, the properties of highly oriented films of MOFs on functionalized surfaces will be investigated.

4 Single Layer Growth of Sub-micron Metal-Organic Framework Crystals Observed by *In Situ* Atomic Force Microscopy

This chapter is based on a manuscript submitted to the RSC journal "Chemical Communications".

The work results from the cooperation with Dr. Maryiam Shöâeè, Dr. Neena John, Dr. Martin Attfield and Prof. Michael Anderson from the *School of Chemistry*, *The University of Manchester*.

4.1 Introduction

Crystalline nanoporous metal-organic frameworks (MOFs), constructed from metal ions and organic linkers offer vast potential for the design of porous materials with molecularly selective interfaces, novel physical properties, enormous surface areas and a diverse array of functionality.[44, 53, 186] The metamorphosis of MOFs to functional materials necessitates a detailed understanding of their crystal growth to produce desirable crystal forms, for instance defect-free crystallites or single crystal films that will open new avenues for application. Atomic force microscopy (AFM), with its capability for sub-nanometre vertical resolution, has emerged as a powerful tool to investigate such crystal growth and has been applied to a wide variety of crystalline materials including nanoporous inorganic[187-190] and more recently hybrid materials.[160, 191-193] In particular, *in situ* AFM is an essential technique to provide

definitive real-time evidence about crystal growth including the mechanism, rates, fundamental growth units, and the effect of the surface form, supersaturation and impurities on growth.[193-197] Crucial fundamental knowledge can often only be gained from *in situ* AFM measurements if individual processes can be isolated on crystal faces with low defect concentrations, which is achievable using small crystals. However, growing such defect-free crystals and anchoring them during *in situ* AFM measurements is non facile. Here we report, for the first time, the direct observation of single layer growth on a monolayer-supported low-defect MOF crystal by *in situ* AFM.

The copper trimesate $Cu_3(C_9H_3O_6)_2(H_2O)_3$ (HKUST-1)[178] is a significant crystalline nanoporous MOF[67, 154, 159, 198] built from $Cu_2(H_2O)_2$ units and benzene-1,3,5-tricarboxylate (BTC) groups to form a cubic framework with a three-dimensional nanoporous channel system (see section 3.1). Some of the above mentioned AFM studies on hybrid materials deal with the crystal growth features of HKUST-1. The first high-resolution microscopic study, using AFM of the surface of a (111) face of HKUST-1, revealed spiral growth with steps heights directly correlated to the d_{111} and d_{222} lattice plane distances.[192] In a second study, the first high-resolution *in situ* AFM study of the crystal growth of a crystalline nanoporous material, the observed features of the *ex situ* images could be verified.[193] Both these studies were dealing with single crystals of HKUST-1 synthesized in DMF.

For this work, HKUST-1 crystals were grown under ambient conditions in an oriented manner on gold substrates functionalized with self-assembled monolayers (SAMs) (for detailed description see Chapter 3),[176] they provide a unique platform for *in situ* AFM studies since the crystals are directly attached to a gold-coated glass substrate that

can be easily mounted in the *in situ* chamber of the AFM. More importantly, the orientation of the crystals can be tuned by using different functional groups for surface functionalization, such that the growth of the (111) face can be monitored directly (Figure 4.1). A similar approach has been used successfully to collect *ex situ* AFM images of this material only. The reported results are differing from the previous *ex situ* AFM study mentioned above for the (111) surface of HKUST-1 crystals prepared in the conventional way. The main observation emerging from the previous study was the very high density of screw dislocations and frequent fracturing which result in a high density of very short terraces. Moreover, as evidenced by the frequently observed steps with a height corresponding to the multiple of 1.52/2 height, this surface exhibits also (222) termination, which makes it chemically non-homogenous. In contrast, the surface-grown crystals are essentially free from screw dislocation, and exhibit large micrometer-sized terraces with a homogeneous (111) termination.[160]

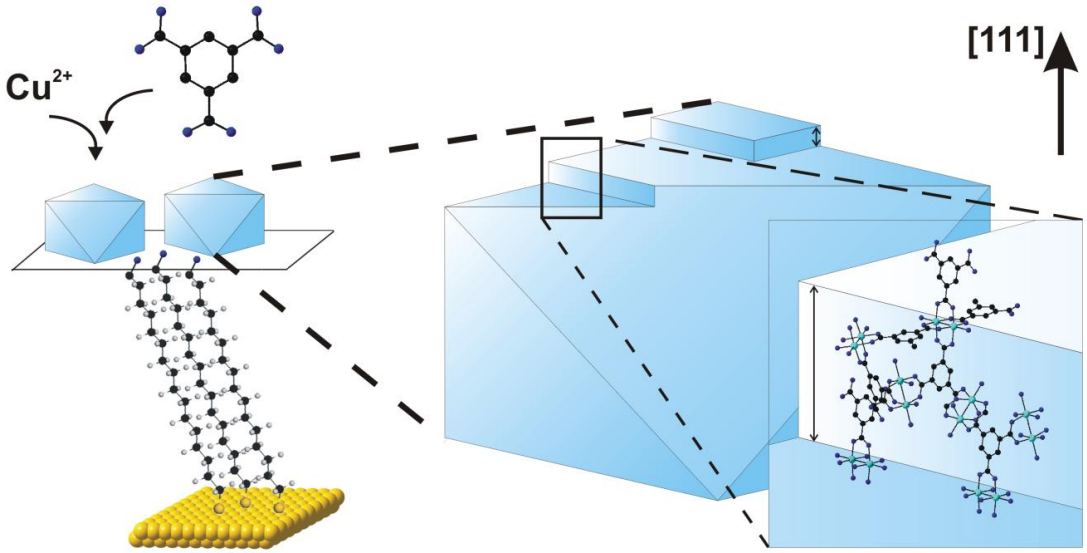

Figure 4.1: **Octahedral HKUST-1 crystals attached to 16-mercapto-1-hexadecanol-SAM on a gold substrate in [111] orientation; attachment of copper and BTC molecules during terrace growth on the (111) face (d_{111}-steps are shown).**

4.2 Experimental

Self-assembled monolayers on gold

The gold-coated slides (glass slides (76 × 26 mm^2) coated with 10 nm Ti / 100 nm Au by electron-beam evaporation, Advalytix AG) were cut in smaller pieces (10 × 13 mm^2) and cleaned in ethanol and methanol. The cleaned gold slides were immersed in a 1 mmol ethanolic solution (6 pieces in 30 mL) of 16-mercaptohexadecanol (MHD) (99 %, *Frontier Scientific*) and left at RT for 48 h. The SAM-functionalized gold slides were repeatedly washed with ethanol, and stored in fresh absolute ethanol till needed.

HKUST-1 synthesis mixture and Preparation of HKUST-1 Thin Films

The synthesis of the crystals of HKUST-1 supported on self-assembled monolayers of 16-mercapto-1-hexadecanol on gold was performed as described in the previous chapter (Section 3.2).

Preparation of the crystallisation solution for in situ AFM Measurements

A solution of 0.139 g (0.6 mmol) $Cu(NO_3)_2 \cdot 2.5H_2O$ (98%, Aldrich) in 6 ml water was added to a solution of 0.070 g (0.334 mmol) of 1,3,5-benzentricarboxylic acid (97%, Fluka) in 6 mL absolute ethanol, resulting in a $[Cu^{2+}]$ concentration of 0.05 mmol/mL in the solution, that was injected directly into the AFM liquid cell.

In Situ AFM measurements

The gold-coated glass slide supporting the crystals was fixed on to a cover glass using a Bi : Sn alloy (58 : 42 wt % - Alfa Aesar) and sealed in the liquid cell of a Nanowizard II, JPK Instruments A.G. AFM used to collect all the micrographs. Ex situ scanning was initially performed to image the topography of crystals and then 0.5 mL of the growth solution (see above), was injected directly into the AFM liquid cell. The laser intensity of the AFM was re-adjusted and the scanning continued under ambient conditions. The time at which the solution was injected was taken as time zero. The solution within the liquid cell was static and hence the supersaturation dropped as the growth proceeded. Stable scans of the growing crystal were possible once the supersaturation was sufficiently low. Imaging was done in contact mode using

commercial silicon nitride cantilevers with a low spring constant of 0.06 N/m and a scan rate of 2.5 or 3.5 Hz.

Quantitative Analyses of AFM Scans

Height analysis was performed using the JPK software. Plane fitting was done with respect to a flat terrace prior to height measurements. Approximately ten measurements were taken on every step to determine the precision of the step heights. The advancement of points at the vertex of the triangular growth step in the [11-2] direction and the [2-1-1] step were tracked in consecutive images in relation to the opposite crystal edge, with the latter assumed to be constant throughout the growth. The time for the points to advance between consecutive images was calculated from the pixel values of the particular point in the images and the scan rate. The distance measurements were repeated several times to provide mean deviations for each value plotted in Figure 4.7. The velocities were determined from the gradients of the linear fits to the data.

4.3 Results and Discussion

The high-resolution AFM deflection images of the growing (111) facet of a *ca.* 600 nm sized crystal of HKUST-1 as a function of time are presented in Figure 4.2 and Figure 4.3. The crystal growth could be clearly monitored 56 minutes after injection of the growth solution The image at t = 56 min (Figure 1a) reveals an extremely flat and relatively defect free crystal surface exemplifying the utility of this synthetic protocol to produce high quality crystal surfaces. In the subsequent images, growth of the surface is seen to proceed by a two-dimensional crystal growth mechanism[199, 200] in

which each new crystal layer nucleates at the same point on the crystal surface, indicated by an asterisk in Figure 4.2 b. A defect on the crystal edge that is beyond the resolution limits of the microscope is likely to be present at this point. The growth steps emerge from this single nucleation point and spread across the entire exposed crystal face. The low supersaturation of the growth solution, the small crystal face area and the low defect concentration on the crystal surface prevent additional two-dimensional surface nucleation. This offers the unique opportunity to monitor growth of *ca.* 0.2 μm^2 single steps across the crystal face without influence from other co-altitudinal growth steps. After 77 minutes of growth, the supersaturation level is low enough that the growth of a single step, from nucleation to coverage of the whole crystal face, can be observed as seen in Figure 4.2 b – j.

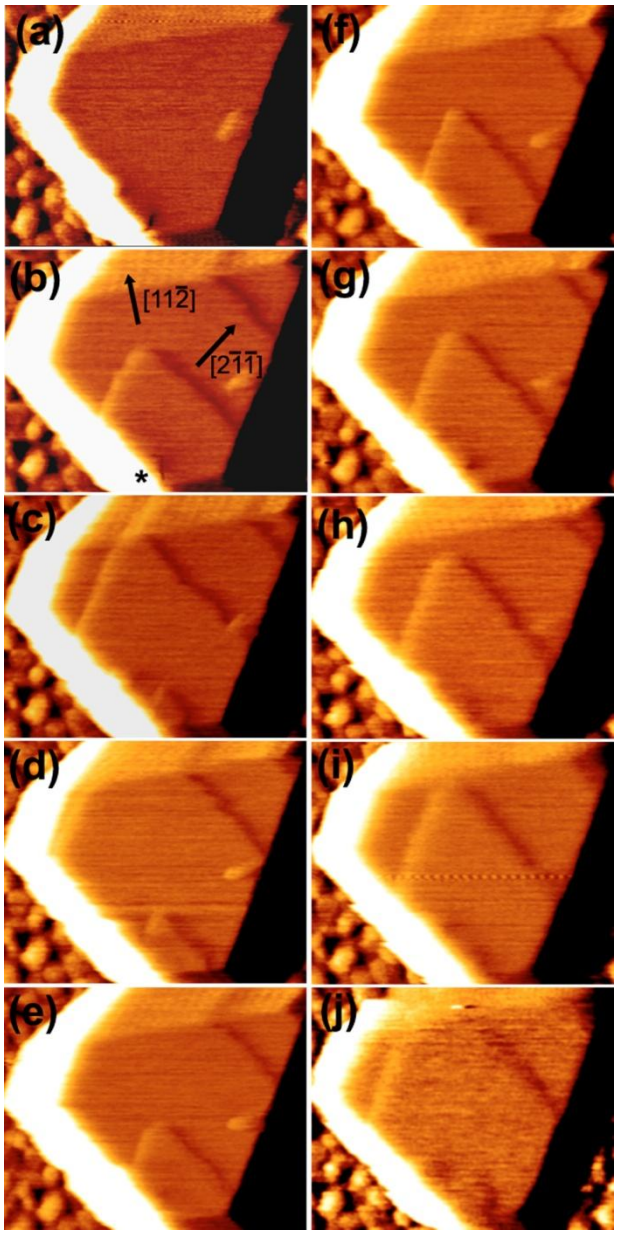

Figure 4.2: **Real time deflection AFM images of the growing (111) facet of a HKUST-1 crystal at a) 56 b) 77 c) 79 d) 82 e) 85 f) 88 g) 91 h) 94 i) 97 j) 108 min, after injection of the growth solution. (Times refer to the end of the each scan). Image sizes are 0.763 × 0.613 μm^2.**

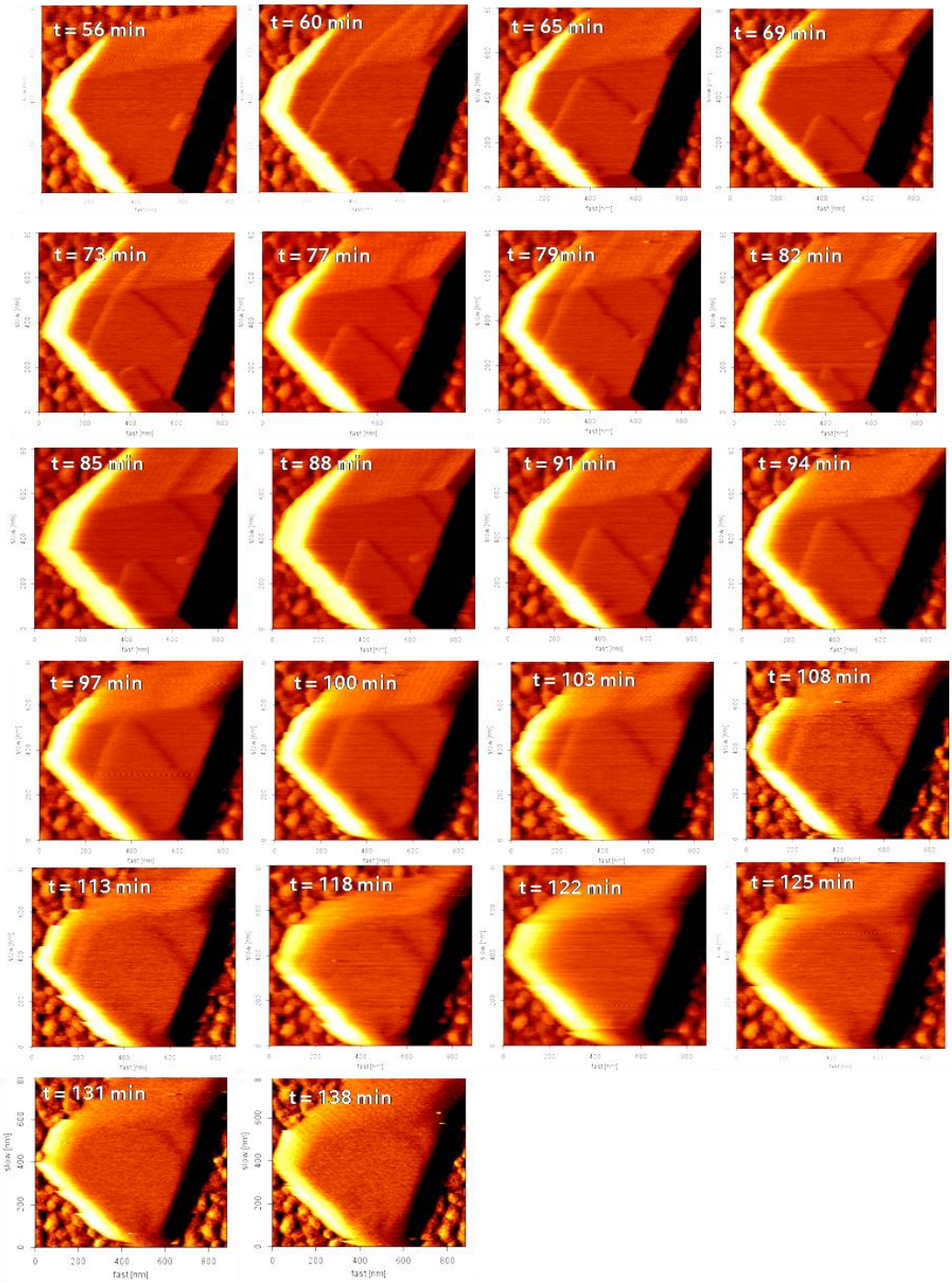

Figure 4.3: **Full series of AFM deflection images of a (111) facet of a *ca.* 600 nm HKUST-1 crystal in the growth medium (starting concentration of Cu^{2+} = 0.05 M) as a function of time (time is indicated in each image). The decrease in image clarity after 97 min is likely to be due to slight crystal movement. Image size is 885 × 800 nm^2.**

Real time images of the growth process of a single step provide exclusive details concerning the growth of this material. The images reveal the presence of anisotropic growth steps that are triangular in nature and exhibit the ternary symmetry of the (111) face.

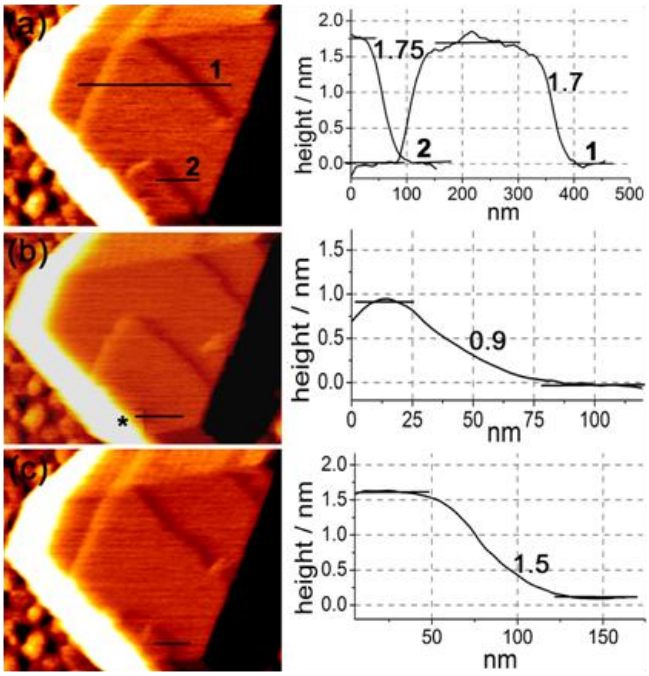

Figure 4.4: **Cross-sectional analyses of growing steps on the (111) facet (b); cross-sectional analysis of the single growth step (c) – (d); Step heights were measured from height images, although deflection images are shown in (b) – (d) for clarity.**

Cross-sectional analyses of height images at each time during the growth reveals that the vast majority of growth steps have heights of 1.5 ± 0.1 nm (see Figure 4.4) corresponding to the 1.5 nm d_{111} crystal spacing of the HKUST-1 structure, as shown in Figure 4.5 and previously reported for HKUST-1 crystals grown under a variety of conditions.[160, 192, 193]

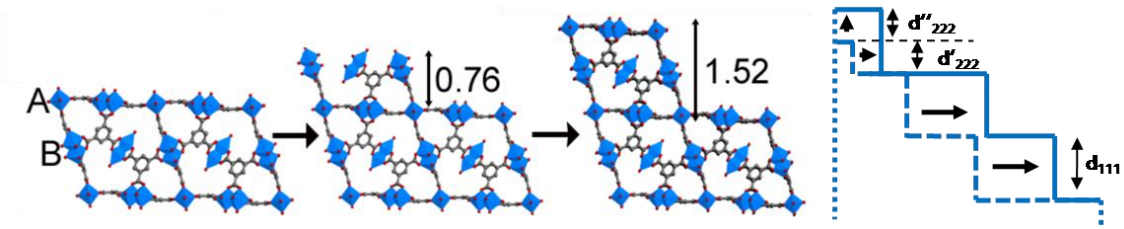

Figure 4.5: **<110> view of HKUST-1 framework, illustrating the observed steps during crystal growth.**

At 77 minutes after growth started, a small area at the nucleation point corresponding to the nucleation of a fresh layer can be noticed before it appears as a clear terrace at t = 79 min (Figure 4.4). Analysis of this small emerging area marked in Figure 4.2 b gives the step height of 0.9 ± 0.1 nm, corresponding to the 0.8 nm d_{222} crystal spacing. In the consecutive image (t = 79 min) the clear terrace with a triangular habit reveals a characteristic step height of 1.5 ± 0.2 nm. The growth of this terrace continues across the complete crystal face in the subsequent images (Figure 4.2 c-j). Considering the structure of HKUST-1, there are two different possible terminations of the (111) face, (depicted as termination *A* and *B* in Figure 4.6) of which *A*, due to symmetry and planarity, is viewed to be more stable than B.[192, 193, 201]

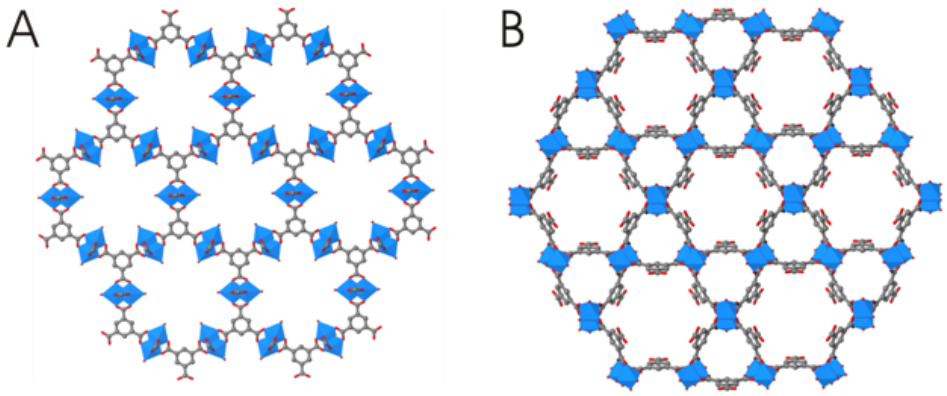

Figure 4.6: **Projection of *A and B* layers along (111). The *A* layer is 2D and more symmetric while the B layer features a corrugated 3D structure.**

The results suggest that crystal growth starts with the attachment of a single BTC molecule and a dimeric copper unit, corresponding to the 0.8 nm d'_{222} crystal spacing, onto the stable layer A (see Figure 4.5 and Figure 4.6). We propose that attachment of additional reagent to the crystal occurs more rapidly at this newly created layer with metastable termination B than at the surface with termination A. This process leads to the rapid growth of a second 0.8 nm d''_{222} crystal spacing step to create a 1.5 nm d_{111} crystal spacing step with a stable A-terminated surface. In this model, the growth subsequently takes place *via* the slow attachment of a d'_{222} layer onto a stable layer A, followed by rapid growth of the second d''_{222} layer to complete the next d_{111} layer with termination A.

The growth rate of the vertex of the triangular terrace in the [11-2] and the [2-1-1] direction (see Figure 4.2 b for directions) was measured and plotted in Figure 4.7. During the time period in which the vertex propagates to the crystal boundary (Figure 4.2 b – i), a linear growth rate of 25 nm min^{-1} is observed, while the edge in [2-1-1]

direction advances at approximately half the step speed of 13 nm min^{-1}. The constant step speed implies that the supersaturation is at a low enough level to remain essentially constant. At 96 minutes, after the vertex has reached the crystal boundary, the [2-1-1] edge still advances at a constant but slower speed of 2 nm min^{-1}. The sudden drop in step speed could be associated with a sudden change in supersaturation; however as the drop in step speed is observed when the growing vertex reaches the boundary of the crystal we attribute this drop to the removal of the influence of the vertex. We suggest that the vertex exhibits a "point effect" in which the rate of mass transport to the vertex is greater than that to a point elsewhere on the linear [2-1-1] and [-12-1] step edges.[202, 203] The vertex can also provide kink sites that will enhance edge-growth via a terrace-ledge-kink mechanism.

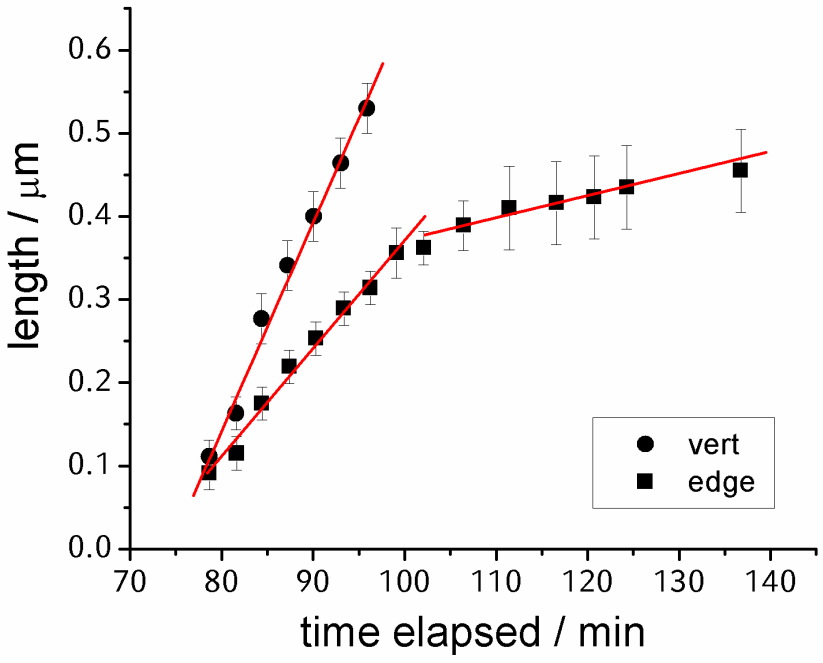

Figure 4.7: **Plot of the terrace advancement in [2-1-1] and [-12-1] direction as a function of time.**

The crystal growth of HKUST-1 we report here strongly contrasts with a previous *in situ* study of the group of Prof. Anderson where a 2D crystal growth mechanism and isotropic advancement of the growth steps was observed at multiple sites across the crystal surface.[193] This reflects the use of a much larger (*ca.* 50 μm) crystal with a high surface defect concentration and multiple nucleation sites in a different growth medium, i.e. dimethylformamide.[200, 204]

4.4 Conclusion

In summary, *in situ* atomic force microscopy was successfully used to directly investigate the growth processes of oriented HKUST-1 crystals grown on self-assembled monolayers on gold substrates. This approach has allowed the growth of a single growth step to be monitored extensively, which has provided direct evidence for a layer-by-layer mechanism of a constituent 1.5 nm d_{111} crystal spacing step of HKUST-1, its form during growth, and the influence of the step vertex on the rate of growth. This information enhances current understanding of the crystal growth of MOF materials, will support the development of crystals of these materials of specific form for future application, and demonstrates clearly the potential of the unique platform of SAM-supported oriented crystals to provide further insights into the chemistry and structural evolution of coordination polymers.

4.5 Additional Details

In this section the experiments prior to the observation of crystal growth described in the previous sections shall be presented.

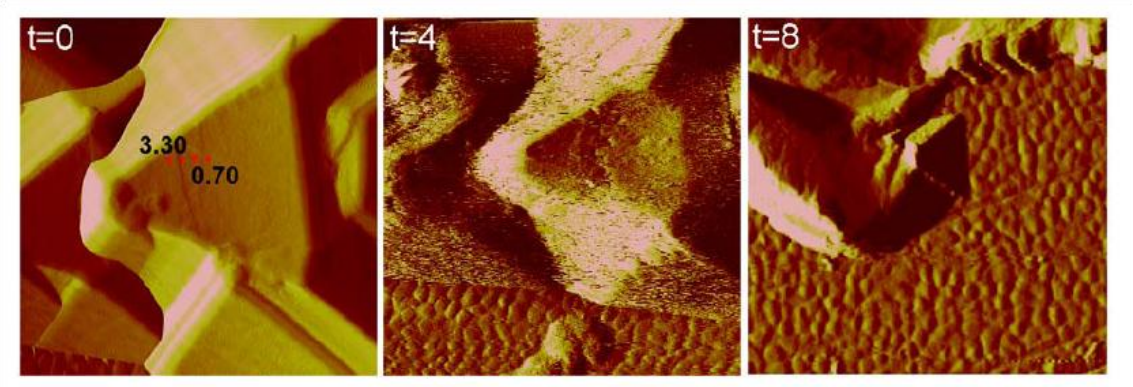

Figure 4.8: Dissolution of the [111]-oriented HKUST-1 crystals under a mixture of water: ethanol (1 : 1). Scan size is 2.48 × 2.48 µm^2.

The first exposure of a sample of oriented surface-grown crystals to a water/ethanol mixture (ratio 1:1) in the *in situ* chamber of the AFM led to rapid dissolution of the crystal, such that after 4 minutes, the majority of the crystal appears to have dissolved (Figure 4.8). The sample was scanned using contact mode and a scan speed of 3.02 Hz.

DISSOLUTION IN PURE ETHANOL

In a second experiment, a [111]-oriented HKUST-1 crystal was scanned in pure ethanol at a rate of 4.2 Hz. Dissolution takes place immediately under these conditions. Deflection images given in Figure 4.9 show little change in the topography of the chosen crystal. However, height analyses reveal that the lateral dimension of the crystal at t = 48 minutes has decreased by 100 nm. After 48 minutes the dissolution seems to slow down, resulting in a more obvious topographical change. This decrease in dissolution rate might be due to the increase in concentration in the supernatant solution because of the dissolving crystals all over the sample. At

t = 60 minutes it can be seen that the top terrace has dissolved and the remaining surface is smooth. A new layer begins to dissolve, as observed at t = 71 minutes. The boundary of the dissolved area appears to be at approximately the same position as the terrace seen in images taken between t = 12 and 48 minutes, (white line on t = 33 minutes) after which the dissolution of that top terrace slows down and a rapid dissolution of another layer up to approximately the said point follows, which results in multiple terraces that are observed at t = 89-160 minutes. The step heights in many instances are equal to the d_{222} spacing of 0.76 nm or to multiples thereof.

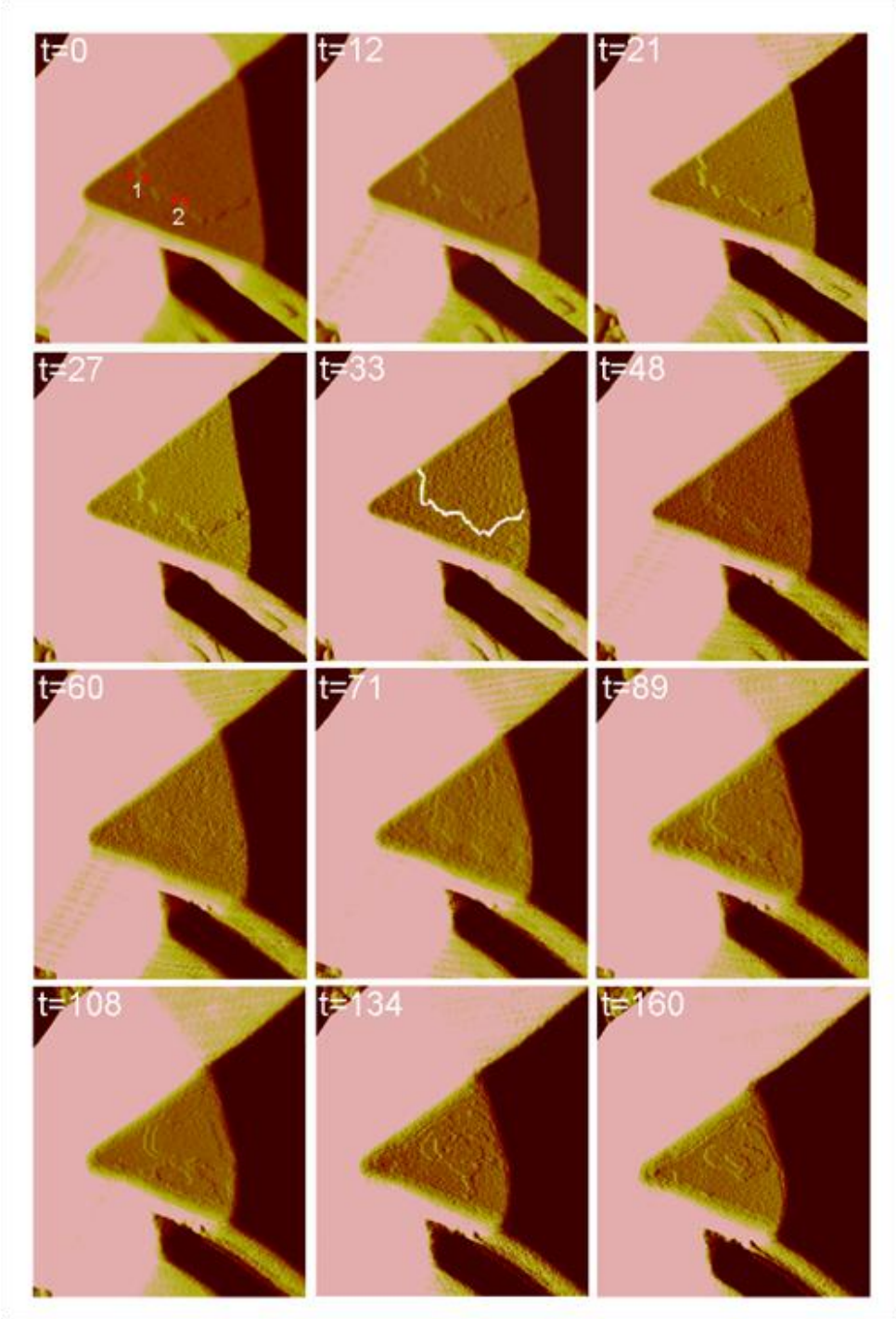

Figure 4.9: **Deflection images of the (111) face of a HKUST-1 crystal; times are quoted in minutes; scan size is 1.45 × 1.65 µm^2.**

GROWTH AND DISSOLUTION IN CU(II)/BTC SOLUTIONS

The AFM images using pure ethanol reveal fast dissolution of HKUST-1 crystals during scanning. To observe the reverse, i.e., *in situ* crystal *growth* at rates compatible with the AFM it is necessary to use a crystallisation solution with a concentration of nutrients as close to equilibrium concentration as possible. Due to the semi-static conditions under which the AFM experiments were carried out and the very small volume of the solution in the liquid cell, the saturation concentration has to be determined very carefully. It was found that the solution prepared in the same way as the solution used for prior synthesis of the films ($[Cu^{2+}]$ = 0.04 mmol/mL, see experimental section) led to dissolution of the crystal under study (Figure 4.10). In contrast, very fast crystal growth was observed when using a freshly prepared solution containing 0.06 mmol/mL $[Cu^{2+}]$ (Figure 4.11).

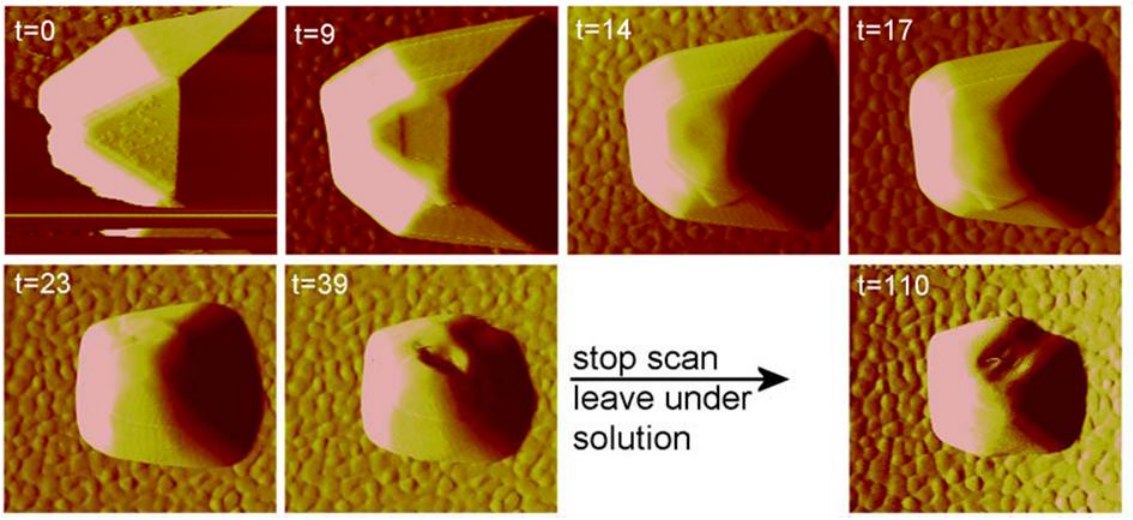

Figure 4.10: Deflection images of the dissolution process under a solution with $[Cu^{2+}]$ = 0.04 mmol/mL.

Figure 4.11: Deflection images of crystal growth under a solution with $[Cu^{2+}]$ = 0.06 mmol/mL.

A HKUST-1 crystal was scanned at 4.6 Hz in a solution with a concentration of $[Cu^{2+}]$ = 0.05 mmol/mL. The experiment resulted in the direct *in situ* observation of growth and dissolution processes of the crystal under study. The chosen octahedral crystal is much smaller (size of about 600 nm) than the crystals described above but still shows the characteristic triangular top face. Figure 4.12 shows a crystal with a triangular top face at t = 6 minutes progressing to a hexagonal top face at t = 180 minutes. This change in crystal topography is accompanied by a change in height and area, so that the aspect ratio of the crystal changed significantly, resulting in a more plate-like morphology. The change in aspect ratio and topography of the crystal under study is a perfect example of the effect of supersaturation on both morphology and topography.

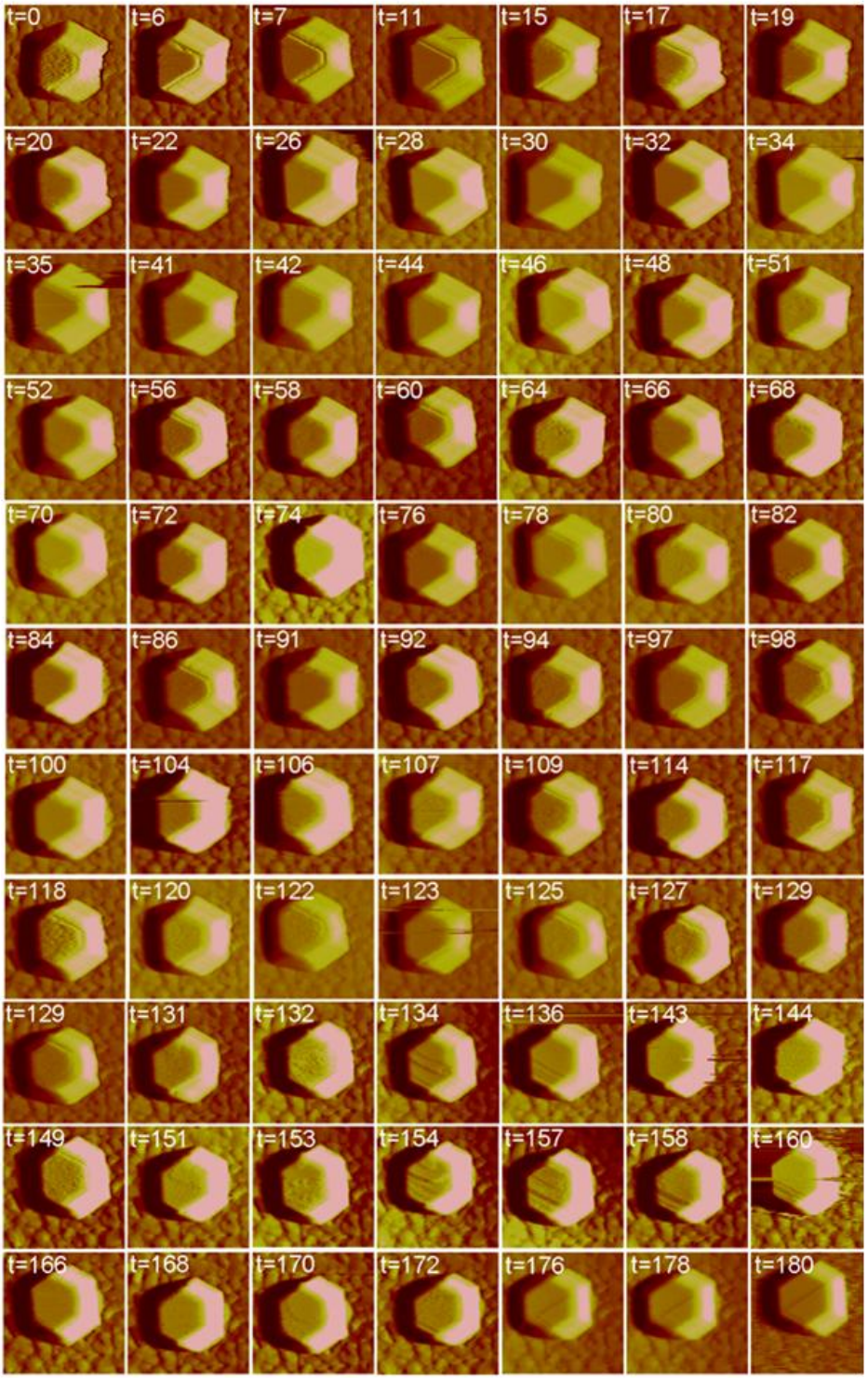

Figure 4.12: **Deflection images of a HKUST-1 crystal under a solution with $[Cu^{2+}] = 0.05$ mmol/mL; times are quoted in minutes; scan size is $1.45 \times 1.65\ \mu m^2$.**

An important issue to consider here is the effect of the scanning AFM-tip in contact mode on the surface properties of the crystal. As both crystal growth and dissolution was observed in the very same experiment, we assume that the gentle force applied on the crystal does not play an important role in these studies.

The solution was prepared at the beginning of the experiment and all the amounts injected are from the same batch. It is believed that due to depletion of nutrients in the initial solution during the experiment, dissolution will be occurring more readily at a later point compared to the beginning of the experiment. This is apparent at t≈115-135 minutes, where a sharp drop in crystal height is observed within a relatively short time window.

Step height analyses of the observed crystals show the height of most of the shortest terraces to be about 0.76 nm. Other steps such as 1.5 nm (but also around 0.4 nm) high were observed as well.

As discussed in section 4.3, the d_{111} spacing of HKUST-1 is 1.52 nm. The step heights observed during growth and dissolution processes are in most cases equal to the d_{222} spacing of 0.76 nm or to multiples thereof. Steps smaller than d_{111} or d_{222} were observed as well and can be explained by different terminations of the crystals surface; i.e., either the paddlewheel units or the BTC molecules can be the face-terminating species. Additionally, as the mechanism of dissolution and growth of MOFs must involve changes in the coordination chemistry of the copper ions, the departure of the copper-coordinating BTC molecule will be accompanied by the substitution of this ligand by another, in this case water or ethanol. Varying step heights in-between d_{111} and d_{222} distances can be explained this way. Deflection images of the growth processes (Figure 4.12) show clearly that growth as well as

dissolution takes place via a layer-by-layer mechanism. The layers correspond to the incremental attachment of BTC molecules and copper dimers.

The experiments summarized in this Supporting Information were the first steps in learning more about the mechanism of crystal growth of MOFs employing our surface grown oriented crystals. The conditions specified during these studies later on led to the monitoring of single layer growth described in section 4.3.

5 Directing the structure of metal-organic frameworks by oriented surface growth on an organic monolayer

This chapter is based on a publication in the journal "Angewandte Chemie, (International Edition)"[205].

5.1 Introduction

The concept of biomineralization implies the control of crystallization in terms of phase and orientation through interactions with organic macromolecules.[135-137] This is of particular interest for the synthesis of biomimetic materials.[142] If one strives to mimic the enormous structure-directing power of biomineralization in materials science, an artificial organic interface is needed. For example, functionalized self-assembled monolayers (SAMs)[141] have been shown to affect the oriented growth and phase direction of the dense phase calcium carbonate.[143, 206] The oriented growth of other dense materials such as lead sulphide[144] or zinc oxide,[146] and even the oriented growth of porous materials such as zeolites[148] on SAMs has been reported. Studies on the growth of MOF-5 and HKUST-1 phases on organic monolayers were recently reported (for detailed discussion see also chapters 1.4 and 3).[151, 153] However, to our knowledge so far it has not been possible to control the crystal structure of a porous material through interactions with molecular layers. This is

expected to be particularly difficult due to the large, complex unit cells featured by these systems.

Due to their many potential applications such as gas sorption, molecular separation, storage and catalysis, metal-organic frameworks (MOFs) have been intensively studied.[50, 67, 207] In chapter 3 the tuneable, oriented growth of the porous metal-organic framework HKUST-1 on different functionalized self-assembled monolayers is discussed.[176] Here we investigate the crystal growth of metal-organic frameworks on SAMs in the system Fe(III) / BDC (benzenedicarboxylic acid or terephthalic acid).

In this system several open framework structures are known, including MIL-53, MIL-88, and MIL-101 (MIL = Matériaux de l'Institut Lavoisier). MIL-101 is very famous for its large zeotype unit cell and its large surface area. The structures of MIL-53 and MIL-88 are very flexible and the cell constants of these materials are strongly dependent on the pore content.[208, 209] The framework flexibility of these materials enables their use for the adsorption of different organic molecules and makes them interesting candidates for sensors.

The monoclinic structure (space group *I2/a*) of $Fe(OH)(BDC)(py)_{0.85}$, the Fe(III)-analogue of MIL-53, consists of chains of FeO_6 octahedra that are connected by benzenedicarboxylate anions. Thus, as presented in Figure 5.1, rhomb-shaped one-dimensional channels are formed that run along the *a* axis of the structure.[210] The group of Férey first synthesized MIL-53 with the metal ions chromium[211] and aluminium[88]. The Fe(III)-analogue was synthesized from Whitfield *et al.*,[210] using iron nitrate and BDC in the presence of pyridine in dimethylformamide (DMF).

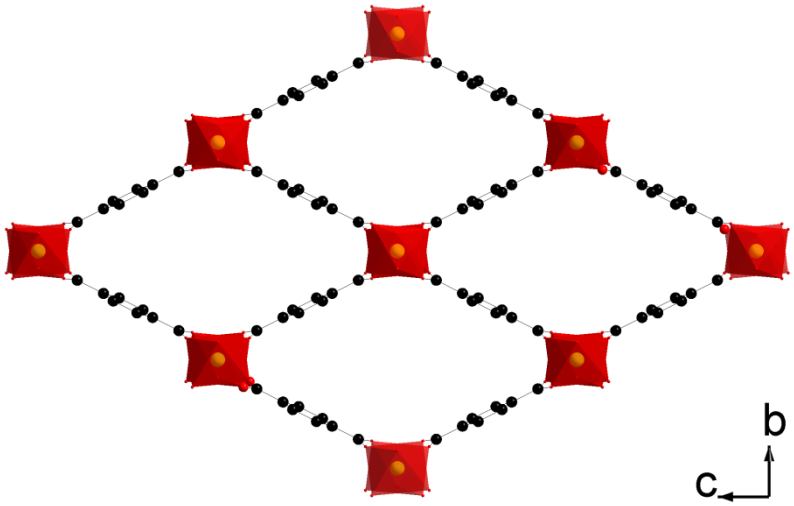

Figure 5.1: **Crystal structure of Fe-MIL-53 with view along chains of FeO_6 octahedra (along *a* axis).**

The first synthesis of MIL-101 was with chromium (III) as the metal component[72], but up to now the structure is known with different metal (III) ions.[212] The composition of MIL-101 is $Cr_3F(H_2O)_2O(BDC)_3 \cdot n\,H2O$ ($n \sim 25$). It crystallizes in the cubic space group *Fd-3m* with a lattice parameter of $a = 89$ Å. For frameworks with such a large unit cell it is difficult to obtain single crystals, which is why a special approach was employed to solve this complicated crystal structure, the AASBU (automated assembly of secondary building units).[213] The AASBU method explores how an inorganic cluster and an organic linker, or even predefined hybrid building blocks, may connect in 3D space to form periodic lattices. A set of possible framework structures is produced, along with their crystallographic features (space group, cell parameters, and atomic coordinates) and their simulated X-ray diffraction patterns. The comparison of the simulated pattern of each candidate structure with the experimental one identifies the experimental structure. The final solution of the crystal structure is obtained by fitting the theoretical data to the experimental results

with the help of Rietveld refinement.[214-217] In the crystal structure of MIL-101 four trimers of metal-oxygen octahedra are linked via BDC molecules to so-called supertetrahedra (ST). Corner sharing STs are linked in a way to give a MTN-zeotype framework structure. (Figure 5.2)

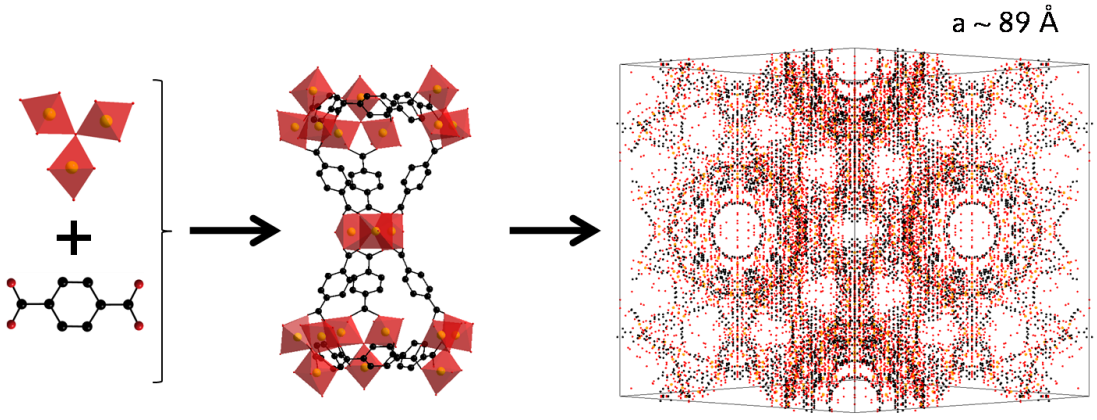

Figure 5.2: **Trimers of metal-oxygen octahedra are linked to Supertetrahedra; Corner sharing ST are linked to give a MTN-zeotype framework structure with a lattice parameter of *a* = 89 Å.**

The framework structure of MIL-101 consists of mesoporous cages with a diameter of 29 Å and 34 Å. Evaluation of the sorption data with the help of the Langmuir method gives a surface area for MIL-101 of 4500 – 5900 m^2/g, which is a higher value than ever observed for any other MOF structure.[72]

The hexagonal 3D structure of MIL-88B with the chemical composition $Fe_3O(BDC)_3 \cdot solv$ (*solv* = MeOH) is built up from trimers of FeO_6 octahedra linked to benzenedicarboxylate anions. Thus, the 3D pore system of MIL-88B consists of tunnels along the *c* axis connected by bipyramidal cages (Figure 5.3 and Figure 5.4).[43] The other members of the isoreticular MIL-88 family have the same crystal

structure; the only difference is the organic linker, which can vary in size from fumaric acid (MIL-88A) over naphthalenedicarboxylic acid (MIL-88C) to biphenyldicarboxylic acid (MIL-88D).

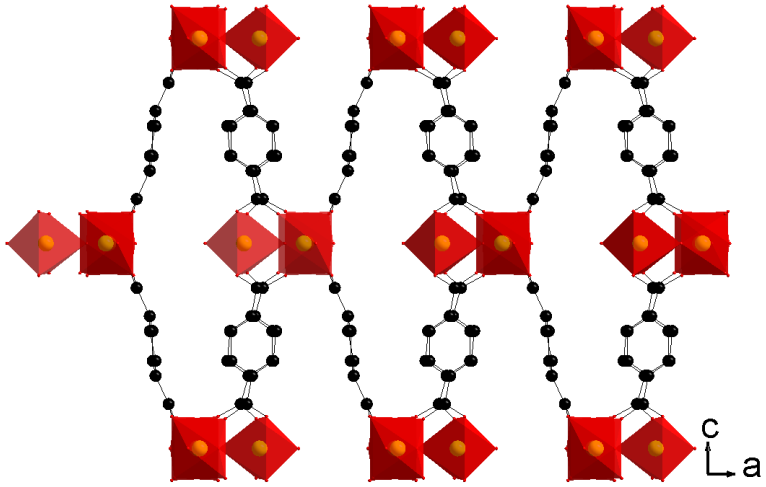

Figure 5.3: **Crystal structure of Fe-MIL-88B with view along *b* axis.**

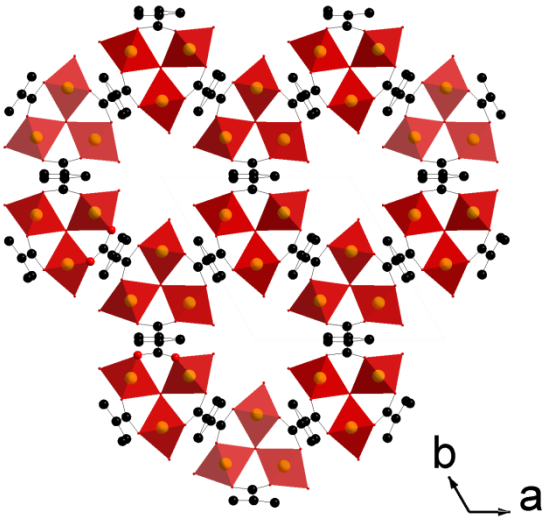

Figure 5.4: **View along the channels of Fe-MIL-88B structure (along *c* axis).**

All of these interesting structures have been investigated with regard to their properties since their discovery.[208, 209, 218-224] The prospects for applications vary from gas sorption and storage, including selectivity towards certain substances,[77, 86, 88, 225-241] over electrolytic[242] and catalytic[243, 244] properties ending up with drug delivery systems.[245, 246] The structures of MIL-53, MIL-88B, and MIL-101 all consist of the same building blocks. Therefore it is easy to understand, that the particular synthesis conditions have to play an important role in getting the desired structure. In the following chapter the dramatic change in the crystallization of a porous metal-organic framework upon moving from homogeneous nucleation to heterogeneous nucleation on an ordered self-assembled monolayer is presented. (see Figure 5.5)

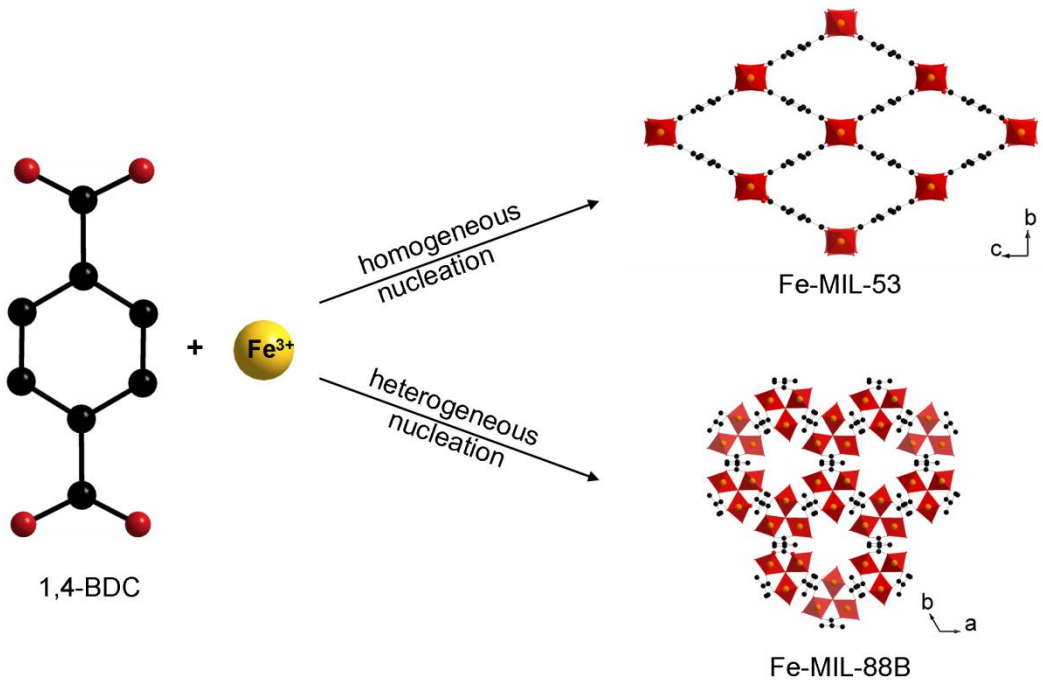

Figure 5.5: **In the system Fe^{III}/BDC we observe Fe-MIL-53 as product of homogeneous nucleation, and oriented Fe-MIL-88B as product of heterogeneous nucleation, i.e., on functionalized gold surfaces.**

5.2 Experimental Section

Preparation of self-assembled monolayers on gold

The gold-coated slides (glass slides (76 × 26 mm^2) coated with 10 nm Ti / 100 nm Au by electron-beam evaporation, Advalytix AG) were cut in smaller pieces (10 ×13 mm^2) cleaned in ethanol, methanol and then treated 3 min in an oxygen-plasma. The cleaned gold slides were immersed in a 1 mmol ethanolic solution (6 pieces in 30 mL) of 16-mercaptohexadecanoic acid (MHDA) (90 %, *Aldrich*) and left at RT for 48 h. The SAM-functionalized gold slides were repeatedly washed with ethanol, and stored in fresh absolute ethanol till needed.

Fe-MIL-53 synthesis mixture

In a glass reactor, 0.2492 g (1.5 mmol) of 1,4-benzenedicarboxylic acid (98 %, *Aldrich*) were dissolved in 10 mL dimethylformamide (DMF) (p.a., *Acros Organics*). To the clear solution 0.2703 g (1 mmol) $FeCl_3 \cdot 6\,H_2O$ (p.a., *Merck*) was added. The sealed-glass reactor was left for 2 days in a preheated oven at 150 °C. After cooling the synthesis mixture to room temperature, the crystalline product was filtrated and stored for further characterization. The filtrated solution was filled into a glass reactor and left for 5 days in a preheated oven at 150 °C. The clear solution was cooled down to room temperature and used for growth of thin films.

Thin film growth

The SAM-functionalized gold-slides were placed upside-down on Teflon®-supports into the previous prepared crystallization solution (3 pieces in 10 mL). The growth

step takes place at RT in a closed glass reactor. Immersion times were varied between 16 h to16 d.

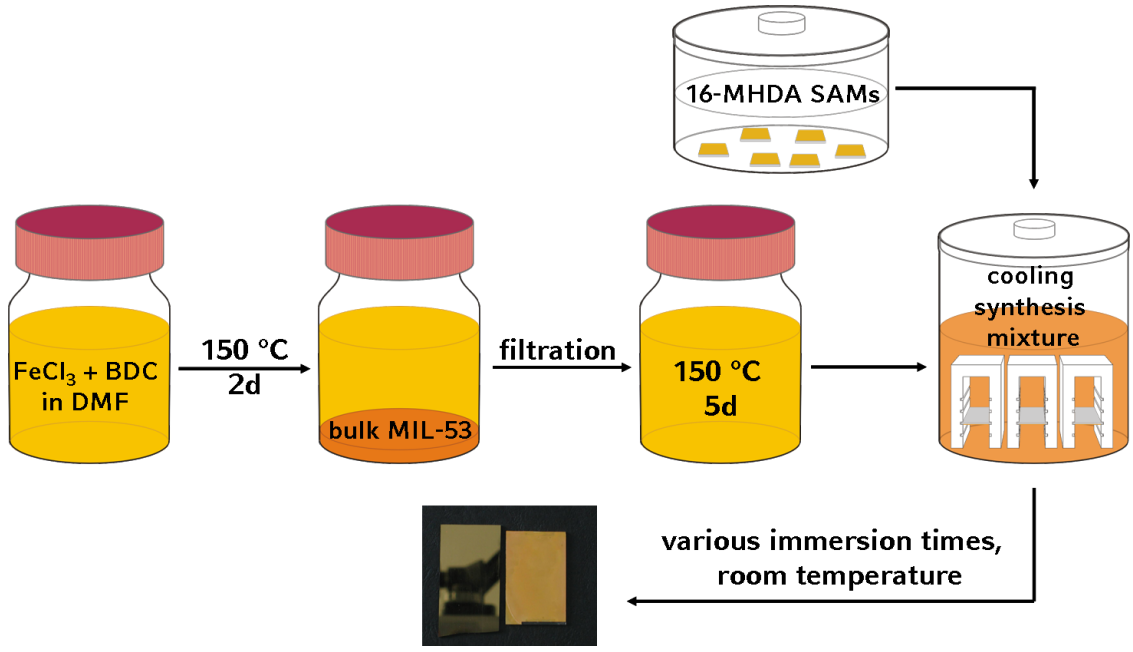

Figure 5.6: **Schematic illustration of the preparation procedure of Fe-MIL-88B thin films on MHDA SAM-functionalized gold slides.**

Fe-MIL-88B synthesis

The synthesis was carried out according to the literature procedure,[43, 247] In a glass reactor, 3.987 g (24 mmol) of 1,4-benzenedicarboxylic acid (98 %, *Aldrich*) were mixed with 160 mL methanol (MeOH) (p.a., *Fluka*). To the mixture 10 mL 1M NaOH and 4.326 g (24 mmol) $FeCl_3$ 6 H_2O (p.a., *Merck*) was added. The sealed-glass reactor was left for 3 days in a preheated oven at 100 °C. The orange crystals were filtered, washed with MeOH and dried under nitrogen before further characterization.

5.3 Characterization

X-ray diffraction (XRD) measurements of powders were performed on a STOE powder diffractometer in transmission geometry (Cu-$K_{\alpha 1}$, $\lambda = 1.5406$ Å) and of films using a Scintag Inc. XDS 2000 in theta-theta geometry (Cu-$K_{\alpha 1}$, $\lambda = 1.5406$ Å; Cu-$K_{\alpha 2}$, $\lambda = 1.5444$ Å). Characterization of the self-assembled monolayers was performed by RAIR spectroscopy, using a Bruker IFS 66v FT-IR spectrometer. The sample chamber mounting a high performance variable angle reflection accessory (A-513) is maintained at 2 mbar during the entire measurement by means of an Edwards rotary-pump. In a typical measurement for gold surfaces, an incidence angle of 83 ° to the surface normal was used. Furthermore, a cleaned gold slide was measured as background prior to the measurements. The morphology of the crystals on the substrates and as bulk material was investigated with the help of a JEOL JSM-6500F scanning electron microscope.

5.4 Results and Discussion

Highly ordered thin films of MOF crystals were formed on the carboxylate terminated SAMs. X-ray diffraction patterns of all synthesized thin films show two reflections at 9.2 ° and 18.4 ° two theta (Figure 5.7). The intensity of the reflections increases with longer immersion times. In Figure 5.8 the increase in intensity of the first reflection is given as a function of the immersion time.

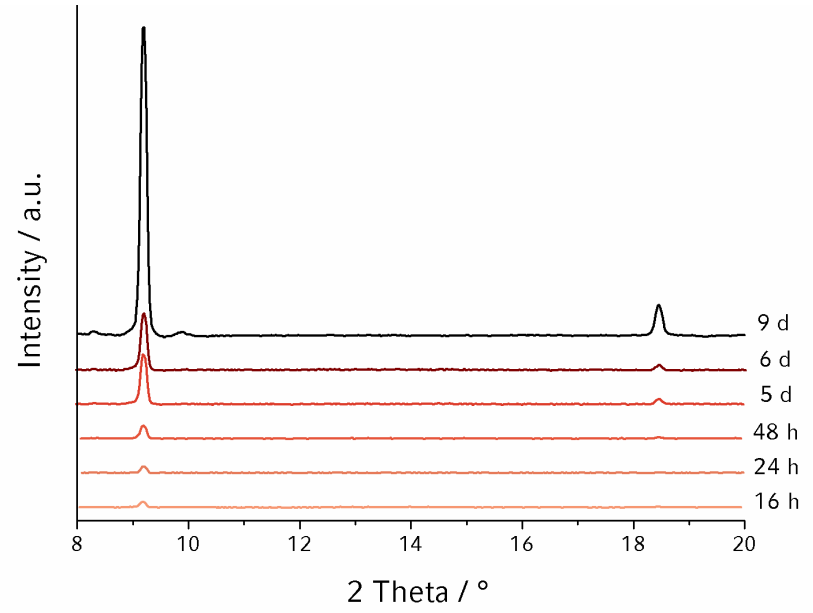

Figure 5.7: X-ray diffraction measurements of crystals grown on functionalized gold substrates. The immersion time of the substrates in the crystallization solution varied between 16 h and 9 d.

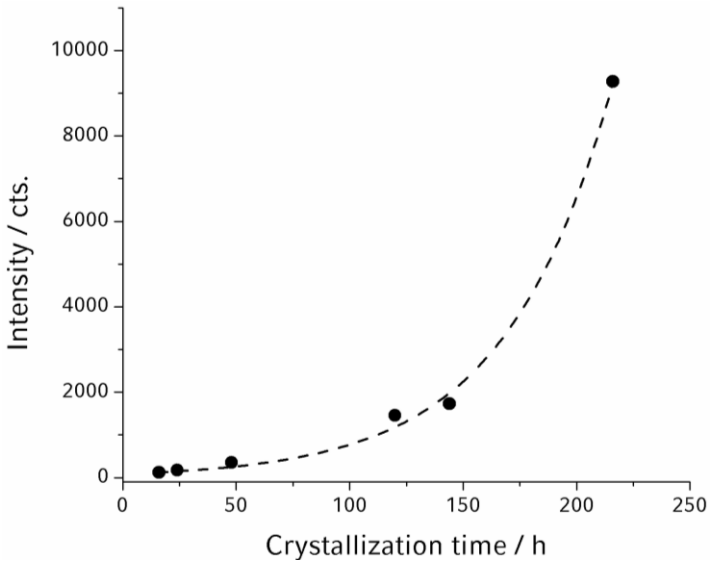

Figure 5.8: Increase in intensity of the main reflection as a function of crystallization time.

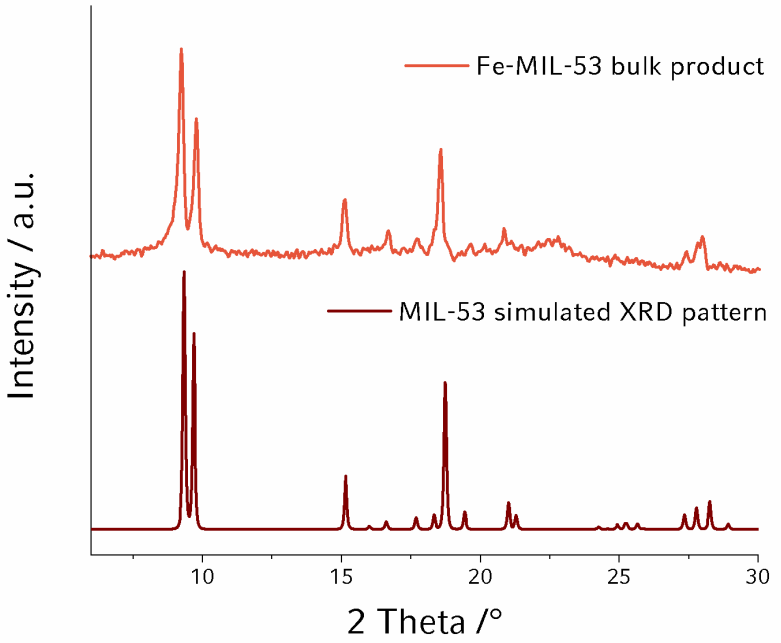

Figure 5.9 **X-ray diffraction data of product in the crystallization solution during surface growth compared to the simulated pattern of Fe-MIL-53.**[210]

The lack of any additional reflections in the XRD patterns of the film samples strongly suggests the oriented assembly of the crystals on the functionalized gold surface.

The reflections in the XRD pattern of the synthesized films fit both the (011) and (022) reflections of MIL-53 as well as the (002) and (004) reflections of MIL-88B. The precipitate in the crystallization solution during film synthesis can be identified as the iron MIL-53 analogue (Figure 5.9).

For further characterization the crystals were removed from the gold surface. The powder pattern of the surface-removed crystals shows several additional reflections in comparison to the XRD patterns of the films (see Figure 5.10).

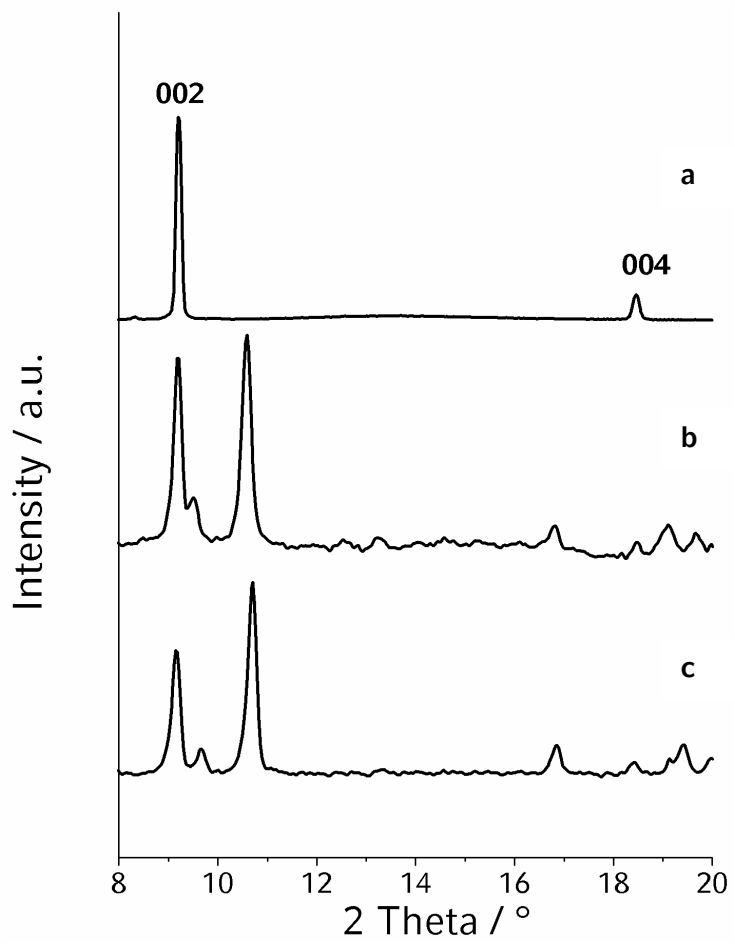

Figure 5.10 **(a) XRD pattern of film on gold substrate, (b) powder pattern of the removed crystals and (c) powder pattern of bulk Fe-MIL-88B.**

In spite of the fact, that the product of homogenous nucleation during surface crystal growth is Fe-MIL-53, the powder pattern of the surface-removed crystals does not fit to the powder pattern of bulk MIL-53. In a bulk synthesis an authentic sample of MIL-88B was prepared.[43, 247] The XRD pattern of the product (Figure 5.10c) agrees very well with the XRD pattern of the surface-removed crystals. It is possible to index the reflections of the XRD pattern of the removed crystals in the space group of MIL-88B

as P-62c[222] (Figure 5.11). The lattice constants are determined as 10.751 Å for *a*, and 19.211 Å for *c*, respectively.

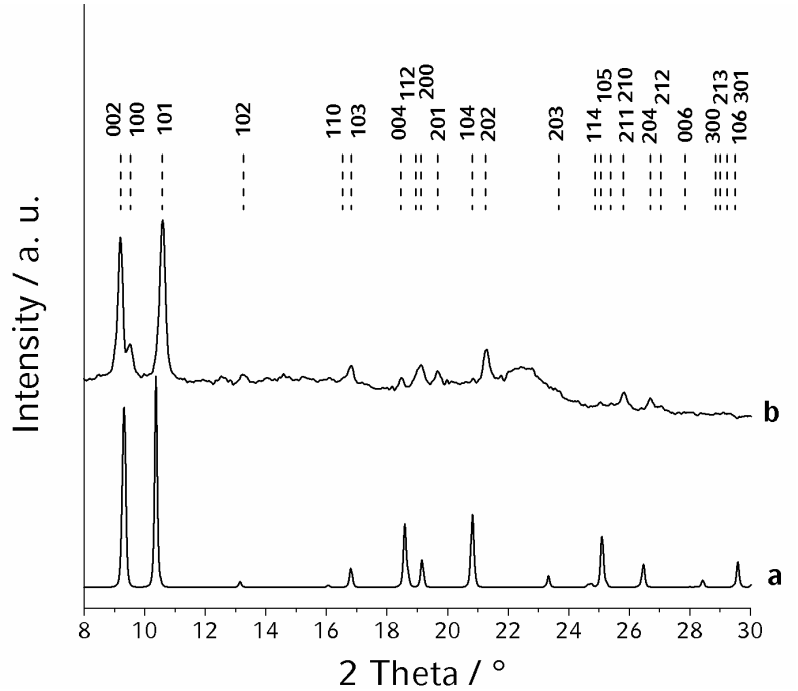

Figure 5.11: **(a) Simulated X-ray diffraction pattern of MIL-88B *as*[222]. (b) XRD powder pattern of surface removed crystals. The indexation of reflections of sample (b) is given on top of the figure. The lattice constants for MIL-88B *as* are *a* = 11.1 Å, *c* = 19.0 Å. The determined lattice constants for sample (b) are *a* = 10.751 Å, *c* = 19.211 Å.**

As indicated above (Figure 5.5) there is a drastic change from Fe-MIL-53, the product of the homogeneous nucleation from the crystallisation solution to Fe-MIL-88B, the product of the heterogeneous nucleation on the functionalized gold surface. We attribute this dramatic effect to symmetry transfer, i.e., the different symmetry relationships between the carboxylate-terminated SAMs and the two different crystal systems. Carboxyl-terminated thiolates, as well as thiolates in general, adsorb on an

Au (111) surface to form a (√3×√3)R30 ° overlayer.[106, 248] The order of carboxylic acid SAMs responds sensitively to the deposition conditions.[129] The SAMs used in this study feature carboxylate termini and high crystallinity in the alkyl-part of the film, as evidenced by the reflection-absorption infrared spectra presented in Figure 5.12. No crystal growth was observed with hydroxyl- and alkyl-terminated SAMs or with non-treated gold slides. Being presented with a surface exposing (approximately) hexagonal symmetry, the reactants (Fe^{III} and BDC) clearly prefer to crystallize in the form of hexagonal MIL-88B instead of monoclinic MIL-53.

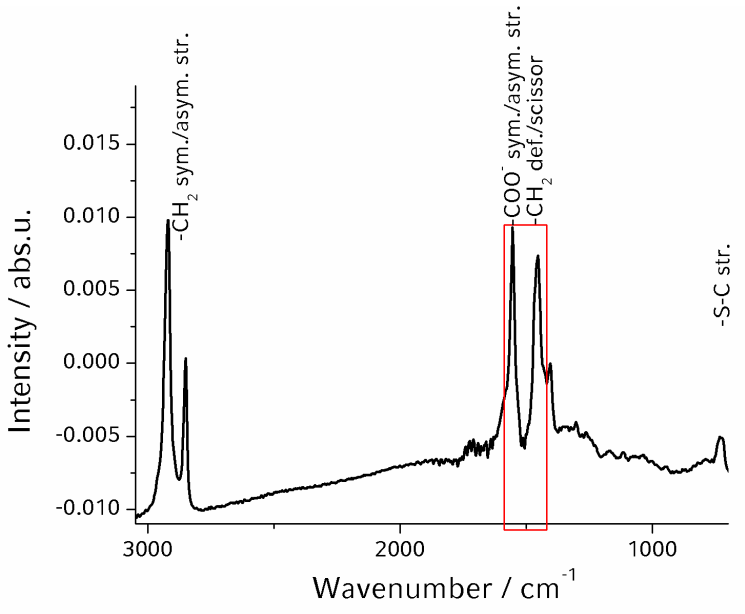

Figure 5.12: RAIR-spectra of a MHDA self-assembled monolayer on a gold substrate.

In order to investigate the morphology of the crystals grown on gold substrates, scanning electron micrographs of samples after different immersion times were taken. The scanning electron micrographs of two different samples are shown in Figure 5.13.

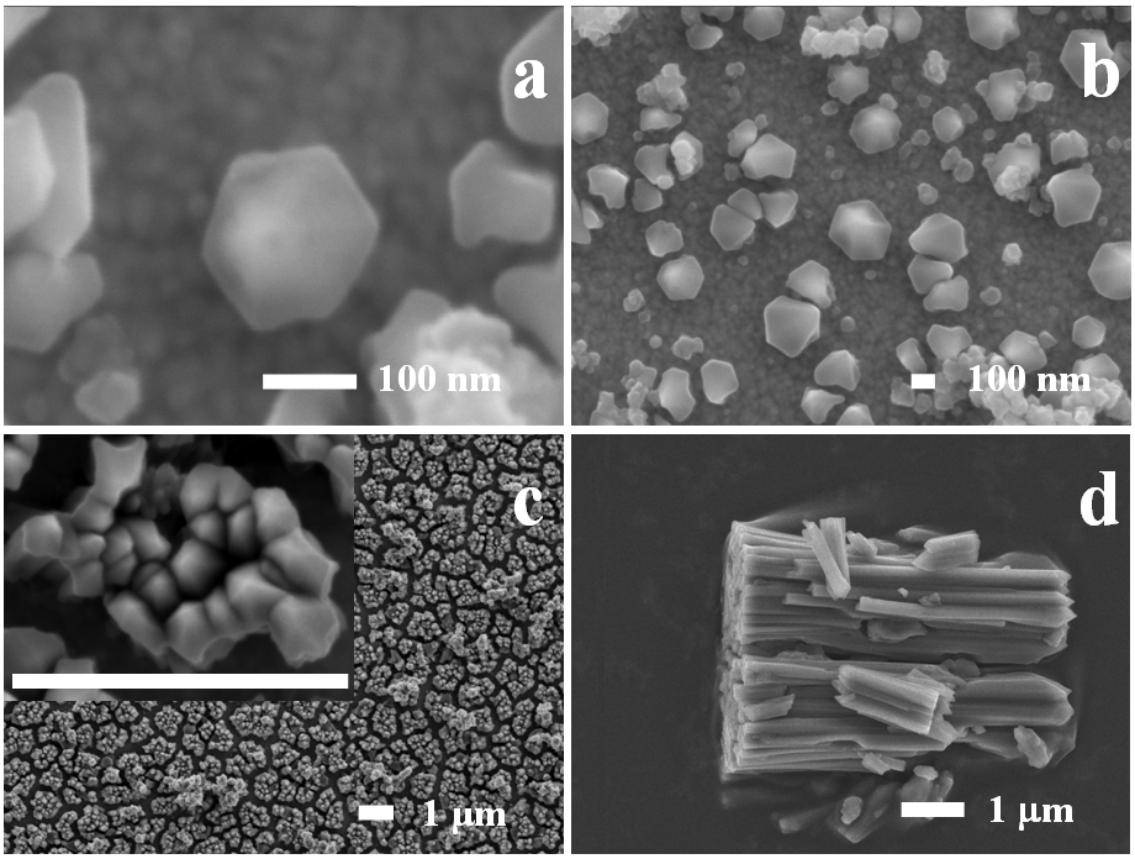

Figure 5.13: **(a, b) Scanning electron micrographs of samples after immersion times of 24 h, (c) 3 days and (d) a bundle of removed crystals.**

After an immersion time of 24 h, small hexagonally-shaped pyramids with almost vertical orientation can be observed. The diameter of the pyramids is about 200 nm. Crystal intergrowth already starts after immersion times of 24 h. After an immersion time of 3 days the gold surface is almost completely covered with pillar-like hexagonally shaped crystals that are about 500 nm long. Samples with longer immersion times show cracked films in the SEM. The cracking might be due to the post-synthesis treatment of the samples (i.e., drying under nitrogen or evacuating during scanning electron microscopy).

The morphology and the symmetry of the crystals agree well with the structure of MIL-88B. The XRD pattern of the film shows exclusive orientation of the crystals in [001] direction. This implies that the (001) plane of the crystals is parallel to the gold substrate. Figure 3 shows schematically the connection of MIL-88B to the carboxylate groups of the MHDA SAMs on the gold surface. The sixfold axis of the MIL-88B crystal lattice is aligned with the hexagonal symmetry of the SAM-liquid interface. In addition, the oriented crystal growth on the carboxylate-terminated self-assembled monolayers can be explained by the coordination of the carboxylate at the metal atom of the metal-organic framework. Since all terephthalic acid molecules are oriented along [001], substitution of the carboxylates of terephthalic acid through carboxylates of the SAM will enable crystal growth only in the [001] direction (Figure 5.14).

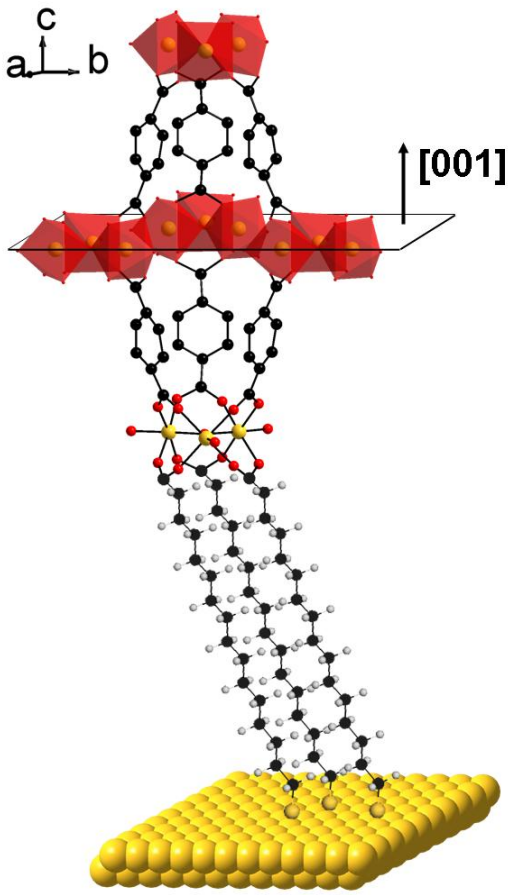

Figure 5.14: Oriented growth of MIL-88B crystals on MHDA SAMs on Au (111) (schematic). Crystals grow in [001] direction.

To investigate the properties of the grown crystals, particularly with regard to the sorption properties, the samples were exposed to saturated DMF vapour for 24 h. Due to the framework flexibility of MIL-88B as a function of the pore content, the DMF form of MIL-88B shows different reflection positions than the as-synthesized form.[222] Our results show clearly that the structure changed during uptake of DMF (Figure 5.15).

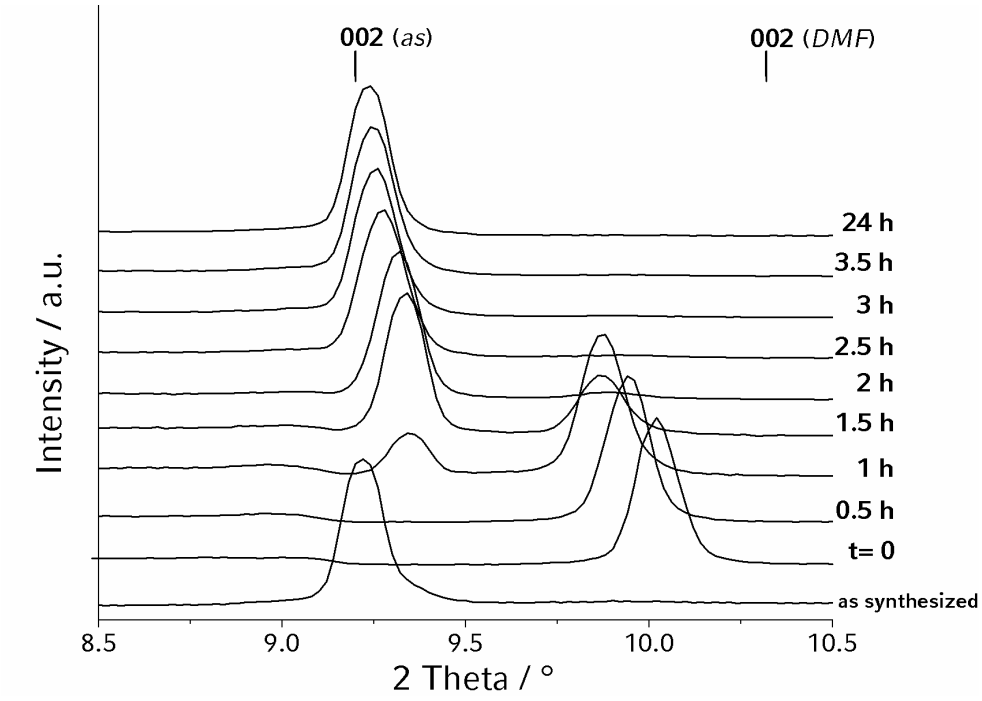

Figure 5.15: XRD patterns of a MIL-88B film as synthesized, after exposure to DMF vapour for 24 h during desorption in air (diffraction data were collected every 30 min), and after drying for 24 h.

The (002) reflection after DMF uptake lies at 10.02 ° 2θ, at a value fairly similar to the reported value of 10.4 ° 2θ for bulk MIL-88B.[222] Small differences are attributed to different partial pressures of DMF in these experiments, and to the surface attachment of the crystals. During desorption of DMF the XRD measurements were performed every thirty minutes. At the beginning desorption evokes a continuous structural change which after 24 h ends with the state shown in Figure 5.15, similar to the initial state. The surface-bound MIL-88B crystals were synthesized in their expanded, DMF-loaded form, and shrinkage upon drying provides space for expansion upon renewed uptake of DMF (see Figure 5.16). Obviously their elasticity

can accommodate the shrinkage and expansion cycles demonstrated in the experiment.

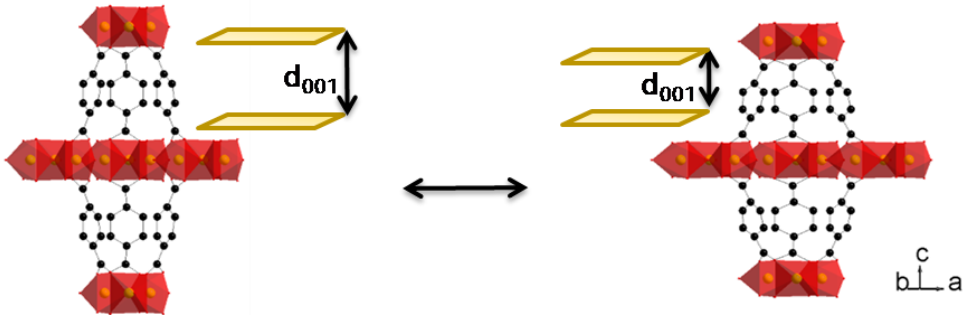

Figure 5.16: Changes of the framework in MIL-88B during uptake and desorption of DMF are depicted schematically.

5.5 Conclusion

The results presented above show the striking structure-directed and oriented growth of MIL-88B on MHDA SAMs. MIL-53 is the product of homogeneous nucleation, whereas in the same crystallisation solution, oriented MIL-88B grows on the functionalized gold surface. These remarkable results can be explained through favourable symmetry relationships between the hexagonally ordered SAMs and the hexagonal structure of MIL-88B. The carboxylate functionality of the MHDA SAMs can mimic the carboxylate groups of the BDC molecules und thus direct oriented growth on the surface. We could also show that the pores of MIL-88B crystals in the film are accessible for DMF molecules and that the characteristic associated structural changes during the adsorption and desorption processes can be observed.

Future studies will show if the concept of symmetry transfer between functional monolayers and complex crystalline materials can be adapted to other MOFs, thus

providing a powerful means to control structure and orientation in biomimetic materials systems.

In the next chapter the sorption properties of the highly oriented films of MIL-88B will be discussed in detail.

5.6 Additional Details

Optimization of the Synthesis pathway for MIL-88B films

To find the right conditions for the film synthesis of MIL-88B, several experiments were carried out. The parameter field in the system Fe(III)/BDC was investigated with regard to the synthesis temperature, the synthesis time and the concentration of the reactants. In the series of experiments we distinguish between the first and the second crystallization step. The first crystallization step refers to the product of the reaction after mixing the reagents in the given ratio followed by thermal treatment. In the second crystallization we use the filtrated synthesis solution of a first crystallisation step to investigate the precipitation products after a second thermal treatment and/ or after a certain reaction time. The reason for this approach is our interest in the crystallisation of MOFs under mild conditions to make sure, that the SAM on the gold substrate survives the synthesis conditions. During film synthesis of HKUST-1 (chapter 3), we observed, that it is possible to obtain crystalline products in a second crystallisation step, so we transferred this synthesis pathway to different framework structures.

Table 5.1: **Composition of the crystalline products after synthesis under the given conditions; blue: unknown crystalline phase, red: Fe-MIL-101, orange: Fe-MIL-53.**

	75 °C	100 °C	150 °C
1 d			
2 d			
5 d			
8 d	-		

For 75 °C and 100 °C only mixtures of two products where obtained, as shown schematically in Table 5.1. At 75 °C the mixture contained more of the unknown crystalline phase, while at 100 °C the product was mainly Fe-MIL-101. After a reaction time of two days, the only obtained product at 150 °C was Fe-MIL-53. In a second series of experiments the effect of dilution on the resulting products was examined. For more concentrated solutions than in the original composition (Fe : BDC : DMF = 1 mmol : 1.5 mmol : 10 mL), Fe-MIL-53 was the only obtained product. For reaction mixtures with lower iron concentrations, again a mixture of the unknown phase and Fe-MIL-101 precipitated. Fe-MIL-101 was obtained as only product for very dilute systems, i.e. c_{Fe} = 0.006 mmol/mL.

Table 5.2: **Composition of the crystalline products after synthesis at 150 °C for 2 d with the given Fe(III)/DMF ratio (the Fe/BDC ratio remained constant at 1:1.5); blue: unknown crystalline phase, red: Fe-MIL-101, orange: Fe-MIL-53.**

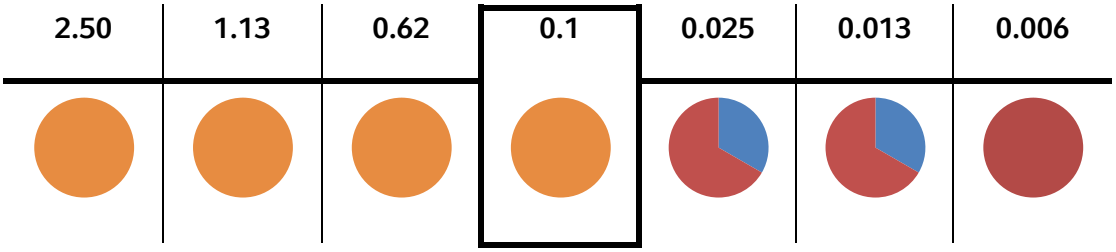

As the more diluted system did not result in the formation of Fe-MIL-53, we chose the original batch composition as a starting point for the investigation of the second crystallisation step. The bulk Fe-MIL-53 crystals were filtrated after two days reaction time and the clear yellow solution was used for further investigations. In a second solvothermal step (150 °C, 5 d) no product was obtained during the heating period. While the reaction mixture was cooling, Fe-MIL-53 precipitated. This observation caused us to investigate surface crystal growth in the solution produced via this synthesis pathway, as described in section 5.4:

$$FeCl_3 \times 6H_2O + 1.5\ BDC + 10\ ml\ DMF \xrightarrow{150°,2d} bulk\ FeMIL53 + clear\ solution$$

$$clear\ solution \xrightarrow{150°,5d} bulk\ FeMIL53.$$

Synthesis and Characterization of Fe-MIL-53

During the optimization of the synthesis pathway for MIL-88B films, Fe-MIL-53 was synthesized and characterized. The results will be presented in the following section.

The synthesis was carried out as described in section 5.2. The X-ray diffraction pattern of the orange, needle like crystals is displayed in Figure 5.17. The comparison with the simulated X-ray pattern from the literature[210] shows relatively good agreement, nevertheless the reflection positions are slightly shifted in relation to the simulated pattern. This shift results from the different synthesis conditions, as in the synthesis from Whitfield pyridine was present in the reaction mixture and subsequently in the pores of MIL-53. As described in chapter 5.1, MIL-53 has a flexible framework structure and the dimensions of the unit cell are dependent on the pore content. It is possible to treat the MIL-53 crystals post-synthetically with pyridine to demonstrate the flexibility of the framework and to prove the successful synthesis of Fe-MIL-53 (see Figure 5.17).

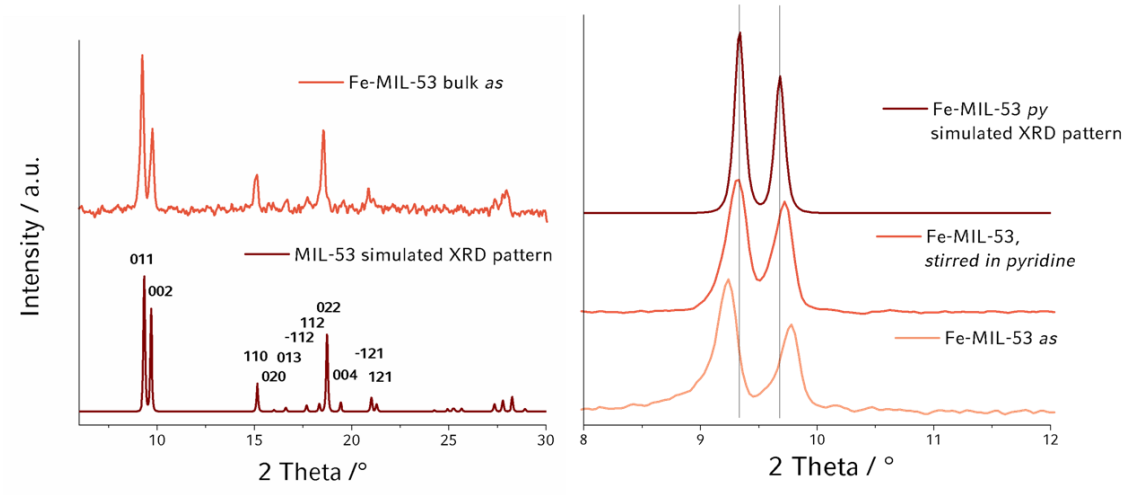

Figure 5.17: **left: comparison of the XRD pattern of bulk Fe-MIL-53 crystals to the simulated pattern of $Fe(OH)(BDC)(py)_{0.85}$; right: shift of the (011) and (002) reflections due to treatment with pyridine.**

The needle-like crystals of Fe-MIL-53 are relatively large. The scanning electron micrographs presented in Figure 5.18 show the ca. 500 µm sized needles that often

appear to be intergrown to bundles of crystals. The top face of the needles has a distorted triangular shape.

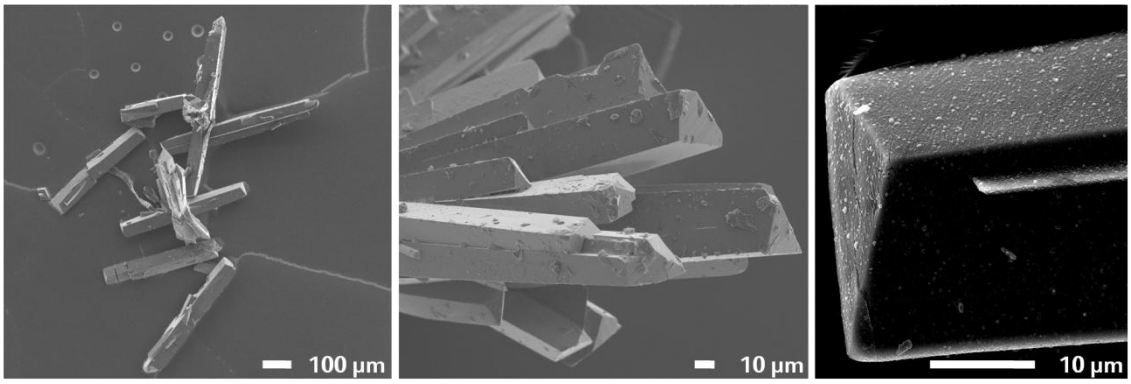

Figure 5.18: **Scanning electron micrographs of 500 µm sized, needle-like Fe-MIL-53 crystals.**

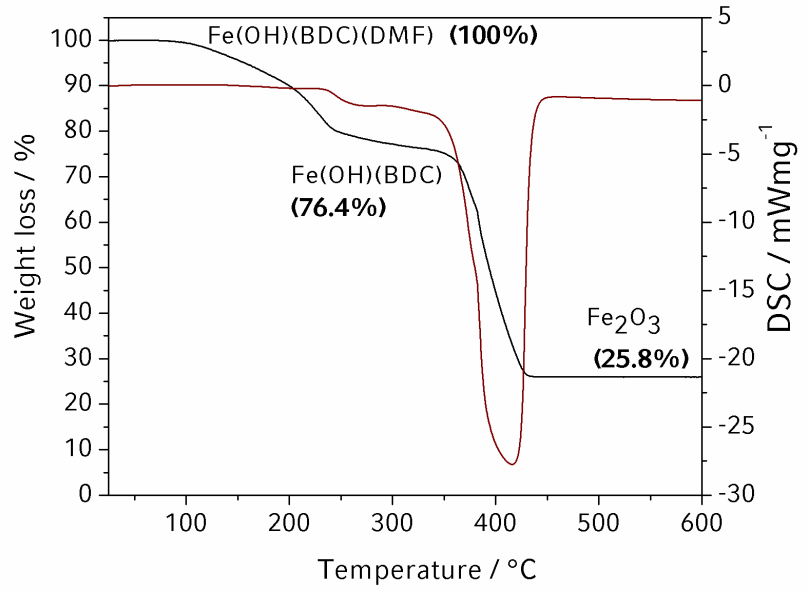

Figure 5.19: **Thermogravimetric (TG) and Differential Scanning Calorimetric (DSC) Analysis of Fe-MIL-53.**

The thermogravimetric analysis of Fe-MIL-53, displayed in Figure 5.19, shows a first weight loss of 24 % in one broad step between 90 and 250 °C. As there is no strong signal in the DSC corresponding to this weight loss, it is assigned to the removal of the solvent molecules, i.e. DMF from inside the pores. This results in a chemical composition of $Fe(OH)(BDC)(DMF)_{0.84}$ for the compound synthesized in DMF without addition of pyridine. The solvent-free structure is stable up to 400 °C. The weight loss of about 50 %, which occurs in a relative steep, exothermic step is in good agreement with the combustion of the organic linker (BDC; FW = 166.11 g/mol), leaving Fe_2O_3 (FW = 159.69 g/mol) as the tentative product.

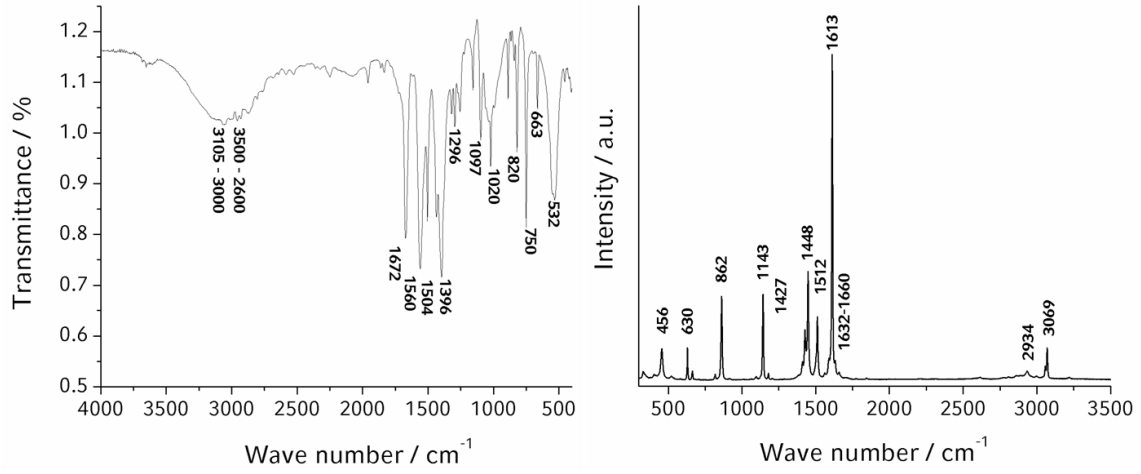

Figure 5.20: IR (left) and Raman (right) powder spectra of Fe-MIL-53.

The IR spectrum of Fe-MIL-53 and the Raman spectrum (Figure 5.20) were collected under the same conditions. The assignment of the observed bands to the particular groups is accomplished as follows.[249] The IR spectrum shows vibrational bands at 1560 cm^{-1} and 1396 cm^{-1} characteristic for the asymmetric and symmetric stretching vibration of the carboxylic groups of the BDC coordinated to a metal centre. The

absence of bands in the region of 1715-1680 cm^{-1}, typical of protonated carboxylic groups, is in agreement with the known framework structure where no protonated carboxylic acid groups are present. Other characteristic bands of the ligand due to the C=C stretching vibration of the p-disubstituted aromatic ring were found at 1504 cm^{-1}. Overtone and combination bands due to the C—H out-of-plane deformation vibration and characteristic for 1,4-disubstituted benzene rings occur in the region 2000 - 1750 cm^{-1}. The Fe-O stretching vibration from the FeO_6 octahedra is present at 532 cm^{-1}. The absorption band at 1672 cm^{-1} can be assigned to the C=O stretching of the amide (DMF), which is still present in the framework after synthesis. In the Raman spectrum, the peak at 456 cm^{-1} can be assigned to the Fe-O vibration of the iron-oxygen octahedron. The deformation vibrations of the aromatic CH-groups can be found between 630 and 1143 cm^{-1}. The absorption bands within the region between 1400 and 1460 cm^{-1} can be assigned to the symmetric stretch of the carboxylate groups and to the C=C vibrations. The absorption band with the highest intensity (1613 cm^{-1}) is assigned to the asymmetric stretch of the carboxylate group.

6 Sorption properties of oriented, thin-film Fe-MIL-88B crystals studied by X-ray diffraction

6.1 Introduction

The increasing interest in the assembly of porous crystals on defined surfaces is motivated by the potential applications of these materials in the fields of catalysis, gas storage and sensor devices. Metal-organic frameworks (MOFs) or inorganic-organic hybrid materials, emerging as an important class in the family of porous solids,[44, 53, 67, 186, 207] are excellent candidates for surface assembly. The existing studies concerning the production of MOF thin-films, including films of $[Zn_4O(bdc)_3]$ (MOF-5; bdc = 1,4-benzenedicarboxylate), $[Cu_3(btc)_2]$ (HKUST-1; btc = 1,3,5-benzenetricarboxylate), $[Zn_2(bdc)_2(dabco)]$ (dabco = 1,4-diazabicyclo[2.2.2]octane), [Mn(HCOO)], $[Cu_2(pzdc)_2(pyz)]$ (CPL-1; pzdc = pyrazine-2,3-dicarboxylate, pyz = pyrazine), [Fe(OH)(bdc)] (MIL-53(Fe)) and $[Fe_3O(bdc)_3]$ (MIL-88B), have been recently summarized by Zacher *et al.*[250] Due to the coexistence of organic and inorganic units in the framework, the MOF crystals can be attached to a substrate functionalized with an organic self assembled monolayer (SAM). We have recently shown that, by tuning the functional head group of the SAM, it is possible to direct the orientation and the structure of these materials.[176, 205] Depending on the framework structure, it is thus possible to direct the orientation of the pores with respect to the substrate. Highly oriented assemblies of crystals with pores perpendicular to the surface represent interesting candidates for sensor applications.

We have demonstrated the oriented and structure directed growth of the flexible framework structure Fe-MIL-88B on carboxylate terminated SAMs, where the pores were aligned perpendicular to the surface (see Figure 6.1 and Chapter 5 for a detailed description of the results). Among the known MOF structures, those possessing flexible frameworks are of particular interest.[251] The flexibility of these MOFs results in different cell parameters of the unit cell depending on the pore content.

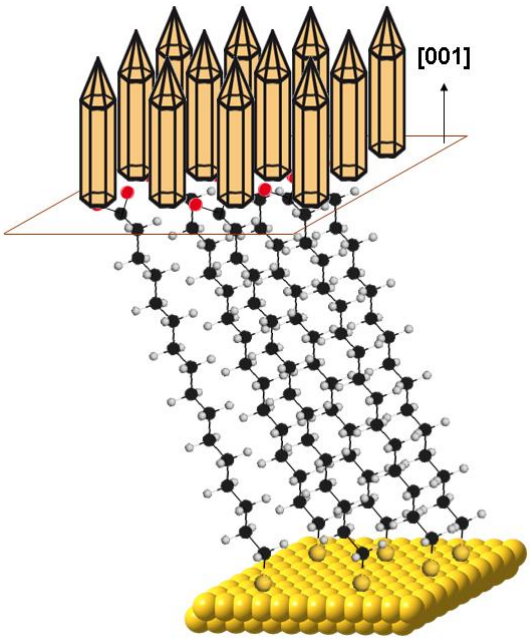

Figure 6.1: Highly oriented hexagonal crystals of Fe-MIL-88B on a 16-mercaptohexadecanoic acid SAM on gold.

The gas sorption behaviour of these materials often results in isotherms that do not conform to any of the IUPAC isotherm types.[1] For example, Cr-MIL-53 as well as its aluminium analogue, well known representatives of flexible porous materials, have been subject to many studies on sorption behaviour towards gases such as CO_2 or

methane.[219, 226, 227, 231, 237, 252] Another flexible framework structure is Fe-MIL-88B. The hexagonal 3D structure of MIL-88B is built up from trimers of FeO_6 octahedra linked to benzenedicarboxylate anions. Thus the 3D pore system of MIL-88B consists of tunnels along the c axis connected by bipyramidal cages.[43] The framework flexibility of crystals of the MIL-88 series has been demonstrated by the group of Gerard Férey.[209, 222, 253] Powder diffraction data of crystals exposed to different liquid solvents and the strong dependence of the lattice parameters on the type of the solvent was shown for the Cr(III) analogue of MIL-88B. However, to our knowledge the gas sorption properties of MIL-88B have not been reported yet.

Here, we present an investigation of the structural changes of the flexible porous material MIL-88B during the uptake of water vapour. The MIL-88B structure was grown in the form of oriented layers on functionalized gold substrates and its sorption behaviour was also studied with bulk crystals. The structural changes of this flexible framework material during ad- and desorption of water could be followed by X-ray diffraction and thus be correlated to the partial pressure of water.

6.2 Methods

Experimental setup of the flow controlling system

The flow controlling system consists of mainly three parts: the gas flow controller system, the liquid mass flow controller and the controlled evaporation mixer (CEM) (Figure 6.2).

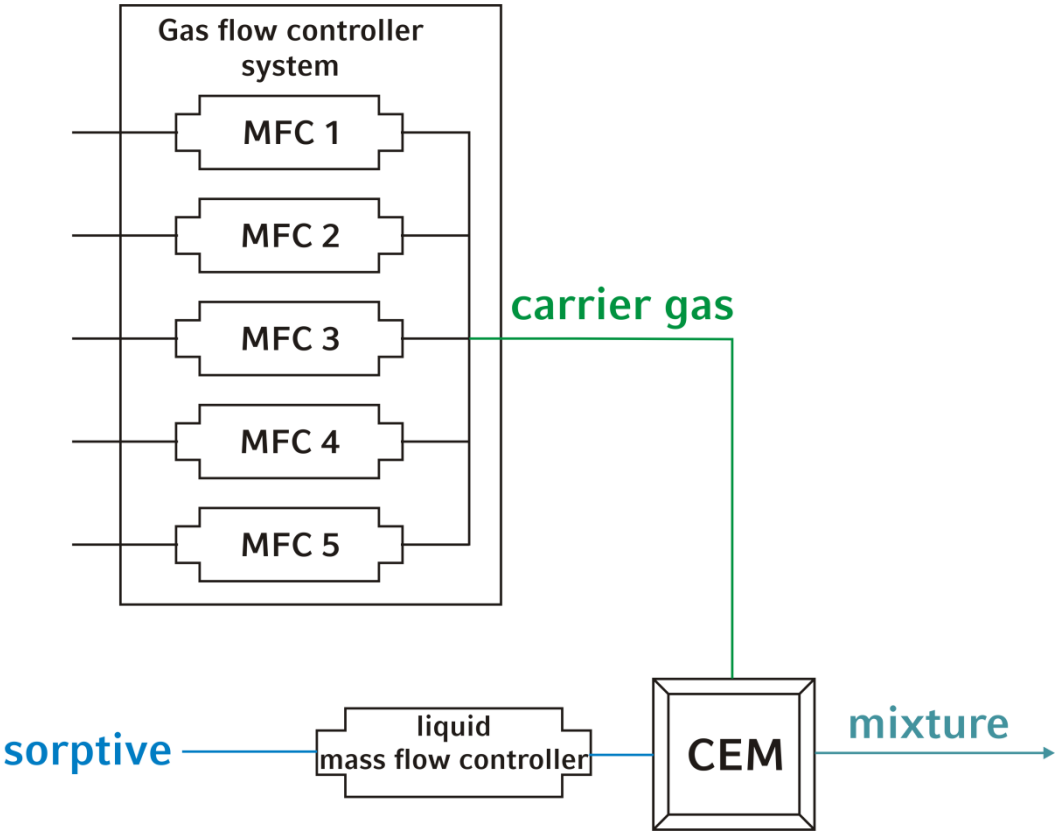

Figure 6.2: **Experimental setup of the flow controlling system employed in this work, consisting of the gas flow controlling system, a liquid mass flow controller and a controlled evaporation mixer (CEM).**

Five digital gas flow controllers purchased from *Bronkhorst High-Tech, Netherlands* (MFC 1- 5) can be used for the dosing of gases. The types of flow controllers with their maximum flow for the calibrated gases are listed in Table 6.1. In the setup depicted in Figure 6.2 the gas is used as carrier gas; in most of the measurements nitrogen is chosen for this purpose and the MFC 4 is used.

The liquid mass flow controller purchased from *Bronkhorst High-Tech, Netherlands* (Table 6.1) delivers a maximum flow of 1 g/h if water is used as sorptive. It is, however, possible to use different solvents as well. The liquid conversion factor to

calculate the maximum flow of the particular sorptive is taken from the official *Bronkhorst* web page.[254] In the setup, a reservoir of the particular liquid is connected to the liquid MFC and nitrogen is used to ensure continuous flow from the reservoir to the flow controller.

Table 6.1: **Types of digital mass flow controllers with their maximum flow (in mLn = normalized volume at 1013 hPa and 0.0 °C) for the calibrated gases, their labels in the Labels in the LabView control programme and the node they are connected to.**

Number	Gas/Liquid	max. Flow	Model	Node	Label
MFC 1	H_2	2000 mLn/min	F-201 C	Node 2	C1
MFC 2	O_2	400 mLn/min	F-201 C	Node 4	C4
MFC 3	CO	10 mLn/min	F-200D	Node 6	C5
MFC 4	N_2	2000 mLn/min	F-201C	Node 3	C6
MFC 5	CO	10 mLn/min	F-200D	Node 7	C7
Liquid MFC	H_2O	1 g/h	W-101A-110-P	Node 5	C3

The central unit, for ensuring the accurate mixing of the carrier gas and the sorptive is the CEM (Label C2, Node 1). In this unit the liquid analyte and the carrier gas are mixed and heated above the specific boiling point of the liquid to ensure a homogeneous mixture of both components.

The settings for the MFCs for the carrier gas and the sorptive were calculated assuming van-der-Waals behaviour to take into account the repulsive and attractive molecular interactions and the non-zero volume taken up by the molecules themselves. Van-der-Waals parameters for the solvents were taken from reference 255. To determine the measurement settings, an *MS Excel* sheet was used (see Table

6.6 for representation of the redesigned sheet), where the parameters for the measurement are set: temperature, pressure, vapour pressure of the solvent at the given temperature, liquid conversion factor and the actual gas flow of the carrier gas. The maximum flow is given in *mLn/min*, which is defined at 0.0 °C and 1013 hPa, and has to be recalculated to mL/min at the actual conditions with the help of the gas conversion factor from the official *Bronkhorst* web page.[254] In the *MS Excel* sheet the volume of the gas is first calculated, assuming ideal gas behaviour. In order to obtain a volumetric flow from the evaporated liquid the molar volume according to

$$pV^3 - (pnb + nRT)V^2 + an^2V + an^3 = 0$$

was evaluated with the mathematical programme Maple.[256]

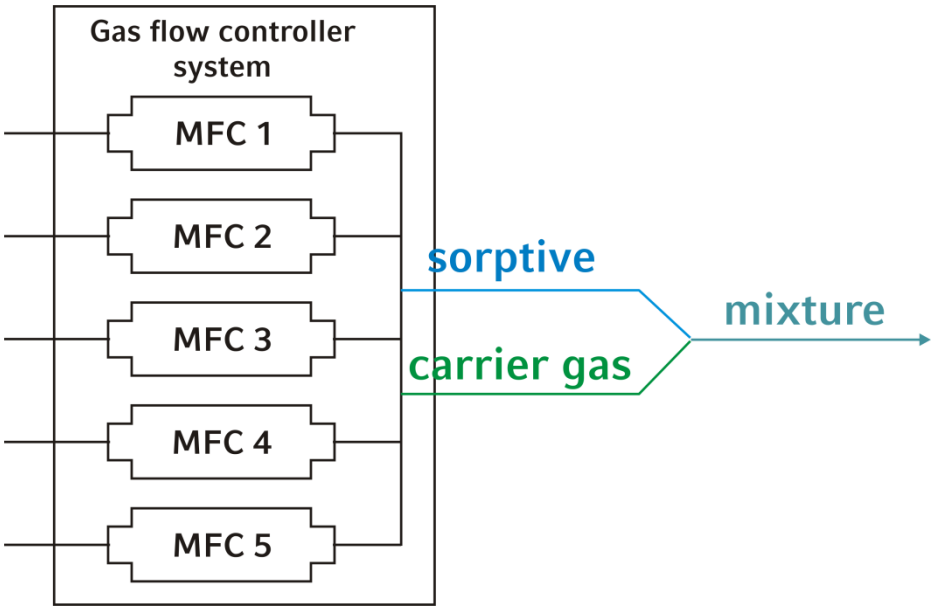

Figure 6.3: **Alternative experimental setup of the flow controlling system in the case of using gaseous sorptives.**

It is also possible to use the flow controlling system to mix two gases. In this case no liquid MFC and no CEM is necessary; the partial pressures may be adjusted by the two employed MFCs, one for the carrier gas (if necessary) and one for the sorptive. (Figure 6.3).

DEVELOPMENT OF THE NEW SAMPLE CELL FOR SORPTION@XRD MEASUREMENTS

A new sample cell was constructed to allow the measurement of X-ray diffraction patterns under controlled partial pressures of a sorptive. (Figure 6.4) The cell consists of a lower and an upper part. The lid of the cell is made out of Kapton, which is transparent to X-rays. The lid is fixed to the lower part of the sample holder, on which either the film or the powder samples are positioned with the help of two screws. The gas input in the lower part of the cell is connected to the flow controlling system described above.

The cell was positioned onto the sample holder of a Scintag XDS 2000 X-ray diffractometer, (Cu K-α radiation, $\lambda = 1.54$ Å) measuring in *theta-theta* geometry. The powder patterns were recorded at angles between 5 ° and 35 ° two theta with an interval of 0.01 ° two theta and at a scan rate of 5 ° to 10 ° two theta per minute.

Sorption@XRD data were recorded using automatic measurement routines. The valve opening of the liquid flow controller was increased by the desired increment every 90 minutes (for detailed description see below).

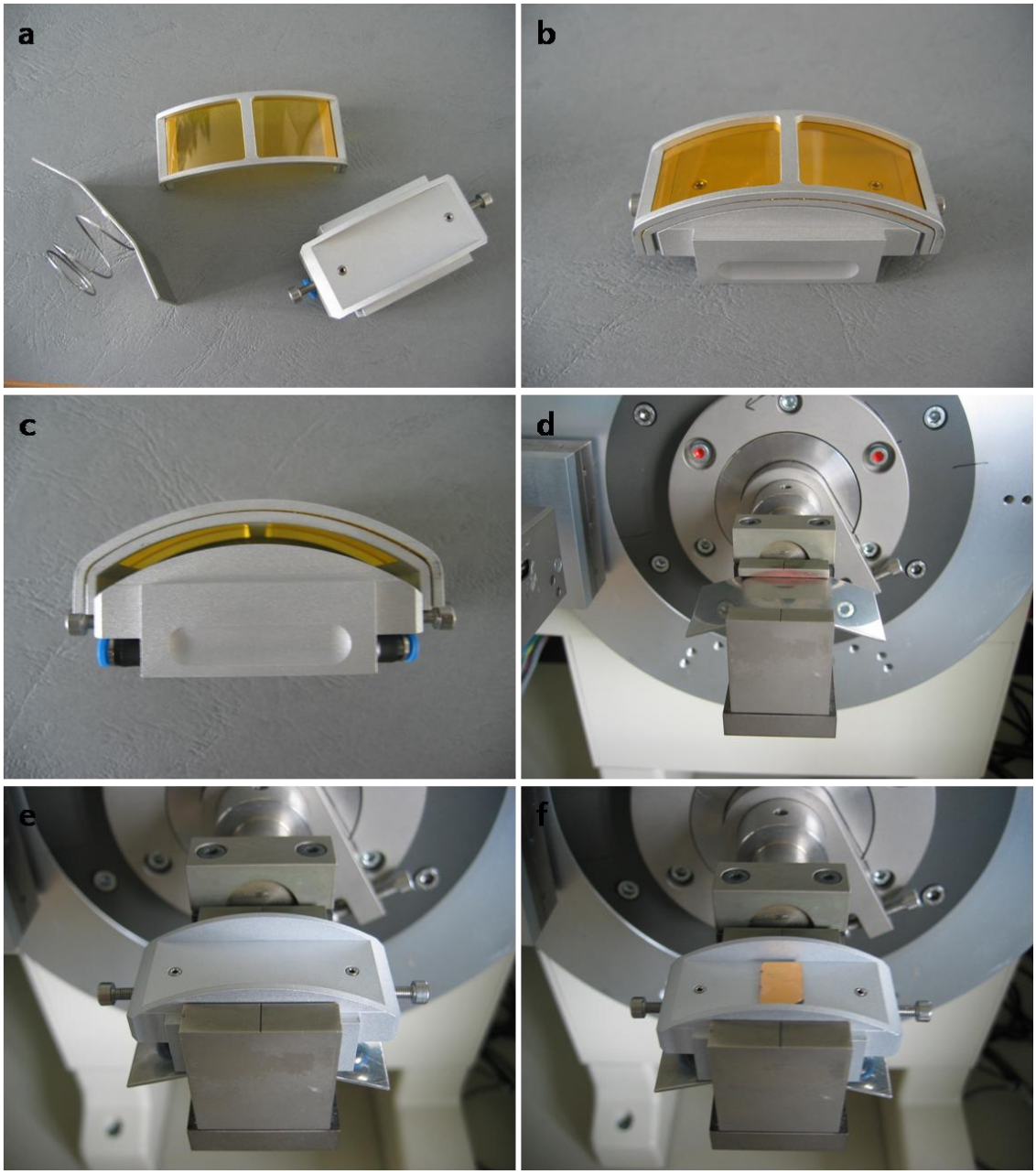

Figure 6.4: **Pictures of sample cell for Sorption@XRD measurements (a-c) and the positioning of the cell into the Scintag XDS 2000 X-ray diffractometer (d-f).**

Synthesis and Sample Preparation

The synthesis of Fe-MIL-88B crystals with [001] orientation on the functionalized gold slides was carried out as described previously.[205] Film samples were dried under nitrogen for two hours in the sample cell for sorption@XRD and then directly used for measurements.

The synthesis was carried out according to the literature procedure for MIL-88A,[43, 247] using 1,4-benzenedicarboxylic acid (98 %, *Aldrich*) and $FeCl_3 \cdot 6\ H_2O$ (p.a., *Merck*) in methanol (MeOH) (p.a., *Fluka*). Powder samples were washed in dimethylformamide (DMF) (p.a., *Acros Organics*) and MeOH for 24 h at RT each to remove any additional 1,4-benzenedicarboxylic acid molecules from inside the pores. The dry powder was deposited on the sample holder to give a flat surface of about 2 cm^2, dried under nitrogen for two hours within the sample cell for sorption@XRD, and then directly used for measurements.

Further sample characterization

Conventional water sorption measurements were carried out using volumetric sorption experiments (Quantachrome Autosorb MP) at 298 K. Prior to the adsorption experiments, the samples were outgassed under vacuum at 120 °C overnight.

6.3 Results and Discussion

The films used in this study were obtained by oriented growth of MIL-88B on MHDA SAMs, as described earlier.[205] The oriented growth of Fe-MIL-88B crystals has been demonstrated with the help of X-ray diffraction of the crystals grown on the film and the XRD pattern of the surface-removed crystals compared to Fe-MIL-88B crystals from a bulk synthesis. As depicted in Figure 6.5, the XRD pattern of the surface removed crystals is in good agreement with the XRD pattern of the bulk MIL-88B crystals. The XRD data of the crystals grown on the functionalized surface clearly demonstrate the [001] orientation as only the (002) and the (004) reflection of Fe-MIL-88B is observed. The SEM images, also presented in Figure 6.5, show small hexagonally-shaped pyramids with almost vertical orientation after an immersion time of 24 h. The diameter of the pyramids is about 200 nm. After an immersion time of 3 days the gold surface is almost completely covered with pillar-like hexagonally shaped crystals that are about 500 nm long. In Chapter 5, it is described that during the synthesis procedure MIL-53 is the product of homogeneous nucleation, whereas in the same crystallisation solution, oriented MIL-88B grows on the functionalized gold surface. We address the structure directing effect of the SAM to the carboxylate functionality of the MHDA SAMs mimicking the carboxylate groups of the BDC molecules und thus directing oriented growth on the surface.

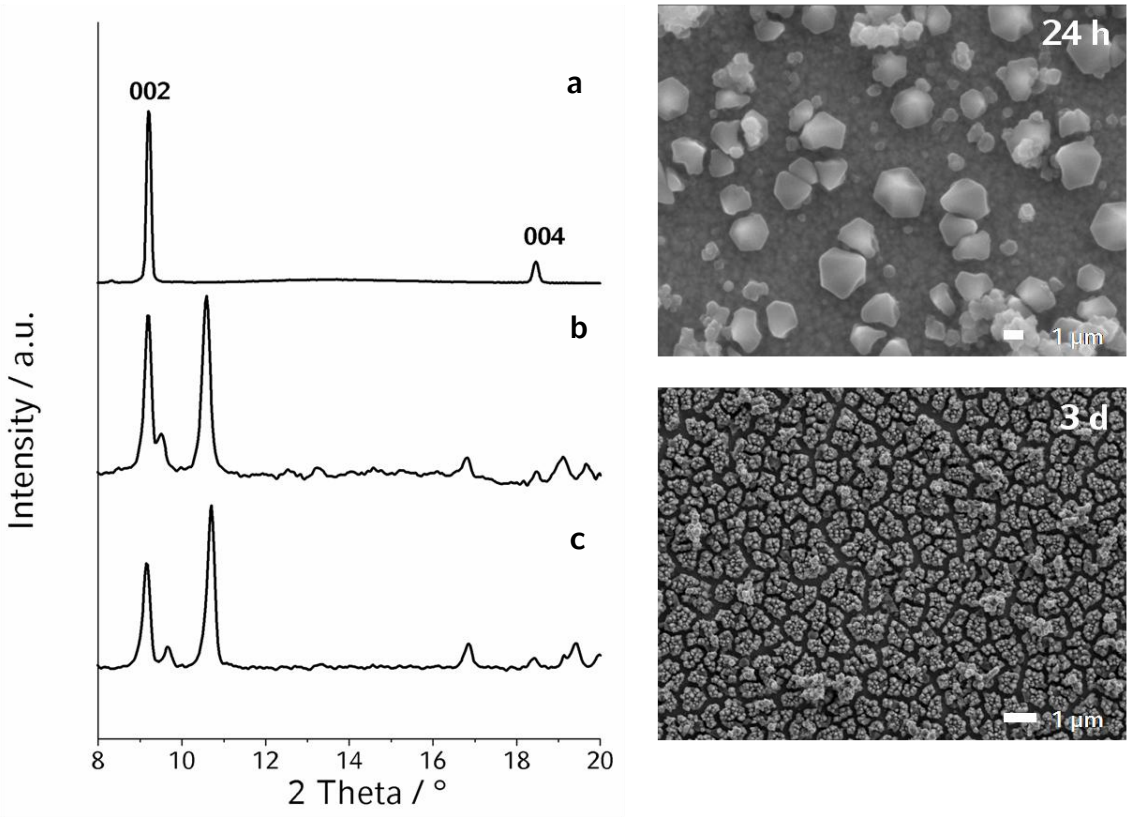

Figure 6.5: **Left: (a) XRD pattern of film on gold substrate, (b) powder pattern of the removed crystals and (c) powder pattern of bulk Fe-MIL-88B; right: Fe-MIL-88B crystals grown on a functionalized gold substrate for 24 h (top) and 3 d (bottom).**

The sorption measurement of the SAM-supported, oriented Fe-MIL-88B crystals on the gold substrates was performed by increasing the partial pressure of water by an increment of 5 % every 90 minutes. The (002) reflection of the crystals is subject to a shift to higher two theta values during adsorption of water, while during desorption the reflection is shifted towards lower values back to its original position. The shift during adsorption and desorption of water is displayed in Figure 6.6.

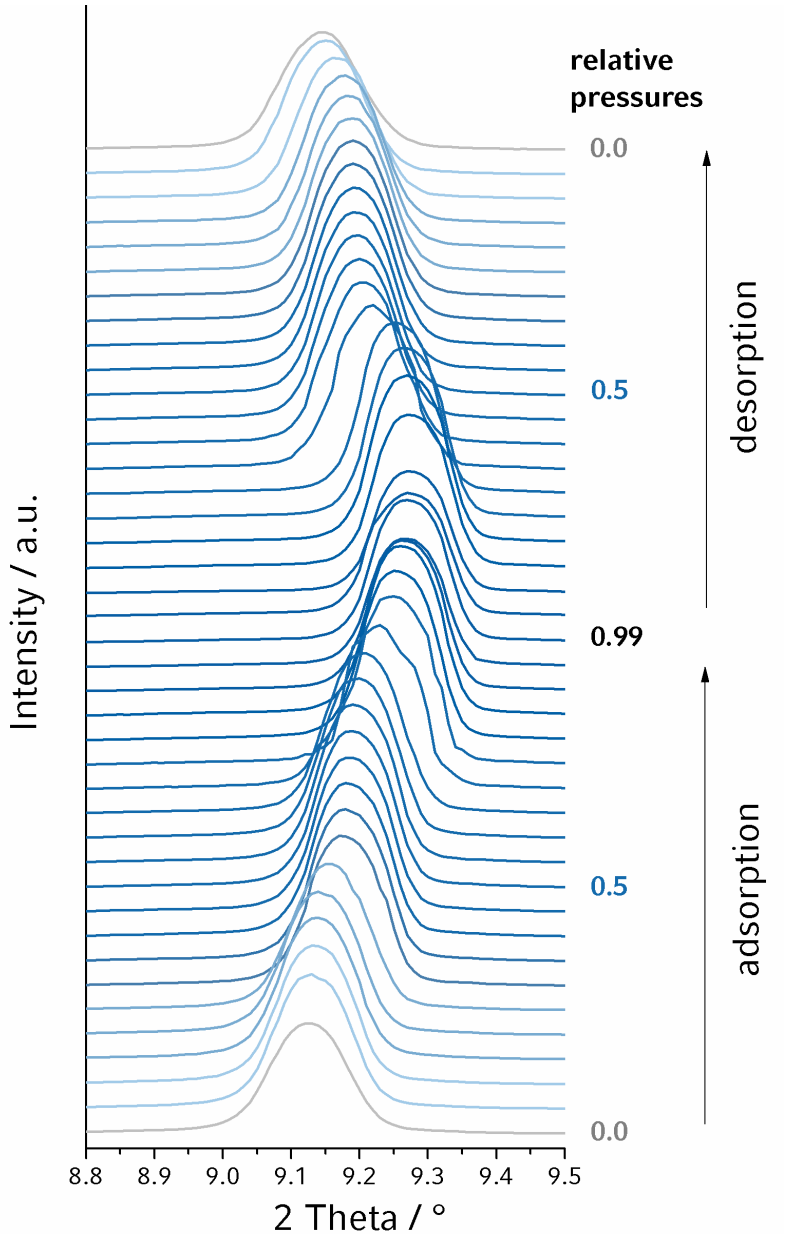

Figure 6.6: **Shift of (002) reflection of oriented MIL-88B crystals on MHDA substrates upon water adsorption and desorption.**

In Figure 6.7 the shift of the two theta values as well as the change of the lattice parameter *c* are displayed as a function of the partial pressure of water. It becomes clear that the adsorption as well as the desorption of water takes place within two

distinct steps. During adsorption the first step ocurs between a relative pressure $p/p_0 = 0.2$ and 0.3 and gives rise to a shift of 0.04 ° two theta. The second step takes place between $p/p_0 = 0.65$ and 0.75, the reflection position is shifted by 0.05 ° two theta. The sorption process recorded in X-ray diffraction shows a hysteresis, most notably in the lower part of the isotherm between $p/p_0 = 0.0$ and 0.3. The structural changes of the crystals appear delayed in desorption in comparison to adsorption.

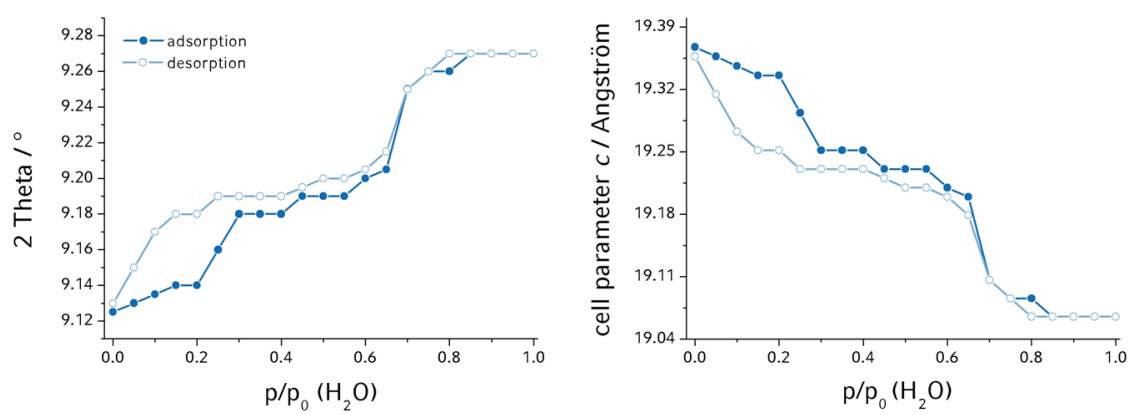

Figure 6.7: **Water sorption isotherm of crystal film recorded in a sorption@XRD measurement. Left: The two theta values of the (002) reflection are plotted versus the relative pressure of H_2O; right: the plot of the lattice parameter *c* against the relative pressure.**

Due to the orientation of the crystals on the film it is only possible to obtain information about the (002) reflection and therefore about the change of the *c* lattice parameter of the crystal structure. Therefore the same sorption experiment, combined with X-ray diffraction, was carried out with a thin layer of bulk Fe-MIL-88B crystals. In this way, it is possible to obtain information about the change of all three lattice parameters in dependence on the relative pressure, deduced from the shift of the (002), (100) and (101) reflection positions. (Figure 6.8)

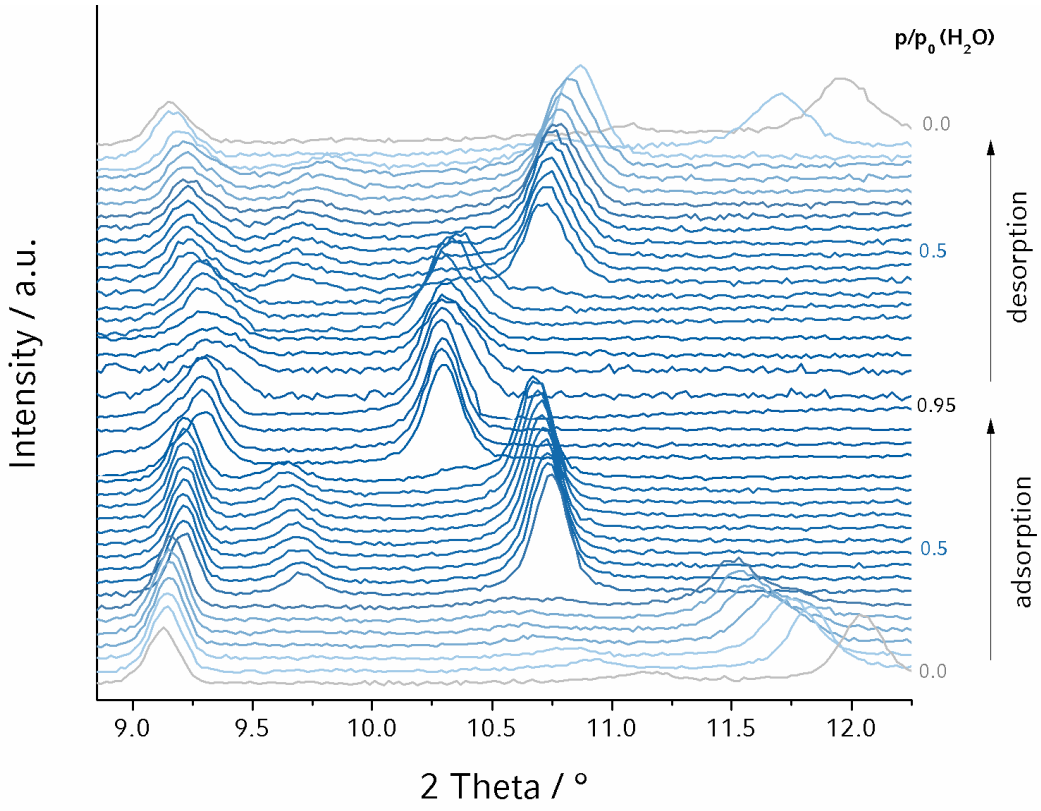

Figure 6.8: **Shift of reflection positions of (002), (100) and (101) of a thin layer of randomly oriented bulk MIL-88B crystals during a sorption@XRD measurement.**

The results for the *c* parameter obtained for both, film and bulk sorption@XRD measurements, are in good agreement. As on the film, in the bulk measurement the c lattice parameter decreases during uptake of water molecules and increases during desorption within two distinct steps (see Figure 6.9, top). The hysteresis of the desorption relative to the adsorption is more pronounced in the case of bulk-MIL-88B crystals, especially during the first desorption step. However, the overall decrease of about 0.3 Å of the lattice parameter *c* is the same for both the film and the powder sample.

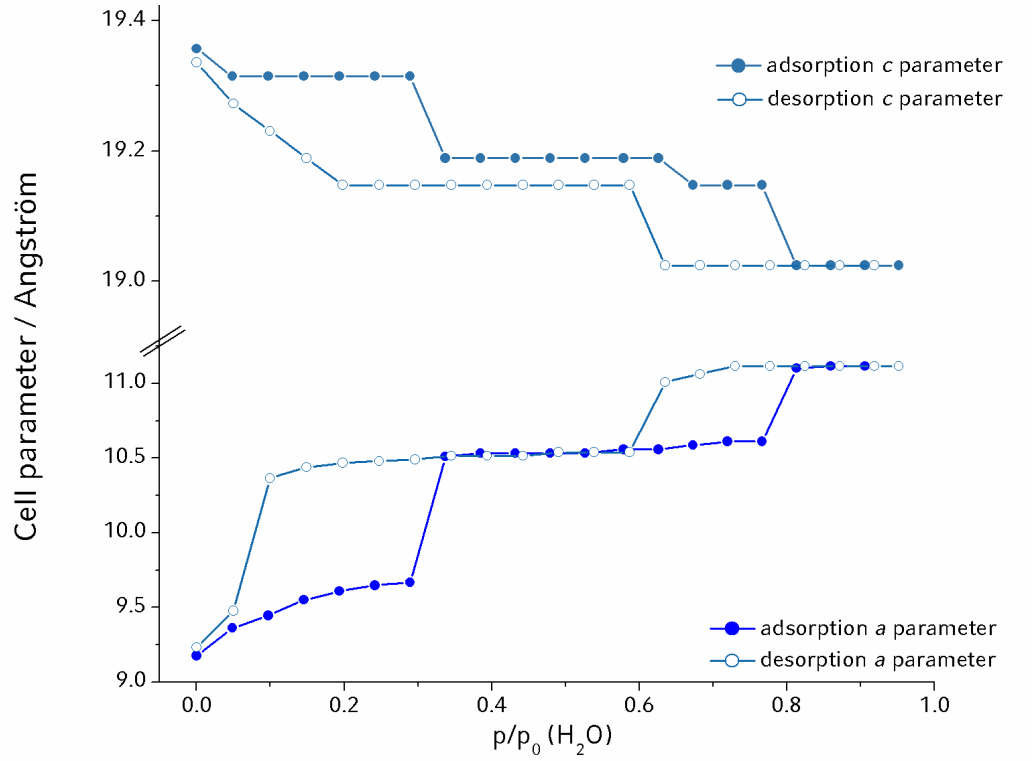

Figure 6.9: **Top: change of cell parameter *c* during adsorption and desorption of water of bulk MIL-88B crystals; bottom: change of cell parameter *a* during the same measurement. Note that the scale bars are different for the *c* and *a* parameters.**

The reverse and a much stronger effect is observed for the (101) and even more so for the (001) reflection position. The *a* parameter increases during adsorption of water molecules and decreases during desorption. The shift of these two reflection positions is much larger than in the case of the (002) reflection position (*c* parameter). We emphasize that the two distinct stepwise structural changes with increasing water pressure are reflected in shifts of both the *a* and *c* parameter of the unit cell. The change of the *a* parameter as a function of the partial pressure is given in Figure 6.9, bottom.

The hysteresis of the structural conversion becomes even more obvious in the case of the (100) direction. Above a relative pressure of approximately 0.3 p/p_0 during adsorption there is a large increase of *a* of about 0.8 Å in one step. Between $p/p_0 = 0.4$ and 0.75 there is a plateau and no change of the lattice constant *a* can be observed. The second distinct step occurs at a partial pressure of 0.8 p/p_0 and the lattice parameter *a* increases by approximately 0.5 Å. The impact of these structural changes can be seen when referring to the structure of MIL-88B (Figure 6.10). While the d_{001} distance shrinks (increase of the two theta values of the (002) reflection position) there is an expansion in the 100 and 010 directions respectively, which leads to an increase of the volume enclosed by the cages of the Fe-MIL-88B structure.

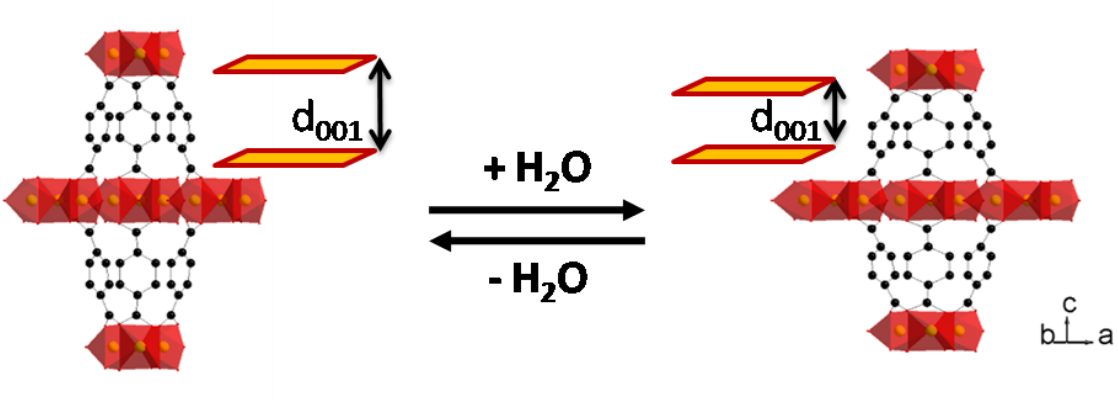

Figure 6.10: Changes of the MIL-88B framework during uptake and desorption of water depicted schematically.

The complete diffraction patterns of Fe-MIL-88B crystals at various partial pressures were also recorded and are displayed in Figure 6.11. It is possible to index these patterns in the hexagonal space group of MIL-88B, that is *P-62c*,[43] by variation of the lattice parameters of *a* and *c*. The resulting lattice parameters and cell volumes are listed in Table 6.2.

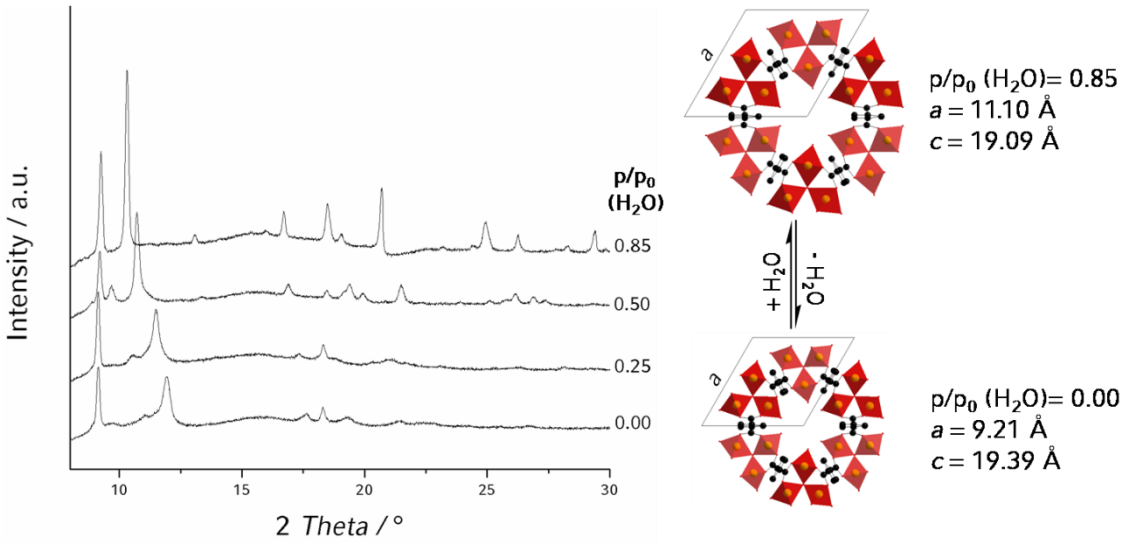

Figure 6.11: **Left: complete diffraction patterns under relative pressures of water of 0.00, 0.25, 0.50, 0.85; right: schematic of change of lattice parameter *a* at partial pressures of water of 0.00 and 0.85.**

Table 6.2: **Lattice parameters a and c after indexing using Werner algorithm at different partial pressures.**

p/p_0	lattice parameter a / Å	lattice parameter c / Å	cell volume / Å^3	Figure of Merit
0.00	9.21	19.39	1425	18.6
0.25	9.70	19.39	1581	16.9
0.50	10.57	19.21	1858	64.1
0.85	11.10	19.09	2038	24.2

From the full diffraction patterns at various partial pressures (Figure 6.11) it can be seen, that the completely empty and dry powder shows less intense and partially broader reflections than the powders containing water. This suggests that the empty form is less ordered than the forms where water molecules are present within the

pores. This peak broadening is only observed for reflections with an *a* component, which implies that the variations of the lattice plane distances in the *c* direction are smaller than the variations in *a* direction. This is consistent with the much greater structural changes upon water adsorption in the *a* direction. The powder patterns compared to their simulated patterns are depicted in Figure 6.12.

For Cr-MIL-88B, and for the other members of the MIL-88 series, the structural changes upon exposure to various liquid solvents have been discussed by Serre *et al.*[222] The authors show the slow swelling kinetics of Cr-MIL-88B crystals upon exposure to liquid water. The structure (obtained from the lattice parameters) of Cr-MIL-88B dispersed in liquid water is different from the structure that we observe for crystals exposed to water vapour. It seems that less water can be adsorbed from the gas phase. We also examined the time-dependent structural evolution of Fe-MIL-88B; the powder responds quickly to changes in partial pressure and the structural change is complete after 45 min (Figure 6.13).

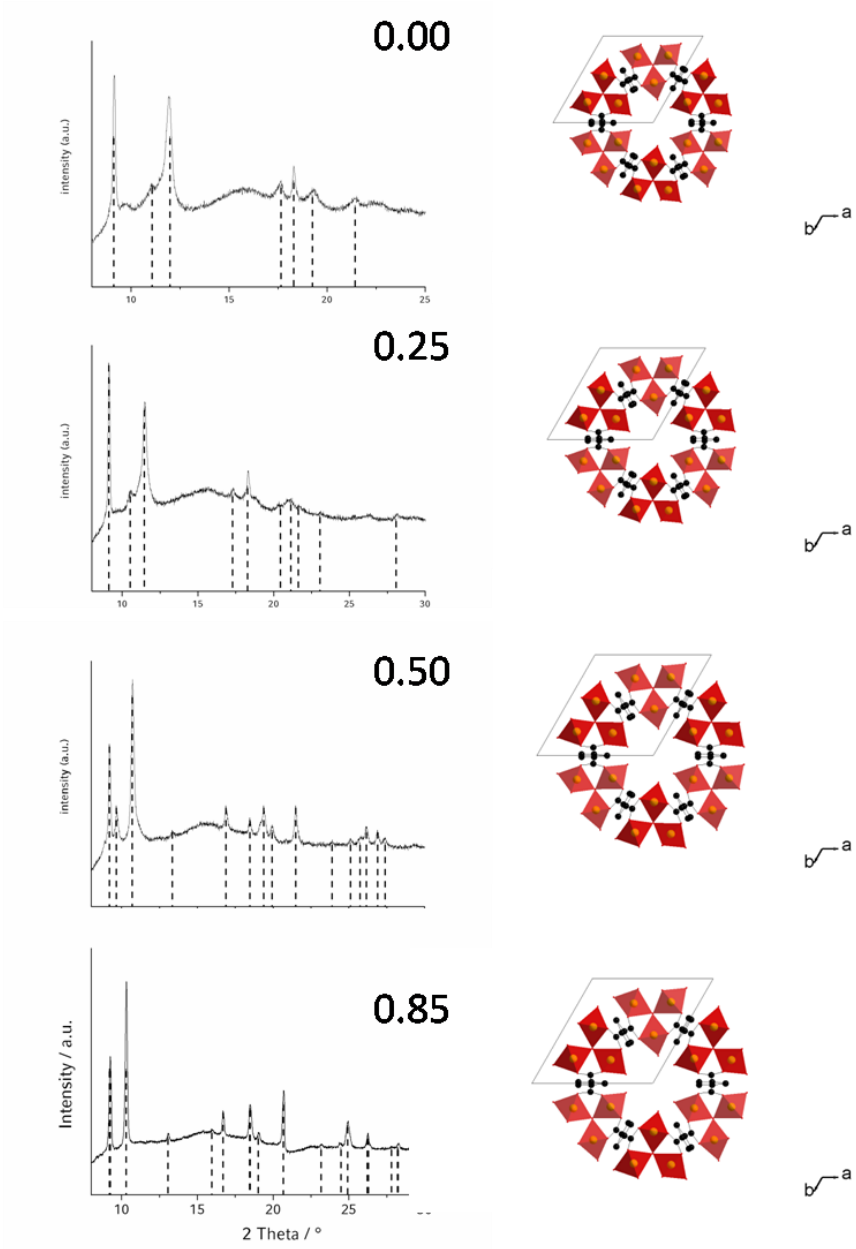

Figure 6.12: **Comparison of the measured X-ray patterns under the given relative pressures with the simulated patterns. Parameters of indexation are given in Table 6.2. The size of the unit cell as a function of relative pressure is depicted schematically.**

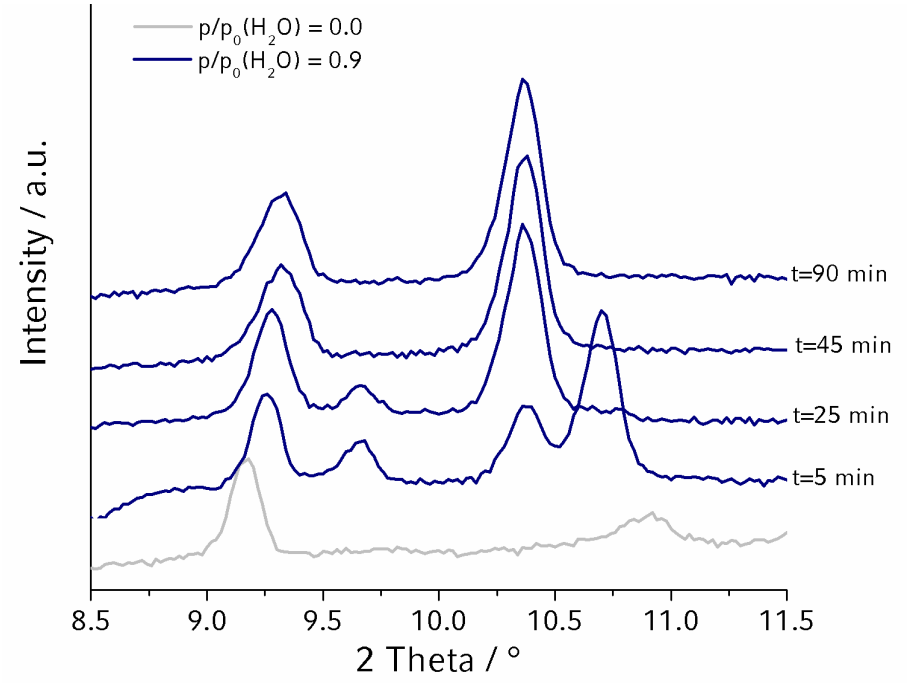

Figure 6.13: **Evolution of structural changes of dry MIL-88B exposed to a relative pressure of water of 0.9.**

To quantify the uptake of water and to verify the employed method of sorption@XRD the sorption isotherm of water with bulk-Fe-MIL-88B was recorded (albeit under different conditions); it is shown in Figure 6.14. The sorption@XRD measurements were obtained from thin films under a continuous flow of dry nitrogen, and the partial pressure was adjusted by mixing water vapour and nitrogen at a particular ratio. In contrast, the conventional bulk sorption measurement was performed volumetrically, that is, the sample was outgassed in vacuum for one night at 120 °C, followed by incremental dosing of water vapour into the sample cell.

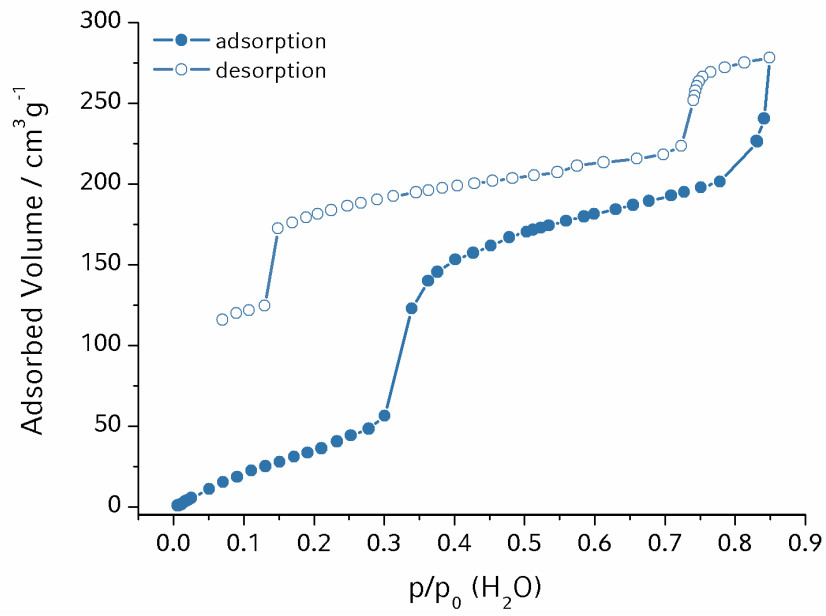

Figure 6.14: Water sorption isotherm of bulk MIL-88B crystals after outgassing (120 °C, overnight).

Beginning at low pressures, there is continuously increasing adsorption of water. Above a relative pressure of 0.3, a drastic stepwise increase of the adsorbed amount is observed. The second distinct step occurs above a partial pressure of 0.8; between those two steps, there is a continuous increase of the adsorbed volume. These results are in good agreement with the data obtained from the sorption@XRD measurements. The desorption also proceeds in two distinct steps, but these are shifted to lower relative pressures, thus reflecting the hysteresis observed in the sorption@XRD measurements. As equilibration for the last data points upon desorption took longer than three days for each point, complete closure of the isotherm could not be obtained. The adsorbed volume of water at a partial pressure of 0.85 can be calculated to be 278 cm^3/g, which corresponds to 15 mmol/g.

6.4 Conclusions

In this chapter we have reported the development of a new sample cell, which was employed for in situ sorption@XRD measurements. This method allows us to follow the structural changes of flexible, porous materials during adsorption and desorption of guest molecules. Employing this new method we were able to obtain information about the water sorption behaviour of Fe-MIL-88B crystals. Oriented, surface-grown Fe-MIL-88B crystals on SAM-functionalized gold substrates showed the same structural changes during sorption of water as randomly oriented bulk Fe-MIL-88B crystals. The sorption isotherms recorded with the help of the employed sorption@XRD method show two distinct steps of structural change. An increase of the relative pressure of water leads to a small decrease of the *c* parameter of both the surface-grown MIL-88B crystals and the bulk material and in the same instance a larger increase of the *a* parameter, resulting in an overall increase of the cell volume of more than 40 %. Based on their large pore volume and crystalline micropore system, surface grown porous MOFs with accessible pores are interesting candidates for sensor and membrane applications.

6.5 Additional Details

Table 6.3: Two theta values of the (002) reflection and resulting lattice parameter c, taken from the sorption@XRD measurement of the Fe-MIL-88B film sample.

p/p_0	$2\,\theta_{002}$ / °	d_{002}	parameter c
0.000	9.125	9.684	19.367
0.051	9.130	9.678	19.357
0.102	9.135	9.673	19.346
0.153	9.140	9.668	19.336
0.203	9.140	9.668	19.336
0.254	9.160	9.647	19.293
0.304	9.180	9.626	19.251
0.354	9.180	9.626	19.251
0.404	9.180	9.626	19.251
0.454	9.190	9.615	19.231
0.504	9.190	9.615	19.231
0.553	9.190	9.615	19.231
0.602	9.200	9.605	19.210
0.652	9.205	9.600	19.199
0.701	9.250	9.553	19.106
0.750	9.260	9.543	19.086
0.798	9.260	9.543	19.086
0.847	9.270	9.532	19.065
0.895	9.270	9.532	19.065
0.944	9.270	9.532	19.065
0.992	9.270	9.532	19.065
0.944	9.270	9.532	19.065
0.895	9.270	9.532	19.065
0.847	9.270	9.532	19.065
0.798	9.270	9.532	19.065
0.750	9.260	9.543	19.086
0.701	9.250	9.553	19.106
0.652	9.215	9.589	19.179
0.602	9.205	9.600	19.199
0.553	9.200	9.605	19.210
0.504	9.200	9.605	19.210
0.454	9.195	9.610	19.220
0.404	9.190	9.615	19.231
0.354	9.190	9.615	19.231

0.304	9.190	9.615	19.231
0.254	9.190	9.615	19.231
0.203	9.180	9.626	19.251
0.153	9.180	9.626	19.251
0.102	9.170	9.636	19.272
0.051	9.150	9.657	19.314
0.000	9.130	9.678	19.357

Table 6.4: **Two theta values of the (002) and (101) reflections and resulting lattice parameters (lp) *a* and *c*. The theoretical value for the reflection position of (100) is calculated and compared to the observed value.**

p/p_0	$2\theta_{002}/°$	d_{002}	lp c	$2\theta_{101}/°$	d_{101}	lp a	d_{100} (calc.)	$2\theta_{100}/°$ (calc.)	$2\theta_{100}/°$ (obs.)
0.00	9.13	9.678	19.357	12.03	7.351	9.176	7.946	11.126	11.15
0.04	9.15	9.657	19.314	11.83	7.475	9.361	8.106	10.905	10.91
0.09	9.15	9.657	19.314	11.74	7.532	9.445	8.179	10.808	10.81
0.14	9.15	9.657	19.314	11.63	7.603	9.550	8.271	10.688	10.69
0.19	9.15	9.657	19.314	11.57	7.642	9.609	8.321	10.623	10.63
0.24	9.15	9.657	19.314	11.53	7.669	9.648	8.355	10.579	10.59
0.28	9.15	9.657	19.314	11.51	7.682	9.668	8.373	10.558	10.57
0.33	9.21	9.594	19.189	10.75	8.223	10.509	9.101	9.710	9.71
0.38	9.21	9.594	19.189	10.73	8.238	10.533	9.122	9.688	9.71
0.43	9.21	9.594	19.189	10.73	8.238	10.533	9.122	9.688	9.69
0.47	9.21	9.594	19.189	10.73	8.238	10.533	9.122	9.688	9.69
0.52	9.21	9.594	19.189	10.73	8.238	10.533	9.122	9.688	9.69
0.57	9.21	9.594	19.189	10.71	8.254	10.557	9.143	9.666	9.67
0.62	9.21	9.594	19.189	10.71	8.254	10.557	9.143	9.666	9.67
0.67	9.23	9.574	19.147	10.69	8.269	10.587	9.168	9.639	9.67
0.72	9.23	9.574	19.147	10.67	8.285	10.611	9.189	9.617	9.63
0.76	9.23	9.574	19.147	10.67	8.285	10.611	9.189	9.617	9.63
0.81	9.29	9.512	19.024	10.3	8.581	11.103	9.615	9.190	-
0.86	9.29	9.512	19.024	10.29	8.590	11.116	9.627	9.179	-
0.90	9.29	9.512	19.024	10.29	8.590	11.116	9.627	9.179	-
0.95	9.29	9.512	19.024	10.29	8.590	11.116	9.627	9.179	-
0.91	9.29	9.512	19.024	10.29	8.590	11.116	9.627	9.179	-
0.87	9.29	9.512	19.024	10.29	8.590	11.116	9.627	9.179	-
0.82	9.29	9.512	19.024	10.29	8.590	11.116	9.627	9.179	-
0.77	9.29	9.512	19.024	10.29	8.590	11.116	9.627	9.179	-
0.73	9.29	9.512	19.024	10.29	8.590	11.116	9.627	9.179	-

0.68	9.29	9.512	19.024	10.33	8.557	11.062	9.580	9.224	-
0.63	9.29	9.512	19.024	10.37	8.524	11.009	9.534	9.268	-
0.58	9.23	9.574	19.147	10.73	8.238	10.538	9.126	9.683	9.67
0.53	9.23	9.574	19.147	10.73	8.238	10.538	9.126	9.683	9.69
0.49	9.23	9.574	19.147	10.73	8.238	10.538	9.126	9.683	9.69
0.44	9.23	9.574	19.147	10.75	8.223	10.514	9.106	9.705	9.71
0.39	9.23	9.574	19.147	10.75	8.223	10.514	9.106	9.705	9.71
0.34	9.23	9.574	19.147	10.75	8.223	10.514	9.106	9.705	9.69
0.29	9.23	9.574	19.147	10.77	8.208	10.491	9.085	9.728	9.73
0.24	9.23	9.574	19.147	10.78	8.200	10.479	9.075	9.739	9.77
0.19	9.23	9.574	19.147	10.79	8.193	10.467	9.064	9.750	9.73
0.14	9.21	9.594	19.189	10.81	8.178	10.438	9.040	9.777	9.810
0.09	9.19	9.615	19.231	10.87	8.133	10.363	8.975	9.847	9.83
0.05	9.17	9.636	19.272	11.71	7.551	9.477	8.207	10.771	10.81
0.00	9.14	9.668	19.336	11.97	7.388	9.231	7.994	11.059	11.15

6.6 Documentation of the LabView control programmes

LabView control programme for automated Sorption@XRD measurements

Within this work a new programme was designed to ensure a fully automated collection of sorption@XRD data, in the following it will be referred to as Sorption@XRD.

The Sorption@XRD programme controls the valve opening of the MFCs for the sorptive and the carrier gas and allows the automated increase or decrease of the valve opening of the liquid MFC. The automated collection of the XRD data is ensured by the software programme[257] of the diffractometer *via* writing an event list including scans and breaks.

The front panel of the programme Sorption@XRD is presented in Figure 6.15. The different options for the possible settings will be explained with reference to the programme code.

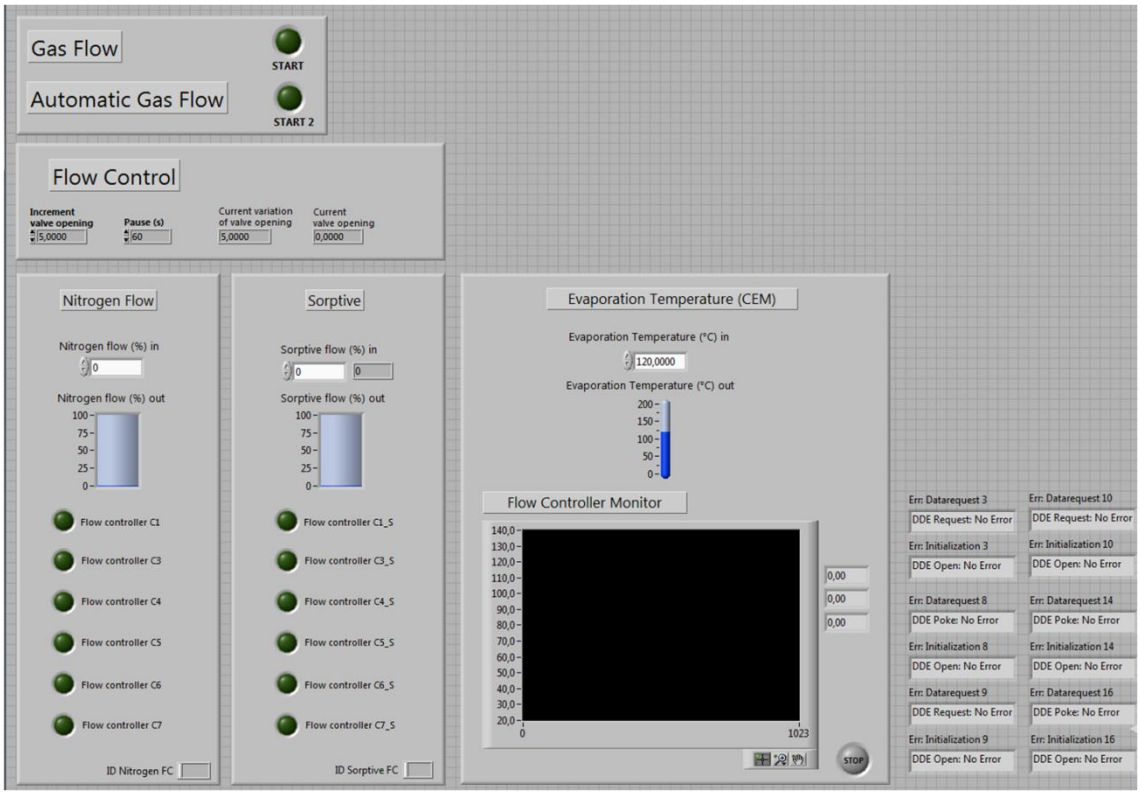

Figure 6.15: Front panel of the LabView programme Sorption@XRD.

As described above, different MFCs are selectable for the carrier gas (*Nitrogen Flow*). In the case of nitrogen *Flow controller C6* is selected by clicking on the green button next to its name. For liquid sorptives *Flow controller C3_S* has to be selected. If one flow controller is selected, all others will automatically be deselected and the ID of the flow controller will be written to variable *ID nitrogen FC* or *ID sorptive FC*, respectively (see Figure 6.16).

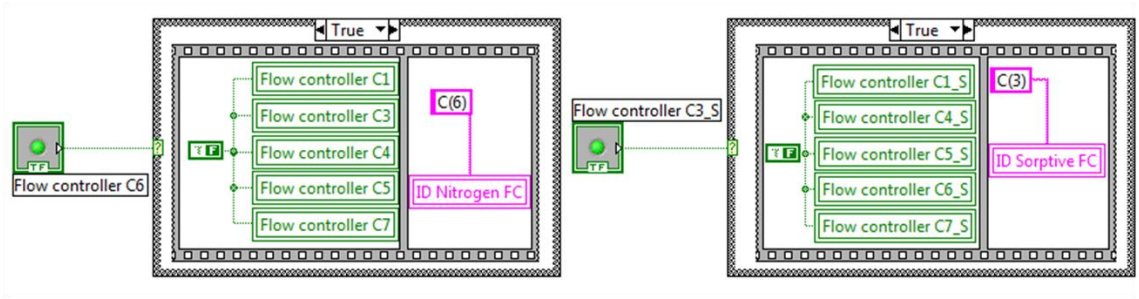

Figure 6.16: Cut-out from the block diagram of the Sorption@XRD programme demonstrating the flow controller selection.

This selection process is running within a while loop as long as either *Start* or *Start 2* is selected. (Figure 6.17).

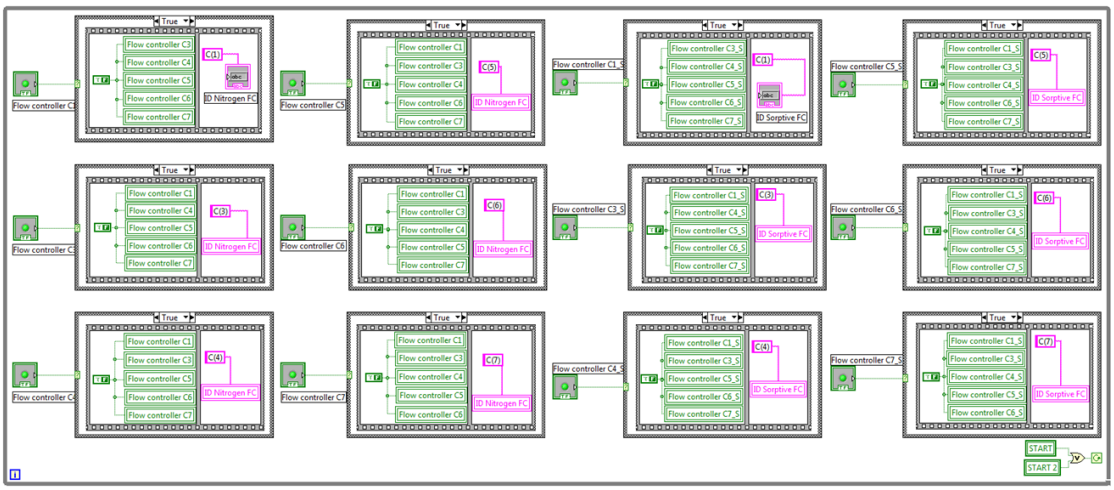

Figure 6.17: While loop containing the process of flow controller selection.

The communication with the flow controllers and the CEM is started as soon as either *Start* or *Start 2* is selected (case selector for case structure). The communication consists of two different main steps. The first being the request of the current valve opening and current evaporation temperature and display of the three requested

values in the *Flow controller monitor* (front panel, Figure 6.15). The second step is the transfer of the defined values for *Nitrogen flow in*, *Sorptive flow in* and *Evaporation Temperature in* to the digital MFCs (see Figure 6.19).

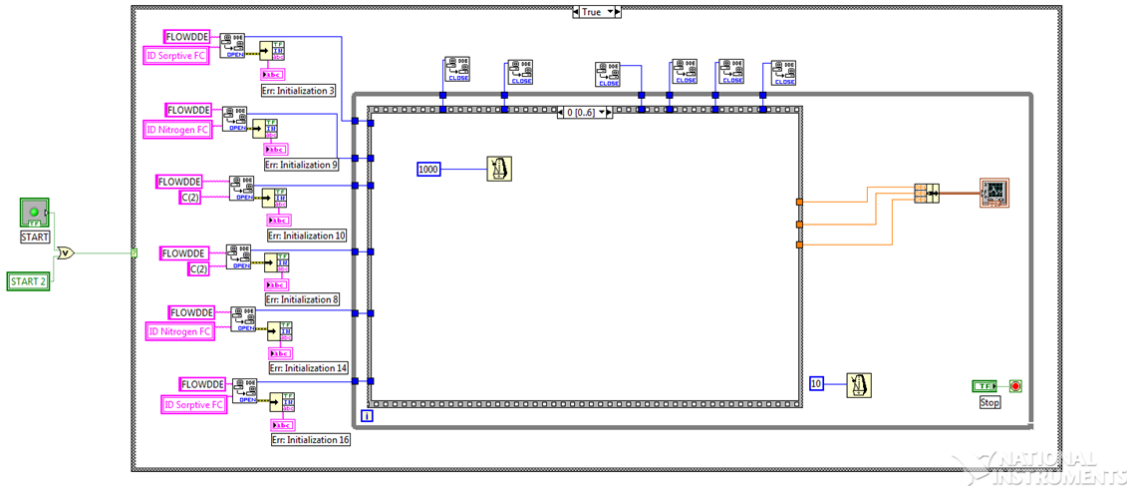

Figure 6.18: **Case structure containing the communication with the digital MFCs and the CEM. The communication is processed via SubVis delivered from Bronkhorst along with the MFCs. The case structure contains a stacked sequence structure within a while loop. The first process within the stacked sequence (No. 0) is a waiting step to ensure synchronization of the following multiple steps (see Figure 6.19).**

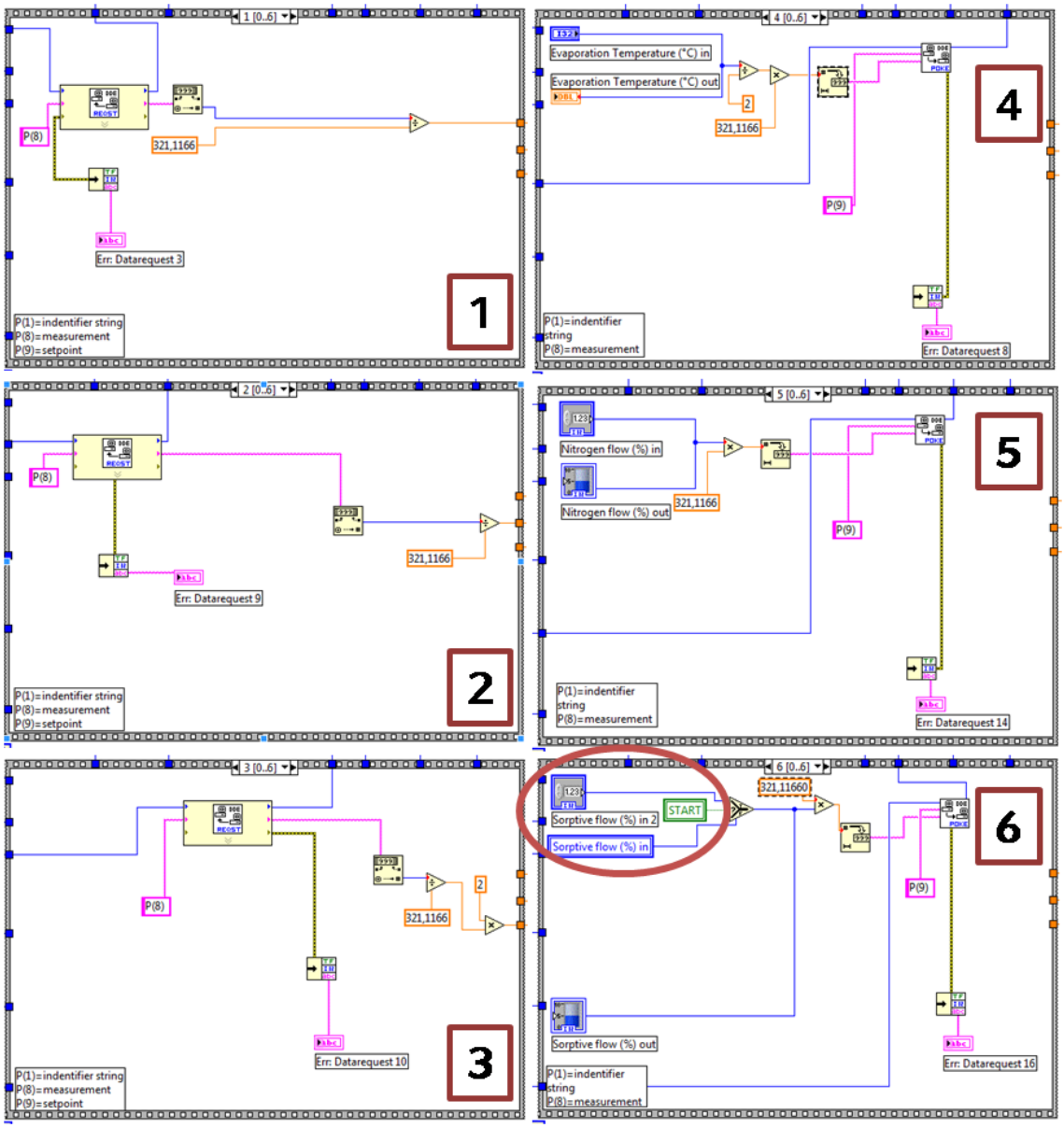

Figure 6.19: Steps 1 to 6 of the stacked sequence structure within the flow controller communications window (see Figure 6.18). Steps 1 – 3 request the current values for valve openings and evaporation temperature of the MFCs for the sorptive, the carrier gas and the CEM. The obtained value is handed over to the flow controller monitor and displayed there. Steps 4 – 6 transfer the set values for *Evaporation Temperature*, *Nitrogen flow in* and *Sorptive flow in* to the digital MFCs with the help of the SubVi DDE Poke.

The address of the particular flow controller is read from the variables filled in the flow controller selection step (*ID Nitrogen FC* and *ID Sorptive FC*). The main advantage of this design is that different combinations of flow controllers may be chosen by the user without changing the programme code. The CEM is addressed directly (ID *C(2)*) as there is physically only one CEM in the experimental setup.

As can be seen from the front panel (Figure 6.15), there are two different running modes for the Sorption@XRD programme: *Gas Flow* (*Start*) and *Automatic Gas Flow* (*Start 2*). If the programme is running in *Gas Flow* mode, the current values for valve openings *Nitrogen flow in*, *Sorptive flow in* and *Evaporation Temperature in* are transferred to the MFCs and the CEM, as described above. The difference when running in *Automatic Gas Flow* mode, instead of the *Sorptive flow in*, the variable *Sorptive flow in 2* is transferred to the digital MFCs (as marked red in Figure 6.19). The value of this variable results from a calculation within an automated sequence structure. (Figure 6.20) If *Start 2* is selected a sequence starts, beginning with a pause, defined by the user (front panel, Figure 6.15) and filling of the variable *Current variation of valve opening*, the value is taken from the user defined parameter *Increment valve opening* (for example 5 %). The central part of the sequence structure is an inner sequence consisting of five steps. In the first step, it is checked if the sum of the set value for the *Increment valve opening* (see also front panel, Figure 6.15) and the *Current valve opening* is bigger than 100. If that is true, the *Increment valve opening* (see also front panel) is multiplied with minus one and the new value is written to the variable *Current variation of valve opening*. In the next step the variable *Current variation of valve opening* is added to the *Current valve opening*, resulting in a new *Current valve opening*, that is written to the variable *Sorptive flow in 2*. The

third step consist in a pause, which is set by the user (see front panel, Figure 6.15) and corresponds to the time for which a certain partial pressure shall be held constant. The next two steps control the end of the process, i.e. if the *Current valve opening* is bigger than zero, the inner sequence is started from the beginning, if not the *Start 2* button is deselected and the *Current valve opening* and the *Current variation of valve opening* are set to zero. If the *Start 2* button is deselected, the while loop containing the described inner sequence structure is stopped (exit condition).

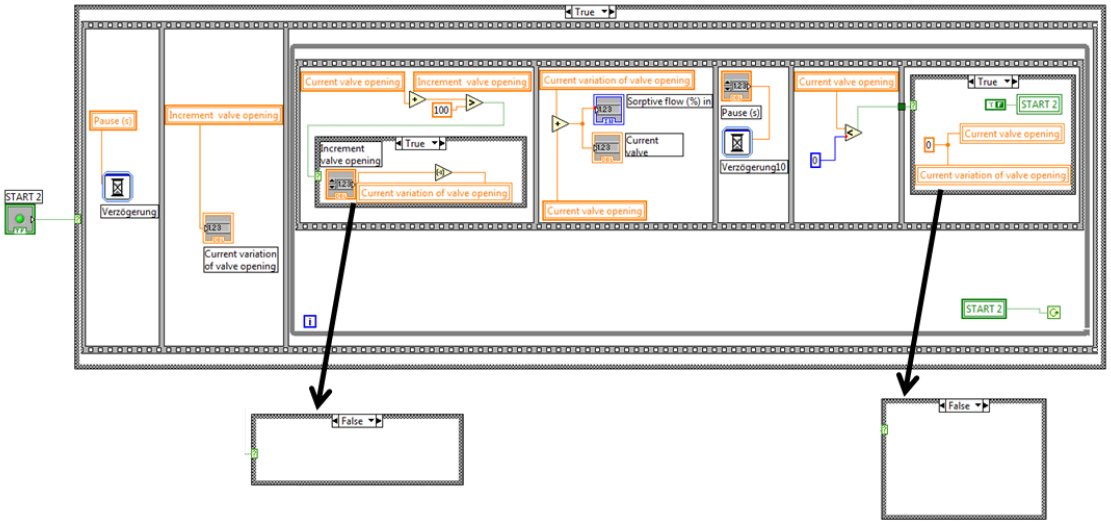

Figure 6.20: **Process for the automated increase and decrease of the sorptive valve opening during *Automatic Gas Flow*.**

To summarize, the functions of the Sorption@XRD process are either simple gas flow at a defined partial pressure or an automatic gas flow with variations of partial pressure in a user-set increment. The possible user settings are listed in Table 6.5.

Table 6.5: **For the two different running modes, different parameters may be set by the user (marked with an X).**

Possible User Settings	Gas Flow mode	Automatic Gas flow mode
Nitrogen Flow (%) in	X	X
Evaporation Temperature (°C) in	X	X
Sorptive Flow (%) in	X	
Increment valve opening		X
Pause (s)		X

The features of the simple Gas Flow mode are also implemented in a second control programme (*Ellipsometer porosimetry*) for usage of the flow controlling system in combination with an ellipsometer.

Redesigned LabView control programme for automated QCM measurements

The already existing LabView programme for automated QCM measurements in our group was cleaned up during this work, existing problems were solved and new features were implemented. Within this section the possible settings and their programme code shall be explained.

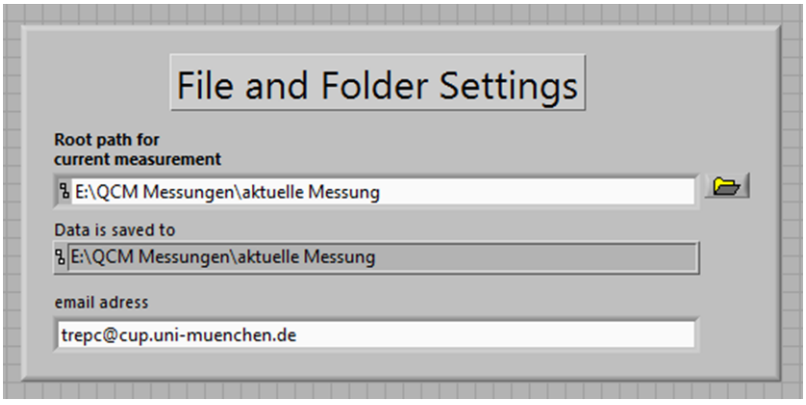

Figure 6.21: File and Folder Settings in the Front panel of the QCM Main.vi.

The first settings the user should check are the so-called “File and Folder Settings” (Figure 6.21), where the root path for the produced files during the measurement is defined. The default setting for the root path is the folder “aktuelle Messung” in the directory “E:\QCM Messungen”. It is also possible to have the produced files sent via email to the entered email address.

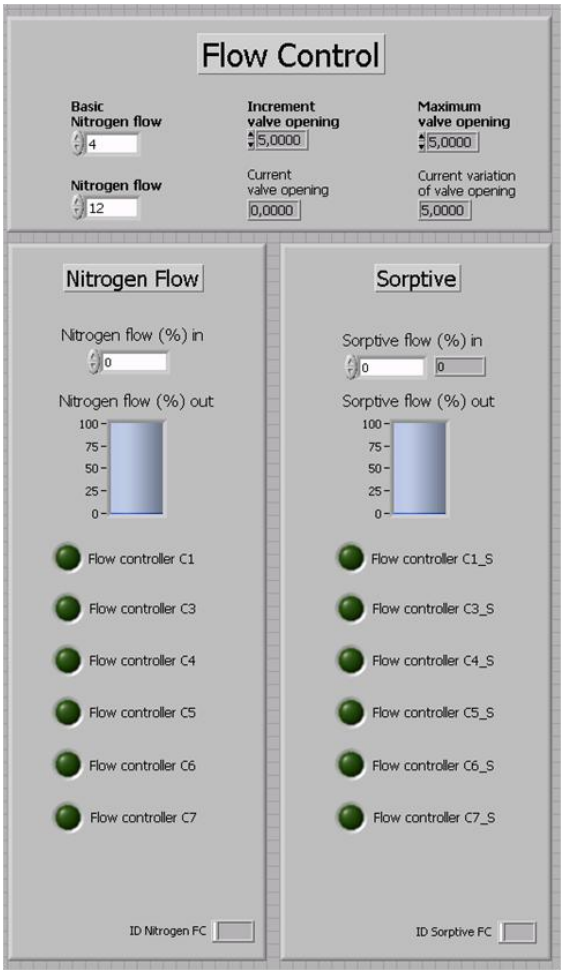

Figure 6.22: Front panel for the flow control

The flow controller system that is used to control partial pressures in the sample cell of the QCM is the same as employed for sorption@XRD measurements and its

features were already described above. The only difference consists of a delay of one second inserted within the while loop containing the flow controller selection, to achieve a better overall performance. (see Figure 6.23)

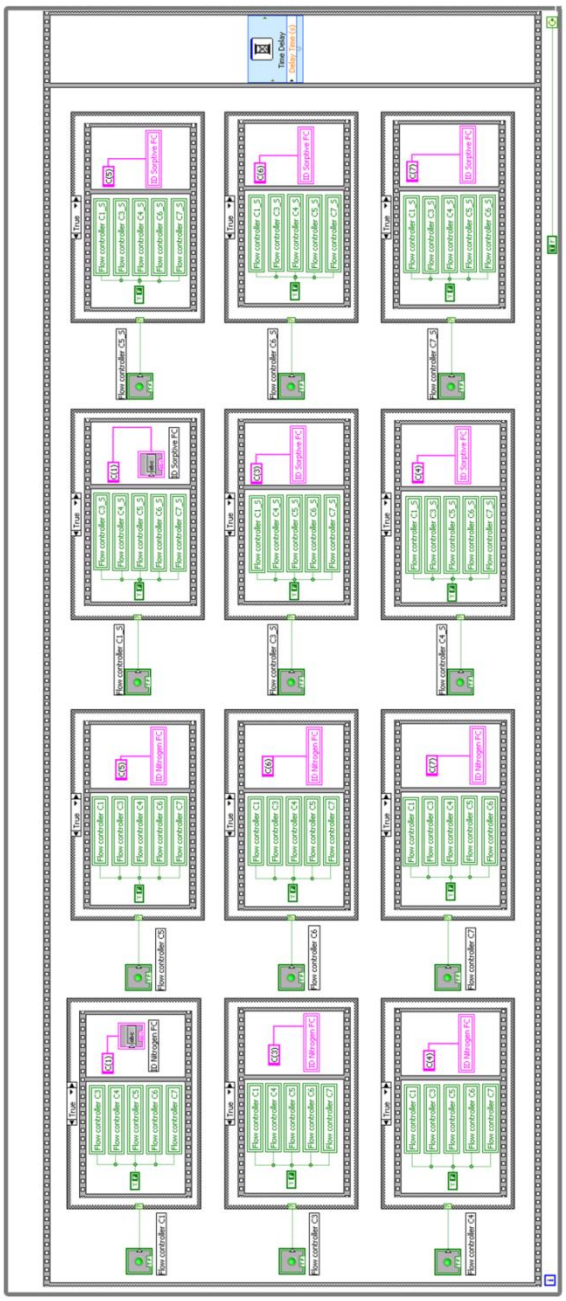

Figure 6.23: While loop containing the sequence structure with the flow controller selection; the time delay in the second step is one second.

The determination of the correct settings for the valve opening for the carrier gas and the sorptive is performed exactly the same way as for sorption@XRD measurements. The front panel for the flow control, already known from the Sorption@XRD programme is slightly extended (Figure 6.22); the new parameters will be discussed in the course of this section. The communication with the flow controllers is also nearly identical to the one discussed in the previous section, apart from the fact that the settings for the flow controllers are recorded during the QCM measurement (see Figure 6.24).

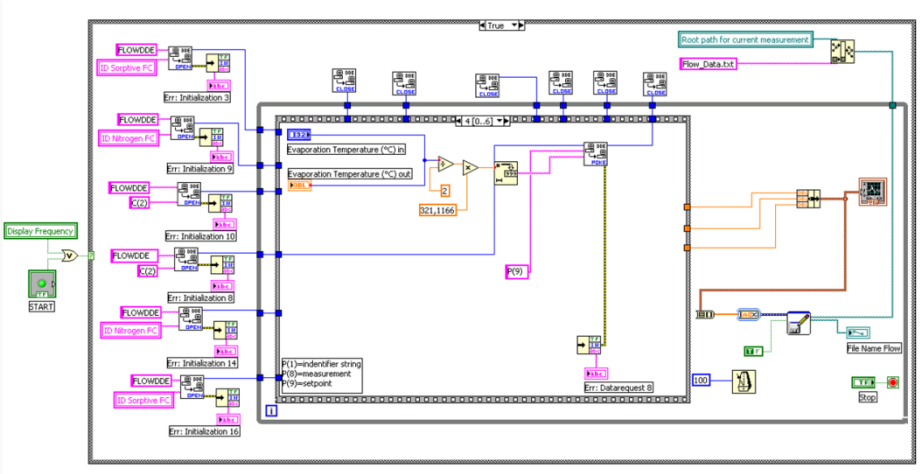

Figure 6.24: **Case structure containing the communication with the digital MFCs and the CEM within the QCM Main.vi. The structure is identical to the one within the Sorption@XRD programme (see Figure 6.18 and Figure 6.19) apart from the writing of the file Flow_Data.txt, which records the settings for the FCs every 100 milliseconds and saves the file to the root path for current measurement.**

The programme code for the automated QCM measurements is constructed within a case structure, the case selector of which is the *START Measurement* button above the frequency measurement part in the front panel (Figure 6.25 and Figure 6.26). A

while loop within the case structure ensures the automated procedure, the exit condition of this while loop will be discussed at the end of this section. The sequence consists of 17 single steps; the first two of these are displayed in Figure 6.25. In the first step of the main sequence the step temperature for the following measurement is calculated. This is done by multiplying the iteration of the surrounding while loop with the *Step Size*, set by the user (see Figure 6.27, Temperature control panel) and adding the result to the variable *Start Temperature* (also set by the user, Figure 6.27). The iteration of the while loop (depicted as small i in a blue frame in Figure 6.25) is a zero-based counter, which means that for the first iteration the *Step Temperature* is equal to the *Start Temperature*. The resulting *Step Temperature* is further used within this step 1 to create a folder to which the resulting files of this temperature step will be saved. The name of this folder will be the actual date and the calculated *Step Temperature* (e.g. 22.02.2009 T=25) and the user will be able to read the created path for this folder from the field "Data is saved to" within the "File and Folder settings" panel (Figure 6.21).

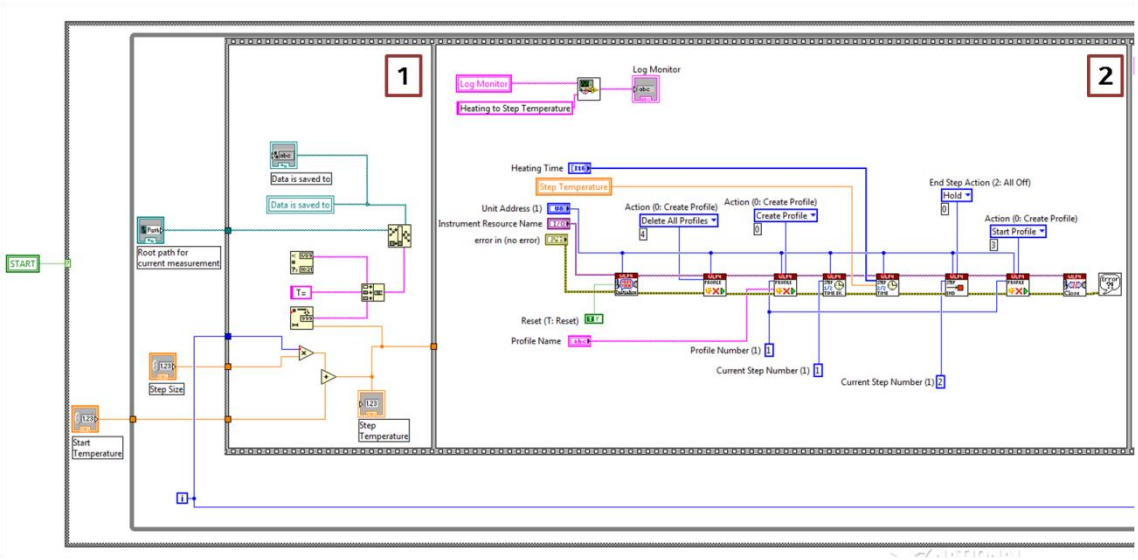

Figure 6.25: Case structure, while loop and step 1 and 2 of the sequence structure for the automated QCM measurements.

In step 2 the communication with the temperature controller is started. The new temperature controller for this setup is a *Watlow F4* device. The communication with this device is accomplished with the help of several so-called SubVis provided by *National Instruments* especially for the *Watlow F4* product series (for a complete list of all SubVis employed in the programme QCM Main.vi see Table 6.7). The combination of these SubVis must be adjusted to the requirements of the particular setup. The unit address and the port of the controller are set per default to 1 and COM 1 (Figure 6.27), the settings required to ensure the communication with the controller in the actual experimental setup. Here the communication starts with an initialization step in which the controller is reset, followed by the deletion of all profiles that might have been running at that point. In the next steps a new profile is created, which consists of a ramp time step and an end step. The temperature set point for the ramp step is the variable *Step Temperature*, the value of which was determined in step 1.

The time for the ramp time step is set by the user in the Temperature Control panel (see Figure 6.27) where it says *Heating Time* and refers to the time that is needed to reach the *Step Temperature*. The *Profile Name*, per default set to *HEATING*, may also be changed by the user, but only capital letters may be written in this field. For the end step the option “Hold” is selected, that means that the set point is held constant by the temperature controller until a new profile is started. The end step is followed by the starting of the created profile and afterwards the communication with the flow controller is terminated. If any errors occur during this process, they will be displayed in the error log within the Output front panel (Figure 6.28). The Output front panel also includes the Flow Controller monitor as well as the Step Logging monitor, which displays the message “Heating to Step Temperature” during step 2 of the main sequence structure.

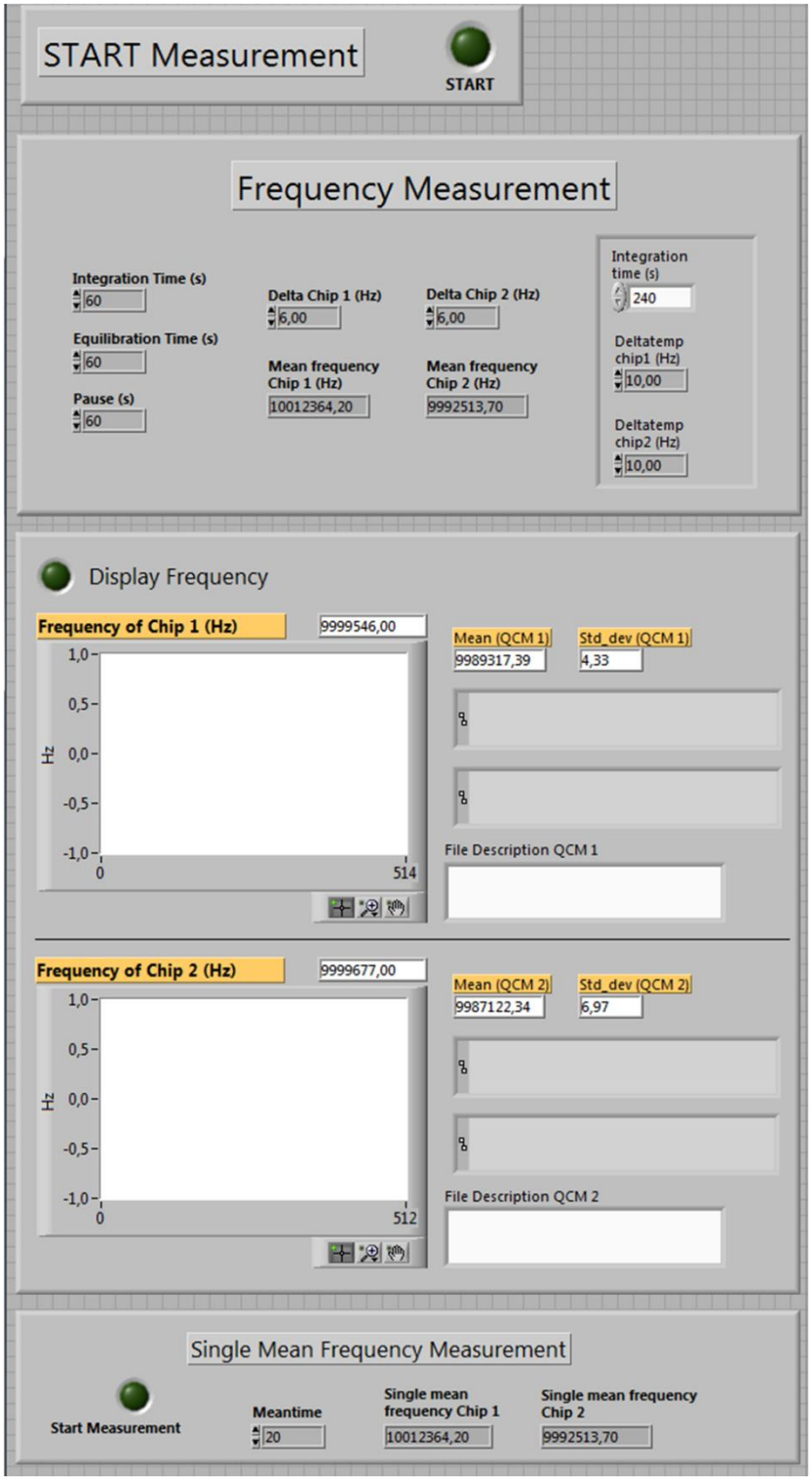

Figure 6.26: **Control panel for the frequency measurement, including the START button for the automated QCM measurements.**

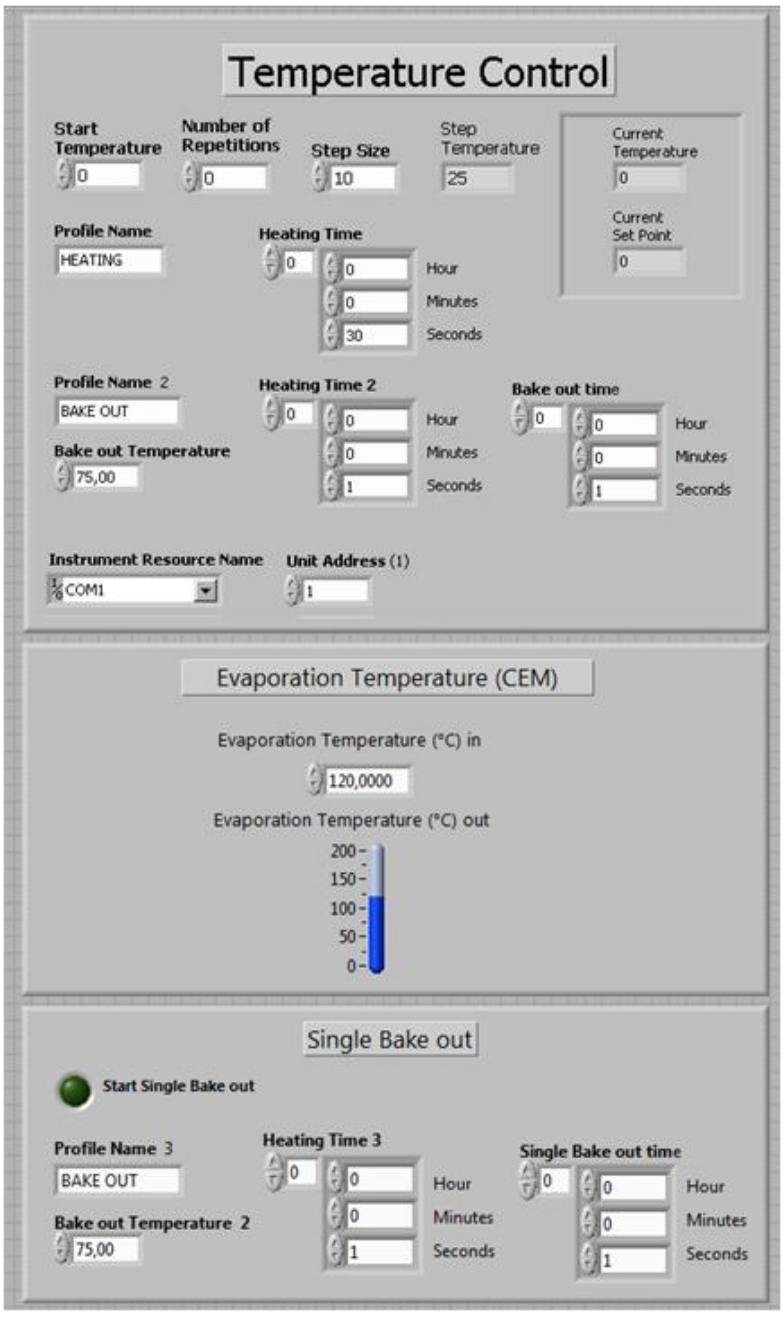

Figure 6.27: Temperature control front panel.

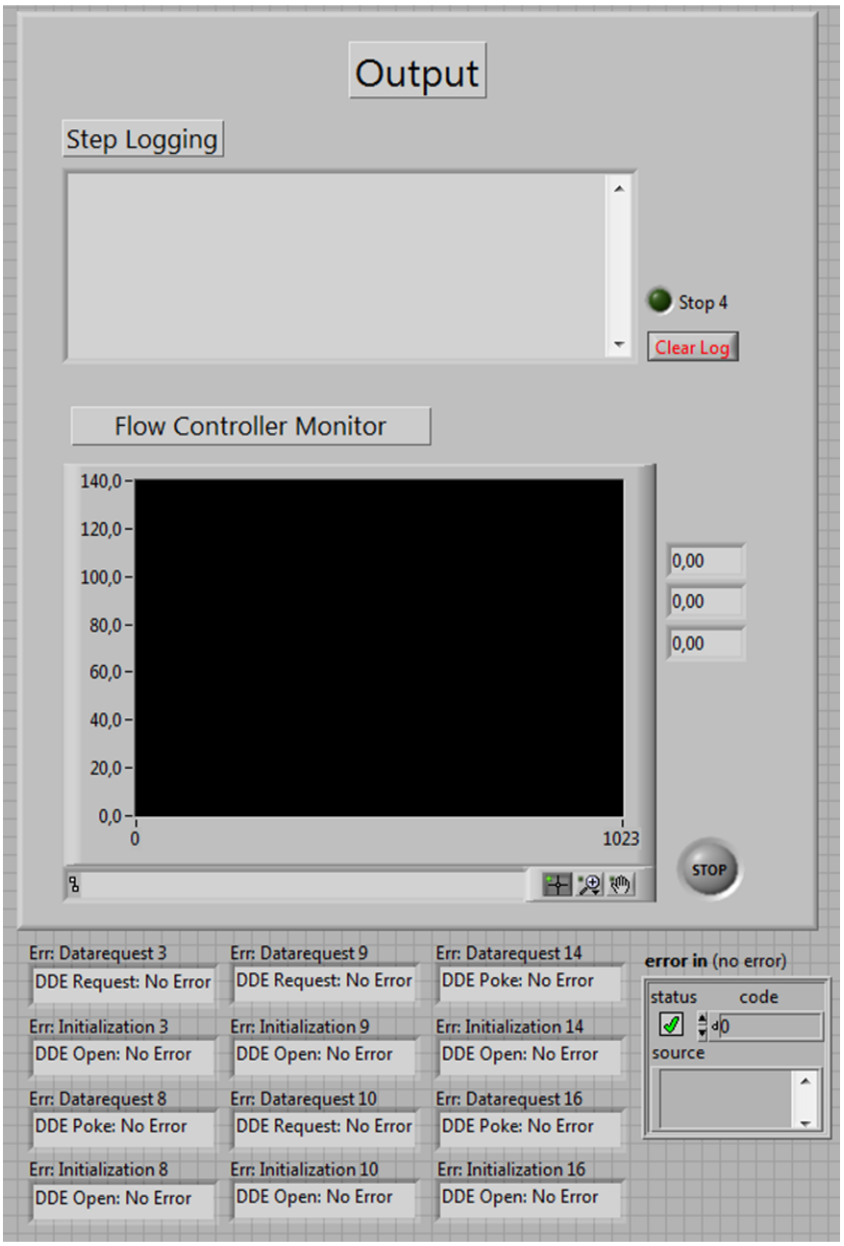

Figure 6.28: **Output front panel, including window for step logging, flow controller monitor and error logs for the communication with flow controllers and with the temperature controller. For the element in the block diagram controlling the clearing of the log monitor see Figure 6.29.**

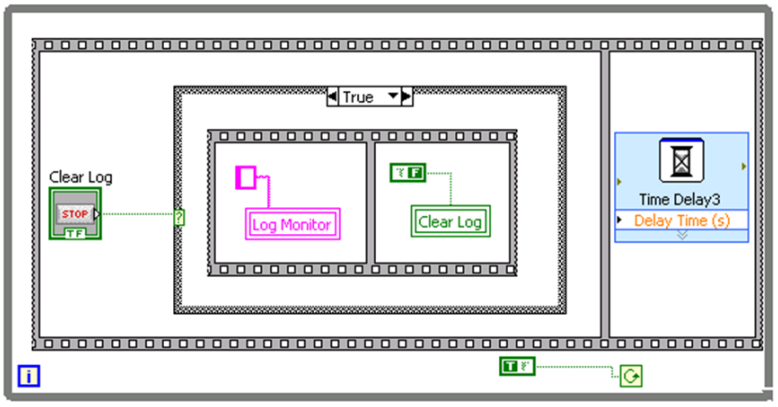

Figure 6.29: **Permanently running while loop, controlling the deletion of the content of the flow controller monitor, if the *Clear Log* button is selected; a delay of one second is inserted in the second step of the sequence structure.**

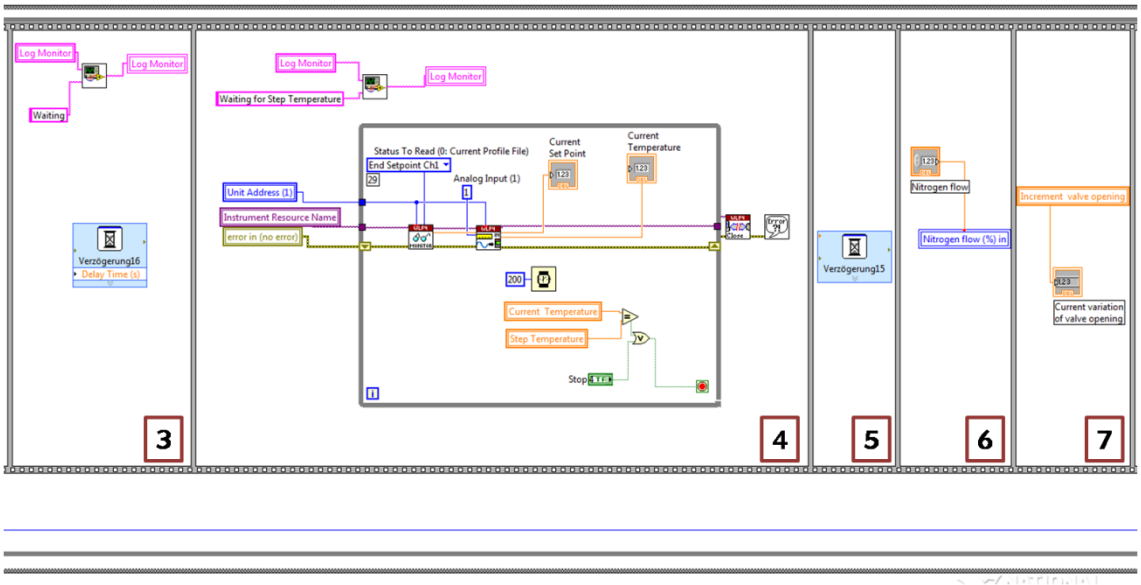

Figure 6.30: **Steps 3 - 7 of the sequence structure for the automated QCM measurements.**

Step 3 (Figure 6.30) contains a delay time of 60 seconds; the message in the step logging monitor is “Waiting”. During step 4, which is announced with “Waiting for

Step Temperature" within the Step Logging monitor, the values for the variables *Current Set Point* and the *Current Temperature* are read from the temperature controller within a while loop. As soon as the *Current Temperature* equals the *Step Temperature* the while loop is stopped and the communication with the temperature controller is terminated. After a one second delay time (step 5), the user defined value for the nitrogen flow (see Figure 6.22) during the measurement is written to the variable *Nitrogen flow in*, which is used for the direct communication with the digital flow controllers (see description of flow controlling system above). In step 7, the *Increment valve opening* (defined by the user in the flow control panel, Figure 6.22) is written to the variable *Current Variation of valve opening*.

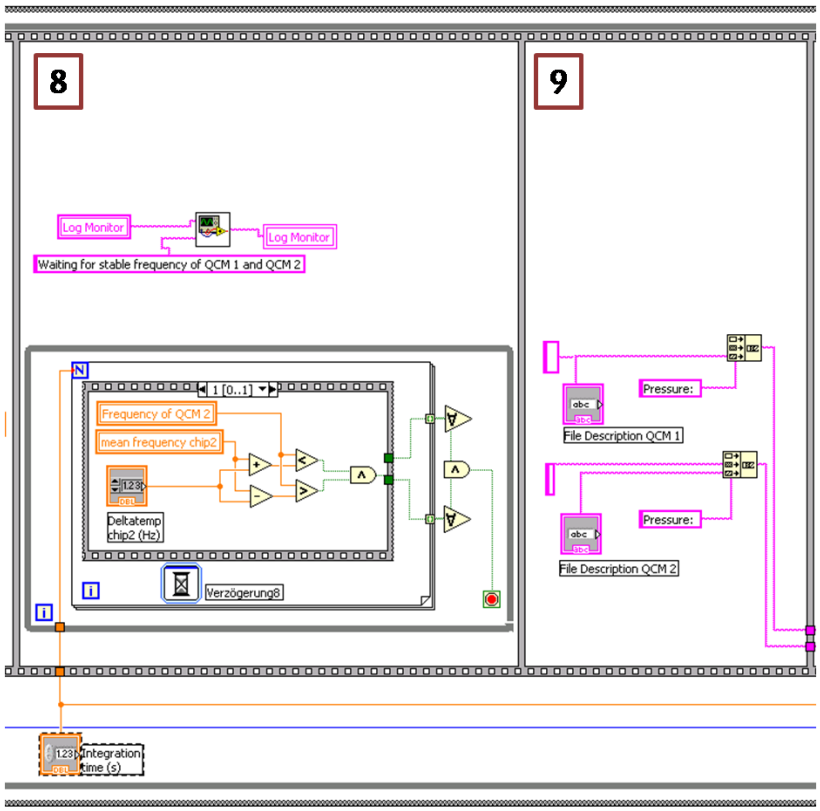

Figure 6.31: Steps 8 and 9 of the sequence structure for the automated QCM measurements.

Before the actual measurement starts, the stability of the frequency of the QCM chips has to be guaranteed. This is accomplished with the help of a while loop, which is only stopped, if the measured frequencies of both QCM chips are varying within a defined interval (*Deltatemp chip 1/2*) from the mean frequency of the particular chip. The time interval for which this condition has to be true is also defined by the user (*Integration time (s)*) in the frequency measurement panel (Figure 6.26). The values of the variables *Frequency of QCM 1/2* and *mean frequency chip1/2* are obtained within different structure blocks of the QCM Main.vi block diagram.

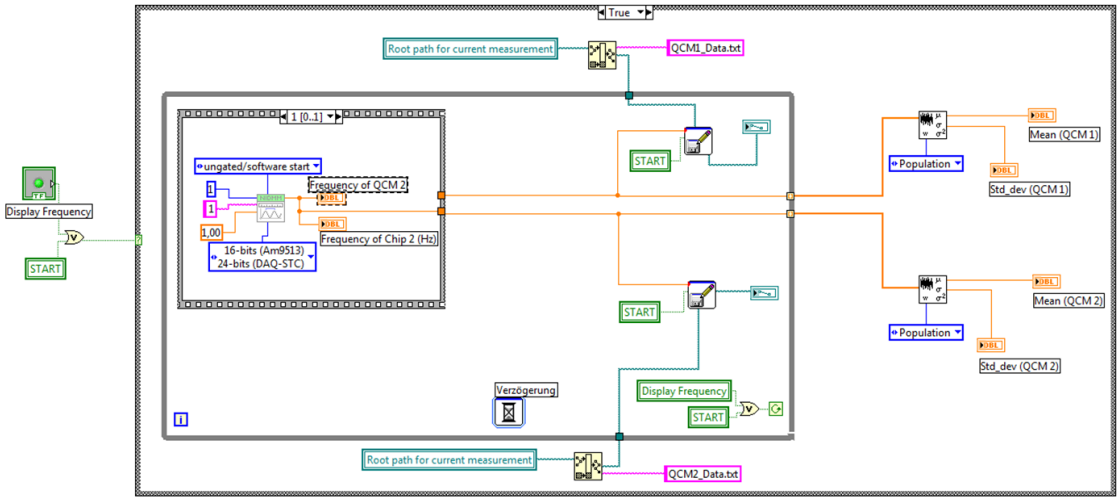

Figure 6.32: Case structure controlling the communication with the frequency counter.

The communication with the frequency counter is performed within a separated case structure, which becomes active either during the automated QCM measurement or if the *Display Frequency* button is selected (which may be the case during the preparation of a QCM measurement or for determining basic frequencies of QCM chips). A *NI* standard SubVi *Measure Frequency.vi* is used to determine the

Frequencies of QCM 1 and QCM 2 (stacked sequence within while loop, Figure 6.32). During an automated measurement, i.e., if *START* is selected, each measured frequency is written into a text file named QCM1_Data.txt and QCM2_Data.txt and saved to the root path defined by the user. The mean frequencies of both chips are determined in a separated while loop, which is running permanently (Figure 6.33). The time interval for which a mean value shall be given, is settable in the field *Integration Time (s)* in the front panel for the frequency measurement settings (Figure 6.26).

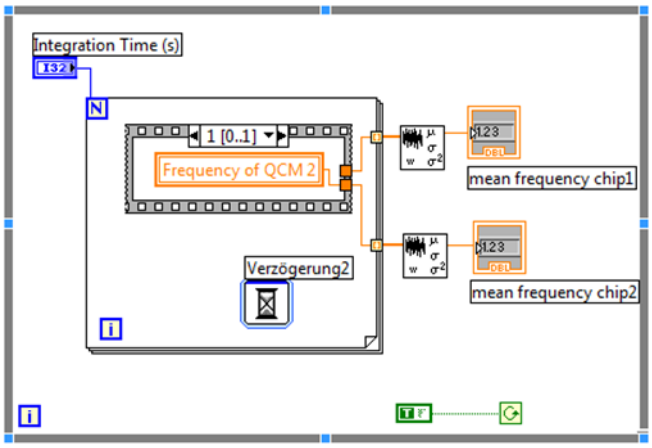

Figure 6.33: Determination of mean frequencies of QCM chip 1 and QCM chip 2.

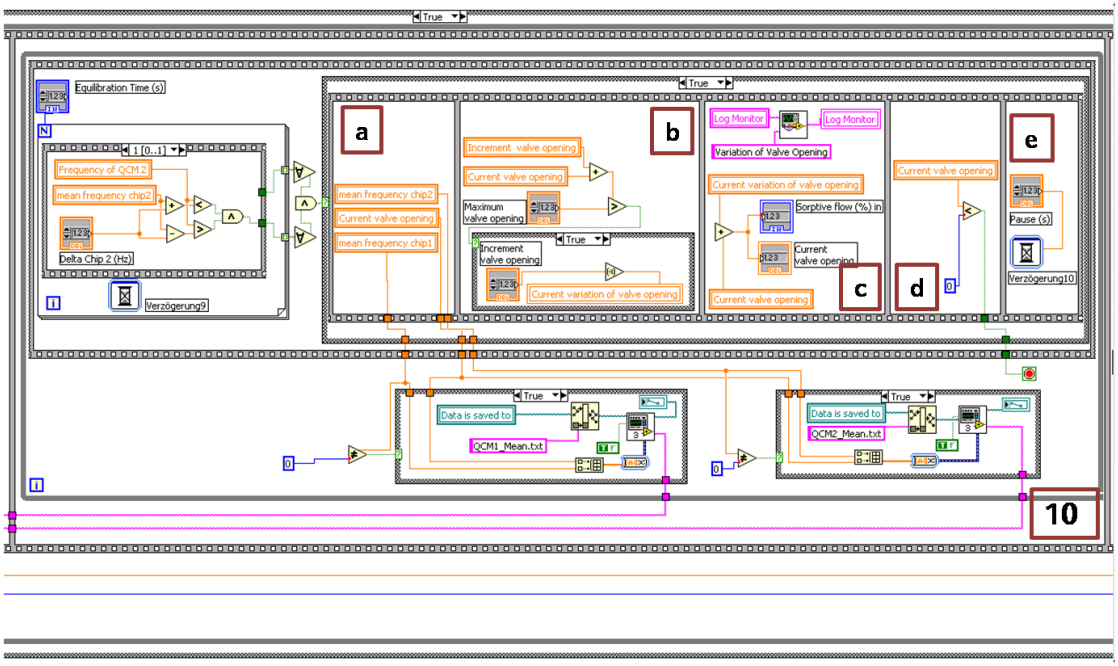

Figure 6.34: Step 10 of the sequence structure for the automated QCM measurements.

If stability of the frequencies of both chips is reached in step 8, the main sequence continues with step 9 (Figure 6.31), in which the text entered by the user under *File Description* (Figure 6.26) is transferred to a string, which later on will be added to the file containing the measurement data. Step 10 contains a while loop consisting of several sub-structures. Within the upper sequence structure the stability of the frequencies of both chips is ensured. If the frequencies are not stable within the given timeframe and frequency interval (set by the user in the frequency measurement panel, Figure 6.26), for all variables zero is handed over to the lower case structure, leading to no action unless the frequencies are stable (Figure 6.35).

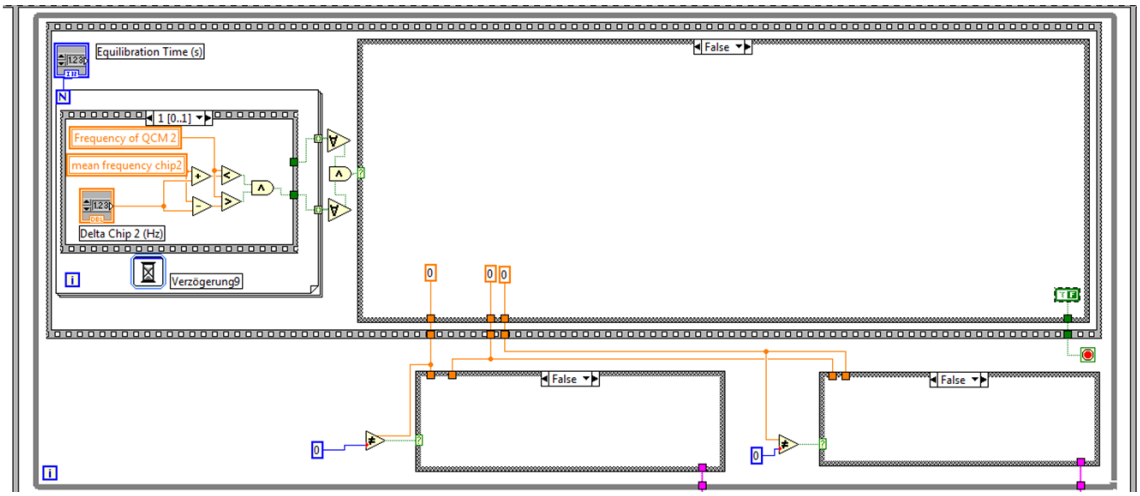

Figure 6.35: If frequencies are not stable within the given timeframe (*Integration Time*) and the given frequency interval (*Delta Chip 1/2*), no data will be written to files.

If the frequencies are stable, a sequence consisting of five steps is started. In step a the variables for mean frequency chip1/2 and the current valve opening are handed over to the case structures containing the data saving. Within these case structures (one for each QCM chip) the values for the current valve opening and the mean frequency of the particular chip are arranged into a table and written to the files QCM1_mean.txt and QCM2_mean.txt with the help of the SubVi Write QCMx _mean.vi. In step b, the *Current variation of valve opening* is multiplied with minus one, if the sum of the *Current variation of valve opening* and the *Current valve opening* is bigger than the value entered for the variable *Maximum valve opening*. This means that if the desired maximum valve opening for the sorptive is reached, the valve is closed again in the subsequent steps. Step c contains the actual variation of the valve opening, which is also displayed in the Step Logging monitor. The variable *Current variation of valve opening* is added to the *Current valve opening* and the

result is written into the variables *Current valve opening* and *Sorptive flow in,* which is directly used for the communication with the digital mass flow controllers. In step d the value for the *Current valve opening* is checked, if it is not below zero, the process, beginning with the waiting for stable frequencies, is starting again after a user defined pause (step e). If the *Current valve opening* is smaller than zero, the while loop containing this whole process is stopped, resulting in the end of this temperature step, being announced in the Step Logging within step 11 (Figure 6.36). Also in step 11, the value for *Nitrogen flow in* is taken from the user defined value for the *Basic nitrogen flow*. In Step 12 the values for *Sorptive flow in, Current valve opening* and *Current variation of valve opening* are reset to zero and in the Step Logging monitor the message "Reset of variables" is displayed. After the first temperature step is completed it is necessary to remove any remaining sorptive molecules. This is accomplished with the help of a bake out step, which means that the temperature is raised, similar to a calcination process. This bake out process is done within step 13; the communication with the temperature controller is almost the same as described for the heating step, the only differences being the insertion of a soaking step (the user is able to define the time for which the bake out process should last) and the different end type (here: all off), as the next temperature will be defined at the beginning of the next temperature step.

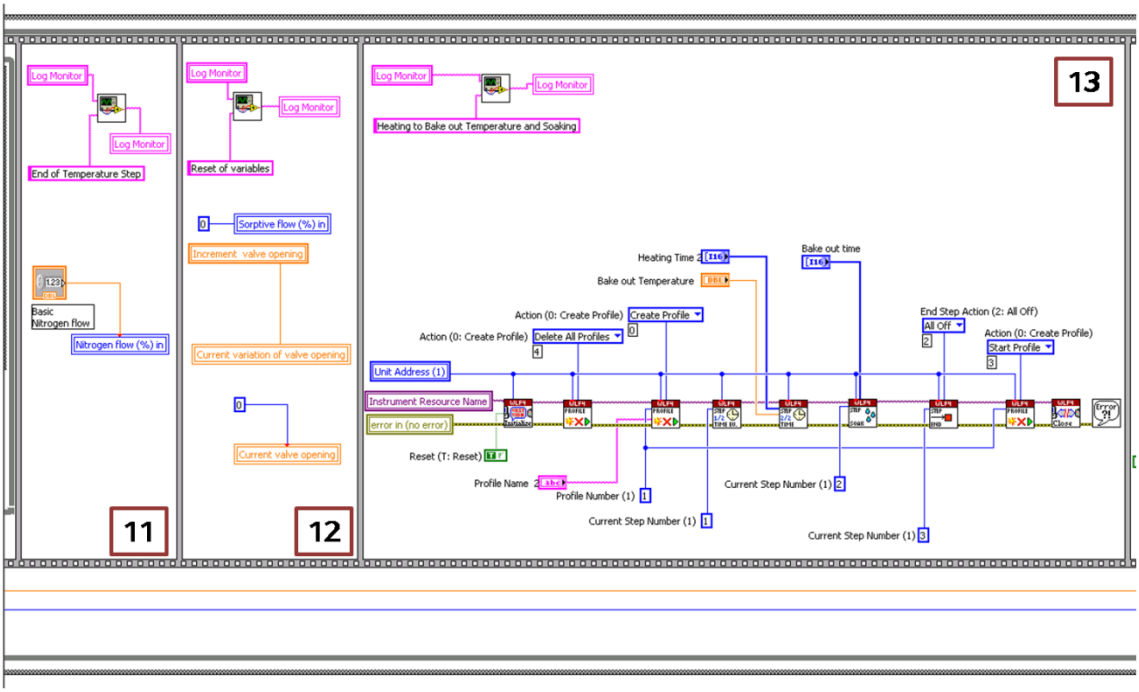

Figure 6.36: Steps 11 - 13 of the sequence structure for the automated QCM measurements.

Step 14 contains the SubVi that sends the produced files (QCM1_mean.txt and QCM2_mean.txt) to the entered email address (Figure 6.37). This feature is currently disabled in the programme (case structure, case selector set to false).

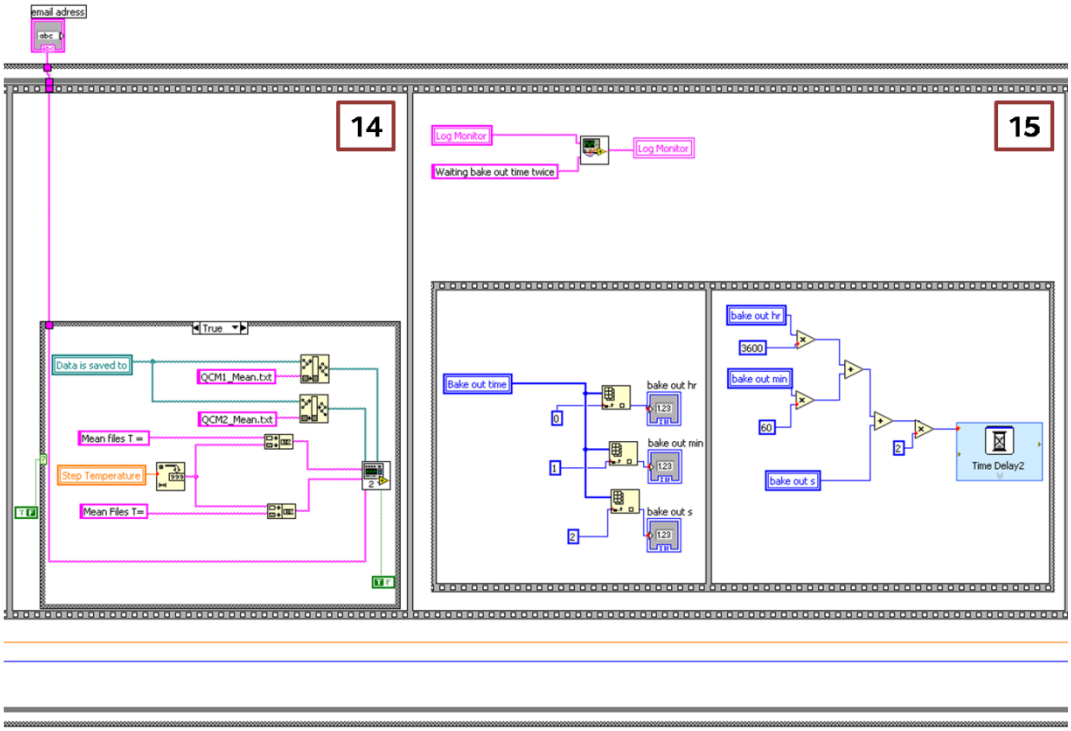

Figure 6.37: Steps 14 and 15 of the sequence structure for the automated QCM measurements

After waiting twice the time of the bake out process during step 15 to ensure that the sample cell is cooled down before the process continues (Step Logging delivers the message "Waiting bake out time twice"), step 16 ensures that the process does not go on without the frequencies being stable; the message in the Step Logging delivered during that step is "Waiting for stable frequencies after bake out" (Figure 6.38). Step 17 regulates the abortion of the surrounding while loop. The user defines, at the beginning of an automated QCM measurement, how many steps, i.e. at how many different temperatures shall be measured (*Number of Repetitions*, Temperature Control panel, Figure 6.27). The while loop is aborted as soon as the *Number of Repetitions* equals the iteration of the while loop, i.e. for one temperature step the

Number of Repetitions to enter is zero, for two steps (two different temperatures) it is one. If the *Number of Repetitions* does not equal the iteration of the while loop, the sequence starts again, beginning with step 1.

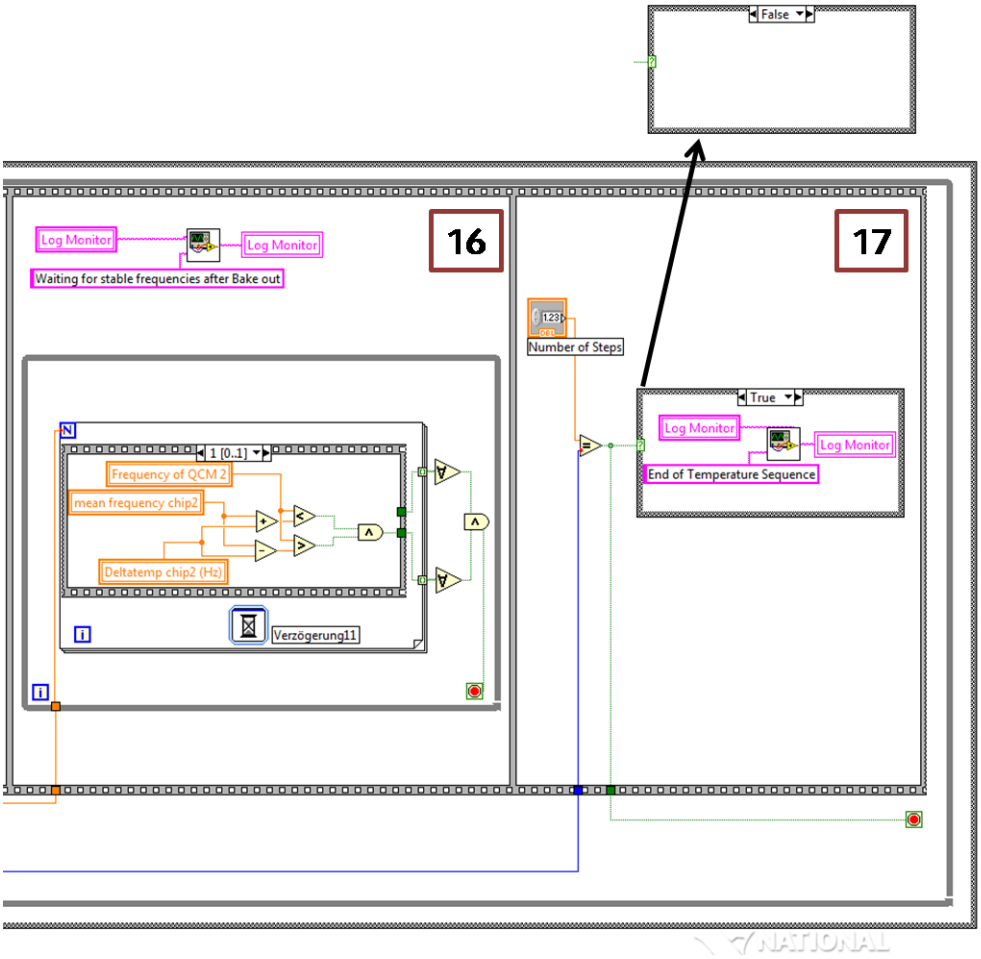

Figure 6.38: Steps 16 and 17 of the sequence structure for the automated QCM measurements.

Excel sheet for the calculation of settings of digital MFCs during Sorption@XRD and QCM measurements

Table 6.6: Excel sheet for the calculation of valve openings and partial pressures for Sorption@XRD and QCM measurements.

N2 valve	N2 flow	Sorptive valve	Sorptive flow	Sorptive quantity	Sorptive volume	Sorptive VdW volume	Volume ratio	Partial pressure	p/p*
(%)	(mL/ min)	(%)	(g/min)	(mol/min)	(l/min)	(l/min)	p/p0	(Pa)	
T (°C)	actual flow	Water	Liquid conversion factor (g/h)	M (g/mol)		V_{mol} (l/mol)		Luft-druck (p0) [Pa]	Saetti-gungs-dampf-druck (p*) [Pa]
24	2298.00		1.0000	18.00		22.4		95955	2983
T (K)			Liquid conversion factor (g/min)						
297			0.0167						
34	781.32	0	0.0000	0.0000	0.0000	0.00E+00	0.000	0.000	0.000
34	781.32	5	0.0008	0.0000	0.0010	1.20E-03	0.002	147.436	0.049
34	781.32	10	0.0017	0.0001	0.0021	2.40E-03	0.003	294.420	0.099
34	781.32	15	0.0025	0.0001	0.0031	3.61E-03	0.005	440.954	0.148
34	781.32	20	0.0033	0.0002	0.0041	4.81E-03	0.006	587.039	0.197
34	781.32	25	0.0042	0.0002	0.0052	6.01E-03	0.008	732.678	0.246
34	781.32	30	0.0050	0.0003	0.0062	7.21E-03	0.009	877.873	0.294
34	781.32	35	0.0058	0.0003	0.0073	8.42E-03	0.011	1022.626	0.343
34	781.32	40	0.0067	0.0004	0.0083	9.62E-03	0.012	1166.939	0.391
34	781.32	45	0.0075	0.0004	0.0093	1.08E-02	0.014	1310.814	0.439
34	781.32	50	0.0083	0.0005	0.0104	1.20E-02	0.015	1454.252	0.488
34	781.32	55	0.0092	0.0005	0.0114	1.32E-02	0.017	1597.257	0.535
34	781.32	60	0.0100	0.0006	0.0124	1.44E-02	0.018	1739.829	0.583
34	781.32	65	0.0108	0.0006	0.0135	1.56E-02	0.020	1881.971	0.631
34	781.32	70	0.0117	0.0006	0.0145	1.68E-02	0.021	2023.379	0.678
34	781.32	75	0.0125	0.0007	0.0156	1.80E-02	0.023	2164.668	0.726
34	781.32	80	0.0133	0.0007	0.0166	1.92E-02	0.024	2305.532	0.773
34	781.32	85	0.0142	0.0008	0.0176	2.04E-02	0.025	2445.974	0.820

34	781.32	90	0.0150	0.0008	0.0187	2.16E-02	0.027	2585.995	0.867
34	781.32	95	0.0158	0.0009	0.0197	2.28E-02	0.028	2725.597	0.914
34	781.32	100	0.0167	0.0009	0.0207	2.40E-02	0.030	2864.782	0.960
34	781.32	100	0.0167	0.0009	0.0207	2.40E-02	0.030	2864.782	0.960
34	781.32	95	0.0158	0.0009	0.0197	2.28E-02	0.028	2725.597	0.914
34	781.32	90	0.0150	0.0008	0.0187	2.16E-02	0.027	2585.995	0.867
34	781.32	85	0.0142	0.0008	0.0176	2.04E-02	0.025	2445.974	0.820
34	781.32	80	0.0133	0.0007	0.0166	1.92E-02	0.024	2305.532	0.773
34	781.32	75	0.0125	0.0007	0.0156	1.80E-02	0.023	2164.668	0.726
34	781.32	70	0.0117	0.0006	0.0145	1.68E-02	0.021	2023.379	0.678
34	781.32	65	0.0108	0.0006	0.0135	1.56E-02	0.020	1881.971	0.631
34	781.32	60	0.0100	0.0006	0.0124	1.44E-02	0.018	1739.829	0.583
34	781.32	55	0.0092	0.0005	0.0114	1.32E-02	0.017	1597.257	0.535
34	781.32	50	0.0083	0.0005	0.0104	1.20E-02	0.015	1454.252	0.488
34	781.32	45	0.0075	0.0004	0.0093	1.08E-02	0.014	1310.814	0.439
34	781.32	40	0.0067	0.0004	0.0083	9.62E-03	0.012	1166.939	0.391
34	781.32	35	0.0058	0.0003	0.0073	8.42E-03	0.011	1022.626	0.343
34	781.32	30	0.0050	0.0003	0.0062	7.21E-03	0.009	877.873	0.294
34	781.32	25	0.0042	0.0002	0.0052	6.01E-03	0.008	732.678	0.246
34	781.32	20	0.0033	0.0002	0.0041	4.81E-03	0.006	587.039	0.197
34	781.32	15	0.0025	0.0001	0.0031	3.61E-03	0.005	440.954	0.148
34	781.32	10	0.0017	0.0001	0.0021	2.40E-03	0.003	294.420	0.099
34	781.32	5	0.0008	0.0000	0.0010	1.20E-03	0.002	147.436	0.049
34	781.32	0	0.0000	0.0000	0.0000	0.00E+00	0.000	0.000	0.000

List of included SubVIs in the programme QCM Main.vi

Table 6.7: List of all employed SubVis within the QCM Main.vi, including their source, location on the computer and their function.

Title	Level	Source	Location (path)	Function
DDE_open conversation_cs.vi	1	Bronkhorst	E:\LabView Steuerung\SubVIs	Communication with MFCs
DDE_close conversation_cs.vi	1	Bronkhorst	E:\LabView Steuerung\SubVIs	Communication with MFCs
DDE poke_cs.vi	1	Bronkhorst	E:\LabView	Communication

			Steuerung\SubVIs	with MFCs
DDE request_cs.vi	1	Bronkhorst	E:\LabView Steuerung\SubVIs	Communication with MFCs
WLF4 Initialize.vi	1	NI	E:\LabView Steuerung\T Control_WLF4.llb	Communication with temperature controller
WLF4 Configure Profile.vi	1	NI	E:\LabView Steuerung\T Control\WLF4.llb	Communication with temperature controller
WLF4 Insert Ramp Time Step Event.vi	1	NI	E:\LabView Steuerung\T Control\WLF4.llb	Communication with temperature controller
WLF4 Insert Ramp Time Step.vi	1	NI	E:\LabView Steuerung\T Control\WLF4.llb	Communication with temperature controller
WLF4 Insert Soak Step.vi	1	NI	E:\LabView Steuerung\T Control\WLF4.llb	Communication with temperature controller
WLF4 Insert End Step.vi	1	NI	E:\LabView Steuerung\T Control\WLF4.llb	Communication with temperature controller
WLF4 Read.vi	1	NI	E:\LabView Steuerung\T Control\WLF4.llb	Communication with temperature controller
WLF4 Monitor.vi	1	NI	E:\LabView Steuerung\T Control\WLF4.llb	Communication with temperature controller
WLF4 Close.vi	1	NI	E:\LabView Steuerung\T Control\WLF4.llb	Communication with temperature controller
Measure Frequency.vi	1	NI	C:\Programme\National Instruments\LabView	Communication with frequency

			7.1\vi.li\daq\1easiyo.llb	counter
Simple Error Handler_cs.vi	1	Ni	E:\LabView Steuerung\SubVIs	Display of error messages
Std deviation and variance_cs.vi	1	NI	E:\LabView Steuerung\SubVIs	Calculation of mean values
Email versenden.vi	1	self-written	E:\LabView Steuerung\SubVIs	Send email to given email address
Write Flow_Data.vi	1	self-written	E:\LabView Steuerung\SubVIs	Save Flow_Data.txt
Write QCM1_Data.vi	1	self-written	E:\LabView Steuerung\SubVIs	Save QCM1_Data.txt
Write QCM2_Data.vi	1	self-written	E:\LabView Steuerung\SubVIs	Save QCM2_Data.txt
Write QCM1_mean.vi	1	self-written	E:\LabView Steuerung\SubVIs	Save QCM1_mean.txt
Write QCM2_mean.vi	1	self-written	E:\LabView Steuerung\SubVIs	Save QCM1_mean.txt
Write to logmon.vi	1	self-written	E:\LabView Steuerung\SubVIs	Display status of process in Step Logging Monitor

7 Extending the structure-directing concept to functionalized metal-organic frameworks

The work described in this chapter was undertaken as part of a joint project in collaboration with Dr. Jennifer Williams of the University of Edinburgh.

7.1 Introduction

Extending the concept of directing the structure and orientation of MOFs using self-assembled monolayers for surface functionalization invokes the question, which framework structures could offer enhanced properties. Interesting candidates for new MOF structures directly grown on substrates are those with implemented functionalities. Here the modification of the pore walls offers the possibility of improving the properties of existing MOF structures. This could, for example, result in more selective materials with a higher storage capacity in fields such as gas separation or storage.[45]

There are two different approaches to implementing functionalities in MOFs. The first employs organic ligands with additional functional groups that are not involved in coordination of the metal centres but rather change the functionality of the pore walls. The group of S. Kitagawa have focused their research efforts on this challenge. They modified the organic linkers in such a way that the host-guest interactions desired for a particular application were obtained by inserting unsaturated metal-centres.[61] In a different study, the same group reports the implementation of hydrogen-bonding

groups for specific host-guest interactions within dynamic porous coordination polymers.[251] The second approach is, in a strict sense, an extension of this first approach, as it refers to the post-synthetic modification of the organic linkers, which in most cases requires the presence of at least one modifiable functional group.[258] For example, Kim and co-workers showed that the pendant pyridyl groups in a chiral zinc network could be methylated.[70] Burrows *et al.* reported a post-synthetic modification starting from an aldehyde-functionalized dicarboxylate to a hydrazone ligand.[259] In different studies it has been demonstrated that the amino groups in 2-amino-1,4-benzenedicarboxylate MOFs can be converted into amides, urethanes,[260-263] or salicylidenes.[264]

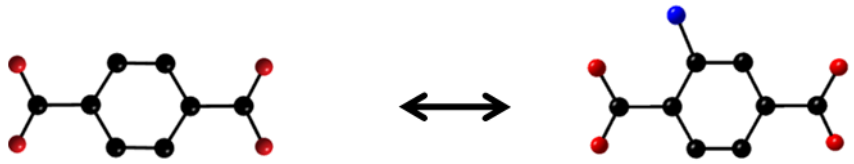

Figure 7.1: Substitution of 1,4 benzenedicarboxylic acid through 2-amino-1,4-benzenedicarboxylic acid leads to the formation of the amino-functionalized structures of MIL-53, Mil-88B and MIL-101.

In chapter 5 of this thesis the system iron(III)/ 1,4 benzenedicarboxylic acid has been discussed and the three most important structures within this system, namely MIL-53, MIL-88B and MIL-101, have been introduced. By employing high-throughput synthetic methods, Bauer *et al.* were able to obtain the amino-functionalized isoreticular compounds of these three structures.[58] Their study revealed that the insertion of functional groups in the organic linker may strongly change the synthesis conditions required for a desired structure. It was found that the nature of the

reaction medium has the most profound impact on structure formation. Furthermore, the concentration of the starting mixture (i.e., the solvent content) and the temperature have also been identified as key parameters for the formation of the different competing hybrid phases.

Within this section the growth of amino-functionalized MILs on SAMs will be discussed, representing the extension of the described concept of structure-directed, oriented growth of MIL-88B crystals.

7.2 Experimental

Preparation of self-assembled monolayers on gold

The gold-coated slides (glass slides (10 × 13 mm^2) coated with 10 nm Ti / 100 nm Au by electron-beam evaporation, Advalytix AG) were cleaned in ethanol and methanol. The cleaned gold slides were immersed in a 1 mM ethanolic solution (6 pieces in 30 mL) of 16-mercaptohexadecanoic acid (MHDA; 90 %, *Aldrich*) and left at RT for 48 h. The SAM-functionalized gold slides were repeatedly washed with ethanol, and stored in fresh absolute ethanol until needed.

Synthesis of bulk NH_2-MIL-101

In a glass reactor, 0.25 g (1.4 mmol) of 2-amino-1,4-benzenedicarboxylic acid (99 %, *Aldrich*) was dissolved in 15 mL dimethylformamide (DMF, p.a., *Acros Organics*). To the clear solution 0.746 g (2.7 mmol) $FeCl_3 \cdot 6\,H_2O$ (p.a., *Merck*) was added. The sealed-glass reactor was left for 1 day in a preheated oven at 150 °C. After cooling the

synthesis mixture to room temperature, the crystalline product was filtrated and stored for further characterization.

Preparation of the crystallization solution for film growth of NH_2-MIL-101

In a glass reactor, 0.25 g (1.4 mmol) of 2-amino-1,4-benzenedicarboxylic acid (99 %, *Aldrich*) was dissolved in 15 mL dimethylformamide (DMF) (p.a., *Acros Organics*). To the clear solution 0.746 g (2.7 mmol) $FeCl_3 \cdot 6\,H_2O$ (p.a., *Merck*) was added. The sealed-glass reactor was left for 1 day in a preheated oven at 150 °C. After cooling the synthesis mixture to room temperature, the crystalline product was filtered and stored for further characterization. The filtrated solution was used for the growth of thin films.

Film Growth of NH_2-MIL-101

The SAM-functionalized gold-slides were placed upside-down on Teflon®-supports into the filtrated synthesis solution of NH_2-MIL-101 (3 pieces in 15 mL). The growth step took place at RT in a closed glass reactor. Immersion times were varied between 3 d and 10 d.

7.3 Characterization

X-ray diffraction (XRD) measurements of powders were performed on a STOE powder diffractometer in transmission geometry (Cu-$K_{\alpha 1}$, $\lambda = 1.5406$ Å), those of films using a Bruker D8 in theta-theta geometry (Cu-$K_{\alpha 1}$, $\lambda = 1.5406$ Å; Cu-$K_{\alpha 2}$, $\lambda = 1.5444$ Å). Characterization of the self-assembled monolayers was performed by RAIR

spectroscopy, using a Bruker IFS 66v FTIR spectrometer. The sample chamber with a high performance variable angle reflection accessory (A-513) was maintained at 2 mbar during the entire measurement by means of an Edwards rotary-pump. In a typical measurement on gold surfaces, an incidence angle of 83 ° to the surface normal was used. Furthermore, a cleaned gold slide was measured as background prior to the measurements. The morphology of the crystals was studied using a JEOL JSM-6500F scanning electron microscope.

7.4 Results and Discussion

In our experiments on the direct growth of amino-functionalized MIL structures on carboxylate terminated SAMs, we observe, for the first time, direct growth of a MOF with an exceptionally large unit cell, namely NH_2-MIL-101.

For the direct growth of the amino-functionalized MIL crystals, the gold substrates were modified with monolayers of $HS(CH_2)_{16}COOH$ following known procedures[119, 185] (see section 7.2). The formation of the self-assembled monolayers was confirmed by RAIR, as shown in Figure 7.2. The characteristic absorption band at 1554 cm^{-1} indicating the carboxylate group is indicated in the spectrum. The methylene groups of the aliphatic chains present high-frequency modes at 2920 and 2850 cm^{-1} associated with the asymmetric and symmetric C-H stretching vibrations, respectively; we also observe the band at 721 cm^{-1} assigned to the stretching vibration of the S-C bond.

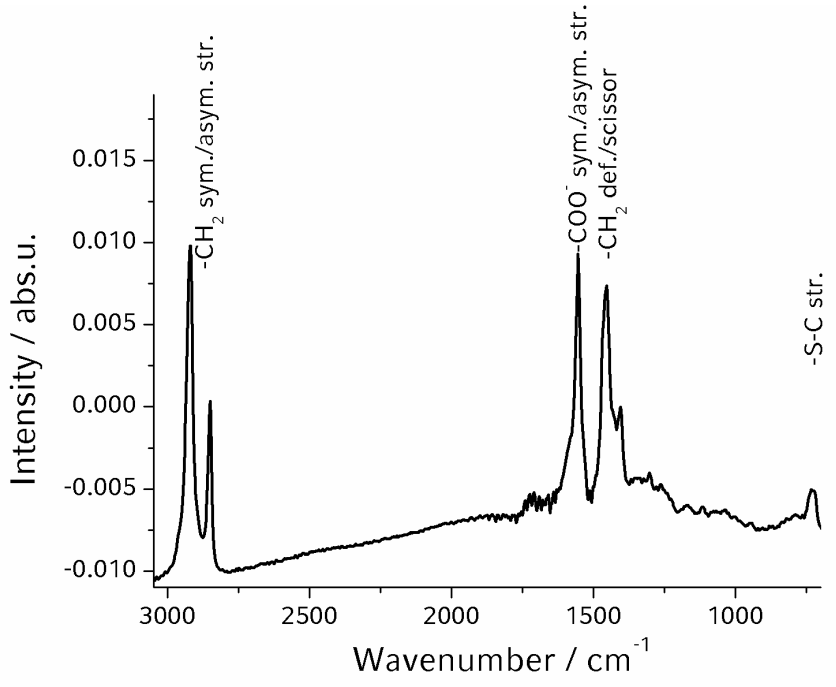

Figure 7.2: RAIR-spectrum of the MHDA self-assembled monolayer on a gold substrate.

As described in section 7.1, NH_2-MIL-101 is isoreticular to MIL-101, which has a cubic unit cell with a cell parameter of 89 Å. After an immersion time of 3 d, the (222) reflection at 3.4 ° two theta and the (333) reflection at 5.1 ° two theta of NH_2-MIL-101 can be clearly detected, as shown in the XRD patterns of the synthesized film samples compared to the powder pattern of bulk MIL-101 crystals (Figure 7.3). The increase of the immersion time to 7 d leads to a strong increase of the intensities of the (222) and (333) reflections. Small additional reflections at 8.6 ° and 10.3 ° two theta , which can be assigned to the (662) and the (1022) reflection of NH_2-MIL-101, indicate the appearance of a small second population of less oriented crystals. We conclude that the crystal populations on the SAM have a strongly preferred orientation in [111]-direction.

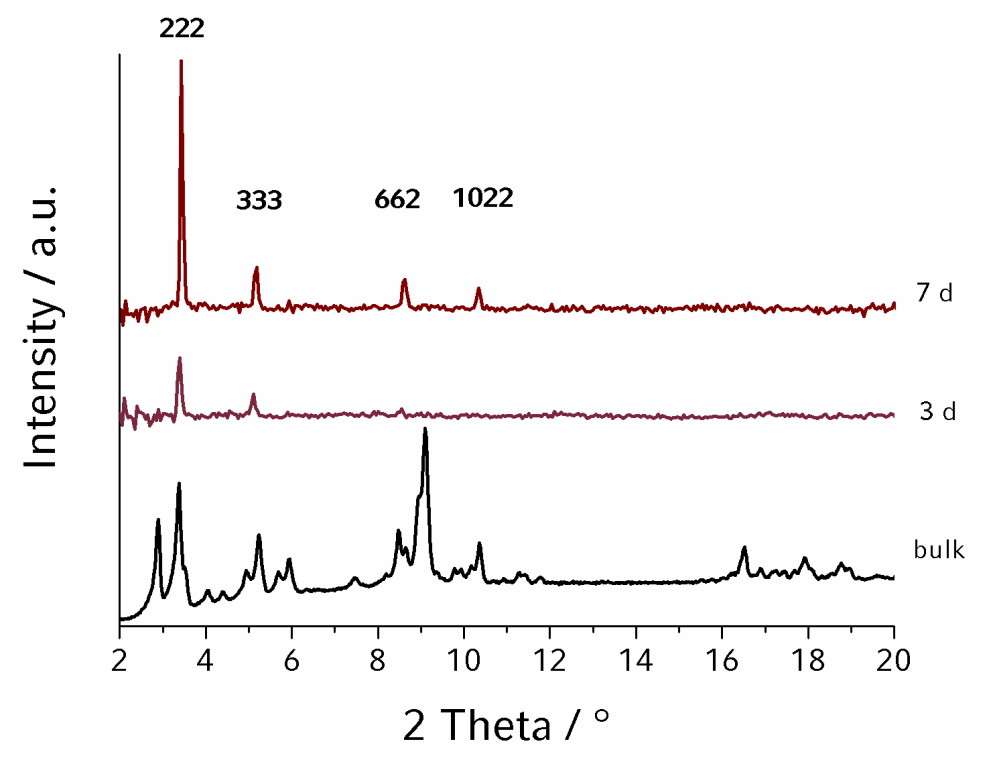

Figure 7.3: **X-ray diffraction data of NH_2-MIL-101 crystals grown on functionalized gold substrates (immersion times of the substrates in the crystallization of 3 d and 7 d) compared to the powder pattern of bulk NH2-MIL-101 crystals. The background of the XRD patterns of the film samples was subtracted.**

To further investigate the crystal growth on the functionalized substrates, SEM images were taken. (Figure 7.4) The crystals feature a distinct sphere-like morphology with sizes between 100 – 500 nm.

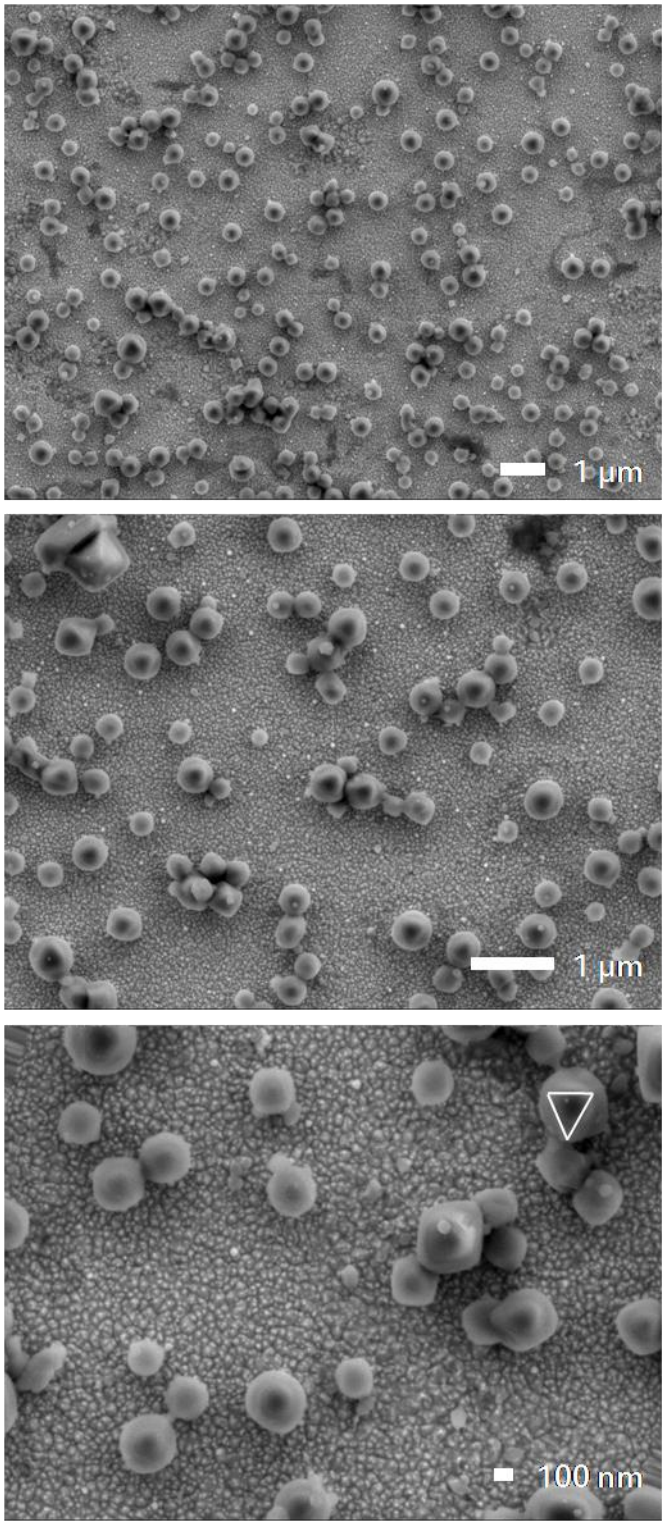

Figure 7.4: **Scanning electron micrographs of NH_2-MIL-101 samples after immersion times of 10 days at different magnifications.**

Higher magnification reveals that most of the crystals have a triangular top-face (Figure 7.4) This is in good agreement with the preferred [111]-orientation of the crystals, deduced from the XRD results. NH_2-MIL-101 crystallizes in a cubic symmetry and the bulk crystals show an octahedral morphology, which would appear with triangular habit from in top-view if oriented in [111] direction.

To demonstrate the interesting properties of NH_2-MIL-101 a thermogravimetric analysis (TGA) and nitrogen sorption data were recorded of the corresponding bulk material; the results are depicted in Figure 7.5 and Figure 7.6. The first step of 56 wt. % in the TGA is assigned to the loss of solvent and water molecules from inside the pores. The decomposition of the organic parts of NH_2-MIL-101 subsequently takes place above 250 °C within two steps, which can also be seen from the differential scanning Calorimetry (DSC) in red in Figure 7.5. These two steps show a weight loss of 30 % and of 70 % corresponding to the crystals with filled pores and those with empty pores respectively. This 70 % weight loss is in good agreement with the weight fraction of the organic parts of NH_2-MIL-101 ($Fe_3O(NH_2BDC)_3$), which can be calculated as 75 wt. %.

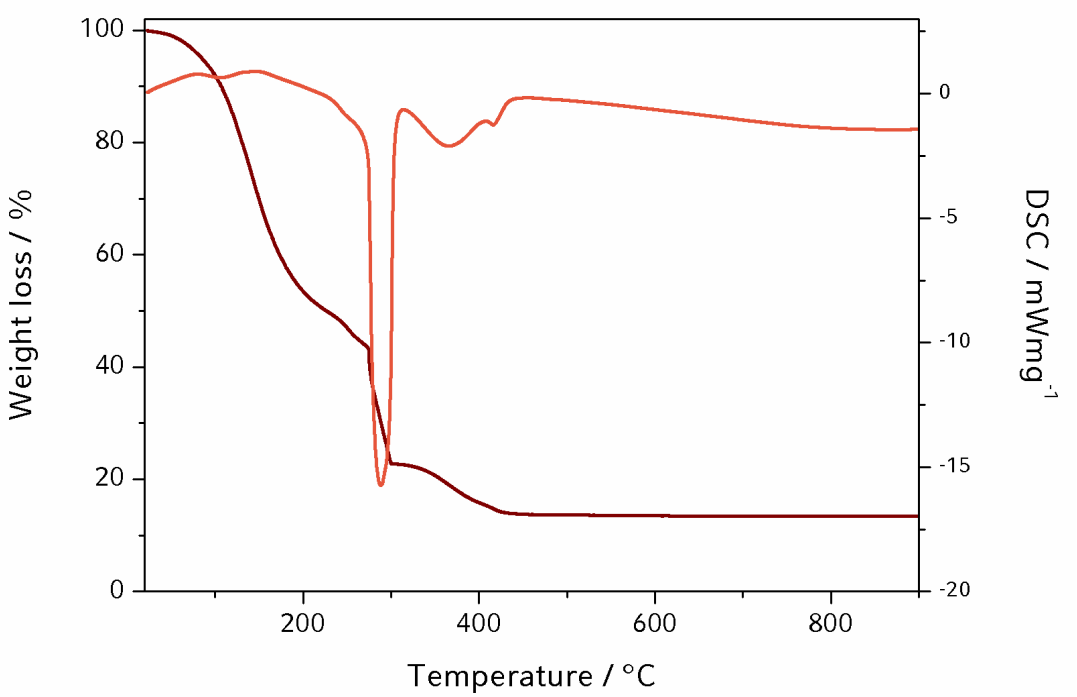

Figure 7.5: **TGA and DSC data of NH_2-MIL-101.**

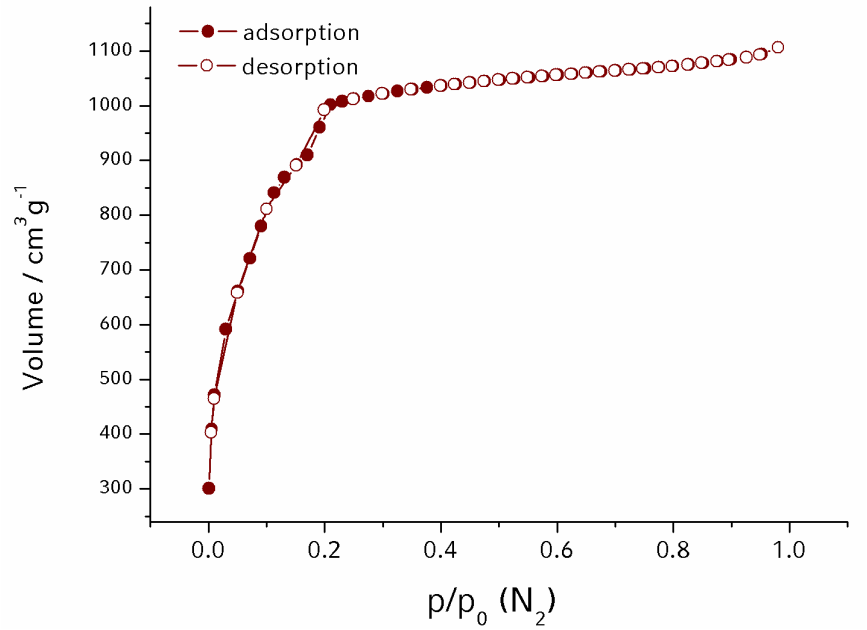

Figure 7.6: **Nitrogen gas sorption isotherm at 77 K for bulk NH2-MIL-101.**

The high porosity of NH_2-MIL-101 crystals can be demonstrated using nitrogen sorption, recorded at 77 K. The Type I isotherm of the amino functionalized MIL-101 is very similar to the isotherm of the unfunctionalized compound reported in the literature.[72] The shapes of the isotherms are nearly identical, both providing a small step in the adsorption curve at 0.2 p/p_0. The overall adsorbed volume of nitrogen is slightly smaller for NH_2-MIL-101 than for MIL-101, which can be attributed to the amino groups being present in the framework. The fact that the adsorption capacity of the material is only slightly reduced by the amino functionalization is of great interest for the thin film growth and for further investigations concerning possible applications of these functionalized MOF thin films.

7.5 Conclusion

In chapters 3 to 5, the complete molecular control of the growth orientation of MOFs was demonstrated on HKUST-1 and MIL-88B. After this proof of concept, the next important step is to extend these methods to functionalized MOFs - this work is the subject of the present chapter.

An inherent advantage of MOFs over more traditional porous materials, such as zeolites or activated carbons, is the possibility of tuning the host-guest interactions by functionalizing the organic linker molecules. In this chapter, we have demonstrated that advantages of functionalization can also be realized in oriented film synthesis of MOFs: We have shown for the first time that functionalized MOFs can be grown on self-assembled monolayers and that a preferred orientation of the crystals is achieved. This was demonstrated for NH_2-MIL-101 and to a lesser extent for NH_2-MIL-88B. (see Additional Details within section 7.6) It was also shown that the adsorption capacity of

NH_2-MIL-101 was not significantly reduced by the amino functionalization; this is important for potential storage applications.

We envisage that by carrying out systematic investigations of the synthesis parameters such as described in this work, MOFs with different functionalities or entirely different functionalised MOFs could be grown with a preferred orientation. We anticipate that the ability to direct the growth of functionalized MOFs will be of particular interest in applications such as selective chemical sensors, where both the control of crystal growth orientation and functionalization of the organic linker to control host-guest interactions are advantageous.

7.6 Additional Details

Oriented growth of another amino-functionalized MOF, NH_2-MIL-88B, was observed in several instances in fairly similar synthesis batches. The details for these experiments are presented at the end of this section. Apparently, the position of these syntheses in the crystallization parameter field is close to the crystallization boundary between NH_2-MIL-101 and NH_2-MIL-88B, as both phases can be observed when incrementally changing synthesis parameters.

As with unfunctionalized MIL-88B crystals, we observe crystal growth of NH_2-MIL-88B in the [002] direction on functionalized gold substrates with $-COO^-$ termination. In the X-ray diffraction patterns of the crystals grown directly on the film, we observe only two reflections at 9.2 ° and 18.4 ° two theta (Figure 7.7). The absence of the other peaks observed in the corresponding bulk XRD indicates that the crystals grow on the SAM in a highly oriented fashion.

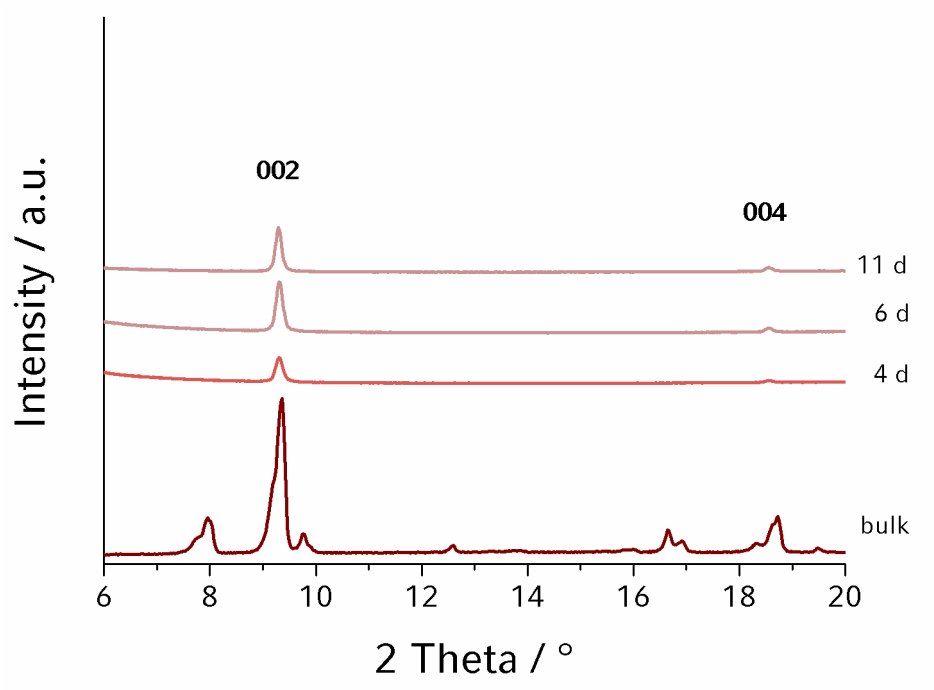

Figure 7.7: **X-ray diffraction measurements of crystals grown on functionalized gold substrates compared to the XRD pattern of bulk NH_2-MIL-88B crystals. The immersion time of the substrates in the crystallization solution varied between 4 d and 11 d.**

SEM images of the samples, represented in Figure 7.8, show small hexagonally shaped crystals with almost vertical orientations, very similar to the SEM images of the earlier stages of MIL-88B crystal growth. The size distribution of the surface-grown crystals is inhomogeneous and the surface coverage is fairly low.

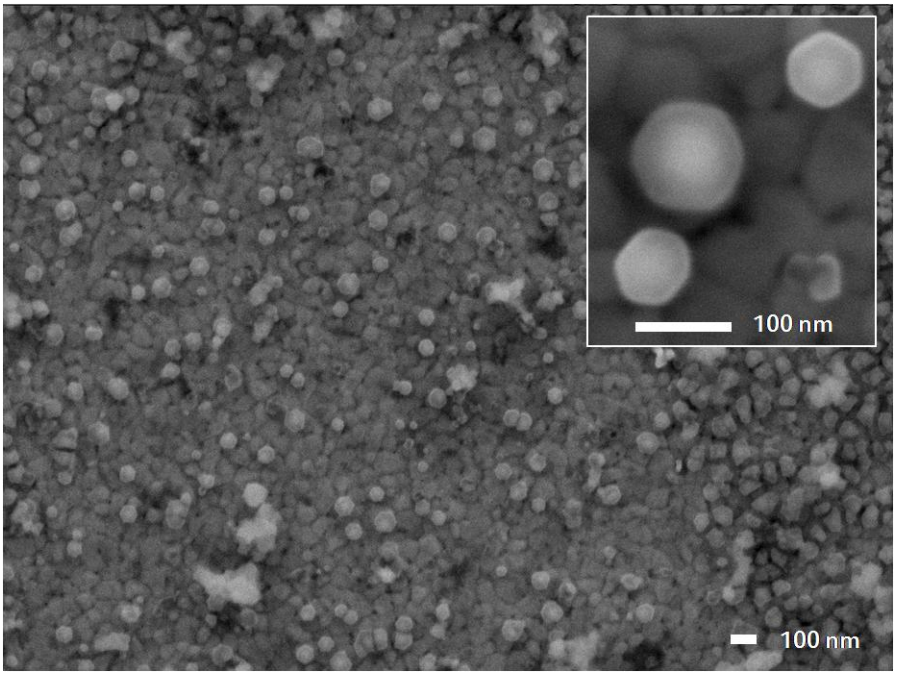

Figure 7.8: **Scanning electron micrographs of NH_2-MIL-88B crystals after an immersion time of 11d.**

The results presented on the direct growth of NH_2-MIL-88B show that the insertion of a functional group into the framework strongly influences the synthesis conditions for the bulk crystals and for the oriented growth on functionalized substrates. We have demonstrated that the extension of the observed structure- and orientation-directing behaviour of carboxylate-terminated SAMs for unfunctionalized MIL-88B is possible for the amino-functionalized analogs as well.

Synthesis of NH_2-MIL-88B

In a glass reactor, 1.00 g (5.52 mmol) of 2-amino-1,4-benzenedicarboxylic acid (99 %, *Aldrich*) were dissolved in 15 mL dimethylformamide (DMF) (p.a., *Acros Organics*). To the solution 2.784 g (11.04 mmol) of $FeCl_3 \cdot 6\ H_2O$ (p.a., *Merck*) was

added. The sealed-glass reactor was left for 1 day in a preheated oven at 150 °C. After cooling the synthesis mixture to room temperature, the crystalline product was filtrated and stored for further characterization.

Preparation of self-assembled monolayers on gold

The synthesis of the SAMs was performed as described in section 7.2.

Preparation of the crystallization solution for film growth of NH_2-MIL-88B on –COOH terminated SAMs

In a glass reactor, 0.25 g (1.4 mmol) of 2-amino-1,4-benzenedicarboxylic acid (99 %, *Aldrich*) were dissolved in 15 mL dimethylformamide (DMF) (p.a., *Acros Organics*). To the clear solution 0.696 g (2.5 mmol) $FeCl_3 \cdot 6\,H_2O$ (p.a., *Merck*) was added. The sealed-glass reactor was left for 2 days in a preheated oven at 150 °C. After cooling the synthesis mixture to room temperature, the crystalline product was filtrated and stored for further characterization. The filtered solution was used for the growth of thin films.

Film-Synthesis of NH_2-MIL-88B

The SAM-functionalized gold-slides were placed upside-down on Teflon®-supports into the filtrated synthesis solution of NH_2-MIL-88B (3 pieces in 15 mL). The growth step takes place at RT in a closed glass reactor. Immersion times were varied between 4 d and 11 d.

8 General conclusions

Within this thesis several aspects of the controlled direct growth of metal-organic frameworks on functionalized self-assembled monolayers were investigated.

It could be demonstrated that different molecular functionalities of the self-assembled monolayers induce different, well-defined orientations of HKUST-1 crystals. A model for explaining the still unknown mechanism of this remarkable effect could be developed, suggesting selective interactions of crystal building blocks in solution with the functionalized surfaces. The thermal pre-treatment of the synthesis solution induces a crystallization process which results in bulk HKUST-1 crystals and, presumably, in the existence of colloidal or molecular building blocks of $Cu_3(BTC)_2$ in the solution. Taking into account the copper-carboxylate-based paddle-wheel motif in the open framework structure, different coordination modes of the carboxylic or the alcoholic groups might control the selective nucleation/growth on the substrate, thus mimicking either axial (as with water) coordination with the alcohol terminus or chelating coordination (as with BTC) with the -COOH terminus of the SAM, respectively.

These results represent the first “proof of concept” that by mimicking characteristic structural features of metal-organic frameworks in the terminal group of self-assembled monolayers, it is possible to control the orientation of crystals during direct growth on functionalized gold surfaces.

This synthetic concept for oriented film growth gave us the opportunity to directly monitor successfully the growth processes of oriented HKUST-1 crystals grown on

self-assembled monolayers with the help of *in situ* atomic force microscopy. The development of a single growth step could be followed extensively, which has provided direct evidence for a layer-by-layer mechanism of a constituent 1.5 nm d_{111} crystal spacing step of HKUST-1, its shape during growth, and the influence of the step vertex on the rate of growth. This information helps to enhance current understanding of the crystal growth of MOF materials, will support the development of crystals of these materials of specific form for future application, and demonstrates clearly the potential of the unique platform of SAM-supported oriented crystals to provide further insights into the chemistry and structural evolution of coordination polymers.

A different aspect of the control on surface-grown MOFs could be demonstrated with the structure-directed and oriented growth of MIL-88B on carboxylate-terminated SAMs. The results suggest that structure direction is evoked through favourable symmetry relationships between the hexagonally ordered SAMs and the hexagonal structure of MIL-88B, which is competing with MIL-53, the product of homogeneous nucleation in the very same crystallisation solution. In agreement with our previous studies, the carboxylate functionality of the SAMs is proposed to mimic the carboxylate groups of the BDC molecules und thus to direct oriented growth on the surface.

The oriented crystals of the flexible framework structure of MIL-88B provide channels perpendicular to the surface, thus representing a promising model system for studies of the sorption properties of MOF crystals assembled as thin films. For this purpose a new sample cell was developed, which allowed us to follow the structural changes of flexible, porous materials during adsorption and desorption of guest molecules

("sorption@XRD"). Oriented Fe-MIL-88B crystals grown on SAM-functionalized gold substrates showed similar structural changes during sorption of water as randomly oriented bulk Fe-MIL-88B crystals. The sorption isotherms recorded with the help of the sorption@XRD method show two distinct steps of structural changes upon loading and unloading the channel system with water vapour, including two well-defined hystereses.

In the latest study, we have demonstrated that the advantages of molecular functionalization can also be realized in oriented film synthesis of MOFs: We have shown for the first time that amino-functionalized MOFs can be grown on SAMs and that a preferred orientation of the crystals is achieved. We envisage that by carrying out systematic investigations of the synthesis parameters such as described in this work, MOFs with different functionalities or entirely different functionalised MOFs could be grown with a preferred orientation. We anticipate that the ability to direct the growth of functionalized MOFs will be of particular interest in applications such as selective chemical sensors, where both the control of crystal growth orientation and functionalization of the organic linker to control host-guest interactions are advantageous.

The ability of functionalized molecular surfaces to act as crystallisation substrates has been demonstrated in this work and first studies on the properties of these systems have led to promising results. These investigations lay the foundation for future studies directed at the mechanism of oriented growth of MOF crystals, thus providing a powerful means to control structure and orientation in biomimetic materials systems. Furthermore, the selective adsorption and separation behaviour of the

resulting thin MOF films will be of interest for the development of selective chemical sensors and separation concepts.

9 References

[1] K. S. W. Sing, D. H. Everett, R. A. W. Haul, L. Moscou, R. A. Pierotti, J. Rouquerol, T. Siemieniewska, *Pure and Applied Chemistry* **1985**, *57*, 603.

[2] P. B. Venuto, E. T. Habib, Jr., *Chemical Industries, Vol. 1: Fluid Catalytic Cracking with Zeolite Catalysts*, **1979**.

[3] C. J. Adams, A. Araya, S. W. Carr, A. P. Chapple, K. R. Franklin, P. Graham, A. R. Minihan, T. J. Osinga, J. A. Stuart, *Studies in Surface Science and Catalysis* **1997**, *105B*, 1667.

[4] C. G. Coe, *Gas Separation Technology*, Elsevier, **1990**.

[5] A. F. Cronstedt, *Akad. Handl. Stockholm* **1756**, *18*, 120.

[6] C. S. Cundy, P. A. Cox, *Chemical Reviews* **2003**, *103*, 663.

[7] A. Corma, *Journal of Catalysis* **2003**, *216*, 298.

[8] F. Schueth, *Chemie in Unserer Zeit* **1995**, *29*, 42.

[9] A. Damour, *Ann. Mines.* **1840**, *17*, 191.

[10] H. Eichhorn, *Poggendorf Annual Review of Physical Chemistry* **1858**, *105*, 126.

[11] W. H. Taylor, *Zeitschrift fuer Kristallographie, Kristallgeometrie, Kristallphysik, Kristallchemie* **1930**, *74*, 1.

[12] L. Pauling, *Zeitschrift fuer Kristallographie, Kristallgeometrie, Kristallphysik, Kristallchemie* **1930**, *74*, 213.

[13] R. M. Barrer, *Journal of the Chemical Society* **1948**, 2158.

[14] R. M. Barrer, D. W. Riley, *Journal of the Chemical Society* **1948**, 133.

[15] R. M. Milton, in *Molecular sieve adsorbents, US 2882243*, **1959**.

[16] R. M. Barrer, D. W. Riley, *Journal of the Chemical Society* **1948**, 127.

[17] E. M. Flanigen, *Introduction to zeolite science and practice*, Elsevier, Amsterdam, **1991**.

[18] http://www.iza-online.org.

[19] S. T. Wilson, B. M. Lok, C. A. Messina, T. R. Cannan, E. M. Flanigen, *Journal of the American Chemical Society* **1982**, *104*, 1146.

[20] B. M. Lok, C. A. Messina, R. L. Patton, R. T. Gajek, T. R. Cannan, E. M. Flanigen, *Journal of the American Chemical Society* **1984**, *106*, 6092.

[21] M. Cavellec, D. Riou, C. Ninclaus, J.-M. Greneche, G. Ferey, *Zeolites* **1996**, *17*, 250.

[22] Q. Huang, M. Ulutagay, P. A. Michener, S.-J. Hwu, *Journal of the American Chemical Society* **1999**, *121*, 10323.

[23] A. I. Bortun, S. A. Khainakov, L. N. Bortun, D. M. Poojary, J. Rodriguez, J. R. Garcia, A. Clearfield, *Chemistry of Materials* **1997**, *9*, 1805.

[24] M. G. Nijkamp, J. E. M. J. Raaymakers, A. J. Van Dillen, K. P. De Jong, *Applied Physics A: Materials Science & Processing* **2001**, *72*, 619.

[25] V. B. Kazansky, V. Y. Borovkov, A. Serich, H. G. Karge, *Microporous and Mesoporous Materials* **1998**, *22*, 251.

[26] T. Dueren, L. Sarkisov, O. M. Yaghi, R. Q. Snurr, *Langmuir* **2004**, *20*, 2683.

[27] S. Mintova, S. Mo, T. Bein, *Chemistry of Materials* **2001**, *13*, 901.

[28] A. R. Pradhan, S. Uppili, J. Shailaja, J. Sivaguru, V. Ramamurthy, *Chemical Communications* **2002**, 596.

[29] A. Z. Ruiz, H. Li, G. Calzaferri, *Angewandte Chemie, International Edition* **2006**, *45*, 5282.

[30] M. Alvaro, E. Carbonell, P. Atienzar, H. Garcia, *ChemPhysChem* **2006**, *7*, 1996.

[31] M. Tather, A. Erdem-Senatalar, *Applied Thermal Engineering* **1999**, *19*, 1157.

[32] J. Jaenchen, D. Ackermann, H. Stach, W. Broesicke, *Solar Energy* **2004**, *76*, 339.

[33] H. Chiku, M. Matsui, S. Murakami, Y. Kiyozumi, F. Mizukami, K. Sakaguchi, *Analytical Biochemistry* **2003**, *318*, 80.

[34] G. Cerri, M. de' Gennaro, M. C. Bonferoni, C. Caramella, *Applied Clay Science* **2004**, *27*, 141.

[35] C. Platas-Iglesias, L. Vander Elst, W. Zhou, R. N. Muller, C. F. G. C. Geraldes, T. Maschmeyer, J. A. Peters, *Chemistry--A European Journal* **2002**, *8*, 5121.

[36] K. Kubo, M. Ichikawa, K. Yoshikawa, Y. Koyama, T. Niidome, T. Yamaoka, S.-I. M. Nomura, *Applied Physics Letters* **2003**, *83*, 2468.

[37] J. S. Beck, J. C. Vartuli, W. J. Roth, M. E. Leonowicz, C. T. Kresge, K. D. Schmitt, C. T. W. Chu, D. H. Olson, E. W. Sheppard, et al., *Journal of the American Chemical Society* **1992**, *114*, 10834.

[38] C. T. Kresge, M. E. Leonowicz, W. J. Roth, J. C. Vartuli, J. S. Beck, *Nature* **1992**, *359*, 710.

[39] M. G. Kanatzidis, *Advanced Materials* **2007**, *19*, 1165.

[40] O. M. Yaghi, G. Li, H. Li, *Nature* **1995**, *378*, 703.

[41] E. A. Tomic, *Journal of Applied Polymer Science* **1965**, *9*, 3745.

[42] S. Bauer, N. Stock, *Chemie in Unserer Zeit* **2008**, *42*, 12.

[43] S. Surble, C. Serre, C. Mellot-Draznieks, F. Millange, G. Ferey, *Chemical Communications* **2006**, 284.

[44] J. L. C. Rowsell, O. M. Yaghi, *Microporous and Mesoporous Materials* **2004**, *73*, 3.

[45] O. M. Yaghi, M. O'Keeffe, N. W. Ockwig, H. K. Chae, M. Eddaoudi, J. Kim, *Nature* **2003**, *423*, 705.

[46] H. Li, M. Eddaoudi, M. O'Keeffe, M. Yaghi, *Nature* **1999**, *402*, 276.

[47] M. Eddaoudi, J. Kim, N. Rosi, D. Vodak, J. Wachter, M. O'Keeffe, O. M. Yaghi, *Science* **2002**, *295*, 469.

[48] T. J. Barton, L. M. Bull, W. G. Klemperer, D. A. Loy, B. McEnaney, M. Misono, P. A. Monson, G. Pez, G. W. Scherer, J. C. Vartuli, O. M. Yaghi, *Chemistry of Materials* **1999**, *11*, 2633.

[49] A. K. Cheetham, G. Ferey, T. Loiseau, *Angewandte Chemie, International Edition* **1999**, *38*, 3268.

[50] N. W. Ockwig, O. Delgado-Friedrichs, M. O'Keeffe, O. M. Yaghi, *Accounts of Chemical Research* **2005**, *38*, 176.

[51] J. L. C. Rowsell, O. M. Yaghi, *Journal of the American Chemical Society* **2006**, *128*, 1304.

[52] J. Kim, B. Chen, T. M. Reineke, H. Li, M. Eddaoudi, D. B. Moler, M. O'Keeffe, O. M. Yaghi, *Journal of the American Chemical Society* **2001**, *123*, 8239.

[53] S. Kitagawa, R. Kitaura, S.-I. Noro, *Angewandte Chemie, International Edition* **2004**, *43*, 2334.

[54] S. R. Batten, R. Robson, *Angewandte Chemie, International Edition* **1998**, *37*, 1461.

[55] J. L. C. Rowsell, O. M. Yaghi, *Angewandte Chemie, International Edition* **2005**, *44*, 4670.

[56] P. M. Forster, N. Stock, A. K. Cheetham, *Angewandte Chemie, International Edition* **2005**, *44*, 7608.

[57] S. Bauer, N. Stock, *Angewandte Chemie, International Edition* **2007**, *46*, 6857.

[58] S. Bauer, C. Serre, T. Devic, P. Horcajada, J. Marrot, G. Ferey, N. Stock, *Inorganic Chemistry* **2008**, *47*, 7568.

[59] M. Plabst, T. Bein, *Inorganic Chemistry* **2009**, in press.

[60] C. Mellot-Draznieks, J. Dutour, G. Ferey, *Angewandte Chemie, International Edition* **2004**, *43*, 6290.

[61] S. Kitagawa, S.-i. Noro, T. Nakamura, *Chemical Communications* **2006**, 701.

[62] N. G. Pschirer, D. M. Ciurtin, M. D. Smith, U. H. F. Bunz, H.-C. zur Loye, *Angewandte Chemie, International Edition* **2002**, *41*, 583.

[63] Y. Cui, H. L. Ngo, W. Lin, *Chemical Communications* **2003**, 1388.

[64] Y. Cui, H. L. Ngo, P. S. White, W. Lin, *Chemical Communications* **2003**, 994.

[65] R.-G. Xiong, X.-Z. You, B. F. Abrahams, Z. Xue, C.-M. Che, *Angewandte Chemie, International Edition* **2001**, *40*, 4422.

[66] C.-D. Wu, A. Hu, L. Zhang, W. Lin, *Journal of the American Chemical Society* **2005**, *127*, 8940.

[67] U. Mueller, M. Schubert, F. Teich, H. Puetter, K. Schierle-Arndt, J. Pastre, *Journal of Materials Chemistry* **2006**, *16*, 626.

[68] R. Eberhardt, M. Allmendinger, M. Zintl, C. Troll, G. A. Luinstra, B. Rieger, *Macromolecular Chemistry and Physics* **2004**, *205*, 42.

[69] U. Mueller, G. Luinstra, O. M. Yaghi, (BASF Aktiengesellschaft, Germany; University of Michigan). Application: US, **2003**, p. 16 pp.

[70] J. S. Seo, D. Whang, H. Lee, S. I. Jun, J. Oh, Y. J. Jeon, K. Kim, *Nature* **2000**, *404*, 982.

[71] H. K. Chae, D. Y. Siberio-Perez, J. Kim, Y. B. Go, M. Eddaoudi, A. J. Matzger, M. O'Keeffe, O. M. Yaghi, *Nature* **2004**, *427*, 523.

[72] G. Ferey, C. Mellot-Draznieks, C. Serre, F. Millange, J. Dutour, S. Surble, I. Margiolaki, *Science* **2005**, *309*, 2040.

[73] Y. Kubota, M. Takata, R. Matsuda, R. Kitaura, S. Kitagawa, K. Kato, M. Sakata, T. C. Kobayashi, *Angewandte Chemie, International Edition* **2005**, *44*, 920.

[74] J. Perles, M. Iglesias, M.-A. Martin-Luengo, M. A. Monge, C. Ruiz-Valero, N. Snejko, *Chemistry of Materials* **2005**, *17*, 5837.

[75] Q. Yang, C. Zhong, *Journal of Physical Chemistry B* **2005**, *109*, 11862.

[76] P. Krawiec, M. Kramer, M. Sabo, R. Kunschke, H. Froede, S. Kaskel, *Advanced Engineering Materials* **2006**, *8*, 293.

[77] M. Latroche, S. Suble, C. Serre, C. Mellot-Draznieks, P. L. Llewellyn, J.-H. Lee, J.-S. Chang, S. H. Jhung, G. Ferey, *Angewandte Chemie, International Edition* **2006**, *45*, 8227.

[78] B. Panella, M. Hirscher, H. Puetter, U. Mueller, *Advanced Functional Materials* **2006**, *16*, 520.

[79] S. Surble, F. Millange, C. Serre, T. Dueren, M. Latroche, S. Bourrelly, P. L. Llewellyn, G. Ferey, *Journal of the American Chemical Society* **2006**, *128*, 14889.

[80] J. L. Belof, A. C. Stern, M. Eddaoudi, B. Space, *Journal of the American Chemical Society* **2007**, *129*, 15202.

[81] D. J. Collins, H.-C. Zhou, *Journal of Materials Chemistry* **2007**, *17*, 3154.

[82] S. S. Han, W.-Q. Deng, W. A. Goddard, III, *Angewandte Chemie, International Edition* **2007**, *46*, 6289.

[83] S. S. Han, W. A. Goddard, III, *Journal of the American Chemical Society* **2007**, *129*, 8422.

[84] Y. Liu, J. F. Eubank, A. J. Cairns, J. Eckert, V. C. Kravtsov, R. Luebke, M. Eddaoudi, *Angewandte Chemie, International Edition* **2007**, *46*, 3278.

[85] H. J. Choi, M. Dinca, J. R. Long, *Journal of the American Chemical Society* **2008**, *130*, 7848.

[86] Y. Li, R. T. Yang, *AIChE Journal* **2008**, *54*, 269.

[87] K. Seki, W. Mori, *Journal of Physical Chemistry B* **2002**, *106*, 1380.

[88] G. Ferey, M. Latroche, C. Serre, F. Millange, T. Loiseau, A. Percheron-Guegan, *Chemical Communications* **2003**, 2976.

[89] D. N. Dybtsev, H. Chun, S. H. Yoon, D. Kim, K. Kim, *Journal of the American Chemical Society* **2004**, *126*, 32.

[90] R. Matsuda, R. Kitaura, S. Kitagawa, Y. Kubota, R. V. Belosludov, T. C. Kobayashi, H. Sakamoto, T. Chiba, M. Takata, Y. Kawazoe, Y. Mita, *Nature* **2005**, *436*, 238.

[91] E.-Y. Choi, K. Park, C.-M. Yang, H. Kim, J.-H. Son, S. W. Lee, Y. H. Lee, D. Min, Y.-U. Kwon, *Chemistry--A European Journal* **2004**, *10*, 5535.

[92] A. P. Cote, A. I. Benin, N. W. Ockwig, M. O'Keeffe, A. J. Matzger, O. M. Yaghi, *Science* **2005**, *310*, 1166.

[93] M. Mastalerz, *Angewandte Chemie, International Edition* **2008**, *47*, 445.

[94] A. P. Cote, H. M. El-Kaderi, H. Furukawa, J. R. Hunt, O. M. Yaghi, *Journal of the American Chemical Society* **2007**, *129*, 12914.

[95] R. W. Tilford, W. R. Gemmill, H.-C. zur Loye, J. J. Lavigne, *Chemistry of Materials* **2006**, *18*, 5296.

[96] H. M. El-Kaderi, J. R. Hunt, J. L. Mendoza-Cortes, A. P. Cote, R. E. Taylor, M. O'Keeffe, O. M. Yaghi, *Science* **2007**, *316*, 268.

[97] H. M. El-Kaderi, O. M. Yaghi, *Abstracts of Papers, 233rd ACS National Meeting, Chicago, IL, United States, March 25-29, 2007* **2007**, INOR.

[98] H. Furukawa, H. M. El-Kaderi, K. S. Park, J. R. Hunt, J. L. Mendoza-Cortes, A. P. Cote, O. M. Yaghi, *Abstracts of Papers, 233rd ACS National Meeting, Chicago, IL, United States, March 25-29, 2007* **2007**, INOR.

[99] S. S. Han, H. Furukawa, O. M. Yaghi, W. A. Goddard, III, *Journal of the American Chemical Society* **2008**, *130*, 11580.

[100] E. Klontzas, E. Tylianakis, G. E. Froudakis, *Journal of Physical Chemistry C* **2008**, *112*, 9095.

[101] R. W. Tilford, S. J. Mugavero, III, P. J. Pellechia, J. J. Lavigne, *Advanced Materials* **2008**, *20*, 2741.

[102] G. E. Poirier, E. D. Pylant, *Science* **1996**, *272*, 1145.

[103] L. H. Dubois, B. R. Zegarski, R. G. Nuzzo, *Journal of Chemical Physics* **1993**, *98*, 678.

[104] R. G. Nuzzo, D. L. Allara, *Journal of the American Chemical Society* **1983**, *105*, 4481.

[105] M. D. Porter, T. B. Bright, D. L. Allara, C. E. D. Chidsey, *Journal of the American Chemical Society* **1987**, *109*, 3559.

[106] L. H. Dubois, R. G. Nuzzo, *Annual Review of Physical Chemistry* **1992**, *43*, 437.

[107] C. D. Bain, G. M. Whitesides, *Journal of the American Chemical Society* **1988**, *110*, 3665.

[108] C. D. Bain, G. M. Whitesides, *Science* **1988**, *240*, 62.

[109] C. D. Bain, J. Evall, G. M. Whitesides, *Journal of the American Chemical Society* **1989**, *111*, 7155.

[110] C. D. Bain, E. B. Troughton, Y. T. Tao, J. Evall, G. M. Whitesides, R. G. Nuzzo, *Journal of the American Chemical Society* **1989**, *111*, 321.

[111] C. D. Bain, G. M. Whitesides, *Journal of the American Chemical Society* **1989**, *111*, 7164.

[112] P. E. Laibinis, G. M. Whitesides, D. L. Allara, Y. T. Tao, A. N. Parikh, R. G. Nuzzo, *Journal of the American Chemical Society* **1991**, *113*, 7152.

[113] P. E. Laibinis, G. M. Whitesides, *Journal of the American Chemical Society* **1992**, *114*, 1990.

[114] J. C. Love, L. A. Estroff, J. K. Kriebel, R. G. Nuzzo, G. M. Whitesides, *Chemical Reviews* **2005**, *105*, 1103.

[115] J. Kang, P. A. Rowntree, *Langmuir* **2007**, *23*, 509.

[116] N. G. Semaltianos, E. G. Wilson, *Thin Solid Films* **2000**, *366*, 111.

[117] M. Wanunu, A. Vaskevich, I. Rubinstein, *Journal of the American Chemical Society* **2004**, *126*, 5569.

[118] G. M. Whitesides, P. E. Laibinis, *Langmuir* **1990**, *6*, 87.

[119] A. Ulman, *Chemical Reviews* **1996**, *96*, 1533.

[120] F. Schreiber, *Progress in Surface Science* **2000**, *65*, 151.

[121] M. Kind, C. Woell, *Chemie in Unserer Zeit* **2008**, *42*, 128.

[122] D. L. Allara, R. G. Nuzzo, *Langmuir* **1985**, *1*, 52.

[123] D. Roy, J. Fendler, *Advanced Materials* **2004**, *16*, 479.

[124] A.-S. Duwez, *Journal of Electron Spectroscopy and Related Phenomena* **2004**, *134*, 97.

[125] G. E. Poirier, *Chemical Reviews* **1997**, *97*, 1117.

[126] S. M. Mendoza, I. Arfaoui, S. Zanarini, F. Paolucci, P. Rudolf, *Langmuir* **2007**, *23*, 582.

[127] G. E. Poirier, *Langmuir* **1997**, *13*, 2019.

[128] N. Camillone, III, C. E. D. Chidsey, G. Y. Liu, G. Scoles, *Journal of Chemical Physics* **1993**, *98*, 3503.

[129] R. Arnold, W. Azzam, A. Terfort, C. Woell, *Langmuir* **2002**, *18*, 3980.

[130] A. Y. Lee, A. Ulman, A. S. Myerson, *Langmuir* **2002**, *18*, 5886.

[131] Y. Xia, X.-M. Zhao, G. M. Whitesides, *Microelectronic Engineering* **1996**, *32*, 255.

[132] A. M. Rawlett, T. J. Hopson, I. Amlani, R. Zhang, J. Tresek, L. A. Nagahara, R. K. Tsui, H. Goronkin, *Nanotechnology* **2003**, *14*, 377.

[133] K. K. Berggren, A. Bard, J. L. Wilbur, J. D. Gillaspy, A. G. Helg, J. J. McClelland, S. L. Rolston, W. D. Phillips, M. Prentiss, et al., *Science* **1995**, *269*, 1255.

[134] C. E. D. Chidsey, R. W. Murray, *Science* **1986**, *231*, 25.

[135] S. Mann, *Nature* **1993**, *365*, 499.

[136] L. Addadi, S. Weiner, *Angewandte Chemie* **1992**, *104*, 159.

[137] H. A. Lowenstam, S. Weiner, *On Biomineralization*, Oxford Univ. Press, New York, **1989**.

[138] D. Braga, *Angewandte Chemie, International Edition* **2003**, *42*, 5544.

[139] E. Dujardin, S. Mann, *Advanced Engineering Materials* **2002**, *4*, 461.

[140] S. Weiner, L. Addadi, *Journal of Materials Chemistry* **1997**, *7*, 689.

[141] J. Aizenberg, *Advanced Materials* **2004**, *16*, 1295.

[142] B. C. Bunker, P. C. Rieke, B. J. Tarasevich, A. A. Campbell, G. E. Fryxell, G. L. Graff, L. Song, J. Liu, J. W. Virden, G. L. McVay, *Science* **1994**, *264*, 48.

[143] J. Aizenberg, A. J. Black, G. M. Whitesides, *Journal of the American Chemical Society* **1999**, *121*, 4500.

[144] F. C. Meldrum, J. Flath, W. Knoll, *Langmuir* **1997**, *13*, 2033.

[145] J. W. P. Hsu, W. M. Clift, L. N. Brewer, *Langmuir* **2008**, *24*, 5375.

[146] J. W. P. Hsu, Z. R. Tian, N. C. Simmons, C. M. Matzke, J. A. Voigt, J. Liu, *Nano Letters* **2005**, *5*, 83.

[147] D. Wang, J. Liu, Q. Huo, Z. Nie, W. Lu, R. E. Williford, Y.-B. Jiang, *Journal of the American Chemical Society* **2006**, *128*, 13670.

[148] S. Feng, T. Bein, *Nature* **1994**, *368*, 834.

[149] S. Feng, T. Bein, *Science* **1994**, *265*, 1839.

[150] Y. Lee, W. Ryu, S. S. Kim, Y. Shul, J. H. Je, G. Cho, *Langmuir* **2005**, *21*, 5651.

[151] S. Hermes, F. Schroeder, R. Chelmowski, C. Woell, R. A. Fischer, *Journal of the American Chemical Society* **2005**, *127*, 13744.

[152] S. Hermes, D. Zacher, A. Baunemann, C. Woell, R. A. Fischer, *Chemistry of Materials* **2007**, *19*, 2168.

[153] D. Zacher, A. Baunemann, S. Hermes, R. A. Fischer, *Journal of Materials Chemistry* **2007**, *17*, 2785.

[154] O. Shekhah, H. Wang, S. Kowarik, F. Schreiber, M. Paulus, M. Tolan, C. Sternemann, F. Evers, D. Zacher, R. A. Fischer, C. Woell, *Journal of the American Chemical Society* **2007**, *129*, 15118.

[155] O. Shekhah, H. Wang, T. Strunskus, P. Cyganik, D. Zacher, R. Fischer, C. Woell, *Langmuir* **2007**, *23*, 7440.

[156] C. Munuera, O. Shekhah, H. Wang, C. Woell, C. Ocal, *Physical Chemistry Chemical Physics* **2008**, *10*, 7257.

[157] M. Kubo, W. Chaikittisilp, T. Okubo, *Chemistry of Materials* **2008**, *20*, 2887.

[158] M. Kondo, T. Okubo, A. Asami, S.-I. Noro, T. Yoshitomi, S. Kitagawa, T. Ishii, H. Matsuzaka, K. Seki, *Angewandte Chemie, International Edition* **1999**, *38*, 140.

[159] M. D. Allendorf, R. J. T. Houk, L. Andruszkiewicz, A. A. Talin, J. Pikarsky, A. Choudhury, K. A. Gall, P. J. Hesketh, *Journal of the American Chemical Society* **2008**, *130*, 14404.

[160] K. Szelagowska-Kunstman, P. Cyganik, M. Goryl, D. Zacher, Z. Puterova, R. A. Fischer, M. Szymonski, *Journal of the American Chemical Society* **2008**, *130*, 14446.

[161] M. F. Toney, *Encyclopedia of materials characterization - Surfaces, Interfaces, Thin Films; XRD - X-Ray Diffraction*, Manning Publications, Greenwich, **1992**.

[162] J. B. Bindell, *Encyclopedia of materials characterization - Surfaces, Interfaces, Thin Films; SEM - Scanning Electron Microscopy*, Manning Publications, Greenwich, **1992**.

[163] K. E. Sickafus, *Encyclopedia of materials characterization - Surfaces, Interfaces, Thin Films; TEM - Transmission Electron Microscopy*, Manning Publications, Greenwich, **1992**.

[164] G. Binnig, H. Rohrer, *Reviews of Modern Physics* **1987**, *59*, 615.

[165] G. Binning, H. Rohrer, C. Gerber, E. Weibel, *Physical Review Letters* **1982**, *49*, 57.

[166] G. Binnig, C. Gerber, E. Stoll, T. R. Albrecht, C. F. Quate, *Surface Science* **1987**, *189-190*, 1.

[167] Y. Martin, C. C. Williams, H. K. Wickramasinghe, *Journal of Applied Physics* **1987**, *61*, 4723.

[168] J. N. Cox, *Encyclopedia of materials characterization - Surfaces, Interfaces, Thin Films; FTIR - Fourier Transform Infrared Spectroscopy*, Manning Publications, Greenwich, **1992**.

[169] W. B. White, *Encyclopedia of materials characterization - Surfaces, Interfaces, Thin Films; Raman Spectroscopy*, Manning Publications, Greenwich, **1992**.

[170] M. Trenary, *Annual Review of Physical Chemistry* **2000**, 381.

[171] J. B. Condon, *Surface Area and Porosity Determinations by Physisorption Measurements and Theory*, Elsevier, Amsterdam, **2006**.

[172] F. Rouquerol, J. Rouquerol, K. Sing, *Adsorption by Powders & Porous Solids - Principles, Methodology and Application*, Academic Press, San Diego, **1999**.

[173] A. W. Adamson, A. P. Gast, *Physical Chemistry of Surfaces*, John Wiley & Sons, New York, **1997**.

[174] K. S. Walton, R. Q. Snurr, *Journal of the American Chemical Society* **2007**, *129*, 8552.

[175] G. Sauerbrey, *Zeitschrift fuer Physik* **1959**, *155*, 206.

[176] E. Biemmi, C. Scherb, T. Bein, *Journal of the American Chemical Society* **2007**, *129*, 8054.

[177] J. S. Lee, Y.-J. Lee, E. L. Tae, Y. S. Park, K. B. Yoon, *Science* **2003**, *301*, 818.

[178] S. S. Y. Chui, S. M. F. Lo, J. P. H. Charmant, A. G. Orpen, I. D. Williams, *Science* **1999**, *283*, 1148.

[179] K. Schlichte, T. Kratzke, S. Kaskel, *Microporous and Mesoporous Materials* **2004**, *73*, 81.

[180] L. Alaerts, E. Seguin, H. Poelman, F. Thibault-Starzyk, P. A. Jacobs, D. E. De Vos, *Chemistry--A European Journal* **2006**, *12*, 7353.

[181] J. Lee, J. Li, J. Jagiello, *Journal of Solid State Chemistry* **2005**, *178*, 2527.

[182] A. Vishnyakov, P. I. Ravikovitch, A. V. Neimark, M. Buelow, Q. M. Wang, *Nano Letters* **2003**, *3*, 713.

[183] C. Prestipino, L. Regli, J. G. Vitillo, F. Bonino, A. Damin, C. Lamberti, A. Zecchina, P. L. Solari, K. O. Kongshaug, S. Bordiga, *Chemistry of Materials* **2006**, *18*, 1337.

[184] Q. M. Wang, D. Shen, M. Bulow, M. L. Lau, S. Deng, F. R. Fitch, N. O. Lemcoff, J. Semanscin, *Microporous and Mesoporous Materials* **2002**, *55*, 217.

[185] H. Wang, S. Chen, L. Li, S. Jiang, *Langmuir* **2005**, *21*, 2633.

[186] G. Ferey, *Chemical Society Reviews* **2008**, *37*, 191.

[187] M. W. Anderson, J. R. Agger, L. I. Meza, C. B. Chong, C. S. Cundy, *Faraday Discussions* **2007**, *136*, 143.

[188] S. Yamamoto, S. Sugiyama, O. Matsuoka, K. Kohmura, T. Honda, Y. Banno, H. Nozoye, *Journal of Physical Chemistry* **1996**, *100*, 18474.

[189] L. I. Meza, M. W. Anderson, J. R. Agger, *Chemical Communications* **2007**, 2473.

[190] R. Brent, M. W. Anderson, *Angewandte Chemie, International Edition* **2008**, *47*, 5327.

[191] L. Carlucci, G. Ciani, M. Moret, D. M. Proserpio, S. Rizzato, *Angewandte Chemie, International Edition* **2000**, *39*, 1506.

[192] M. Shoaee, J. R. Agger, M. W. Anderson, M. P. Attfield, *Crystal Engineering Communications* **2008**, *10*, 646.

[193] M. Shoaee, M. W. Anderson, M. P. Attfield, *Angewandte Chemie, International Edition* **2008**, *47*, 8525.

[194] R. E. Sours, A. Z. Zellelow, J. A. Swift, *Journal of Physical Chemistry B* **2005**, *109*, 9989.

[195] S. R. Qiu, A. Wierzbicki, C. A. Orme, A. M. Cody, J. R. Hoyer, G. H. Nancollas, S. Zepeda, J. J. De Yoreo, *Proceedings of the National Academy of Sciences of the United States of America* **2004**, *101*, 1811.

[196] K. Wang, D. Sun, J. Zhang, W. Yu, H. Liu, X. Hu, S. Guo, Y. Geng, *Journal of Crystal Growth* **2004**, *261*, 63.

[197] H. H. Teng, P. M. Dove, J. J. De Yoreo, *Geochimica et Cosmochimica Acta* **2000**, *64*, 2255.

[198] B. Xiao, P. S. Wheatley, X. Zhao, A. J. Fletcher, S. Fox, A. G. Rossi, I. L. Megson, S. Bordiga, L. Regli, K. M. Thomas, R. E. Morris, *Journal of the American Chemical Society* **2007**, *129*, 1203.

[199] M. Volmer, *Kinetic der Phasenbildung*, Leipzig, **1939**.

[200] J. W. Mullin, *Crystallization*, Butterworth Heinemann, Oxford, **2001**.

[201] A. M. Walker, B. Slater, *Crystal Engineering Communications* **2008**, *10*, 790.

[202] O. Lehmann, *Molekularphysik*, Leipzig, **1888/1889**.

[203] T. Michely, J. Krug, *Islands, Mounds, and Atoms, Patterns and Processes in Crystal Growth Far from Equilibrium*, Springer, Berlin, Heidelberg, **2004**.

[204] Z. Berkovitch-Yellin, *Journal of the American Chemical Society* **1985**, *107*, 8239.

[205] C. Scherb, A. Schoedel, T. Bein, *Angewandte Chemie, International Edition* **2008**, *47*, 5777.

[206] L. Addadi, S. Raz, S. Weiner, *Advanced Materials* **2003**, *15*, 959.

[207] A. K. Cheetham, C. N. R. Rao, R. K. Feller, *Chemical Communications* **2006**, 4780.

[208] T. Loiseau, C. Serre, C. Huguenard, G. Fink, F. Taulelle, M. Henry, T. Bataille, G. Ferey, *Chemistry—A European Journal* **2004**, *10*, 1373.

[209] C. Mellot-Draznieks, C. Serre, S. Surble, N. Audebrand, G. Ferey, *Journal of the American Chemical Society* **2005**, *127*, 16273.

[210] T. R. Whitfield, X. Wang, L. Liu, A. J. Jacobson, *Solid State Sciences* **2005**, *7*, 1096.

[211] F. Millange, C. Serre, G. Ferey, *Chemical Communications* **2002**, 822.

[212] P. Horcajada, C. Serre, M. Sebban, F. Taulelle, M. Vallet-Regi, G. Ferey, *Abstracts of Papers, 235th ACS National Meeting, New Orleans, LA, United States, April 6-10, 2008* **2008**, INOR.

[213] C. Mellot-Draznieks, S. Girard, G. Ferey, J. C. Schon, Z. Cancarevic, M. Jansen, *Chemistry--A European Journal* **2002**, *8*, 4102.

[214] C. Mellot-Draznieks, G. Ferey, *Progress in Solid State Chemistry* **2006**, *33*, 187.

[215] C. Mellot Draznieks, J. M. Newsam, A. M. Gorman, C. M. Freeman, G. Férey, *Vol. 39*, **2000**, pp. 2270.

[216] C. Mellot-Draznieks, S. Girard, G. Ferey, *Journal of the American Chemical Society* **2002**, *124*, 15326.

[217] S. Girard, J. D. Gale, C. Mellot-Draznieks, G. Ferey, *Studies in Surface Science and Catalysis* **2001**, *135*, 2763.

[218] F. Millange, N. Guillou, R. I. Walton, J.-M. Greneche, I. Margiolaki, G. Ferey, *Chemical Communications* **2008**, 4732.

[219] P. L. Llewellyn, G. Maurin, T. Devic, S. Loera-Serna, N. Rosenbach, C. Serre, S. Bourrelly, P. Horcajada, Y. Filinchuk, G. Ferey, *Journal of the American Chemical Society* **2008**, *130*, 12808.

[220] Y. Liu, J.-H. Her, A. Dailly, A. J. Ramirez-Cuesta, D. A. Neumann, C. M. Brown, *Journal of the American Chemical Society* **2008**, *130*, 11813.

[221] D. S. Coombes, R. G. Bell, C. Mellot-Draznicks, N. A. Ramasahye, G. Maurin, *Studies in Surface Science and Catalysis* **2007**, *170A*, 918.

[222] C. Serre, C. Mellot-Draznieks, S. Surble, N. Audebrand, Y. Filinchuk, G. Ferey, *Science* **2007**, *315*, 1828.

[223] O. I. Lebedev, F. Millange, C. Serre, G. Van Tendeloo, G. Ferey, *Chemistry of Materials* **2005**, *17*, 6525.

[224] M. O'Keeffe, *Materials Research Bulletin* **2006**, *41*, 911.

[225] F. Salles, H. Jobic, G. Maurin, M. M. Koza, P. L. Llewellyn, T. Devic, C. Serre, G. Ferey, *Physical Review Letters* **2008**, *100*, 245901/1.

[226] N. Rosenbach, Jr., H. Jobic, A. Ghoufi, F. Salles, G. Maurin, S. Bourrelly, L. Llewellyn Philip, T. Devic, C. Serre, G. Ferey, *Angewandte Chemie, International Edition* **2008**, *47*, 6611.

[227] N. A. Ramsahye, G. Maurin, S. Bourrelly, P. L. Llewellyn, C. Serre, T. Loiseau, T. Devic, G. Ferey, *Journal of Physical Chemistry C* **2008**, *112*, 514.

[228] B. Panella, K. Hoenes, U. Mueller, N. Trukhan, M. Schubert, H. Puetter, M. Hirscher, *Angewandte Chemie, International Edition* **2008**, *47*, 2138.

[229] F.-X. Coudert, M. Jeffroy, A. H. Fuchs, A. Boutin, C. Mellot-Draznieks, *Journal of the American Chemical Society* **2008**, *130*, 14294.

[230] C. M. Brown, Y. Liu, J.-H. Her, A. Dailly, D. A. Neumann, A. J. Ramirez-Cuesta, *Abstracts of Papers, 236th ACS National Meeting, Philadelphia, PA, United States, August 17-21, 2008* **2008**, FUEL.

[231] A. Vimont, A. Travert, P. Bazin, J.-C. Lavalley, M. Daturi, C. Serre, G. Ferey, S. Bourrelly, P. L. Llewellyn, *Chemical Communications* **2007**, 3291.

[232] M. Schindler, S. Ernst, *DGMK Tagungsbericht* **2007**, *2007-2*, 221.

[233] N. A. Ramsahye, G. Maurin, S. Bourrelly, P. L. Llewellyn, T. Devic, C. Serre, T. Loiseau, G. Ferey, *Adsorption* **2007**, *13*, 461.

[234] N. A. Ramsahye, G. Maurin, S. Bourrelly, P. Llewellyn, T. Loiseau, G. Ferey, *Physical Chemistry Chemical Physics* **2007**, *9*, 1059.

[235] Y.-Y. Liu, J.-L. Zeng, J. Zhang, F. Xu, L.-X. Sun, *International Journal of Hydrogen Energy* **2007**, *32*, 4005.

[236] P. L. Llewellyn, S. Bourrrelly, C. Serre, Y. Filinchuk, G. Ferey, *Angewandte Chemie, International Edition* **2006**, *45*, 7751.

[237] S. Bourrelly, P. L. Llewellyn, C. Serre, F. Millange, T. Loiseau, G. Ferey, *Journal of the American Chemical Society* **2005**, *127*, 13519.

[238] S. H. Jhung, J.-H. Lee, J. W. Yoon, C. Serre, G. Ferey, J.-S. Chang, *Advanced Materials* **2007**, *19*, 121.

[239] P. L. Llewellyn, S. Bourrelly, C. Serre, A. Vimont, M. Daturi, L. Hamon, G. De Weireld, J.-S. Chang, D.-Y. Hong, Y. K. Hwang, S. H. Jhung, G. Ferey, *Langmuir* **2008**, *24*, 7245.

[240] G. Pirngruber, E. Jolimaitre, L. Wolff, D. Leinekugel le Coq, (IFP, Fr.). Application: WO, **2008**, p. 30pp.

[241] I. Senkovska, S. Kaskel, *Microporous and Mesoporous Materials* **2008**, *112*, 108.

[242] F. Millange, G. Ferey, M. Morcrette, C. Serre, M. L. Doublet, J. M. Greneche, J. M. Tarascon, *Studies in Surface Science and Catalysis* **2007**, *170B*, 2037.

[243] Y. K. Hwang, D.-Y. Hong, J.-S. Chang, S. H. Jhung, Y.-K. Seo, J. Kim, A. Vimont, M. Daturi, C. Serre, G. Ferey, *Angewandte Chemie, International Edition* **2008**, *47*, 4144.

[244] N. V. Maksimchuk, M. N. Timofeeva, M. S. Melgunov, A. N. Shmakov, Y. A. Chesalov, D. N. Dybtsev, V. P. Fedin, O. A. Kholdeeva, *Journal of Catalysis* **2008**, *257*, 315.

[245] P. Horcajada, C. Serre, M. Vallet-Regi, M. Sebban, F. Taulelle, G. Ferey, *Angewandte Chemie, International Edition* **2006**, *45*, 5974.

[246] P. Horcajada, C. Serre, G. Maurin, A. Ramsahye Naseem, F. Balas, M. Vallet-Regi, M. Sebban, F. Taulelle, G. Ferey, *Journal of the American Chemical Society* **2008**, *130*, 6774.

[247] C. Serre, F. Millange, S. Surble, G. Ferey, *Angewandte Chemie, International Edition* **2004**, *43*, 6286.

[248] J. Li, K. S. Liang, G. Scoles, A. Ulman, *Langmuir* **1995**, *11*, 4418.

[249] G. Socrates, *Infrared and Raman Characteristic Group Frequencies - Tables and Charts*, Third ed., John Wiley & Sons, Ltd., New York, **2005**.

[250] D. Zacher, O. Shekhah, C. Woll, R. A. Fischer*, Vol. 38*, **2009**, pp. 1418.

[251] S. Kitagawa, K. Uemura, *Chemical Society Reviews* **2005**, *34*, 109.

[252] C. Serre, S. Bourrelly, A. Vimont, N. A. Ramsahye, G. Maurin, P. L. Llewellyn, M. Daturi, Y. Filinchuk, O. Leynaud, P. Barnes, G. Ferey, *Advanced Materials* **2007**, *19*, 2246.

[253] G. Ferey, C. Serre*, Vol. 38*, **2009**, pp. 1380.

[254] Bronkhorst, in *http://www.fluidat.com*.

[255] D. Lide, *Handbook of Chemistry and Physics*, CRC Press, **2004-2005**.

[256] A. Darga, Ludwig-Maximilians-Universität (München), **2008**.

[257] DMSNT, Scintag, Inc.

[258] Y.-F. Song, L. Cronin, *Angewandte Chemie, International Edition* **2008**, *47*, 4635.

[259] A. D. Burrows, C. Frost, M. F. Mahon, C. Richardson, *Angewandte Chemie, International Edition* **2008**, *47*, 8482.

[260] Z. Wang, S. M. Cohen, *Angewandte Chemie, International Edition* **2008**, *47*, 4699.

[261] Z. Wang, S. M. Cohen, *Journal of the American Chemical Society* **2007**, *129*, 12368.

[262] K. K. Tanabe, Z. Wang, S. M. Cohen, *Journal of the American Chemical Society* **2008**, *130*, 8508.

[263] J. S. Costa, P. Gamez, C. A. Black, O. Roubeau, S. J. Teat, J. Reedijk, *European Journal of Inorganic Chemistry* **2008**, 1551.

[264] M. J. Ingleson, J. P. Barrio, J.-B. Guilbaud, Y. Z. Khimyak, M. J. Rosseinsky, *Chemical Communications* **2008**, 2680.

10 Appendix:

10.1 List of abbreviations

2D	two dimensional
3D	three dimensional
AASBU	Automated assembly of secondary building units
AFM	Atomic Force Microscopy
BDC	1,4-Benzenedicarboxylic acid
BET	Brunauer, Emmett, Teller
BTC	1,3,5-Benzenetricarboxylic acid
CEM	Controlled evaporation mixer
COF	Covalent organic framework
CPL-1	Coordination polymer with pillared layer structure, number 1
CRT	Cathode ray tube
DFT	Density functional theory
DMF	N,N-Dimethylformamide
DSC	Differential scanning calorimetry
FC	Flow controller
FT	Fourier transformation

HKUST-1	Hong-Kong University structure 1
ID	Identification number
IR	Infrared
IRMOF	Isoreticular metal-organic framework
IUPAC	International Union of Pure and Applied Chemistry
μCP	Micro-Contact printing
MFC	Mass flow controller
MFM	Magnetic Force Microscopy
MHD	16-Mercaptohexadecanol
MHDA	16-Mercaptohexadecanoic acid
MIL	Matériaux de l'Institut Lavoisier
MOF	Metal-organic framework
MS	Microsoft
MUD	11-Mercaptoundecanol
QCM	Quartz-crystal microbalance
RAIRS	Reflection-Adsorption IR spectroscopy
RT	Room temperature
SAM	Self-assembled monolayer
SBU	Secondary building unit
SEM	Scanning electron microscopy
SPM	Scanning probe microscopy

STM	Scanning tunnelling microscopy
TEM	Transmission electron microscopy
TGA	Thermogravimetric analysis
XRD	X-ray diffraction

10.2 Synthesis and Characterization of Fe-MIL-101

During the optimization of the synthesis pathway for MIL-88B films Fe-MIL-101 was also synthesized and characterized. The results will be presented in the following section.

Synthesis of Fe-MIL-101

In a glass reactor, 15.6 mg (0.094 mmol) of 1,4-benzenedicarboxylic acid (98 %, *Aldrich*) were dissolved in 10 mL dimethylformamide (DMF) (p.a., *Acros Organics*). To the mixture 16.9 mg (0.063 mmol) $FeCl_3 \cdot 6\ H_2O$ (p.a., *Merck*) was added. The sealed-glass reactor was left for 2 days in a preheated oven at 150 °C. The orange crystals were filtered, washed with DMF and dried under nitrogen before further characterization.

Characterization of Fe-MIL-101

The synthesis was carried out as described in the experimental section of this chapter (section 5.2). The XRD pattern of the synthesized Fe-MIL-101 compared to the simulated pattern of Cr-MIL-101 crystals is shown in Figure 10.1. The reflection positions are in very good agreement, the intensities, however, vary strongly. This deviation is attributed to the different metal ions in the two products. The first reflection at 1.7 ° two theta was cut off by the beam stop of the diffractometer.

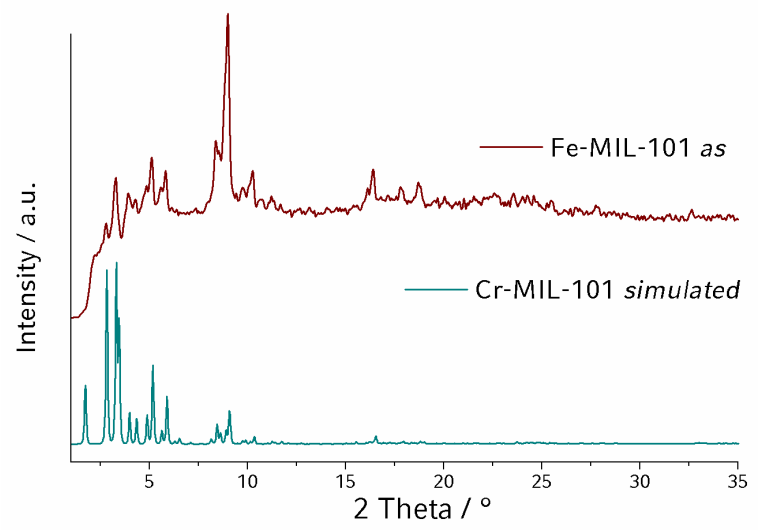

Figure 10.1: **Comparison of the XRD pattern of bulk Fe-MIL-101 crystals to the simulated pattern of Cr-MIL-101.**

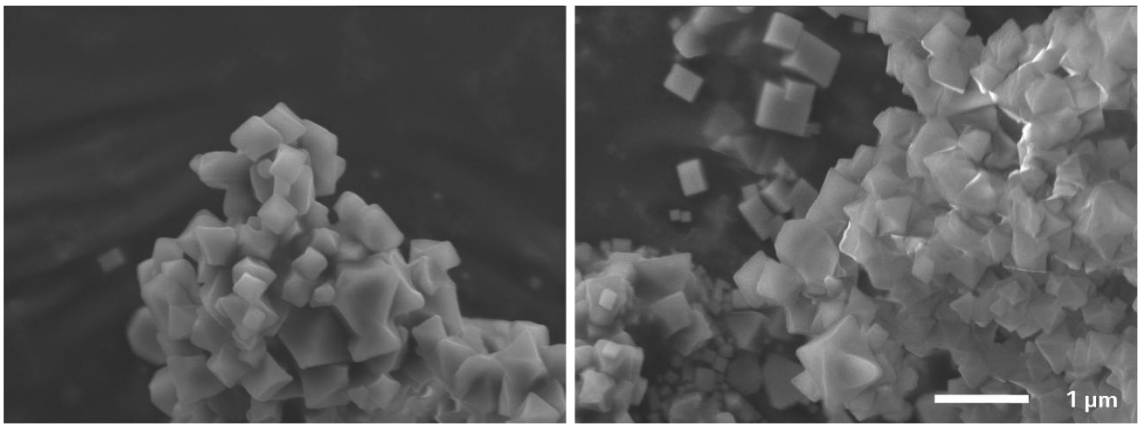

Figure 10.2: **Scanning electron micrographs of small octahedral Fe-MIL-101 crystals.**

The morphology of the Fe-MIL-101 crystals was investigated with the help of scanning electron microscopy (Figure 10.2). The size distribution of the crystals is very inhomogeneous; the size varies from about 50 to 500 nm. As described before, for materials with such large unit cells it is often difficult to obtain crystals that are

large enough for single crystal structure solutions. Due to the large unit cell of MIL-101 and in agreement with the published work for the Cr(III) analogue[72], we were not able to obtain larger single crystals.

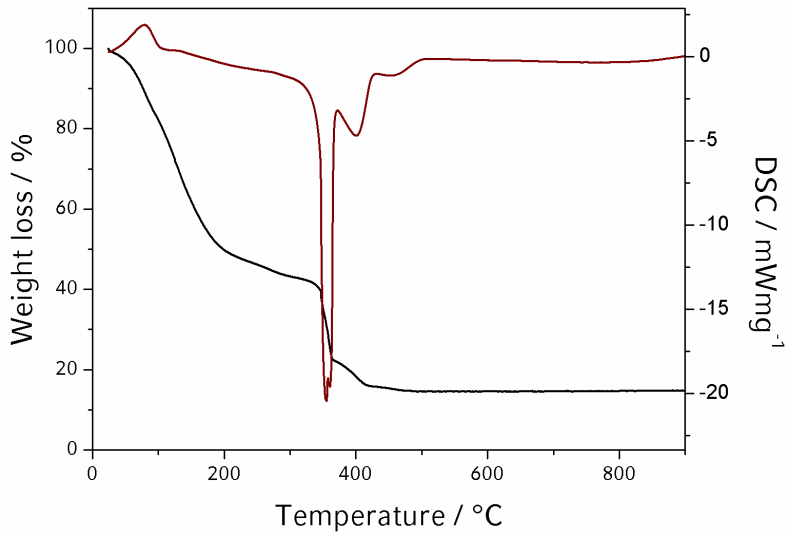

Figure 10.3: Thermogravimetric (TG) and Differential Scanning Calorimetric (DSC) Analysis of Fe-MIL-101.

The thermogravimetric analysis of Fe-MIL-101, displayed in Figure 10.3 shows a first weight loss of 55 % in one step between 25 and 250 °C. As there is only a small endothermic signal in the DSC corresponding to this weight loss, it is assigned to the removal of the guest molecules, i.e. DMF or water from inside the pores. The solvent free structure is stable up to 360 °C. The combustion of the organic part of the framework takes place via three steps (three exothermic peaks in the DSC-curve) and corresponds to a weight loss of about 20 %.

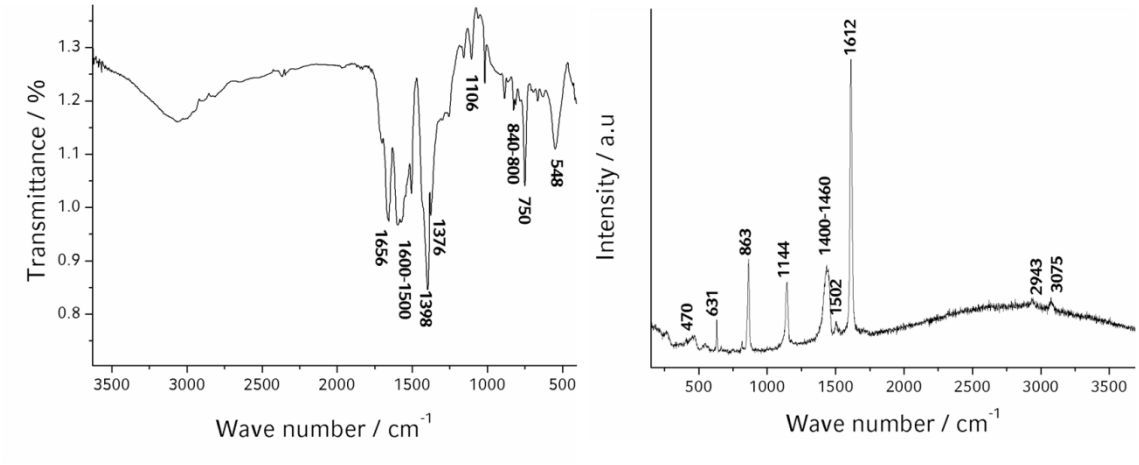

Figure 10.4: IR (left) and Raman (right) spectra of Fe-MIL-101.

The IR spectrum of Fe-MIL-101 and the Raman spectrum are displayed in Figure 10.4. The assignment of the observed bands to the particular groups is accomplished as follows.[249] The IR spectrum shows vibrational bands between 1560 cm^{-1} and 1376 cm^{-1} characteristic for the asymmetric and symmetric stretching vibration of the carboxylic groups of the BDC coordinated to a metal centre. The absence of bands in the region of 1715-1680 cm^{-1}, typical of protonated carboxylic groups, is in agreement with the framework structure of MIL-101 where no protonated carboxylic acid groups are present. Other characteristic bands of the ligand due to the C=C stretching vibration of the p-disubstituted aromatic ring were found between 1500 and 1600 cm^{-1}. Typical C-H vibrations for para-substituted aromatic compounds lie in the region between 800 and 840 cm^{-1}. The deformation vibration of the carboxylate groups is to be found at 750 cm^{-1}. The Fe-O stretching vibration from the FeO_6 octahedra is present at 548 cm^{-1}. The absorption band at 1656 cm^{-1} can be assigned to the C=O stretching of the amide (DMF), which is still present in the framework after synthesis. In the Raman spectrum, the peak at 470 cm^{-1} can be assigned to the Fe-O

vibration of the iron-oxygen octahedron. The deformation vibrations of the aromatic CH-groups can be found at 631, 863 and 1144 cm^{-1}. The absorption bands within the region between 1400 and 1460 cm^{-1} can be assigned to the symmetric stretch of the carboxylate groups. The C=C vibration is at 1502 cm^{-1}. The absorption band with the highest intensity (1612 cm^{-1}) is assigned to the asymmetric stretch of the carboxylate group.

11 Curriculum Vitae

Persönliche Daten

	Camilla Catharina Scherb, geboren am 20.09.1981 in München, ledig, Staatsangehörigkeit: deutsch

Schulen

1987-1991	Grundschule an der Parkstraße, Eichenau
1991-2000	Graf-Rasso Gymnasium, Fürstenfeldbruck
Mai 2000	Abitur (Note 1,1)

Studium und Promotion

Okt 2000 – heute	Chemiestudium an der Ludwig-Maximilians-Universität München, Wahlfach Patentrecht
Juni 2005 – Dez 2005	Diplomarbeit im Arbeitskreis Prof. T. Bein, LMU, Titel: „Templatsynthese und Hochdurchsatz-untersuchungen zur Darstellung von UTD-1“
Dez 2005	Diplom-Chemiker-Univ. (Gesamtnote 1,0)
Feb 2006 – heute	Promotion im Arbeitskreis Prof. T. Bein, LMU, Titel: „Controlling the Surface Growth of Metal-Organic Frameworks”

berufliche Tätigkeiten

Okt 2006 – heute	NanoScape AG, München, Nebentätigkeit als freie Mitarbeiterin
Feb 2006 – heute	Fachliche Anleitung und Ausbildung von Diplomanden und Studenten im Hauptstudium, Betreuung von Praktika in der Anorganischen und Physikalischen Chemie
Feb 2006 – heute	Verantwortliche wissenschaftliche Angestellte für Messgeräte (u.a. Röntgendiffraktometer, Oberflächen-Infrarotspektrometer, Quartz-Crystal Microbalance) im AK Bein: Wartung, Fehlerbehebung, Einweisung, Firmenkontakt

Zusatzqualifikationen

Sprachen:	Englisch (verhandlungssicher) Französisch (gut)
EDV-Kentnisse:	Microsoft Office, Microcal Origin (sehr gut); Corel Draw (gut); Programmiersprache: National Instruments LabView (gut)

12 Publications and Presentations

12.1 Publications

C. Scherb, R. Köhn, T. Bein, „Sorption properties of oriented Fe-MIL-88B crystals studied by X-ray diffraction and QCM", manuscript in preparation.

N. S. John, C. Scherb, M. Shöâeè, M. W. Anderson, M. P. Attfield, T. Bein "Single Layer Growth of Sub-micron Metal-Organic Framework Crystals Observed by *In Situ* Atomic Force Microscopy", manuscript submitted to the RSC journal "*Chemical Communications*" .

C. Scherb, A. Schödel, T. Bein "Directing the structure of metal-organic frameworks by oriented surface growth on an organic monolayer"; *Angewandte Chemie, International Edition* **2008,** *47,* 5777 (*Angewandte Chemie* **2008**, *120,* 5861).

E. Biemmi, C. Scherb, T. Bein, "Oriented Growth of the Metal Organic Framework $Cu_3(BTC)_2(H_2O)_3$ xH_2O – Tuneable with Functionalized Self-Assembled Monolayers"; *Journal of the American Chemical Society* **2007**, *129,* 8054.

12.2 Oral Presentations

C. Scherb, T. Bein, "Oriented growth of different metal-organic framework structures on self-assembled monolayers" *MOF 08*, Augsburg, 08.-10.10.2008.

C. Scherb, E. Biemmi, T. Bein, "Oriented Surface Growth of Metal-Organic Frameworks on Organic Monolayers" *4th International FEZA Conference* "Zeolites and Related Materials: Trends, Targets and Challenges", Paris, 02.-06.09.2008.

C. Scherb, E. Biemmi, T. Bein, "Growth of oriented metal-organic frameworks on self-assembled monolayers" *235th ACS National Meeting*, New Orleans (LA), 06.-10.04.2008.

E. Biemmi, A. Darga, C. Scherb, T. Bein, "Direct growth of HKUST-1 thin films on self-assembled monolayers: control of crystal orientation and vapour sorption measurements" *19. Deutsche Zeolith-Tagung*, Leipzig, 07.-09.03.2007.

12.3 Poster Presentations

C. Scherb, J. Williams, T. Bein „Sorption behaviour of oriented films of metal-organic frameworks“ *EuroNanoForum 2009*, Prague (Czech Republic), 02.-05.06.2009.

J. Williams, C. Scherb, T. Bein, “Functionalized Metal-Organic Framework Thin Films” accepted for the *MOFCAT 2009 Workshop - MOFs on the Road to Catalysis*, Oslo (Norway), 17.-19.06.2009.

J. Williams, C. Scherb, T. Bein, “The Orientated Fabrication of Functionalized Metal-Organic Framework Thin Films” accepted for the *XXXIInd Annual British Zeolite Association Conference*, University of Cumbria, Ambleside (U.K.), 23.-28.08.2009.

C. Scherb, E. Biemmi, T. Bein, “Growth of Metal-organic Framework thin films on gold substrates functionalized with self-assembled monolayers” *Second International Symposium Advanced Micro- and Mesoporous Materials*, Varna (Bulgaria), 06.–09.09.2007.

E. Biemmi, C. Scherb and T. Bein, “Morphological evolution of oriented HKUST-1 crystal layers on –OH, -COOH, and $-CH_3$ functionalized SAMs on gold substrates.” *19. Deutsche Zeolith-Tagung*, Leipzig, 07.-09.03.2007.

E. Biemmi, C. Scherb, T. Bein, “Growth of $Cu_3(BTC)_2$ thin films on gold substrates functionalized with self-assembled monolayers” *CeNS Winter School*, Burg Mauterndorf (Austria), 12.-16.02.2007.